
Heat Transfer, Carryover and Fall Back in PWR Steam Generators During Transients

Prepared by L-H. Liao, A. Parlos, P. Griffith

Massachusetts Institute of Technology

Prepared for
U.S. Nuclear Regulatory Commission

and
Electric Power Research Institute

NOTICE

This report was prepared as an account of work sponsored by an agency of the United States Government. Neither the United States Government nor any agency thereof, or any of their employees, makes any warranty, expressed or implied, or assumes any legal liability of responsibility for any third party's use, or the results of such use, of any information, apparatus, product or process disclosed in this report, or represents that its use by such third party would not infringe privately owned rights.

NOTICE

Availability of Reference Materials Cited in NRC Publications

Most documents cited in NRC publications will be available from one of the following sources:

1. The NRC Public Document Room, 1717 H Street, N.W.
Washington, DC 20555
2. The Superintendent of Documents, U.S. Government Printing Office, Post Office Box 37082,
Washington, DC 20013-7082
3. The National Technical Information Service, Springfield, VA 22161

Although the listing that follows represents the majority of documents cited in NRC publications, it is not intended to be exhaustive.

Referenced documents available for inspection and copying for a fee from the NRC Public Document Room include NRC correspondence and internal NRC memoranda; NRC Office of Inspection and Enforcement bulletins, circulars, information notices, inspection and investigation notices; Licensee Event Reports; vendor reports and correspondence; Commission papers; and applicant and licensee documents and correspondence.

The following documents in the NUREG series are available for purchase from the GPO Sales Program: formal NRC staff and contractor reports, NRC-sponsored conference proceedings, and NRC booklets and brochures. Also available are Regulatory Guides, NRC regulations in the *Code of Federal Regulations*, and *Nuclear Regulatory Commission Issuances*.

Documents available from the National Technical Information Service include NUREG series reports and technical reports prepared by other federal agencies and reports prepared by the Atomic Energy Commission, forerunner agency to the Nuclear Regulatory Commission.

Documents available from public and special technical libraries include all open literature items, such as books, journal and periodical articles, and transactions. *Federal Register* notices, federal and state legislation, and congressional reports can usually be obtained from these libraries.

Documents such as theses, dissertations, foreign reports and translations, and non-NRC conference proceedings are available for purchase from the organization sponsoring the publication cited.

Single copies of NRC draft reports are available free, to the extent of supply, upon written request to the Division of Technical Information and Document Control, U.S. Nuclear Regulatory Commission, Washington, DC 20555.

Copies of industry codes and standards used in a substantive manner in the NRC regulatory process are maintained at the NRC Library, 7920 Norfolk Avenue, Bethesda, Maryland, and are available there for reference use by the public. Codes and standards are usually copyrighted and may be purchased from the originating organization or, if they are American National Standards, from the American National Standards Institute, 1430 Broadway, New York, NY 10018.

Heat Transfer, Carryover and Fall Back in PWR Steam Generators During Transients

Manuscript Completed: July 1985
Date Published: September 1985

Prepared by
L-H. Liao,* A. Parlos,* P. Griffith**

Department of Nuclear Engineering*
Department of Mechanical Engineering**
Massachusetts Institute of Technology
Cambridge, MA 02139

Prepared for
Division of Accident Evaluation
Office of Nuclear Regulatory Research
U.S. Nuclear Regulatory Commission
Washington, D.C. 20555
NRC FIN B7229

and
Electric Power Research Institute
P.O. Box 1042
Palo Alto, CA 94303

ABSTRACT

The concern over Pressurized Thermal Shock(PTS), along with many other concerns, indicates the need for accurate knowledge of the steam generator behavior during the blowdown of the steam generator secondary side. To fulfill this need a computer program, SIT-SG (Simulator of Transient in Steam Generator), is developed. This is a one-dimensional best-estimate code with the assumption that the vapor and liquid phases are in thermal equilibrium but not homogeneous. The drift flux model is used to describe the relationship between the vapor and the liquid phase velocity. No momentum equation is required for SIT-SG because the detailed pressure distribution in the vessel is not important for the blowdown process.

Based on the comparisons between the code predictions and the data obtained from the experiments conducted in Battelle-Frankfurt and GE, the best drift flux model constants for various flow regimes are selected. SIT-SG has been used to predict the carryover, fall back, and heat transfer for the M.I.T. steam generator blowdown experiments. The results are encouraging.

It is found that the measured dryout front is much higher than the calculated mixture level. If the effective heat transfer area is determined from the mixture level, the primary-to-secondary heat transfer will be substantially underpredicted.

From the result of the liquid hold up study we would expect to find two mixture levels, one in the bottom of the steam generator and one above the top tube support plate, provided that flooding occurs at all.

CONTENTS

	<u>Page</u>
ABSTRACT.....	iii
TABLE OF CONTENTS.....	iv
LIST OF TABLES.....	vii
LIST OF FIGURES.....	viii
NOMENCLATURE.....	xv
EXECUTIVE SUMMARY.....	1
1 INTRODUCTION.....	5
1.1 General Need For a Better Steam Generator Modeling...	5
1.2 Objectives of This Work.....	5
1.3 Applications of a Better Steam Generator Model.....	8
1.3.1 Pressurized Thermal Shock Induced by Steam Generator Blowdown.....	8
1.3.1.1 Pressurized Thermal Shock.....	8
1.3.1.2 Pressurized Thermal Shock Induced by Steam Generator Blowdown.....	8
1.3.2 Steam Tube Rupture Induced by Steam Line Break..	9
1.3.3 Reactivity Insertion in the Primary System.....	10
1.3.4 Impact on the Containment Design.....	10
1.3.5 Blowdown in Boiling Water Reactor.....	10
2. ANALYTICAL SYSTEM MODELS.....	11
2.1 Hydrodynamic Model.....	11
2.1.1 Conservation Equations.....	11
2.1.2 Flow Regime and Flow Regime Transition Criteria.	12
2.1.3 Drift Flux Model.....	13
2.1.4 Break Flow Model.....	20
2.1.4.1 Critical Flow Model.....	20
2.1.4.2 Subcritical Flow Model.....	22
2.2 Heat Transfer Model.....	22
2.2.1 Heat Conduction Model.....	23
2.2.2 Lumped Parameter Model.....	23
2.2.3 Heat Transfer Model.....	24
2.3 Water Level Model.....	25
2.3.1 Water Level Propagation Model.....	26
2.3.2 Water Level Reappearance Criteria.....	28

2.4	Radioactive Particle Propagation Model.....	29
2.5	Pool Entrainment Model.....	30
3.	METHODS OF SOLUTION.....	34
3.1	Hydrodynamic Modeling.....	34
3.1.1	The Global Vessel System.....	35
3.1.2	The Local Control Volume System.....	36
3.2	Heat Conduction Model.....	39
3.3	Time Step Control.....	40
3.4	Implementation of Critical Flow Calculation.....	41
3.5	Determination of Void Fraction Distribution in a Control Volume.....	42
4.	VERIFICATION OF MODEL.....	44
4.1	Battelle-Frankfurt Blowdown Test.....	44
4.1.1	Test Description.....	44
4.1.2	Input Model Description.....	45
4.1.3	Code Prediction and Comparison with Data.....	45
4.2	GE Small Vessel Blowdown Test.....	46
4.2.1	Description of the Experiments.....	46
4.2.2	Input Model Description.....	46
4.2.3	Code Prediction and Comparison with Data.....	47
4.2.3.1	Level Swell Test.....	47
4.2.3.2	Blowdown Test 1004-3.....	48
4.2.3.3	Blowdown Test 1004-2.....	48
4.3	GE Large Vessel Blowdown Test.....	48
4.3.1	Description of the Experiment.....	48
4.3.2	Input Model Description.....	48
4.3.3	Code Prediction and Comparison with Data.....	49
4.4	Steam Generator Blowdown Test in M.I.T.....	49
4.4.1	Description of Experimental Facility.....	49
4.4.2	Empty Vessel Test.....	50
4.4.2.1	Test Description.....	50
4.4.2.2	Computer Code Input Model Description.....	50
4.4.2.3	Code Prediction and Comparison with Data....	51
4.4.2.3.1	Initial Pressure of 1055 psi.....	51
4.4.2.3.2	Initial Pressure of 800 psi.....	55
4.4.3	Test with Rod Bundles.....	56

4.4.3.1 Test Description.....	56
4.4.3.2 Computer Code Input Model Description.....	56
4.4.3.3 Code Prediction and Comparison with Data....	56
5. LIQUID HOLD UP EXPERIMENT.....	59
5.1 Facility Description.....	59
5.2 Experimental Procedures and Results.....	60
5.2.1 Experiment with Fixed Water Inventory (F - Series Experiment).....	60
5.2.2 Countercurrent Flow Experiment(W-Series Tests)..	61
5.2.3 Transient Experiment (F-Series Tests).....	62
5.3 Conclusion.....	63
6. SUMMARY AND RECOMMENDATIONS.....	64
6.1 Summary.....	64
6.2 Recommendations.....	64
7. CONCLUSION.....	66
REFERENCES.....	191

LIST OF TABLES

<u>TABLE</u>		<u>PAGE</u>
1	Flow Regime Transition Criteria	69
2	Drift Flux Model Constant V_{gj} Used in Figures 3 and 4	69
3	Effect of Pool Entrainment Model on the Critical Flow Rate	70

LIST OF FIGURES

<u>FIGURE</u>		<u>PAGE</u>
1	Typical Nodalization for Steam Line Break	71
2	Schematic of Four Loop Steam Line Break	72
3	Comparison of Various Weighted Mean Drift Velocities as Function of Void Fraction at a Pressure of 1000 psi	73
4	Comparison of Various Weighted Mean Drift Velocities as Function of Void Fraction at a Pressure of 300 psi	74
5	The Collapsed Water Level and the Mixture Water Level	75
6	The Mixture Level and the Void Fraction Distribution	76
7	Schematic of the Global Vessel System and the Local Control Volume System	77
8	Nodalization for Heat Conduction Model	78
9	Comparison Between the Pressure Step Size and the Time Step Size	79
10	Various Void Fraction Distribution in a Control Volume	80
11	Comparison Between the Measured and Predicted Pressure for Battelle-Frankfurt Blowdown Test SWR-2R	81
12	Comparison Between the Measured and Predicted Break Mass Flow Rate for Battelle-Frankfurt Test SWR-2R	81
13	Comparison Between the Measured and Predicted Mixture Level for Battelle-Frankfurt Test SWR-2R	82
14	Instrumentation for G.E. Small Vessel Blowdown Test	83
15	Comparison Between the Measured and Predicted Pressure for Level Swell Test	84
16	Comparison Between the Measured and Predicted Mixture Level for Level Swell Test	85
17	Comparison Between the Measured and Predicted Pressure for G.E. Small Vessel Test 1004-3	86
18	Comparison Between the Measured and Predicted Mixture Level for G.E. Small Vessel Test 1004-3	87

FIGUREPAGE

19	Comparison Between the Measured and Predicted Pressure for G.E. Small Vessel Test 1004-2	88
20	Comparison Between the Measured and Predicted Mixture Level for G.E. Small Vessel Test 1004-2	89
21	Schematic of G.E. Large Vessel Blowdown Test Facility	90
22	Comparison Between the Measured and Predicted Pressure for G.E. Large Vessel Test 5801-15	91
23	Comparison Between the Measured and Predicted Mixture Level for G.E. Large Vessel Test 5801-15	92
24	Schematic of Steam Generator Simulator Test Facility	93
25	Schematic of U-tube Steam Generator	94
26	Break Geometry(3/8" Case)	95
26a	Pressure Transients with Downcomer Valve Open and Initial Pressure 1055 psi	96
26b	Pressure Transients with Downcomer Temperature 20°F Lower Than the Vessel and Initial Pressure 1055 psi	97
26c	Carryover Mass Transients with Downcomer Valve Open and Initial Pressure 1055 psi	98
26d	Carryover Mass Transients with Downcomer Temperature 20°F lower than the vessel and initial pressure 1055 psi	99
27	Comparison Between the Measured and Predicted Pressure for MIT Test Run 5, 3/8" break	100
28	Comparison Between the Measured and Predicted Carryover for MIT Test Run 5, 3/8" break	101
29	Comparison Between the Measured and Predicted Pressure for MIT Test Run 9, 1/4" break	102
30	Comparison Between the Measured and Predicted Carryover for MIT Test Run 9, 1/4" break	103
31	Comparison Between the Measured and Predicted Pressure for MIT Test Run 19, 1/8" break	104
32	Comparison Between the Measured and Predicted Carryover for MIT Test Run 19, 1/8" break	105
33	Predicted Superficial Vapor Velocity for MIT Test Run 5, 3/8" Break	106

<u>FIGURE</u>		<u>PAGE</u>
34	Predicted Superficial Liquid Velocity for MIT Test Run 5, 3/8" Break	107
35	Trajectory of States for MIT Test Run 5, 3/8" Break, with Lines of Constant Void Fraction	108
36	The Region of Interest and the Flow Regime Boundary for MIT Test Run 5, 3/8" Break	109
37	Pool Entrainment for a Pressure of 1000 psi	110
38	Pool Entrainment for a Pressure of 400 psi	111
39	Predicted Mixture Water Level for MIT Test Run 19, 1/8" Break	112
40	Predicted Break Flow Rate for MIT Test Run 19, 1/8" Break	113
41	Predicted Break Flow Rate for MIT Test Run 9, 1/4" Break	114
42	Predicted Break Flow Rate for MIT Test Run 5, 3/8" Break	115
43	Predicted Break Flow Rate for MIT Test Run 1, 1/2" Break	116
44	Predicted entrainment for MIT Test Run 5, 3/8" Break	117
45	Predicted Time Integration of Heat Transfer for MIT Test Runs 1,5,9,19	118
46	Predicted Time Integration of Heat Transfer for MIT Test Run 25, 1/16" Break	119
47	Predicted Time Integration of Blowdown Energy for MIT Test Runs 1,5,9,19	120
48	Predicted Time Integration of Blowdown Energy for MIT Test Run 25, 1/16" Break	121
49	Measured Pool Temperature for MIT Test Runs 33,34,35,36,37	122
50	Predicted Pool Temperature for MIT Test Runs 33,34,35,36,37	123
51	Comparison Between the Measured and Predicted Pressure for MIT Test Run 7, 3/8" Break	124
52	Comparison Between the Measured and Predicted	

FIGUREPAGE

	Pressure for MIT Test Run 11, 1/4" Break	125
53	Comparison Between the Measured and Predicted Pressure for MIT Test Run 22, 1/8" Break	126
54	Comparison Between the Measured and Predicted Carryover for MIT Test Run 7, 3/8" Break	127
55	Comparison Between the Measured and Predicted Carryover for MIT Test Run 11, 1/4" Break	128
56	Comparison Between the Measured and Predicted Carryover for MIT Test Run 22, 1/8" Break	129
57	Schematic of the Tube Support Plates	130
58	Comparison Between the Measured and Predicted Pressure for MIT Test Run 48, 1/8" Break	131
59	Comparison Between the Measured and Predicted Pressure for MIT Test Run 49, 1/4" Break	132
60	Comparison Between the Measured and Predicted Pressure for MIT Test Run 50, 3/8" Break	133
61	Comparison Between the Measured and Predicted Pressure for MIT Test Run 51, 1/2" Break	134
62	Comparison Between the Measured and Predicted Carryover for MIT Test Run 48,50	135
63	Comparison Between the Measured and Predicted Carryover for MIT Test Run 49,51	136
64	Comparison Between the Predicted Mixture Level and the Measured Dryout Front for MIT Test Run 51, 1/2" Break	137
65	Comparison Between the Predicted Mixture Level and the Measured Dryout Front for MIT Test Run 50, 3/8" Break	138
66	Comparison Between the Predicted Mixture Level and the Measured Dryout Front for MIT Test Run 49, 1/4" Break	139
67	Comparison Between the Predicted Mixture Level and the Measured Dryout Front for MIT Test Run 48, 1/8" Break	140
68	Calculated Superficial Vapor Velocity for MIT Test Run 51, 1/2"Break	141

<u>FIGURE</u>		<u>PAGE</u>
69	Calculated Superficial Vapor Velocity for MIT Test Run 50, 3/8"Break	142
70	Calculated Superficial Vapor Velocity for MIT Test Run 49, 1/4"Break	143
71	Calculated Superficial Vapor Velocity for MIT Test Run 48, 1/8"Break	144
72	Calculated Superficial Liquid Velocity for MIT Test Run 51, 1/2"Break	145
73	Calculated Superficial Liquid Velocity for MIT Test Run 50, 3/8"Break	146
74	Calculated Superficial Liquid Velocity for MIT Test Run 49, 1/4"Break	147
75	Calculated Superficial Liquid Velocity for MIT Test Run 48, 1/8"Break	148
76	Calculated Break Flow Rate for MIT Test Run 51, 1/2" Break	149
77	Calculated Break Flow Rate for MIT Test Run 50, 3/8" Break	150
78	Calculated Break Flow Rate for MIT Test Run 49, 1/4" Break	151
79	Calculated Break Flow Rate for MIT Test Run 48, 1/8" Break	152
80	Calculated Time Integrated Heat Transfer for MIT Test Run 48 to 51	153
81	Calculated Heat Transfer Rate for MIT Test Run 48 to 51	154
82	Comparison Between the Predicted and Measured Pool Temperature for MIT Test Run 40,44	155
83	Comparison Between the Predicted and Measured Pool Temperature for MIT Test Run 39,45	156
84	Flow and Void Fraction Distribution Parameter,C0, For MIT Test Run 51, 1/2" Break	157
85	Flow and Void Fraction Distribution Parameter,C0, For MIT Test Run 50, 3/8" Break	158
86	Flow and Void Fraction Distribution Parameter,C0, For	

FIGUREPAGE

	MIT Test Run 49, 1/4" Break	159
87	Flow and Void Fraction Distribution Parameter, C_0 , For MIT Test Run 48, 1/8" Break	160
88	Weighted Mean Drift Velocity, V_{gj} , for MIT Test Run 51, 1/2" Break	161
89	Weighted Mean Drift Velocity, V_{gj} , for MIT Test Run 50, 3/8" Break	162
90	Weighted Mean Drift Velocity, V_{gj} , for MIT Test Run 49, 1/4" Break	163
91	Weighted Mean Drift Velocity, V_{gj} , for MIT Test Run 48, 1/8" Break	164
92	Predicted Void Fraction Distribution for MIT Test Run 51, 1/2" Break	165
93	Predicted Void Fraction Distribution for MIT Test Run 50, 3/8" Break	166
94	Predicted Void Fraction Distribution for MIT Test Run 49, 1/4" Break	167
95	Predicted Void Fraction Distribution for MIT Test Run 48, 1/8" Break	168
96	Time Step Size for MIT Test Run 51, 1/2" Break	169
97	Time Step Size for MIT Test Run 50, 3/8" Break	170
98	Time Step Size for MIT Test Run 49, 1/4" Break	171
99	Time Step Size for MIT Test Run 48, 1/8" Break	172
100	Trajectory of Radioactive Material for MIT Test Run 51, 1/2" Break	173
101	Trajectory of Radioactive Material for MIT Test Run 50, 3/8" Break	174
102	Trajectory of Radioactive Material for MIT Test Run 49, 1/4" Break	175
103	Trajectory of Radioactive Material for MIT Test Run 48, 1/8" Break	176
104	Schematic of the Apparatus for the Liquid Hold Up Test	177
105	Different Types of Plates Used in the Liquid Hold Up	

<u>FIGURE</u>		<u>PAGE</u>
	Experiment	178
106	Results for Liquid Hold Up Test Run F-A1	179
107	Results for Liquid Hold Up Test Run F-B1	179
108	Results for Liquid Hold Up Test Run F-C1	180
109	Results for Liquid Hold Up Test Run F-D1	180
110	Results for Liquid Hold Up Test Run W-A1	181
111	Results for Liquid Hold Up Test Run W-B3	181
112	Results for Liquid Hold Up Test Run W-C3	182
113	Results for Liquid Hold Up Test Run W-D3	182
114	Results for Liquid Hold Up Test Run W-D1, Bottom Plate Liquid Hold Up	183
115	Results for Liquid Hold Up Test Run W-D1, Top Plate Liquid Hold Up	183
116	Comparison of Liquid Hold Up Experiment and Wallis Flooding Correlation	184
117	Recommended Drift Flux Model Constant C_0 , Churn-Turbulent Flow Regime	185
118	Recommended Drift Flux Model Constant V_{gj} , Churn-Turbulent Flow Regime	186
119	Recommended Drift Flux Model Constant C_0 , Annular Flow Regime	187
120	Recommended Drift Flux Model Constant V_{gj} , Bubbly Flow Regime	188
121	Recommended Drift Flux Model Constant V_{gj} , Annular Flow Regime	189
122	Dryout Front Data from Blowdown Experiment	190

NOMENCLATURE

A_i	- Heat Transfer Area on the Primary Side
A_j	- Flow Area at Junction j
A_m	- Mean Heat Transfer Area
A_o	- Heat Transfer Area on the Secondary Side
C_o	- Drift Flux Model Constant, Flow and Void Fraction Distribution Parameter
D	- Diameter of Flow Passage
e_l	- Liquid Internal Energy
e_v	- Vapor Internal Energy
F_o	- Fourier Modulus
f_o	- Friction Factor in Eqs.(2.38), (2.39)
f	- Fouling Factor in Eqs. (2.47), (2.48)
G	- Mass Flux
g	- 32.2 ft/sec
g_o	- 32.2 lbf ft/(lbf sec ²)
$H(t)$	- Elevation of Radioactive Material at Time t
H_i	- Total Fluid Enthalpy in Control Volume i
h_o	- Initial Elevation of Radioactive Material at Time t_o
h	- Heat Transfer Coefficient in Eq.(2.42)
h_c	- Break Enthalpy
h_g	- Saturated Vapor Enthalpy
h_{gi}	- Heat Transfer Coefficient in the Primary Side
h_l	- Liquid Enthalpy
h_v	- Vapor Enthalpy
j	- Total Superficial Velocity, $j_v + j_l$
j_v	- Superficial vapor velocity
$(j_v)_{2-3}$	- Transition Velocity From Churn-Turbulent Flow Regime to Annular Flow Regime
$(j_v)_{3-3a}$	- Transition Velocity From Annular Flow Regime to Liquid Dispersed Flow Regime
k	- Pressure Loss Coefficient Due to Contraction and Expansion in Eq. (2.38)
k	- Thermal Conductivity in Eq. (2.41)
L	- Length
L_i	- Length of Control Volume
M_i	- Mass of Conductor in Eq. (2.42)
M_i	- Mass of Fluid in Control Volume i
p	- Pressure
p_o	- Stagnation Pressure
p_t	- Pressure at Throat
Δp	- Pressure Drop
Q	- Heat Transfer Rate
Q_{wl}	- heat transfer rate from wall to liquid
Q_{wv}	- heat transfer rate from wall to vapor
q	- Heat Source per Unit Volume
r_i	- Inside Radius of the Steam Generator Tube
r_o	- Outside Radius of the Steam Generator Tube
s_o	- Slip Ratio
T	- Temperature of Conductor
T_f	- Temperature of Fluid
t	- time
U	- Overall Heat Transfer Coefficient From the Primary

	Side to the Secondary Side
V_i	- Volume of Control Volume i
V_B	- Bubble Velocity in Wilson Model
V_l	- Liquid Velocity
V_v	- Vapor velocity
V_{gj}	- Drift Flux Model Constant, Weighted Mean Drift Flux Velocity
V_w	- Propagation Velocity of Mixture Level
x_c	- Quality at Throat

Superscript

n	- State n
$n+1/2$	- State $n+1/2$, Between State n and $n+1$
$n+1$	- State $n+1$
$(-)$	- Location Just Below the Mixture Level
$(+)$	- Location Just Above the Mixture Level

Subscript

G	- Global Vessel System
$i-1$	- Control Volume $i-1$, Located below Control Volume i
i	- Control Volume i
$i+1$	- Control Volume $i+1$, Located Above Control Volume i
$j-1$	- Junction $j-1$, Located Between Control Volumes $i-1, i$
j	- Junction j , Located Between Control Volumes $i, i+1$
in	- Inlet to the Global Vessel System
out	- Exit to the Global Vessel System

Greek

α	- Void Fraction
μ	- Fluid Viscosity
ϵ	- Wall Thickness of the Steam Generator Tube
σ	- Surface Tension
ρ_v	- Vapor Density
ρ_l	- Liquid Density
ρ_g	- Saturated Vapor Density
ρ_f	- Saturated Liquid Density
ρ_{fg}	- Density Difference Between Liquid and Vapor Phase

EXECUTIVE SUMMARY

A computer program, called SIT-SG, has been developed to predict the heat transfer on the secondary side of a steam generator, the pressure, the carryover, the mixture water level, the flow rate distribution, and the void fraction distribution during the steam generator blowdown. This computer program is developed for best estimate predictions with a fast running capability.

Flow regime dependent drift flow model constants are used to take into account the difference between the liquid velocity and the vapor velocity. A large discrepancy has been found for current available drift flux model constants. These discrepancies have a large effect on the water level prediction.

As far as the mixture level is concerned, the drift flux constants in the churn-turbulent flow regime is most important. The following drift flux constants in the churn-turbulent flow regime are recommended. The flow and void fraction distribution parameter C_0 is selected from Ishii's correlation and its value as function of pressure and void fraction is shown in Fig. 117. The weighted mean drift velocity being selected is originated from the equation proposed by Zuber with the coefficient given by Bertodano. This correlation is used in conjunction with the upper limitations provide by the slug flow regime correlation and a constant value of 3 ft/sec, which is the maximum drift velocity having been observed. The weighted mean drift velocity so obtained is plotted in terms of pressure and vessel diameter, in Fig. 118. The recommended drift flux constants for the other flow regimes include: (i) V_{gj} and C_0 from Wallis correlation for bubbly flow regime (ii) V_{gj} and C_0 from Ishii correlation for annular flow regime. For bubbly flow regime, the recommended C_0 is 1.0 while the V_{gj} is shown in Fig. 119. For annular flow regime, the recommended C_0 is shown in Fig. 120 and the V_{gj} , with $D=0.34$ ft, is shown in Fig. 121. The correlations used for the various flow regimes are connected with a smoothing scheme.

From the computer code calculations, the key parameters in the transient can be identified and a better understanding of the transient process has been obtained. With respect to the transient process and the computer code modeling, the following conclusions can be drawn.

- . For the blowdown process in steam line break, there are three periods can be identified: (i) pool swelling period (ii) water level disappearance period (iii) water level reappearance period. Because the characteristic behavior is different for each period, computer modeling should be able to distinguish these periods and simulate them appropriately.

- . As far as the break flow is concerned, the critical flow model is the only model which is important for determining the amount of outgoing flow in the pool swelling period and the water level reappearance period. The drift flux model is as important as the critical flow model in the water level disappearance period.
- . The heat transfer during the transient is very important to the transient response in steam generator secondary side. For the heat transfer calculation, it is very important to know whether the tube is dry or wet. If the tube is wet, the heat transfer is excellent. The secondary side heat transfer coefficient for the wet surface itself is, however, not important because the wall conduction, the primary heat transfer coefficient and the fouling factor are the real limits.
- . The pool entrainment phenomena has a small effect on both the total amount of outgoing fluid and the transient water level response.
- . In general, the thermal hydraulic properties in a control volume can be considered as homogeneous. However, special attention should be focused on the modeling of the node which contains the sharp water-vapor interface. Interpretation of node average quantities can be misleading under many circumstances. For example, using the node average void fraction to determine flow regime can result in significant error. In addition to void fraction, the knowledge of flow developing history and velocity level are also important for determining the flow regime in a control volume.
- . During the transient, the flow regime in the bottom control volume is bubbly flow initially. It changes into churn-turbulent flow regime after a very short period and stays on churn-turbulent flow regime thereafter. The period for which the bubbly flow regime prevails is so short that the modeling of bubbly flow regime can be ignored. This conclusion is drawn from the calculations for our experiment. This experiment is equivalent to a break without feedwater. When this is applied to a real steam generator, the flow rate and the temperature of both the feedwater and auxiliary feedwater will have some effect on this conclusion due to the additional overcooling. These effects are, however, not expected to be very large because the feedwater has high temperature and the auxiliary feedwater has low flow rate. For the control volumes above the initial water level, the flow regime changes from the annular or liquid dispersed flow regime to churn-turbulent flow regime and back to annular or liquid dispersed flow regime. Because the flow regime in a fixed space is changing as the transient proceeds, we do not recommend a fixed drift flux constant for a certain given

space. Instead, we recommend a set of correlations which can be used to calculate the drift flux constants for different flow regimes.

SIT-SG has been used to perform the pressure and the mixture level calculation for the Battelle-Frankfurt blowdown experiment, the G.E. small vessel, and the G.E. large vessel blowdown test. SIT-SG has also been used to predict the pressure, the water level, the carryover, the pool temperature, and the heat transfer from the hot wall for the M.I.T. steam generator simulator. The comparisons between the code prediction and the experimental data give rise to the following conclusions:

- . Good agreement is observed between the code prediction and experimental data for the pressure, the total amount of outgoing fluid and the suppression pool temperature response. These results justify our assumption in the code: (i) The pressure distribution is not important inside the secondary vessel and no momentum equation is required (ii) The behavior of the fluid in the vessel is basically one dimensional and one dimensional equation is capable of describing the system response (iii) Drift flux model is an adequate model for predicting the two-phase flow under blowdown conditions (iv) Thermal equilibrium exists between vapor and liquid phases.
- . The slip equilibrium critical flow model proposed by Fauske is selected for the calculation of two phase critical flow rate. Good agreement has been achieved by comparing the predicted pressure response with the experimental data measured in GE large vessel blowdown test, M.I.T. empty vessel test, and M.I.T. tests with internals. Therefore, this model is good for the venturi nozzle as well as for the blowdown pipe with L/D equals 20. Short L/D nozzles were not tested.
- . The measured dryout front is much higher than the predicted mixture water level. Consequently, the calculated effective heat transfer area is much smaller than the measured effective heat transfer area. The heat transfer rate from steam generator primary side to secondary side and the duration of effective heat transfer will be underpredicted if the dryout front is regarded as the mixture level. However, it should be pointed out that in our experiment, the heat flux is quite low which leads to a reduced evaporation rate of liquid film and consequently results in a larger difference between dryout front and mixture level. Further study on the relation between dryout front and mixture level as function of entrainment rate, deposition rate, evaporation rate is recommended.
- . Our model is developed under the assumption of thermal equilibrium. This assumption is quite good for our empty vessel experiment which shows that the vapor temperature

stays at the saturated temperature throughout the whole blowdown. For the experiment installed with rod bundle, superheat of vapor temperature is observed. Although the assumption isn't consistent with the real vapor state, the pressure and the carryover show the same degree of agreement as the empty vessel experiment. This suggests the effect of vapor superheat is insignificant on the pressure and the total amount of outgoing fluid.

- . From the liquid hold up experiment, we find that flooding can occur at the tube support plates, where the flow area is minimum. The potential for the liquid hold up due to flooding is largest for the top tube support plate. When this is applied to the blowdown in the steam generator secondary side, we would expect to find two mixture level, one in the bottom of the steam generator and one above the top tube support plate, provided that flooding occurs.

Several areas require further investigation are described as the followings:

- . In SIT-SG, the effect of the separator to the blowdown is ignored. During a steam line break or a combined steam line break plus tube rupture, the behavior of the separator is unknown at present. It is expected that as the flashing occurs, the water level swells and the flow direction in the drain line of the separator may reverse. The exact conditions which lead to flow reversal in the drain line have not been delineated. It is also expected that the separator may have large effects on the amount of radioactive material released in the combined steam line break plus tube rupture. Therefore, a study of the performance of separator during blowdown is recommended.
- . The calculation results show that large discrepancies exist between the calculated mixture level and the measured dryout front. It is suspected that the large discrepancy is a result of the low heat flux on the rod bundle surface. In a real steam generator, the difference may be smaller due to the higher surface heat flux in which a little bit of spray won't be able to keep the tube wet. It is recommended to study the effect of heat flux on the discrepancies between the predicted mixture level and the measured dryout front.

1. INTRODUCTION

1.1 General Need For a Better Steam Generator Modeling

The steam generator is the major heat sink and one of the most important dynamic components in pressurized water reactor(PWR) power plants. Suitable heat removal through the steam generator is essential for maintaining a steady state during normal operation conditions and for recovering from transients during off-normal operation conditions. In addition, the steam generator is an important component in normal transients and can, itself, be the cause of transients. An increase in heat removal by the secondary system can be caused by malfunction of feedwater system, of steam pressure regulator, steam system piping failures, etc. On the other hand, a decrease in heat removal by the secondary system can be caused by loss of external electric load, turbine trip, loss of condenser vacuum, loss of normal feedwater flow, etc. Either by being a controlling component or an accident initiating component, the steam generator is important in a wide range of transients. Nevertheless, the present steam generator models though simple are not very accurate. Usually, design calculations are performed by using conservative assumptions so as to produce a bounding calculation. However, there are several drawbacks in this kind of approach:

1. For a specific bounding calculation, it is very difficult or even impossible to quantify the degree of conservatism associated with the calculation. Sometimes it is also difficult to tell which direction is conservative.
2. A bounding calculation will cause distortion in our perception of the overall system behavior and preclude the understanding of actual system response.
3. Due to the distortion in the sequence of events, there are very complex effects resulting from the interaction of the distorted system operations. As a result, conservative assumptions don't necessarily lead to optimum maneuvers. Therefore, the trend is now to switch from the bounding calculations to the best estimate calculations.

The need for a better understanding of the steam generator response to transient conditions is dictated by the increased incidence of steam generator tube ruptures. Among the other general needs for accurate knowledge of the steam generator behavior, attention has been focused on the blowdown of the secondary system in a steam line break. This can be an initiating event leading to the pressurized thermal shock(PTS). The reactivity insertion in the primary system, and the impact of containment design resulting from the steam line break or the feedwater line break are also important. A brief description for each of the scenarios will be given in the following subsections followed by the section describing the objectives of this work.

1.2 Objectives of this Work

As a part of the effort mounted to resolve the pressurized thermal shock issue, this work is directed toward the study of the carryover, fall back and heat transfer on the secondary side of the steam generator which is subjected to a steam line break or a feed line break. A computer program named SIT-SG, stands for Simulator of Transient in Steam Generator, has been established to model the steam generator during blowdown so that realistic estimates of the steam generator thermal hydraulic behavior can be made and appropriate strategies for handling the transient can be identified.

Due to the complexity of current PWR steam generators and associated systems, a large number of assumptions and simplifications are currently employed in performing thermal hydraulic analysis. For example, in the Final Safety Analysis Report (FSAR), a typical calculation for a feedline break assumes the break flow quality to be zero until all the liquid mass is removed from the steam generator. In contrast to this, the break flow quality is commonly assumed to be one for a steam line break. Another assumption for a feedline break includes constant primary to secondary heat transfer at its initial value until the steam generator is completely empty. These assumptions are not realistic in nature and not necessarily conservative. For a feedline break, the heat transfer rate from the primary system to the secondary increases due to the fast depressurization of the secondary system. Therefore, assuming the heat transfer rate to be the same as the initial value should not be considered as conservative. For a steamline break, the assumption of the break flow quality may not be conservative either. Assuming a pure vapor out the break speeds up the pressure reduction, shortens the time required for liquid depletion in the affected steam generator, and predicts earlier timing of downcomer minimum temperature. Many PTS studies (1-3) show that the primary pressure reaches its maximum value at a time much later than that of minimum downcomer temperature. Therefore the primary pressure at the time when the downcomer temperature is minimum is lower for an earlier prediction of minimum downcomer temperature. In this sense, the risk of combined thermal stress and pressure stress may be smaller. The same argument can also be applied to the assumption of break size. The usually assumed 100% break may not necessarily result in the maximum heat transfer from the primary. Therefore, an in depth study of steam generator blowdown is quite necessary.

As far as the heat transfer is concerned. There are some best estimate computer codes, such as TRAC or RELAP5, which are able to do best estimate calculations. However, the two fluid model does not incorporate the mixture level concept and therefore a large number of small control volumes should be used to simulate the propagation of mixture level in the steam generator secondary side. The computation work will be highly time and storage consuming, if it is achievable.

To make a study of the processes in the secondary system easier to

handle, the secondary side of affected steam generator is decoupled from the rest of the system. In other words, the behavior of the secondary side of the affected steam generator is studied without confusing effects of heat transfer and fluid mechanics in both the primary system and the intact secondary system. Figure 1 shows the typical nodalization for the whole system PTS thermal hydraulic analysis. The shadowed region in the Figure 1 is the area where we focus our efforts. The interactions between the systems are not studied, not only because they are too complicated but also because some of the component separate effects are still not clear. One of the key system separate effects that requires proper modeling is predicting the heat transfer on the secondary side of the affected steam generator. This heat transfer is important because it governs the degree and duration of the overcooling on the secondary system, which drives the whole transient.

The principal factors that affect the heat transfer on the secondary side of the affected steam generator include:

1. The local heat transfer coefficient and the corresponding heat transfer area.

As long as the tubes are wet on the secondary, the heat transfer is excellent. On the other hand, whenever the tubes are dry the heat transfer is negligible. Therefore, the fraction of wetted area is particularly important. Carryover, fall back and mixture level propagation are the key parameters for determining the amount of wetted area.

2. The temperature on the steam generator secondary side.

The temperature on the steam generator secondary side is mainly determined by the depressurization rate.

3. The time span for the heat transfer on the pressure vessel wall.

Thermal stress peaks 10 or 20 minutes into the transient. It is the heat transfer up to that time that is most important.

Large heat transfer rates and long heat transfer times are two essential conditions for pressurized thermal shock to occur. These conditions relate closely to the size of break. For a very large steamline break, the amount of carryover is quite large and the steam tubes dry out quickly. Consequently, the period of time during which high rate of cooling prevails is rather short. On the other hand, for a very small steam line break the small and slow overcooling will result in a condition which does not depart greatly from normal conditions. Evidently, neither of these two kinds of break has large chance to cause pressurized thermal shock. For intermediate breaks, however, the pressure decrease is rapid and the cooling of the U tubes is excellent for a rather long time due to the small carryover. As a consequence, the threat of PTS is largest for the intermediate steam line break.

1.3 Applications of a Better Steam Generator Model

1.3.1 Pressurized Thermal Shock Induced by Steam Generator Blowdown

1.3.1.1 Pressurized Thermal Shock

Pressurized thermal shock is designated as unresolved safety issue A-49 by the NRC in December 1981. This issue is mainly addressed to the old pressurized water reactors (PWRs)⁽⁴⁾. Neutron irradiation of reactor vessel wall decreases the fracture toughness of the materials. The vessel wall becomes embrittled and the nil-ductility temperature (NDT) increases. This is especially important for the portion of the welds which have high copper and nickel content. If a severe overcooling event occurs accompanied by high pressure, there is a concern over the pressure vessel integrity. If a small crack is present on the vessel inner surface, such as subcritical flaw in service, that crack may grow to a size that threatens vessel integrity.

Many efforts⁽¹⁻⁸⁾ have been made on this subject to show how likely or unlikely this kind of event is and whether they affect reactor vessel integrity. Among them are: (1) Development of event sequences by Oak Ridge National Laboratory (ORNL) (2) Calculations of thermal hydraulic consequences by Idaho National Engineering Laboratory (INEL) and Los Alamos National Laboratory (LANL) (3) Calculations of probabilistic fracture mechanics by ORNL (4) Integration of results by ORNL. In addition, EPRI, Westinghouse, Brookhaven National Laboratory (BNL), and many companies and universities are also participating in this study.

In addressing this concern, the Nuclear Regulatory Commission (NRC) has selected three plants representing three types of PWRs in use for detailed PTS study. These are Oconee-1 (B&W), Calvert Cliffs-1 (C.E.), and H.B. Robinson-2 (Westinghouse). Transients which are most important contributors to the PTS problem for these power plants are identified and selected by ORNL.

1.3.1.2 Pressurized Thermal Shock Induced by Steam Generator Blowdown

One of the initiating events leading to a possible pressurized thermal shock in a pressurized water reactor is a steamline or a feedline break. When the break occurs, the pressure in the steam generator secondary side drops and the heat transfer rate from the primary side to the secondary side of the affected steam generator increases. The excess amount of heat transfer results in an overcooled primary system. Moreover, the reactor trip following a steam generator blowdown will enhance the effect of overcooling. As a result of this overcooling in the primary system, the emergency core cooling (ECC) may come on and lead to repressurization thereby threatening pressurized thermal shock.

Clearly, the sequence of events depends on the heat generation and

removal rate in the primary system. The heat in the primary system can be removed by both the normal and affected steam generators. Therefore, there are three mutual interacting systems--the primary system, the secondary side of intact steam generator, and the secondary side of the broken steam generator. The system response in each individual system and between systems is complex. As an example to show the interactions between the systems, the effect of the location of the break in a steamline break is described.

A typical steamline piping configuration⁽⁹⁾ for a PWR is shown in Fig 2. After a steam line break, reversed flow in the steamline resulting from check valve failure can be expected to have occurred. If the break of steam line is located at the exit of the steam generator, denoted as break 1 in figure 2, there is a higher energy removal rate from the affected steam generator because the break is located upstream of the flow restrictor. On the other hand, there is lower blowdown rate from any one of the intact steam generators because the flow must blow back through two flow restrictors, one for the intact steam generator and the other for the affected steam generator. If the break of steam line is located downstream of the flow restrictor, indicated as break 2 in Fig. 2, each steam generator blows down through its own flow restrictor to the break. Compared with the blowdown from break 1, there is a higher energy removal rate from the unaffected steam generators and a lower energy removal rate from the affected steam generator. Therefore, the break location is important to the PTS analysis. Some other parameters which are important to the system response include initial core power, reactor coolant pump operation, auxiliary feedwater availability, ECC operation, and MSIV closure timing. Even without dealing with all these complications, as described in section 1.2, a better steam generator model is still very helpful for understanding the transient.

1.3.2 Steam Tube Rupture Induced by Steam Line Break

The normal operating pressure in PWR is 2250 psi in the primary system and about 1000 psi in the secondary system. After a steam line break, the fast depressurization in the secondary system creates a large pressure difference across the steam generator tubes. This causes an additional pressure to act across the steam generator tubes. If this pressure is greater than the steam generator tubes can take, tube ruptures may occur and radioactive materials contained in the primary coolant will enter into the secondary system, mix with the secondary coolant, and flow out of the break into the atmosphere.

When the primary coolant enters the secondary system, the sudden pressure drop results in flashing of the primary coolant which is similar to the flashing of the secondary coolant during steam generator blowdown. The amount of radioactive material, contained in the primary coolant, which can be carried out of the break, depends on the carryover and fall back of the mixed coolant.

Therefore a good steam generator model is important in order to understand the consequences of the steam tube rupture accident induced by steam line break.

1.3.3 Reactivity Insertion in the Primary System

In a reactor with a negative moderator temperature coefficient, such as a standard PWR, a decrease in primary coolant temperature will lead to a reactivity insertion. Such a temperature decrease in the primary coolant can result from a sudden increase in the heat removal rate from the primary system which in turn could be due to the blowdown of the secondary system.

The potential for a recriticality and the resulting core power burst has always been a safety concern. Following a steamline break, the reactivity insertion due to overcooled primary coolant decreases the shutdown margin provided by the control rods. If the negative reactivity from the Doppler effect and the high boron concentration ECC do not become effective within a short period, the positive moderator reactivity may exceed the negative control rod reactivity and lead to a recriticality. The duration of the recriticality then determines the possibility of fuel rod damage. Obviously, a better estimate of heat transfer from the primary side to the secondary side is required for a better modeling of reactivity insertion accident.

1.3.4 Impact on the Containment Design

The containment is a component designed to contain any radioactive material released during both normal and transient operating conditions. It should be able to sustain the maximum possible transient loads without losing its integrity. The primary system blowdown and the secondary system blowdown are the two accidents commonly chosen to show the adequacy of the containment design. The loads experienced by the containment include the force due to an impinging jet and the pressure force resulting from the flashing of the high temperature, high pressure break flow.

For a steamline break, it is usually assumed that the break flow is pure steam. This assumption increases the energy flow rate and decreases the mass flow rate from the generator. A more realistic mass and energy flow rate from the generator can be obtained from a better steam generator blowdown modeling. A better estimate of the impact of the break flow on the containment and the in-containment components can therefore be achieved.

1.3.5 Blowdown in Boiling Water Reactor

The geometry and the operating conditions of a boiling water reactor (BWR) are very similar to those found on a PWR steam generator secondary side. The knowledge learned from the steam generator blowdown can also be applied to the BWR blowdown.

2. ANALYTICAL SYSTEM MODELS

One-dimensional treatment of the conservation equations is established for solving the carryover, fall back, and heat transfer on the secondary system during the steam generator blowdown. The internal space inside the steam generator secondary side is divided into control volumes and the conservation equations are integrated over these control volumes. The methods of solving the integrated equations are described in chapter 3.

2.1 Hydrodynamic Model

The basic hydrodynamic model is based on a one-dimensional, two-equation formulation for the two-phase flow. It consists of one mixture mass equation and one mixture energy equation. The momentum equation is not required because we believe that the detailed pressure distribution in a large vessel is not important during the blowdown process. In other words, the pressure is considered to be uniform in the steam generator secondary side.

The transient two phase flow is assumed to be in thermal equilibrium but not homogeneous. The difference between liquid phase velocity and vapor phase velocity is taken into account by the drift flux model. This model is the simplest one that can adequately describe the important two-phase flow phenomena. In particular, it is the only model which allows us to track the water level in a physically realistic way.

2.1.1 Conservation Equations

In a two-phase flow, it is too complicated to predict the exact motion of each droplet or bubble. Fortunately, we are only interested in knowing the average behavior of each phase. For this reason the averaged conservation equations are used. The parameters in the conservation equations are averaged over a time interval, t , assumed to be long enough to smooth out the random fluctuations present in a two phase flow but short enough to preserve any gross unsteadiness in the flow. The resulting average equations are cast in the mixture form.

Mixture Mass Equation

$$\frac{\partial(\alpha \rho_v + (1-\alpha)\rho_l)}{\partial t} + \nabla \cdot (\alpha \rho_v \bar{V}_v + (1-\alpha)\rho_l \bar{V}_l) = 0 \quad (2.1)$$

Mixture Energy Equation

$$\begin{aligned} & \frac{\partial(\alpha \rho_v e_v + (1-\alpha) \rho_l e_l)}{\partial t} + \nabla \cdot (\alpha \rho_v e_v \bar{V}_v + (1-\alpha) \rho_l e_l \bar{V}_l) \\ & = -p \nabla \cdot (\alpha \bar{V}_v + (1-\alpha) \bar{V}_l) + \dot{Q}_{wv} + \dot{Q}_{wl} \end{aligned} \quad (2.2)$$

2.1.2 Flow Regime and Flow Regime Transition Criteria

The commonly observed two-phase flow regimes⁽¹⁰⁾ for a heated vertical test sections are: (1) the bubbly flow regime (2) the slug flow regime (3) the churn-turbulent flow regime (4) the annular flow regime (5) and the liquid dispersed flow regime. Usually these flow regimes are observed at low pressures in small diameter tubes and under steady state operating conditions. For steam generator blowdown the pressure range is very broad, the vessel diameter is very large, the geometry within the tube bundle is highly complex and the system is under transient conditions. Therefore, we do not expect any current available flow regime criteria to accurately predict the transient flow regime. However, with this study of the characteristics of blowdown and the accompanying flow regimes some useful guidelines can be established. In a bubbly flow the vapor phase is distributed as discrete bubbles in a continuous liquid phase. These bubbles will move randomly, collide with each other and coalesce to form larger bubbles, which are then no longer classified as bubbly flow regime. Therefore, bubbly flow exists only when void fraction is low and the collision frequency is small. It is expected that bubbly flow can exist in the downcomer and the bottom part of steam generator where void fraction is low in the early period of blowdown. In slug flow the vapor bubbles have characteristic diameters which are approximately the diameter of the flow passage. During blowdown the flow is expected to be highly turbulent so that large diameter bubbles do not have chance to develop before they are destroyed. Therefore, the slug flow regime is not expected to occur in the steam generator blowdown. In other words it is assumed that the flow changes from bubbly flow to churn-turbulent flow directly. The annular and liquid dispersed flow regime are likely to occur in the large void fraction region. The annular flow regime may occur in the tube bundle region and the riser of the separator during the later period of blowdown. The liquid dispersed flow regime may occur in the steam dome which is above the tube bundle and below the separator, and the steam dome above the primary separator.

Because the void fraction itself is a good indication of flow regime, the combination of theoretical analysis equation and the void fraction value is used to predict the transition of flow regimes. According to Radovich and Moïssis⁽¹¹⁾ the chance of

bubble collision due to random motion is low when the void fraction is below 0.1. For this reason, the combination of Taitel and Dukler's equation⁽¹²⁾ and a void fraction of 0.1 is used to determine the transition from bubbly flow to churn-turbulent flow. The combination of Ishii's equation⁽¹³⁾ and the void fraction of 0.8 is used to determine the transition between the churn-turbulent flow regime and the annular flow regime. In the Ishii's model there is another criteria for transition between the annular flow regime and the liquid dispersed flow regime. Unfortunately, it is not so obvious that this criteria can be applied generally without question. For example, the annular flow regime is given by the following formula

$$(j_v)_{2-3} < |j_v| < (j_v)_{3-3a} \quad (2.3)$$

In the equation (2.3)

$$(j_v)_{2-3} = ((\Delta\rho)gD/\rho_g)^{0.5} (1/C_o - 0.1) \quad (2.4)$$

is the transition velocity from churn-turbulent flow regime to annular flow regime and

$$(j_v)_{3-3a} = (\sigma g(\Delta\rho)/\rho_g)^{0.25} N_{\mu f}^{-0.2} \quad (2.5)$$

is the transition velocity from annular flow regime to liquid dispersed flow regime. Where

$$N_{\mu f} = \mu_f / (\rho_g \sigma \sqrt{\sigma/g\Delta\rho})^{0.5}$$

For our 4" diameter vessel with the initial pressure of 1000 psi the $(j_v)_{2-3}$ and $(j_v)_{3-3a}$ values can be calculated as

$$(j_v)_{2-3} \approx 2 \text{ ft/sec}, \quad (j_v)_{3-3a} \approx 8 \text{ ft/sec}$$

respectively. When this is compared with formula (2.3), a contradiction is observed because the $(j_v)_{2-3}$ is greater than $(j_v)_{3-3a}$. For this reason there is no attempt to distinguish annular flow regime and liquid dispersed flow regime. For obtaining flexible calculations both the annular flow regime and liquid dispersed flow regime drift flux constants are provided and can be selected accordingly. The criteria for the flow regime determination, obtained from the flow regime transition criteria, is summarized in Table 1.

2.1.3 Drift Flux Model

For a two phase flow the velocity of individual phase can be related by the drift flux model proposed by Zuber⁽¹⁴⁾.

$$\langle j_v \rangle = \langle \alpha \rangle (C_0 \langle j \rangle + V_{gj}) \quad (2.6)$$

where

j = total superficial velocity = $j_v + j_l$

j_v = superficial vapor velocity

α = void fraction

C_0 = distribution parameter = $\langle \alpha j \rangle / \langle \alpha \rangle \langle j \rangle$

V_{gj} = weighted mean drift velocity = $\langle \alpha (V_v - j) \rangle / \langle \alpha \rangle$

V_v = vapor velocity

and $\langle \rangle$ indicates an average over the flow cross section. The drift flux model simply shows that, for a given operational condition, there is a linear relationship between the superficial vapor velocity and the total superficial velocity. The distribution parameter C_0 reflects the effect of void fraction and flow distribution in a cross section. For C_0 greater than one there is more vapor in the center of a cross section than at the periphery. This happens most of the time in a two phase flow. For C_0 smaller than one, there is more vapor at the periphery of the specific cross section. This may be observed when subcooled boiling takes place. The weighted mean drift velocity reflects the effect of velocity difference between the superficial vapor velocity and the mean superficial velocity. The weighted mean drift velocity equals to the terminal bubble rise velocity in both the bubbly flow regime and the churn-turbulent flow regime. The value of C_0 and V_{gj} are function of flow regime and many values have been proposed.

For bubbly flow, the following values are suggested by Wallis (15)

$$\bar{V}_{gj} = 1.53 (1-\alpha)^2 \left(\frac{\sigma g \Delta \rho}{\rho_f} \right)^{0.25} \quad (2.7)$$

$$C_0 = 1.0 \quad (2.8)$$

For churn-turbulent flow, C_0 is calculated from Ishii's model (13)

$$C_0 = (1.20 - 0.2 (\rho_g / \rho_f)^{0.5}) (1 - e^{-18\alpha}) \quad (2.9)$$

while the weighted mean drift velocity are adopted from various

sources. The value recommended by Zuber⁽¹⁴⁾ is

$$\bar{V}_{gj} = 1.53(\sigma g(\Delta\rho)/\rho_f^2)^{0.25} \quad (2.10)$$

The same form is recommended by Ishii⁽¹³⁾, except the constant is 1.414 instead of 1.53. Another form of weighted mean drift velocity is also given by Zuber⁽¹⁴⁾. In a steam-water system in a vertical container of large vessel diameter with a free interface at high pressure, Zuber points out that V_{gj} has a strong dependence upon pressure. To cope with the pressure dependence, he proposes a model of the form:

$$\bar{V}_{gj} = A_p (\sigma g(\Delta\rho)/\rho_g^2)^{0.25} \quad (2.11)$$

Due to the lack of the information about the entrance effect, such as the mode of vapor injection, no single value of A_p is given in Zuber's report. Bertodano⁽¹⁶⁾ suggests that the value of A_p can be chosen as 0.33. Therefore, V_{gj} can be expressed as:

$$\bar{V}_{gj} = 0.33(\sigma g(\Delta\rho)/\rho_g^2)^{0.25} \quad (2.12)$$

The V_{gj} obtained from equations (2.10) and (2.12) are essentially identical at 1000 psi while equation (2.12) predicts higher value of V_{gj} at lower pressure. The work done by Wilson⁽¹⁷⁾ is also of interest. He measures the bubble terminal velocity through saturated water with pressure range from 300 psi to 600 psi in the 19-in diameter and 4-in diameter vessel. According to his definition the bubble velocity V_B is given as:

$$V_B = j_v/\alpha \quad (2.13)$$

Recalling the drift flux model

$$j_v/\alpha = C_o j + \bar{V}_{gj}$$

we can relate V_B to V_{gj} as

$$V_B = C_o j + V_{gj} \quad (2.14)$$

For stationary water column, $j = j_v = V_B$. Therefore Eq(2.14) can be rewritten as

$$V_{gj} = (1-C_o\alpha)V_B \quad (2.15)$$

In this way, the original Wilson correlation

$$\alpha = 0.136 \alpha_T \left(\frac{V_B}{\left(g \left(\frac{\sigma}{g(\rho_f - \rho_g)} \right)^{0.5} \right)^{0.5}} \right)^{1.78}, \text{ if } \alpha/\alpha_T \leq 2.84 \quad (2.16)$$

$$\alpha = 0.75 \alpha_T \left(\frac{V_B}{\left(g \left(\frac{\sigma}{g(\rho_f - \rho_g)} \right)^{0.5} \right)^{0.5}} \right)^{0.78}, \text{ if } \alpha/\alpha_T \geq 2.84 \quad (2.17)$$

where

$$\alpha_T = \left(\frac{\rho_g}{\rho_f - \rho_g} \right)^{0.32} \left(\frac{1}{D} \left(\frac{\sigma}{g(\rho_f - \rho_g)} \right)^{0.5} \right)^{0.19}$$

can be converted into

$$\bar{V}_{gj} = (1 - \alpha_{C_0}) \left(\frac{\alpha}{0.75} \right)^{1.283} \left(\frac{\rho_f - \rho_g}{\rho_g} \right)^{0.41} \left(\frac{gD}{\left(\frac{g\sigma}{\rho_f - \rho_g} \right)^{0.5}} \right)^{0.2436} \left(\frac{g\sigma}{\rho_f - \rho_g} \right)^{0.25}$$

if $\alpha/\alpha_T \leq 2.84$ (2.18)

$$\bar{V}_{gj} = (1 - \alpha_{C_0}) \left(\frac{\alpha}{0.136} \right)^{0.562} \left(\frac{\rho_f - \rho_g}{\rho_g} \right)^{0.1798} \left(\frac{gD}{\left(\frac{g\sigma}{\rho_f - \rho_g} \right)^{0.5}} \right)^{0.1067} \left(\frac{g\sigma}{\rho_f - \rho_g} \right)^{0.25}$$

if $\alpha/\alpha_T \geq 2.84$ (2.19)

When the pressure is very low, unreasonably high V_{gj} 's are obtained from equation (2.12) and the Wilson correlation⁽¹⁰⁾. Hence, the V_{gj} for the slug flow regime

$$\bar{V}_{gj} = 0.35 (gD \Delta \rho / \rho_f)^{0.5} \quad (2.20)$$

is used to provide an upper bound limitation. Although a slug flow may not have chance to develop completely during the transient, the existence of the developing slug flow is expected. The developing slug flow may not be distinguishable from the churn-turbulent flow. Therefore, V_{gj} for developing slug flow can be used. The V_{gj} for a developing slug flow is slightly higher than that for a slug flow. For simplicity, a simple slug flow correlation is used instead. The diameter, D , in the slug flow correlation reflects the geometric effect but it is not the whole story. Let's consider some fixed length test sections of various

diameters and allow bubbles entering the test sections from the bottom and leaving from the top. If the diameter is small, it is very easy for the bubbles to grow to the size of the test section before they exit. This is a diameter controlled process and the diameter in the slug flow correlation adequately provides a maximum value V_{gj} . If the diameter of the test section is large, the bubbles exit before they grow to the size of the test section. This is a length controlled process and the diameter in the slug flow correlation is no longer appropriate. Therefore, for a small diameter test section, the limitation provided by the slug flow correlation is satisfactory while for a larger diameter test section, an other limitation is needed. From the available experimental data, the maximum V_{gj} found anywhere is 3 ft/sec⁽¹⁸⁾. Therefore, this value is chosen as the upper limit for large diameter test section. For a typical U-tube steam generator, the shell diameter is large, the length is long, and there are additional effects come from the tube support plates. When the bubbles go through the tube support plates the size of the bubble is reduced and the bubble growing process starts all over again. Effectively, the U-tube steam generator acts as a large diameter, short length test section and therefore the maximum value of 3 ft/sec is justified. As a final result, after imposing the limitations, the V_{gj} is chosen as the minimum of the following three: (1) V_{gj} for original churn-turbulent flow correlations (2) V_{gj} for the slug flow correlation (3) a constant value of 3 ft/sec.

For annular flow regime Ishii's model⁽¹³⁾ is used.

$$C_o = 1 + (1-\alpha)/(\alpha + 4 (\rho_g/\rho_f)^{0.5}) \quad (2.21)$$

$$\bar{V}_{gj} = (C_o - 1) (\Delta \rho g D (1-\alpha)/(0.015 \rho_f))^{0.5} \quad (2.22)$$

For liquid dispersed flow regime, again the Ishii's model⁽¹³⁾ is used

$$C_o = 1 + (1-\alpha)/(\alpha + 4 (\rho_g/\rho_f)^{0.5}) \quad (2.21)$$

$$\bar{V}_{gj} = 1.414 (1-\alpha) (\sigma g \Delta \rho / \rho_g^2)^{0.25} \quad (2.23)$$

A comparison of all the weighted mean drift velocities is shown in Fig. 3 and 4 and the legends used in Fig 3 and 4 are given in Table 2. Figure 3 is obtained by assuming the pressure is 1000 psi, the diameter is 0.34 ft, and C_o is 1.0 in the Wilson correlation. Same assumption is applied to Fig 4 except the pressure changes into 300 psi. In addition to the above mentioned

models, the V_{gj} derived from modified Wallis correlation⁽¹⁰⁾ is also included in these figures.

In annular flow regime, the modified Wallis correlation is:

$$\frac{j_g^*}{1-3.1(1-\alpha)} - \frac{j_f^*}{3.1(1-\alpha)} = 1 \quad (2.24)$$

From the definition of j_g^* , j_f^*

$$j_g^* = j_g \left(\frac{\rho_g}{gD \Delta \rho} \right)^{0.5} \quad (2.25)$$

$$j_f^* = j_f \left(\frac{\rho_f}{gD \Delta \rho} \right)^{0.5} \quad (2.26)$$

Equation(2.24) can be rewritten as:

$$j_g = \left[\frac{1-3.1(1-\alpha)}{3.1(1-\alpha)} \left(\frac{\rho_f}{\rho_g} \right)^{1/2} \right] j_f + \left[(1-3.1(1-\alpha)) \left(\frac{gD \Delta \rho}{\rho_g} \right)^{1/2} \right] \quad (2.27)$$

Comparing equation (2.27) to the drift flux model equation

$$j_g = \frac{\alpha C_0}{1-\alpha C_0} j_f + \frac{\alpha}{1-\alpha C_0} \bar{V}_{gj} \quad (2.28)$$

one finds

$$\frac{1-3.1(1-\alpha)}{3.1(1-\alpha)} \left(\frac{\rho_f}{\rho_g} \right)^{1/2} = \frac{\alpha C_0}{1-\alpha C_0} \quad (2.29)$$

$$(1-3.1(1-\alpha)) \left(\frac{gD \Delta \rho}{\rho_g} \right)^{1/2} = \frac{\alpha}{1-\alpha C_0} \bar{V}_{gj} \quad (2.30)$$

Solving Eqs.(2.29),(2.30) for C_0 and \bar{V}_{gj} , Eqs.(2.31),(2.32) are obtained

$$C_0 = \frac{\left[1-3.1(1-\alpha) \right] \left(\frac{\rho_f}{\rho_g} \right)^{0.5}}{\alpha \left| \left(\frac{\rho_f}{\rho_g} \right)^{0.5} - 3.1(1-\alpha) \left(\frac{\rho_f}{\rho_g} \right)^{0.5} - 1 \right|} \quad (2.31)$$

$$\bar{V}_{gj} = \frac{(1-3.1(1-\alpha))}{\alpha} \left(\frac{gD \Delta \rho}{\rho_g} \right)^{0.5} \frac{3.1(1-\alpha)}{(1-3.1(1-\alpha)) \left(\frac{\rho_f}{\rho_g} \right)^{0.5} + 3.1(1-\alpha)} \quad (2.32)$$

From Fig 3 and 4 some interesting points are observed:

1. Both the Wilson model and the Zuber model in the form of Eq.(2.12) show that V_{gj} has large dependence upon pressure. The other models do not show this kind of dependence.
2. The value of V_{gj} given by models 3 and 4 are quite close. The difference in the coefficient of 1.53 or 1.414 is insignificant.
3. Ishii's annular flow regime drift flux model, dispersed vapor regime flow drift model, and Wallis' model converge at high void fraction.

All the models, except Wallis' model, in Fig 3 and 4 are incorporated into our program. The Wallis' model is not used because its data base is obtained solely from low pressure tests.

It is noted that the drift flux constants are subjected to abrupt change when the flow regime changes. If smoothing of C_0 and V_{gj} is not provided, an undesired instability in the solution may occur. For this reason, the following smoothing techniques are used.

For the transition from churn-turbulent flow regime to annular flow regime or liquid dispersed flow regime, C_0 is given as:

$$C_0 = 1.2 - 0.2(\rho_g/\rho_f)^{0.5} \text{ if } \alpha \leq \alpha_{2+3} \quad (2.33)$$

$$C_0 = 1 + (1-\alpha)/(\alpha + 4(\rho_g/\rho_f)^{0.5}) \text{ if } \alpha \geq \alpha_{2+3} \quad (2.34)$$

$$\text{where } \alpha_{2+3} = \frac{1 - 0.8((\rho_g/\rho_f)^{0.5} - (\rho_g/\rho_f))}{1.2 - 0.2(\rho_g/\rho_f)^{0.5}}$$

α_{2+3} is the void fraction which makes the C_0 value calculated from Eq.(2.33) and Eq.(2.34) the same. For pressure decreases from 1000 psi to 14.7 psi, the α_{2+3} value decreases from 0.75 to 0.82 which appears to be a reasonable region for transition from churn-turbulent flow regime to annular flow regime. From Fig 3 and 4, it is found that the most natural way of obtaining the V_{gj} value is to choose the minimum V_{gj} value predicted from the churn-turbulent flow regime and from either the annular flow regime or the liquid dispersed flow regime, depending on the option used.

For the transition from bubbly flow regime to churn-turbulent flow regime, similiar smoothing techniques can be applied:

$$C_o = 1.0 \quad \text{if } \alpha < \alpha_{1+2} \quad (2.35)$$

$$C_o = (1.2 - 0.2 (\rho_g/\rho_f)^{0.5}) (1 - e^{-18\alpha}) \quad \text{if } \alpha > \alpha_{1+2} \quad (2.36)$$

where

$$\alpha_{1+2} = - \frac{1}{18.0} \ln \left(\frac{0.2(1 - (\rho_g/\rho_f)^{0.5})}{1.2 - 0.2(\rho_g/\rho_f)^{0.5}} \right)$$

For pressure changes from 1000 psi to 14.7 psi, α_{1+2} varies from 0.111 to 0.101. This is a reasonable value for transition from bubbly flow regime to churn-turbulent regime. There is no attempt to smooth the V_{gj} in the transition region because any smoothing method in the bubbly flow regime will change the slope of V_{gj} in Fig 3 and 4 from downward sloping to upward sloping.

2.1.4 Break Flow Model

The break flow model contains both a critical flow model and a subcritical flow model. When the pressure inside the vessel is much higher than that outside the vessel, the break flow rate is limited by the choking phenomena and the critical flow model is applied. When the blowdown is ending the pressure inside the vessel approaches atmospheric pressure and the subcritical flow model is used.

2.1.4.1 Critical Flow Model

For a given constant upstream pressure p the reduction of the back pressure leads to an increase in the flow rate. When the back pressure is reduced to a certain point, further reduction in the back pressure results in no further increase in the mass flow rate. This maximum flow rate is then called critical flow rate and the flow is said to be choked. For the steam generator blowdown, the back pressure is 14.7 psia and the upstream pressure decreases from 1000 psia to 14.7 psia as the transient proceeds. Except for the period which is close to the end of blowdown, there is a large pressure difference between the pressure inside the steam generator and the back pressure. According to Fauske⁽¹⁹⁾, if the break flow path has L/D ratio greater than 12, the pressure at the throat is about 0.55 times of the vessel pressure. Therefore, a vessel pressure of 26.73 psia, which equals to 14.7 psia divided by 0.55, is chosen as the criteria for the transition between the critical flow model and the subcritical flow model. Because the subcritical flow occurs at such a low pressure, critical flow is expected to occur for almost the whole transient. The break flow rate at the tail of the blowdown will be obtained by the subcritical flow model described in section 2.1.4.2.

The two phase critical flow rate is one of the most important

parameters that governs the transient. Many two-phase critical flow models have been proposed over years. These models can be classified into three categories according to the assumptions about the velocities and temperatures of the individual phases in the two phase flow.

1. Homogeneous Equilibrium Model (HEM)
2. Slip Equilibrium Model
3. Two-fluid Model

In the homogeneous equilibrium model, the vapor and liquid phase is assumed to have equal velocity and equal temperature. In other words the two-phase mixture can be treated as a single fluid. In the slip equilibrium model, the two phases are considered to have different velocities while they are in thermal equilibrium. The Fauske model⁽²⁰⁾, the Moody model⁽²¹⁾ and the Levy model⁽²²⁾ are examples of the slip equilibrium model. In the two fluid models, the two phases are considered separately, each phase can have its own velocity and temperature. The selection of the two-phase critical flow model depends on several factors. Among the most important factors are flow conditions at the entrance, the length to diameter ratio, and the entrance effect. If the flow at the entrance is either subcooled or single phase saturated liquid, the length to diameter ratio has been shown to be very important by Henry⁽²³⁾, Fauske⁽¹⁹⁾, and Edmond and Smith⁽²⁴⁾. The flow rate for a short length break path is shown to be larger than for a long length break path. The nonequilibrium effect can be used to explain this observation. When a liquid is subjected to a rapid decompression, it is possible for the liquid to remain in a nonequilibrium, metastable state for a short time due to the delays inherent in the nucleation, bubble growth and departure processes. Similarly the nonequilibrium effects may occur when subcooled or single phase saturated liquid flows through break. For short test sections, the length to diameter ratio L/D is small and the transit time is short so that nonequilibrium effect becomes significant. This generally occurs when $L/D < 12$. For $12 < L/D < 40$ the assumption of thermal equilibrium is suitable because the test section is long enough for thermal equilibrium to become established.

The above mentioned L/D effects are usually observed with subcooled or saturated one-phase liquid flow entering a sharp-edged entrance. For a sharp-edged entrance the flow will separate. After entering the test section, the liquid is in the form of jet and the vapor at the liquid saturated temperature will fill the space between the jet and the wall. The jet may or may not reattach to the wall depending on the length of the break path. This complication due to flow separation will not occur for a rounded nozzle type entrance. According to Pasqua⁽²⁵⁾ and Sozzi and Sutherland⁽²⁶⁾, the flow rate associated with rounded inlet is greater than the sharp-edged inlet. Also, this effect is larger for small L/D ratio test section and higher subcooled liquid flow. It is concluded that the HEM model and slip equilibrium model are good for high quality flow or low quality

flow with $L/D > 12$ while the low quality flow with short test section can be calculated by the two fluid model or approximately by the incompressible liquid flow equation (27)

$$G = (2 g_c \rho_l (p_o - p_t))^{0.5} \quad (2.37)$$

In general, one should pay attention to the entrance effects. This is especially true when the flow is low quality and the test section is short. For steam generator blowdown, the flow quality at the entrance is high suggesting that the slip equilibrium model is adequate for the steam generator blowdown. Among the familiar slip equilibrium models, the Henry-Fauske model is selected in our code because it is simple and it takes into account the L/D effect explicitly. The implementation of Henry-Fauske's model is given in section 3.4. It has been proven to be a good choice.

2.1.4.2 Subcritical Flow Model

The pressure loss due to friction and geometry change is represented by the standard equation:

$$\Delta p = (k + \frac{fL}{D}) \frac{\rho V^2}{2g_c} \quad (2.38)$$

where k = pressure loss coefficient due to contraction and expansion
 f = friction factor
 L = friction length
 D = hydraulic diameter

The subcritical flow happens when blowdown is ending, the break quality should be very high by then. Assuming pure vapor flows through the break, the mass flux through the break can be written as:

$$G = \left(\frac{2 \rho_g g_c \Delta p}{(k + fL/D)} \right)^{0.5} \quad (2.39)$$

where p is the pressure difference between the system pressure and the atmosphere pressure. Under the same assumption the break enthalpy can be set to the saturated vapor enthalpy, i.e.

$$h_c = h_g \quad (2.40)$$

2.2 Heat Transfer Model

The heat transfer from the primary side to the secondary side is very important to the primary system response. As it is shown in section 4.4.2.3, the heat transfer is equally important to the blowdown process on the steam generator secondary side. This

effect has been ignored or inadequately modeled for many blowdown calculations. The fact that many of these blowdown tests are performed in large diameter vessels results in a large volume to heat transfer area ratio which makes the heat transfer effect small. However, in a steam generator secondary side there are very large amounts of heat transfer area provided by the tubes which suggests that the heat transfer effects should not be ignored.

As far as the stored heat is concerned, two models are used for the calculation of hot metal temperature. If the conductivity of the metal is low, a heat conduction model is adopted to calculate the temperature distribution in the metal. If the conductivity of the metal is very large, the temperature distribution is no longer important and a lumped parameter method is chosen to calculate the metal temperature.

2.2.1 Heat Conduction Model

A finite difference heat conduction model has been incorporated into our code. The axial conduction has been neglected. This assumption is justified by the low conductivity, and the relatively small temperature differences and heat conduction area in the axial direction. The wall of the pressure vessel is treated as slab because it is expected that no significant improvement will be obtained by modeling the pressure vessel wall as a cylinder instead of a slab.

Because the conductivity is not very large for the vessel wall (which is stainless steel), the temperature of the wall is a function of both time and space coordinates. This temperature can be obtained from the heat conduction equation:

$$\nabla^2 T + \frac{q'''}{k} = \frac{\rho C}{k} \frac{\partial T}{\partial t} \quad (2.41)$$

where

q''' = heat source per unit volume

k = thermal conductivity

ρ = density

C_p = heat capacity

The forward differencing scheme is used to solve the heat conduction equation. More detailed description is given in section 3.2.

2.2.2 Lumped Parameter Model

This method is applied to a conductor with uniform temperature. Obviously, this is an idealized method since a temperature gradient must exist in a material in order to establish a heat flow. A reasonably uniform temperature distribution in a metal can be obtained if the conductor size is small and the

conductivity of the conductor is high.

The convection heat loss from a body is equal to the decrease in the internal energy of the body. Thus,

$$\dot{Q} = hA (T - T_f) = - C_p M \frac{dT}{dt} \quad (2.42)$$

where A is the surface area for convection and M is the mass of the conductor. The initial condition is written

$$T = T_o \quad \text{at } t=0 \quad (2.43)$$

If the fluid temperature T_f is constant, the solution to Eq.(2.42) is

$$T = T_f + (T_o - T_f) e^{-(hA/M C_p) t} \quad (2.44)$$

In our case, the fluid temperature is not constant, instead it decreases as time progresses. To take this into account, we assume the fluid temperature is constant in a small time interval t . As a result, the temperature at the time state $n+1$ becomes:

$$\bar{T}^{n+1} = T_f^{n+1} + (T^n - T_f^{n+1}) e^{-(hA/M C_p) \Delta t} \quad (2.45)$$

where T_f^{n+1} is the saturated temperature corresponding to p^{n+1} , the pressure at state $n+1$. Using Eq(2.45) repeatedly, the temperature of conductor at any time step can be obtained. The heat transfer rate can then be obtained by

$$\dot{Q} = MC_p (\bar{T}^n - \bar{T}^{n+1}) / \Delta t \quad (2.46)$$

2.2.3 Heat Transfer Model

During the blowdown process part of the heat transfer area is covered by two phase mixture while the other part of the heat transfer area is covered by almost pure vapor. The heat transfer coefficient for the area which faces the two phase flow is very large while the heat transfer coefficient which faces the pure vapor is very small. From an engineering point of view, the heat transfer coefficient of pure vapor can be considered to be zero. For a real steam generator, the overall heat transfer coefficient "U" is composed of the following terms (29):

$$\frac{1}{U} = \frac{1}{h_i} + \frac{A_o}{A_i} + \frac{r_o - r_i}{K} \frac{A_o}{A_m} + f + \frac{1}{h_o} \quad (2.47)$$

When the thin wall approximation is used, the equation becomes:

$$\frac{1}{U} = \frac{1}{h_i} + \frac{\epsilon}{K} + f + \frac{1}{h_o} \quad (2.48)$$

For the area which faces the two phase flow, the inverse of the two phase heat transfer coefficient is much smaller than the wall thickness to conductivity ratio, which is about $0.0005(\text{Btu/hr ft}^2 \text{ } ^\circ\text{F})^{-1}$, or the inverse of heat transfer coefficient in the primary side, which is about $0.0007(\text{Btu/hr ft}^2 \text{ } ^\circ\text{F})^{-1}$. Therefore, the accuracy of h_o is not important. In our model, a constant value of $8000\text{Btu/hr ft}^2 \text{ } ^\circ\text{F}$, which is the steady state value of h_o , is assumed to be the value of h_o during the transient.

2.3 Water Level Model

In the literature there are two kinds of water levels, namely, the collapsed water level and the mixture water level. After the void below the mixture level is removed, the mixture level becomes the collapsed level. These two water levels are illustrated in Fig.5. The collapsed water level represents the total amount of water inventory while the mixture water level represents the actual liquid distribution. As far as the heat transfer is concerned, the mixture water level is the one which is important and requires careful modeling. Considering the mixture water level it is interesting to know how it behaves and how it can be modeled. From everyday experience we know what the water level is. However, the definition of water level is not so obvious. If we have pure liquid in one side and pure vapor in the other side, it is very clear that the interface is the location of water level. If now, vapor or air is bubbling through a liquid column, we have two phase flow both under and above the distinct water level and we can no longer define mixture level as the interface of liquid phase and vapor phase. Therefore it seems to be reasonable to define mixture level as the location where the void fraction is subject to abrupt change. This kind of approach has been adopted in the computer code TRAC-BD1(30). In TRAC-BD1, a level is assumed to exist in cell i if

$$(\alpha_{i+1} - \alpha_i) > \text{ALPCUT}, \text{ or } (\alpha_i - \alpha_{i-1}) > \text{ALPCUT} \quad (2.49)$$

provided that no level exists in cell $(i+1)$ or $(i-1)$. Here ALPCUT is a predetermined cutoff value. Although this seems to be a reasonable method for level detection, there are several problems remaining:

1. If water level is formed from the top of the vessel, the given criteria has difficulty in defining cell $i+1$.
2. The predetermined cutoff value ALPCUT is somewhat arbitrary.
3. Without examining the absolute value of void fraction in cells $i+1$, i , and $i-1$, the application of the above

criteria can sometimes be misleading.

4. There is no connection between the mixture water level at a particular time step to the time step next to it. In other words, the continuity of mixture level is not properly modeled.

As an attempt to overcome these difficulties the following method is introduced. A water level propagation model is used to decide where the water level is and in which node the water level currently resides. If the water level disappears, a water level reappearance criteria is applied to determine when the water level will reappear. Once the water level reappears, the motion of the water level is once again traced by the water level propagation model.

2.3.1 Water level propagation Model

Two kinds of water level propagation methods are used in the water level propagation model. The first method⁽³¹⁾ is derived from the continuity of matter. If one is attached to the water level front and assuming the mass transformation between the liquid phase and the vapor phase at the interface can be neglected, then the continuity of the vapor phase and the liquid phase requires

$$\alpha^-(V_v^- - V_w) = \alpha^+(V_v^+ - V_w) \quad (2.50)$$

$$(1 - \alpha^-)(V_\ell^- - V_w) = (1 - \alpha^+)(V_\ell^+ - V_w) \quad (2.51)$$

where the superscripts $(-)$ and $(+)$ denote the location just below and above the interface as it is shown in Fig.5. Adding up Equations (2.50) and (2.51) and applying the definition of j implies

$$j^- = j^+ \quad (2.52)$$

From equation (2.50) alone, the water level propagation velocity can be expressed as

$$V_w = \frac{\alpha^+ V_v^+ - \alpha^- V_v^-}{\alpha^+ - \alpha^-} \quad (2.53)$$

This velocity is also referred to as the "continuity shock wave velocity"⁽¹⁵⁾. Using the drift flux notation for vapor velocity V_v

$$V_v = C_o j + V_{gj} \quad (2.54)$$

equation (2.53) becomes:

$$v_w = \frac{(\alpha C_o j + \alpha V_{gj})^+ - (\alpha C_o j + \alpha V_{gj})^-}{\alpha^+ - \alpha^-} \quad (2.55)$$

From Eq. (2.52), $j^- = j^+ = j$ therefore the superscripts can be dropped and equation (2.55) is rewritten as:

$$v_w = \frac{(\alpha^+ C_o^+ - \alpha^- C_o^-)j + (\alpha^+ V_{gj}^+ - \alpha^- V_{gj}^-)}{\alpha^+ - \alpha^-} \quad (2.56)$$

If there is pure vapor above the level $=1.0$, $C_o = 1.0$, and $V_{gj} = 0.0$ so that

$$v_w = \frac{(1 - \alpha^- C_o^-)j - \alpha^- V_{gj}^-}{1 - \alpha^-} \quad (2.57)$$

This model is very good for describing the phenomena involving a continuous water level change such as pool swelling under intermediate transient. Therefore it is used to simulate the pool swelling before the water level has disappeared. The second method is a kind of interpretation. From the given void fraction distribution we can interpolate to obtain the water level of a control volume. The interpolation is made between the control volumes immediately above and below the control volume in question. A control volume i , which contains the mixture water level front, and its nearest top and bottom control volumes $i+1, i-1$, are shown in figure 6. As we know, the void fraction below the mixture level front is quite different from the void fraction above the mixture level front. If we average the void fraction below and above the mixture level front in control volume i and call them α_{bot} , α_{top} respectively, the balance of the void fraction in control volume i requires

$$(ELEV)_i \alpha_i = (MIXL)_i \alpha_{bot} + (ELEV - MIXL)_i \alpha_{top} \quad (2.58)$$

where $MIXL_i$ = mixture level in control volume i

$ELEV_i$ = elevation of control volume volume i

If the void fraction α_{bot} , α_{top} are assumed to be equal to the void fraction α_{i-1} , α_{i+1} respectively, Eq.(2.59) can be rewritten

as

$$(ELEV)_i \alpha_i = (MIXL)_i \alpha_{i-1} + (ELEV - MIXL)_i \alpha_{i+1} \quad (2.59)$$

After a rearrangement, the mixture level is obtained

$$(MIXL)_i = \left(\frac{\alpha_i - \alpha_{i+1}}{\alpha_{i-1} - \alpha_{i+1}} \right) (ELEV)_i \quad (2.60)$$

Therefore, given a control volume which contains the mixture level front, the value of mixture level can be calculated from the void fraction distribution. If the mixture level is smaller than 1% of the elevation height of the control volume, the mixture level front is assumed to cross the lower boundary and appears in the lower control volume.

2.3.2 Water Level Reappearance Criteria

The water level will reappear after it disappears. It is not clear whether the water level will reappear from the top of the vessel or at some lower location. It is believed that under certain situations, the water level may reappear from the top while under the other circumstance the water level may reappear at a lower location. The exact conditions for determining what will happen may be very complicated. However, with some physical insight, a simple approximate criteria can be established.

If the water should reappear from the top, the void fraction in the top control volume probably will be quit high. Most likely, the flow regime in the top control volume will be annular flow regime. Now, if the liquid film is running down the wall, a water level will reappear from the top. Therefore, the water level reappear criteria for the top node is :

$$\alpha_{\text{top node}} > 0.8 \text{ and } j_g < 0.0 \quad (2.61)$$

Should the water level reappear at some lower location, the following argument will be used to establish the criteria. Except for the possible liquid hold up introduced by the tube support plates, which will be discussed in chapter 5, the void fraction distribution will be stable provided that the void fraction is higher at higher elevation. Some temporary inversed void fraction distribution may occur but it probably will not last long enough to be an important pattern. In other words, if the water level front is formed, the void fraction above the interface should be high while the void fraction below the interface should be low. Applying this concept to the control

volumes the following criteria is established for water level to reappear in node i

$$\alpha_{i+1} > \alpha_{re} \quad (2.62)$$

and

$$\alpha_i < \alpha_{re} - \alpha_{cut}$$

where

α_{re} = reappear void fraction

α_{cut} = cut-off void fraction

For simplicity, the cut-off void fraction is assumed to be zero in the code SIT-SG. Obviously, the water level reappearance criteria at a lower location is not an accurate one. It is considered as a back up criteria for the top reappearance criteria.

2.4 Radioactive Particle Propagation model

When a steam line break occurs, the large pressure difference between the primary side and the secondary side may cause a weakened steam generator tube to rupture. This is known as a steam line break induced tube rupture. When the primary coolant enters the secondary side, it is expected to flash to steam. This is much like the flashing of the secondary coolant due to rapid depressurization in blowdown. Because the flashing phenomena is already modeled by our code, the additional mass and energy from the primary side can easily be handled in the thermal hydraulic calculation. With respect to the transportation of the radioactive material, mainly iodine and ionic iodine species, the process is much more complex. During the process of flashing of the primary coolant, iodine will be volatilized or retained in the small droplets formed by hydrodynamic forces while ionic iodine species will be retained entirely in the droplets⁽³²⁾. The interactions between the bubbles and the droplets formed by the flashing of the primary coolant, and the bubbles formed by the flashing of the secondary coolant and the continuous liquid phase of the secondary coolant are complex and are beyond the goals of this project. In spite of these complications, we have constructed a simple model to show the effect of the location of the ruptured steam tube on the transportation of radioactive material. During blowdown the flow in the secondary side of the steam generator is highly turbulent and therefore the primary coolant is likely to mix well with the secondary coolant. Consequently, some portion of iodine or ionic iodine will be attached to or dissolved in the liquid phase of the secondary

coolant and behaves more or less like the liquid phase on the secondary. By calculating the trajectory of the liquid phase of the secondary coolant, one can get the idea of the trajectory of the above mentioned radioactive material. For simplicity, we do not distinguish these two trajectories. Also the axial mixing is ignored. The trajectory of the radioactive material can then be obtained by the integration of the liquid phase velocity.

$$H(t) = H_o + \int_{t_o}^t V_l (H, t') dt' \quad (2.63)$$

where

$H(t)$ = elevation of radioactive material at time t .

H_o = initial elevation of radioactive material at time t_o

t_o = time at which steam tube rupture occurs.

t = any instant of time, $t > t_o$.

V_l = liquid velocity as function of elevation H and time t' .

Using the control volume notation, equation (2.63) becomes:

$$H(n\Delta t) = H_o + \sum_{k=1}^{n-1} V_{l,k}(t) \Delta t \quad (2.64)$$

where

$n\Delta t = t$ = any given instant of time

subscript k = k th control volume, where $H(t-\Delta t)$ resides

2.5 Pool Entrainment Model

Entrainment of liquid drops from a continuous liquid phase interface often occurs in various conditions involving heat and mass transfer. The mechanism of entrainment is different for each condition. For an annular dispersed flow in a pipe, the liquid drops are entrained from liquid film to central region by the gas flow. Several different entrainment mechanisms have been proposed. The shearing-off mechanism of roll-wave crests is proposed for cocurrent flow while the abrupt, large-magnitude waves is considered as typical phenomena for countercurrent flow.

In contrast to the above mentioned phenomena, the continuous liquid phase may be located below the vapor phase. This can occur

when liquid drop is entrained by vapor bubbling through a liquid pool. This is called pool entrainment.

In our simple model, there is no distinction between dispersed liquid phase and continuous liquid phase in annular dispersed flow regime. Therefore, only the pool entrainment phenomena are modeled. However, it should be pointed out that the entrainment from liquid film might be quite important for dryout front prediction. Ishii's model⁽³³⁾ is adopted to calculate the pool entrainment phenomena. This is a physical model developed by considering droplet size distribution, initial velocity of entrained droplets, droplet motion and droplet deposition and it is shown to correlate a variety of data over a wide range of experimental conditions. According to Ishii, there are three different regions in terms of entrainment above a bubbling pool, i.e., near surface, momentum controlled and deposition controlled regions. Furthermore, depending on the droplet generation mechanisms, there are three different correlations in the momentum controlled regions.

The pool entrainment model can be summarized below:

(1) Near surface region

This region is limited to the vicinity of the pool surface given by

$$0 \leq h^* \leq 1.038 \times 10^3 j_g^* N_{\mu g}^{0.5} D_H^{*0.42} \left(\frac{\rho_g}{\Delta \rho} \right)^{0.23}$$

In this region, entrainment is given by

$$E_{fg}(h, j_g) = 4.84 \times 10^{-3} \left(\frac{\rho_g}{\Delta \rho} \right)^{-1.0} \quad (2.65)$$

(2) Momentum Controlled Region

This region is limited to the intermediate height range given by

$$1.038 \times 10^3 j_g^* N_{\mu g}^{0.5} D_H^{*0.42} \left(\frac{\rho_g}{\Delta \rho} \right)^{0.23} \leq h^* \\ \leq 1.97 \times 10^3 N_{\mu g}^{0.33} D_H^{*0.42} \left(\frac{\rho_g}{\Delta \rho} \right)^{0.23}$$

This region is subdivided into three regimes, depending on the gas velocity:

(2-1) For the low gas flux regime limited to

$$j_g^*/h^* < 6.39 \times 10^{-4}$$

the entrainment is given as

$$E_{fg}(h, j_g) = 2.213 N_{\mu g}^{1.5} D_H^{*1.25} \left(\frac{\rho_g}{\Delta \rho} \right)^{-0.31} j_g^* h^{*-1} \quad (2.66)$$

(2-2) For the intermediate gas flux regime bounded by

$$6.39 \times 10^{-4} < j_g^*/h^* \leq 5.7 \times 10^{-4} N_{\mu g}^{-0.5} D_H^{*-0.42} \left(\frac{\rho_g}{\Delta \rho} \right)^{0.10}$$

the entrainment is given as

$$E_{fg}(h, j_g) = 5.417 \times 10^6 j_g^{*3} h^{*-3} N_{\mu g}^{1.5} D_H^{*1.25} \left(\frac{\rho_g}{\Delta \rho} \right)^{-0.31} \quad (2.67)$$

(2-3) For the high gas flux regime limited to

$$j_g^*/h^* \geq 5.7 \times 10^{-4} N_{\mu g}^{-0.5} D_H^{*-0.42} \left(\frac{\rho_g}{\Delta \rho} \right)^{0.10}$$

the entrainment amount increases very rapidly as

$$E_{fg} = (j_g^*/h^*)^{7 \sim 20} \quad (2.68)$$

(3) Deposition Controlled Region Above the height given by

$$h^* \geq 1.97 \times 10^3 N_{\mu g}^{0.33} D_H^{*0.42} \left(\frac{\rho_g}{\Delta \rho} \right)^{0.23}$$

the deposition becomes the main factor determining the amount of entrainment. In this regime, the entrainment decreases gradually with height due to deposition and is given as

$$E_{fg}(h, j_g) = 7.13 \times 10^{-4} j_g^{*3} N_{\mu g}^{0.5} \left(\frac{\rho_g}{\Delta \rho} \right)^{-1.0} \exp(-0.205(h/D_H)) \quad (2.69)$$

In Equations (2.65) through (2.69), the definition of entrainment E_{fg} , h^* and j_g^* are given as

$$E_{fg} = \frac{\rho_l j_l}{\rho_v j_v} \quad (2.70)$$

$$h^* \equiv h / \sqrt{\frac{\sigma}{g \Delta \rho}} \quad (2.71)$$

$$j_g^* \equiv j_g / \left(\frac{\sigma g \Delta \rho}{2 \rho_g} \right)^{1/4} \quad (2.72)$$

This entrainment model is an optional model and the user can decide whether to use it or not.

3. METHODS OF SOLUTION

With the boundary conditions provided by the break flow model and under the assumption that thermal equilibrium exists between vapor phase and liquid phase, the flow distribution inside the secondary side of the steam generator can be established without a momentum equation. This is done by a two-step scheme. First, the pressure is assumed to be uniform inside the pressure vessel and the whole pressure vessel is considered as a single component. The mass and energy equations are solved for the pressure of this component with boundary conditions provided from the calculation of break flow model. This single component system is referred to as the global vessel system and shown in Fig.7. After the pressure is obtained, the local void fraction and flow distribution can be determined using the drift flux model under the assumption of thermal equilibrium. This is referred to as the local control volume system and is also shown in Fig.7. For a local control volume system the flow path is divided into many control volumes, and each control volume is stacked on the top of another control volume. The connection between a pair of control volumes is called a "junction". For each control volume the conservation equations can then be integrated over space and written as:

$$\frac{dM_i}{dt} = - \sum_j (\vec{j}_v \rho_v + \vec{j}_l \rho_l)_j \cdot \vec{n} A_j \quad (3.1)$$

$$\frac{dU_i}{dt} = - \sum_j (\vec{j}_v \rho_v h_v + \vec{j}_l \rho_l h_l)_j \cdot \vec{n} A_j + \dot{Q}_{wv} + \dot{Q}_{wl} \quad (3.2)$$

The energy equation can also be rewritten in terms of enthalpy:

$$\frac{dH_i}{dt} = V_i \frac{dP_i}{dt} - \sum_j (\vec{j}_v \rho_v h_v + \vec{j}_l \rho_l h_l)_j \cdot \vec{n} A_j + \dot{Q}_{wv} + \dot{Q}_{wl} \quad (3.3)$$

A finite difference scheme is used to solve the integrated conservation equations. All the properties inside a control volume are considered to be uniform. State properties such as pressure, density, enthalpy and void fraction are obtained at the center of the control volumes. The fluid velocities are defined at the junctions (control volume boundaries). These velocities are determined from the conditions in the control volume right below the junction.

3.1 Hydrodynamic Modeling

With time discretization the equations (3.1) and (3.3) become:

$$\frac{M_i^{n+1} - M_i^n}{\Delta t} = ((j_v \rho_v + j_l \rho_l)^{n+\frac{1}{2}} A)_{j-1} - ((j_v \rho_v + j_l \rho_l)^{n+\frac{1}{2}} A)_j \quad (3.4)$$

$$\begin{aligned} \frac{H_i^{n+1} - H_i^n}{\Delta t} = & \frac{(P^{n+1} - P^n)V_i}{\Delta t} + ((j_v \rho_v h_v + j_l \rho_l h_l)^{n+\frac{1}{2}} A)_{j-1} \\ & - ((j_v \rho_v h_v + j_l \rho_l h_l)^{n+\frac{1}{2}} A)_j + \dot{Q}_i^n \end{aligned} \quad (3.5)$$

where the subscript i is the index for the control volume and the subscript j is the index for the junction. The superficial velocity j_v , j_l are defined as positive for the cocurrent upflow.

3.1.1 The Global Vessel System

The conservation equations for the global vessel system can be obtained by summing up the conservation equations for individual control volumes,

$$\frac{M_G^{n+1} - M_G^n}{\Delta t} = ((j_v \rho_v + j_l \rho_l)^{n+\frac{1}{2}} A)_{in} - ((j_v \rho_v + j_l \rho_l)^{n+\frac{1}{2}} A)_{out} \quad (3.6)$$

$$\begin{aligned} \frac{H_G^{n+1} - H_G^n}{\Delta t} = & \frac{(P^{n+1} - P^n)V_G}{\Delta t} + ((j_v \rho_v h_v + j_l \rho_l h_l)^{n+\frac{1}{2}} A)_{in} \\ & - ((j_v \rho_v h_v + j_l \rho_l h_l)^{n+\frac{1}{2}} A)_{out} + \dot{Q}_G^n \end{aligned} \quad (3.7)$$

To close these equations, a state equation is required:

$$P^{n+1} = f(\rho_G^{n+1}, h_G^{n+1}) = f\left(\frac{M_G^{n+1}}{V_G}, \frac{H_G^{n+1}}{V_G}\right) \quad (3.8)$$

For a given Δt and boundary conditions, the three unknowns M_G^{n+1} , H_G^{n+1} , P^{n+1} can be solved from equations (3.6) through (3.8). The boundary conditions are provided by the mass and energy flow rate of the feed water flow and the break flow. The mass and energy flow rates of the feed water flow are determined from the action of the feed water pumps, the emergency feed water pumps and the control systems. In this model, the feed water flow condition is assumed to be given. If there is no feed water flow such as, the case in our experiments, this value becomes zero. The break flow is determined by the break flow model. If the break flow is choked the break flow model requires the stagnation pressure, p_o , and the stagnation enthalpy, h_o , at the location upstream of the break. Otherwise, only the pressure, p , is required. In either case the required information can be obtained from the results of previous state calculation.

As mentioned above, the sets of equations can be solved by given a Δt and calculate P^{n+1} , M_G^{n+1} , H_G^{n+1} . In this code, however, the equations are solved by giving the new pressure, P^{n+1} , and

calculating Δt , M_G^{n+1} , H_G^{n+1} . There are two advantages in doing it this way: (i) If $H_G \Delta t$ is given, we need to solve $p^{n+1} = f(\rho_G^{n+1}, h_G^{n+1})$ which requires initial guess and iteration of pressure. If the new pressure, p^{n+1} , is given we now solve $\rho_G^{n+1} = f(p^{n+1}, h_G^{n+1})$ which usually does not require iteration. (ii) The time step is automatically adjusted. For a given constant "pressure step", the corresponding time step size is not constant. If the transient is more severe the depressurization rate is larger and the corresponding time step size becomes smaller as it is shown in Fig 9.

Under saturation conditions with a zero feed water flow, the equations (3.6) and (3.7) become:

$$(\rho_f - \rho_{fg} \alpha_G)^{n+1} V_G - M_G^n = - (G^n A)_{out} \Delta t \quad (3.9)$$

$$\begin{aligned} (\rho_f h_f - (\rho_f h_f - \rho_g h_g) \alpha_G)^{n+1} V_G - H_G^n &= (P^{n+1} - P^n) V_G - (G^n h^n A)_{out} \Delta t \\ &+ \dot{Q}_G^n \Delta t \end{aligned} \quad (3.10)$$

Where $(h^n)_{out}$ is the flow averaged enthalpy at the break junction defined as

$$h^n_{out} = \left(\frac{j_v \rho_v h_v + j_l \rho_l h_l}{j_v \rho_v + j_l \rho_l} \right)_{out}^n \quad (3.11)$$

For simplicity, in the equations (3.9) and (3.10), the break mass and energy flow rate are calculated from the previous state, as a substitution of the intermediate state, and serve as the boundary conditions. Eliminating α_G^{n+1} from equations (3.9) and (3.10), Δt can be obtained.

$$\Delta t = \frac{-\rho_{fg}^{n+1} (H_G^n + (P^{n+1} - P^n) V_G - \rho_f^{n+1} h_f^{n+1} V_G) + (\rho_f h_f - \rho_g h_g)^{n+1} (M_G^n - \rho_f^{n+1} V_G)}{-\rho_{fg}^{n+1} ((G h A)_{out}^n - \dot{Q}_G^n) + (\rho_f h_f - \rho_g h_g)^{n+1} (G A)_{out}^n} \quad (3.12)$$

3.1.2 The Local Control Volume System

Assuming saturation condition prevails, the conservation equations for the local control volume system can be expressed in the following form.

$$(\rho_f(1-\alpha) + (\rho_g \alpha))_i^{n+1} V_i - M_i^n =$$

$$((j_v^{n+1} \rho_g^n + j_\ell^{n+1} \rho_f^n) A)_{j-1} \Delta t - ((j_v^{n+1} \rho_g^n + j_\ell^{n+1} \rho_f^n) A)_j \Delta t \quad (3.13)$$

$$(\rho_f h_f(1-\alpha) + \rho_g h_g \alpha)_i^{n+1} V_i - H_i^n =$$

$$(p^{n+1} - p^n) V_i + ((j_v^{n+1} \rho_g^n h_g^n + j_\ell^{n+1} \rho_f^n h_f^n) A)_{j-1} \Delta t \\ - ((j_v^{n+1} \rho_g^n h_g^n + j_\ell^{n+1} \rho_f^n h_f^n) A)_j \Delta t + \dot{Q}_i^n \Delta t \quad (3.14)$$

Here, we use the old state thermal dynamic properties to represent the intermediate state thermal dynamic properties. To close the equations, we need the drift flux model

$$(j_v)_j^{n+1} = \alpha(C_o j + v_{gj})_j^{n+1} \quad (3.15)$$

Using these three equations, the three unknowns, α_i^{n+1} , $(j_v)_j^{n+1}$, and $(j_1)_j^{n+1}$ can be solved, provided that the flow rates from junction $j-1$ are given. Therefore, if we start from the bottom control volume, the equation set can be solved one by one sequentially. Once the junction flow rates for a control volume are obtained, they serve as the boundary conditions for the next control volume.

It is of great interest to find out the solution of Eq.(3.13), (3.14), and (3.15) can be expressed in an explicit form by means of the following manipulations. First, the superficial liquid velocity j_1 is substituted by $j-j_v$ and Eqs(3.13), (3.14) become

$$(\rho_f - \rho_{fg} \alpha)_i^{n+1} V_i - M_i^n = (GA)_{j-1}^{n+1} \Delta t - (\rho_f^{n+1} j^{n+1} - \rho_{fg}^{n+1} j_v^{n+1})_j A_j \Delta t \quad (3.16)$$

$$(\rho_f h_f - (\rho_f h_f - \rho_g h_g) \alpha)_i^{n+1} V_i - H_i^n = \\ (GhA)_{j-1}^{n+1} \Delta t - (\rho_f^{n+1} h_f^{n+1} j^{n+1} - (\rho_f h_f - \rho_g h_g)^{n+1} j_v^{n+1})_j A_j \Delta t \\ + (p^{n+1} - p^n) V_i + \dot{Q}_i^n \Delta t \quad (3.17)$$

The void fraction α_i^{n+1} can then be eliminated from Eqs.(3.16) and (3.17).

$$\begin{aligned}
& - (\rho_f \rho_g h_{fg})^{n+1} V_i - M_i^n (\rho_f h_f - \rho_g h_g)^{n+1} + H_i^n (\rho_f - \rho_g)^{n+1} \\
& = (GA)_{j-1}^{n+1/2} \Delta t (\rho_f h_f - \rho_g h_g)^{n+1} - (GhA)_{j-1}^{n+1/2} \Delta t (\rho_{fg})^{n+1} \\
& + (-\rho_f^n (\rho_f h_f - \rho_g h_g)^{n+1} + \rho_f^n h_f^n (\rho_f - \rho_g)^{n+1}) (j_v^{n+1/2} A)_j \Delta t \\
& + (\rho_{fg}^n (\rho_f h_f - \rho_g h_g)^{n+1} - \rho_{fg}^{n+1} (\rho_f h_f - \rho_g h_g)^n) (j_v^{n+1/2} A)_j \Delta t \\
& - ((p^{n+1} - p^n) V_i + \dot{Q}_i^n \Delta t) (\rho_{fg})^{n+1} \quad (3.18)
\end{aligned}$$

For simplicity, the $\alpha^{n+1/2}$, $c_0^{n+1/2}$, $v_{gj}^{n+1/2}$ in Eq.(3.15) are replaced by α^n , c_0^n , v_{gj}^n respectively. As a result,

$$(j_v)_j^{n+1/2} = \alpha_i^n (c_0^n j^{n+1/2} + v_{gj}^n)_j \quad (3.19)$$

With Eq(3.19) and a new defined quantity

$$COEF \equiv (\rho_{fg}^n (\rho_f h_f - \rho_g h_g)^{n+1} - \rho_{fg}^{n+1} (\rho_f h_f - \rho_g h_g)^n) \quad (3.20)$$

an explicit form of total superficial velocity for junction j at the intermediate state $n+1/2$ can be obtained as

$$j_j^{n+1/2} = \text{ABOVE/BELOW} \quad (3.21)$$

where

$$\begin{aligned}
\text{ABOVE} = & - (\rho_f \rho_g h_{fg})^{n+1} V_i - M_i^n (\rho_f h_f - \rho_g h_g)^{n+1} + H_i^n \rho_{fg}^{n+1} \\
& - (GA)_{j-1}^{n+1/2} \Delta t (\rho_f h_f - \rho_g h_g)^{n+1} + ((GhA)_{j-1}^{n+1/2} \Delta t + \dot{Q}_i^n \Delta t \\
& + (p^{n+1} - p^n) V_i) \rho_{fg}^{n+1} - (COEF) A_j \Delta t \alpha_i^n v_{gj}^n \quad (3.22)
\end{aligned}$$

$$\begin{aligned}
\text{BELOW} = & (-\rho_f^n (\rho_f h_f - \rho_g h_g)^{n+1} + (\rho_f h_f)^n \rho_{fg}^{n+1} + (COEF) \alpha_i^n c_0^n) A_j \Delta t \\
& \quad (3.23)
\end{aligned}$$

If the control volume i happens to be the control volume where water level resides, the volume flow rate of liquid at the junction located between control volume i and $i+1$ is neglected.

In other words, we can substitute $\alpha_i^n = 1.0$, $c_{0,i}^n = 1.0$, $(v_{g,i})_j^n = 0.0$ into equations (3.21), (3.22), and (3.23). Therefore, the total superficial velocity becomes:

$$j_j^{n+1/2} = A1/B1$$

where

$$\begin{aligned} A1 = & -(\rho_f \rho_g h_{fg})^{n+1} v_i - M_i^n (\rho_f h_f - \rho_g h_g)^{n+1} + H_i^n (\rho_f - \rho_g)^{n+1} \\ & - (GA)_{j-1}^{n+1/2} (\rho_f h_f - \rho_g h_g)^{n+1} \Delta t + ((GA)_{j-1}^{n+1/2} \Delta t + \dot{Q}_i^n \Delta t \\ & + (p^{n+1} - p^n) v_i) \rho_{fg}^{n+1} \end{aligned} \quad (3.24)$$

$$B1 = (h_g^n (\rho_f - \rho_g)^{n+1} + (\rho_f h_f - \rho_g h_g)^{n+1}) \rho_g^n A_j \Delta t \quad (3.25)$$

After $j_j^{n+1/2}$ is calculated, Eq. (3.19) is used to solve the superficial vapor velocity $j_j^{n+1/2}$. The difference between $j_j^{n+1/2}$ and $j_v^{n+1/2}$ is, of course, the superficial liquid velocity j_l . The $j_v^{n+1/2}$, j_l so obtained are then substituted into Eqs (3.13) and (3.14) to get the new void fraction α_i^{n+1} and new mass M_i^{n+1} and enthalpy H_i .

3.2. Heat Conduction Model

The general equation for the heat conduction is given as:

$$\nabla^2 T + \frac{q'''}{k} = \frac{\rho C_p}{k} \left(\frac{\partial T}{\partial t} \right) \quad (3.26)$$

For a heat slab without a heat source, the one-dimensional form of equation is

$$\frac{\partial^2 T}{\partial x^2} = \frac{\rho C_p}{k} \left(\frac{\partial T}{\partial t} \right) \quad (3.27)$$

Considering a slab in Fig.8, with the forward difference scheme, the equation for the interior node is given by

$$\frac{T_{i+1}^n - 2T_i^n + T_{i-1}^n}{\Delta x^2} = \frac{\rho C_p}{k} \frac{T_i^{n+1} - T_i^n}{\Delta t} \quad (3.28)$$

or

$$T_i^{n+1} = \left(1 - \frac{2k\Delta t}{\rho C_p \Delta x^2} \right) T_i^n + \frac{k}{\rho C_p} \frac{\Delta t}{\Delta x^2} (T_{i-1}^n + T_{i+1}^n) \quad (3.29)$$

From the definition of Fourier modulus,

$$F_0 \equiv \frac{k}{\rho C_p} \frac{\Delta t}{\Delta x^2}$$

Eq(3.29) can be rewritten as:

$$T_i^{n+1} = (1-2F_0)T_i^n + F_0(T_{i-1}^n + T_{i+1}^n) \quad (3.30)$$

From the stability analysis it is found that F_0 should not be greater than 1/2.

The expression for surface temperature is slightly different from the expression for interior temperature. Referred to Fig. 8 it is noted that only half a solid layer is involved in the determination of surface. A heat balance at the surface is given by

$$k \frac{T_2^n - T_1^n}{\Delta x} - h(T_1^n - T_f^n) + \frac{q''' \Delta x}{2} = \frac{\rho C_p \Delta x}{2 \Delta t} (T_1^{n+1} - T_1^n) \quad (3.31)$$

where T_f^n is the fluid bulk temperature and h is the heat transfer coefficient by convection. The above equation is rearranged as

$$\begin{aligned} T_1^{n+1} &= T_1^n + 2F_0 (T_2^n - T_1^n - B_{1\Delta x} (T_1^n - T_f^n)) \\ &= (1-2F_0 + 2F_0 B_{1\Delta x}) T_1^n + 2F_0 T_2^n + 2F_0 B_{1\Delta x} T_f^n \end{aligned} \quad (3.32)$$

where F_0 = Fourier modulus

$B_{1\Delta x} = h\Delta x/k$, a Biot number on Δx as a characteristic length

Therefore, both the surface temperature and the temperature of the interior nodes can be calculated explicitly from the previous time step. The stability of this equation requires $F_0 B_{1\Delta x}$ not greater than 1/2.

3.3 Time Step Control

To obtain a reasonably accurate result and to avoid the possible numerical difficulties a small time step is required for a fast transient. This requirement can be relaxed as the transient becomes slower and the changing of system parameters also becomes slower. In order to save computational time, the largest

possible time step size is always desirable. Unfortunately, the transients usually do not proceed with the same speed and a code user can not foresee the appropriate time step sizes for a given transient.

As it is described in section 3.1, the 'pressure step' concept can automatically handle this difficulty. In SIT-SG, the time step size is mainly determined by the given pressure step size. The so obtained time step size is then subject to an upper limitation specified by the computer code user. The user specified maximum time step size should not be greater than (1) the maximum time step size required by the stability of heat conduction equation, described in section 3.2.1 and (2) the Courant condition which requires that the time step size be smaller than the node size divided by the flow velocity. The procedure for this determining process is given below:

1. From the given constant pressure step size, the automatic time step size is calculated.
2. The calculated time step size is compared to the input maximum allowable time step size. If the calculated time step size is too large, the pressure step size is automatically reduced by a factor of 0.9 and the step 1,2 is repeated until the calculated time step size is smaller than the maximum time step size.

3.4 Implementation of Critical Flow Calculation

The detailed procedure of implementation of critical flow model is given as follows:

1. Obtain the stagnation enthalpy h_o :

$$h_o = (1-x_o)h_f + x_o h_g \quad (3.33)$$

where x_o = quality of the control volume at the upstream of the break

By substituting

$$x_o = \frac{1}{1 + (V_l \rho_l (1-\alpha)) / (V_v \rho_v \alpha)} \quad (3.34)$$

h_o can be expressed as

$$h_o = (\rho_v j_v h_v + \rho_l j_l h_l) / (\rho_v j_v + \rho_l j_l) \quad (3.35)$$

where j_v = superficial vapor velocity = $V_v \alpha$

j_l = superficial liquid velocity = $V_l (1-\alpha)$

2. Set a higher limit of local quality $x_H = 1.0$
and a lower limit of local quality $x_L = 0.0$

3. Guess local quality $x_c = (x_H + x_L)/2$ and use x_c to calculate G^2 .

$$G^2 = -g_c s / (((1 - x_c + s x_c) x_c) \frac{dv_g}{dp} + ((1 + 2s x_c - 2x_c) / \rho_g + (2s x_c - 2s - 2s^2 x_c + s^2) / \rho_f) \frac{dx_c}{dp}) \quad (3.36)$$

where

$$s = \text{slip ratio} = \sqrt{\rho_f / \rho_g}$$

v_g = saturated vapor specific volume

$$\frac{dx_c}{dp} = \left(\frac{1-x_c}{h_{fg}} \frac{dh_f}{dp} \right) - \left(\frac{x_c}{h_{fg}} \frac{dh_g}{dp} \right)$$

In the above equation, all the properties are evaluated at the throat pressure

$$p_c = 0.55 p_o. \quad (3.37)$$

where p_o = stagnation pressure

4. Use x_c and G^2 to calculate h_o

$$h_o = (1-x_c)h_f + x_c h_g + \frac{G^2}{2g_c J} ((1-x_c)s/\rho_f - x_c/\rho_g)^2 (x_c + \frac{1-x_c}{s^2}) \quad (3.38)$$

In this equation, again, all the properties are evaluated at the throat pressure.

5. If h_o (step 4) > h_o (step 1), replace x_H by x_c and repeat step 3 to 5. On the other hand, if h_o (step 4) < h_o (step 1), replace x_L by x_c and repeat step 3 to 5. If the two h_o from step 4 and step 1 converge, calculate G from G^2 .

3.5 Determination of Void Fraction Distribution in a Control Volume

For a given control volume and a given volume averaged void fraction, the void can distribute in various ways in the control volume. Figure 10 illustrates some of the possible void fraction distributions for a non-zero vapor flow rate. For a low given void fraction, the void fraction can distribute as Fig.10.a1 and Fig.10.a2. Similarly, for an intermediate void fraction, the distribution can be Fig.10.b1, 10.b2 or 10.b3 and for a high void

fraction, the distribution can be Fig.10.c1, 10.c2, or 10.c3. How the void fraction ends up in its current configuration depends on the history of the development process as well as the value of the void fraction and the flow conditions. For example, for a given high void fraction the tendency for various distributions is discussed. If we know, from the history, that the water level resides in this control volume and the vapor velocity is low then the void is most likely to be distributed as shown in the Figs.10.c1 and 10.c2. On the other hand, if the given control volume is located above the control volume where the water level resides or if the vapor velocity is very high, the void is most likely to be distributed as that shown in Fig.10.c3. If we overlook the differences between these two conditions, the results can be misleading. In an attempt to differentiate these various possibilities, the following selection logic is established:

1. From the previous state information, the control volume where the water level resides is identified.
2. If the water level resides in the given control volume, the flow regime below the mixture level is determined from the average void fraction below the mixture level and the vapor velocity. The average void fraction below the mixture level is assumed to be the same as the average void fraction of the control volume right below the given control volume. A vapor velocity, given in table 1, proposed by Ishii (13), which determines the transition from the churn-turbulent flow regime to the annular flow regime is used to determine whether the annular flow regime shown in Fig.10.c3 actually exists.
3. If the mixture level does not reside in the given control volume, the average void fraction of this control volume and the vapor velocity are used to determine whether the void fraction distribution is 10.a2, 10.b3, or 10.c3.

4. VERIFICATION OF MODEL

This chapter presents the calculations performed by the code SIT-SG and the comparisons with the experimental data. The experiments being simulated include: Battelle-Frankfurt blowdown, General Electric(GE) small vessel blowdown, GE large vessel blowdown, and M.I.T. steam generator blowdown test. For each experiment, a brief description about the test is provided so that a clear picture of the experiment can be obtained and a better understanding of the results can be accomplished.

4.1 Battelle-Frankfurt Blowdown Test

4.1.1 Test Description

The SWR-2R test⁽³⁴⁾ conducted at the Battelle-Institute in Frankfurt is designated as the OECD-CSNI Standard Problem No. 6, and has been simulated by TRAC-PD2 and other codes. Valuable information about the experimental data as well as the results from the code prediction are provided⁽³⁵⁾ and compared.

The test apparatus is a vertically oriented steel vessel of 2.546 ft(0.776 m) in inside diameter and 36.68 ft(11.18 m) in height. The vessel is fitted with a rod bundle heater located between 8.825 ft(2.69 m) and 17.03 ft(5.19 m) from the bottom of the vessel. A horizontal discharge pipe of 0.47 ft(0.143 m) in inside diameter and 1.54 ft(0.47 m) in length is connected to the vessel at an elevation of 32.16 ft(9.94 m) from the bottom of the vessel. A square-edged orifice plate of 2.52 inches(0.064 m) in inside diameter is mounted at the end of the discharge pipe. Blowdown is initiated by destroying a rupture disc installed downstream of the orifice.

To perform the test, the vessel is filled with subcooled water up to a certain level and is then heated up to a pressure of 1024 psi(70.6 bar) and an average water temperature of 545°F (558 K). After this condition is attained, the heater is turned off and the blowdown is initiated.

Several pressure taps are placed at different vessel levels as well as in the discharge pipe to monitor the pressure during the transient. The errors in the pressure measurements are approximately 1%. The fluid density at the discharge nozzle is measured by a two-beam gamma densitometer. The accuracy of this measurement is approximately 12%. There are also two drag bodies to measure the fluid momentum at the discharge nozzle. The break mass flow rate is determined from the fluid density and the drag body measurements. The error in the measured discharge flow rate is estimated to be between 10 to 15%. The time history of the mixture water level

is measured by a stack equipped with electrical contacts at many axial locations. The accuracy of the mixture level measurement is ± 0.02 m.

4.1.2 Input Model Description

The test vessel is represented by 23 nodes. The number of nodes is the same as that calculated by TRAC-PD2 drift flux model so that a fair comparison of computer time usage can be made. The geometric effects of the rod bundle heater is taken into account by decreasing the flow area by 22% and hydraulic diameter by a factor of 10 compared to those for the vessel without heater. To make a simple one-dimensional modeling, the vapor space above the break location is neglected. Two separate calculations are performed with two different drift flux model constants in churn-turbulent flow regime. The first drift flux constant is given by the Wilson's model and the second one is given by equation (2.12) both are limited by the upper bound limitations described in section 2.1.3.

4.1.3 Code Prediction and Comparison with Data

It is found that there is almost no difference between the results performed with the two different drift flux constants. Therefore, no distinction can be made from these two results. Figure 11 shows the comparison of the pressure predictions by our code (SIT-SG), by TRAC-PD2, and the measured data. The slope of our prediction is about the same as that of TRAC prediction and the data. The initial under-shoot of the data, which is present because of the delay in the onset of flashing, is missed by all the code predictions. There is a sudden slope change at about 0.1 sec in both TRAC predictions. It is not clear why the slope changes in the TRAC calculations. There is no slope change in SIT-SG prediction during the initial blowdown period and as a result, the pressure prediction in our code is overestimated. Figure 12 shows the mass flow rate through the break. During the early part of the transient ($t < 2$ seconds), only steam flows through the discharge pipe. As the transient progresses, the two-phase mixture in the vessel swells. When the mixture level arrives at the discharge pipe, the break mass flow rate increases sharply because of a sudden increase in the fluid density. This happens at approximately 2.3 seconds in the test. A very close prediction of this timing has been made by our code. The slightly early arrival of the mixture level at the discharge pipe and the slight overprediction of the break mass flow rate are observed for all code predictions. This can be attributed to the fact that no discharge coefficient is used in any of the calculations while the reduction of the break flow area at the orifice plate is to be expected in the experiment.

Figure 13 shows the measured and the predicted mixture level. Except the first 0.3 seconds, when the mixture water level does not rise due to the delay in flashing, all the models predict a fairly good water level swelling speed.

Finally, it is of interest to compare the computer time usage. For the calculations shown in Fig 11 to 13, it takes 151 seconds on the CDC-7600 computer for the TRAC-PD2 drift-flux model calculation. For the same transient, it takes 14 seconds on the VAX-11/782 computer for our code(SIT-SG) calculation. It is suggested that the running speed of VAX is 15 times slower than that of CDC-7600. With this estimate, the computation time required by using SIT-SG is 150 times smaller than that required by using TRAC-PD2. The saving of computer time is great.

4.2 GE Small Vessel Blowdown Test

4.2.1 Description of the Experiments

The pressure vessel for the small vessel blowdown test⁽³⁶⁾ is a 10 ft³ (0.28m³) carbon steel vessel, 12-inch (0.3m) in diameter and 14 ft (4.3m) in height. Different-sized orifice plates are mounted in the blowdown line to limit the blowdown flow rate and vary the depressurization rate. To perform a test, the vessel is filled with demineralized water and boiled at atmospheric pressure for approximately 30 minutes. This liberates any dissolved gas in the supply water. A vent at the top of the vessel is then closed and the water heated to the starting conditions which are nominally 1000 psi and 545°F (6900KN/M², 385°C). When the blowdown is initiated, there are three basic types of measurements that are made during the test: pressures, pressure differences, and temperatures. Figure 14 shows the instruments used.

Two-phase mixture density in the measurement nodes is obtained from the measurements of the axial differential pressure, i.e. hydrostatic head of the fluid. The density and the volume of the measurement node determines the average void fraction

$$\alpha = (\bar{\rho} - \rho_f) / (\rho_g - \rho_f) \quad (4.1)$$

The two-phase level is determined by a linear extrapolation of the two-phase void profile below the level. The level is

$$L_{2\phi} = \frac{L_1(\bar{\rho}_1 - \rho_g)}{(\bar{\rho}_{1-1} - \rho_g)} \quad (4.2)$$

4.2.2 Input Model Description

Three separate experiments are calculated and compared. The first experiment does not have a test number⁽³⁷⁾ while the other two are designated as test 1004-3⁽³⁶⁾ and 1004-2⁽³⁶⁾. Let's call the

first experiment "level swell test" so that it is easy to refer to. For the level swell test, the initial pressure is 1042 psia, the initial water level is 8.14 ft, and the break diameter is 3/8 inches. For the test 1004-3, the initial pressure is 1011 psia, the initial water level is 10.4 ft, and the break size is 3/8 inches. For the test 1004-2, the initial pressure is 1011 psia, the initial water level is 10.5 ft, and the break size is 7/8 inches.

The test vessel in level swell test is represented by 8 control volumes. For the test 1004-3 and 1004-2 the vapor space above the break location is neglected because the mixture level reaches the break elevation during the transients. To take into account the reduction in flow area, a discharge coefficient of 0.76 is used for all three calculations.

For a mixture water level calculation, the drift flux model constants are selected as the following. Wallis' model is used in the bubbly flow regime and several different models are used in the churn-turbulent flow regime. These models include the Ishii model, Wilson model, and equation (2.12).

4.2.3. Code Prediction and Comparison with Data

4.2.3.1 Level Swell Test

The predicted pressure for the simulated test is shown in Fig. 15. Because the pressure responses for the calculations with three different drift flux constants are the same, only one analytical result is presented. Excellent agreement between the predicted pressure and the measured pressure is achieved. When the pressure curve is compared to the Battelle-Frankfurt experiments in the previous section, it is found that there is no apparent slope change during the early period of blowdown. The mixture water level predicted by the code and the mixture water level obtained from GE test are compared in Fig. 16. The calculations with Ishii's model overpredicts the maximum mixture water level while the V_{gj} given by equation (2.12) predicts the right maximum swelling height and the Wilson model underpredicts the maximum swelling height. All the models overpredict the mixture water level at the later period of the blowdown. To explain the discrepancy of the water level response in each model and to get a feeling of the order of magnitude of V_{gj} given by each model, the plots of V_{gj} vs. in Fig. 3 and 4 are referred. It is noted that the Wilson's model always gives the upper bound V_{gj} value while the Ishii's model always gives the lower bound value in the range of $0.2 < \alpha < 0.8$. For a given void fraction and a total superficial velocity, j , a larger V_{gj} leads to a smaller liquid superficial velocity and consequently a less swelling of mixture water level. This provides the reason why Wilson's model predicts the smallest water level swelling while Ishii's model predicts the largest water level swelling.

4.2.3.2 Blowdown Test 1004-3

The predicted pressure for the simulated test is shown in Fig. 17. The pressure response using the V_{gj} provided by equation (2.12) slightly overpredicts the pressure while the V_{gj} provided by the Wilson model predicts an excellent pressure response.

The predicted mixture level and the mixture level obtained from the test are compared in Fig. 18. The Ishii's model overpredicts the mixture level while both the Wilson's model and equation (2.12) well predict the mixture level.

4.2.3.3 Blowdown Test 1004-2

This experiment is of particular interest because the data covers the whole range of pressure, including the high, intermediate, and low pressure range. The data is valuable for checking the suitability of drift flux model constants in the low pressure range. The experimental pressure and the predicted pressure are shown in Fig. 19. Because the calculated pressure responses are the same only one analytical result is presented. Excellent agreement between the predicted pressure and the measured pressure is achieved. The predicted and the experimental mixture level response are shown in Fig. 20. The calculation with the V_{gj} given by Eq(2.12) predicts a closest mixture water level response.

4.3 GE Large Vessel Blowdown Test

4.3.1 Description of the Experiment

The pressure vessel used in the large vessel blowdown test⁽³⁶⁾ is a 160 ft³ (4.5 m³) carbon steel vessel, 47 inch (1.19m) in diameter and 14 ft (4.3m) in height. While both top and bottom break blowdown tests are conducted, only the top blowdown is chosen for the verification of our code. The specific test number being compared is 5801-15. Figure 21 is a schematic diagram showing the vessel, the blowdown line, and the instrumentation locations for the top blowdown test. The blowdown flow rate and depressurization rate are varied by mounting different sized flow limiting venturi nozzles in the horizontal portion of the blowdown line. Rupture discs are used to initiate the blowdown. Test procedure and test measurements are similar to those discussed in section 4.2 for the small vessel blowdown test.

4.3.2 Input Model Description

The test vessel is represented by 8 control volumes. Three drift flux model constants calculated from the Ishii correlation, the Wilson correlation, and Eq. 2.12 respectively, are selected for churn-turbulent flow regime. No discharge coefficient is used for the break flow calculation.

4.3.3 Code Prediction and Comparison with Data

The comparison between the predicted and measured pressure are presented in Fig. 22. The prediction successfully reproduces the measured pressure trace. As we notice, the break in this experiment is simulated by the venturi nozzle which is different from the break in section 4.2.1 in which the break is simulated by the orifice plate, therefore, the excellent pressure prediction is quite impressive. Since the system pressure depends largely on the break flow rate, the adequacy of the critical flow model is proved indirectly by the good match in pressure. Calculation of the mixture water level are compared to the experimental data in Fig. 23. Large variations of predicted mixture water levels are observed when the calculations are performed with different drift flux constants. The calculation with Ishii's drift flux constant overpredicts the mixture water level while the calculation with Wilson's drift flux constant underpredicts the mixture water level. The closest result to the experimental data is given by Eq. 2.12.

4.4 Steam Generator Blowdown Test in M.I.T.

4.4.1 Description of Experimental Facility

The steam generator simulator(see figure 24), is a simple model of a PWR U-tube steam generator(see figure 25). The vessel of the simulator is made from stainless steel pipe, 4.5 inches in outside diameter, 3.826 inches in inside diameter, and 9.0 ft in height. An external downcomer, 1.5 inches in inside diameter and 6 feet in height, is connected to the steam generator vessel so that downcomer effects can also be studied. The apparatus represents only the secondary side of the steam generator. Instead of receiving heat from the primary side, the water on the secondary side is heated by electric heaters at the bottom of the vessel. The heaters are used to bring the system pressure and temperature to the normal U-tube steam generator operating conditions, namely, 1055 psi and 550 °F respectively. The blowdown section consists of a 10 feet long, 1 inch stainless steel pipe, positioned parallel to the vessel and ended into the suppression pool (as shown in figure 24). The blowdown section is divided by two flanges, between which the simulated breaks are placed. These breaks are built from various sizes of tubing. The lengths of tubing is chosen so that the L/D is constant at 20. (The short L/D tube is not tested and therefore the nonequilibrium effects, which is associated with the short L/D, does not occur in the tests.) To cover the range of break sizes of interest, five break diameters are selected; 1/2, 3/8, 1/4, 1/8, and 1/16 of an inch. The 3/8 inch diameter is selected in order to make the break flow area to vessel flow area ratio in the experiment the same as that of the typical U-tube steam generator. In this way, a realistic range of superficial velocities can be achieved in the experiment. The other four sizes are used to show the effect of the break sizes to the transient. The entrance to these tubes were rounded as shown in Fig. 26. Right below the small size tubing two

valves, a gate valve and a ball valve, in series are installed to prevent leaking. To initiate a run the gate valve is opened and then the ball valve is quickly opened by hand.

The suppression pool consists of a thirty gallon tank, which is counter balanced by another 30 gallon tank through an "I" beam. The blowdown pipe discharges the liquid and vapor into one of the tanks. At the opposite end of this suppression tank the "I" beam is fastened to the floor through two sections of chain jointed by a rod which has strain gage mounted on it. The strain gage is used to measure the mass added to the suppression tank. With this information the total amount of expelled fluid (which is also called carryover in the following context) at any instant can be obtained. For the large breaks, the first few seconds discharge measurement is flawed by the pool dynamics. Thermal couples are installed in the suppression pool to measure the pool temperature throughout the whole transient. The measured temperature is then used to determine the total amount of energy associated with the expelled fluid. The quality of the expelled fluid (break flow) can be obtained from the measured time integrated mass and energy.

4.4.2 Empty Vessel Tests

4.4.2.1 Test Description

The experimental procedure for these tests includes filling up the vessel with approximately 11 liters of water and heating up the system. Initially the vessel is left open for about 10 minutes, so any air trapped in the vessel can escape. The system is then sealed and brought up to pressure. After the system pressure has stabilized at the desired value, the heat source is turned off and the transient initiated.

4.4.2.2 Computer Code Input Model Description

Because the experimental results (38) did not show that the downcomer effect is significant (as it is illustrated in Figs 26a through 26d), only the runs with the downcomer valve full open are calculated and compared. With the one dimensional assumption, the downcomer is lumped into the main vessel. The overall space is represented by a series of control volumes with 9 cells. Each cell has the same height. The total volume of the test section equals to the sum of the space inside the 4 inch diameter vessel and the 1.5 inch diameter downcomer. Because the valve was open there is every reason to expect that the temperature in the vessel and downcomer are the same. Dividing the total volume by the total height of the test section, the flow area of the cell is obtained. The weighted mean drift velocities being selected are from: (1) Wallis' model (equation (2.7)) for bubbly flow regime, (2) Equation (2.12) with the associated upper limits for churn-turbulent flow regime, and (3) Ishii's model (equation (2.22)) for annular flow regime. The selection is based on the results obtained from the comparisons between the predicted mixture level and the experimental mixture level for the five

tests described in section 4.1 through 4.3.

4.4.2.3 Code Prediction and Comparison with Data

The code predictions and comparisons with data obtained by Parlos⁽³⁸⁾ are made with two initial pressures, which are 1055 psi and 800 psi respectively. Except the initial pressure, the test conditions and procedures for 800 psi are exactly the same as that for 1055 psi. The comparison between the code prediction and the experimental results for two initial pressures are used to show the applicability of the code in various initial conditions.

4.4.2.3.1 Initial Pressure of 1055 psi

The three middle break sizes ($3/8"$, $1/4"$, $1/8"$) out of the five tested break sizes ($1/2"$, $3/8"$, $1/4"$, $1/8"$, $1/16"$) are chosen as the object of comparison between code prediction and experimental result.

In Figures 27 thru 32, the transient pressure and percent of carryover are shown. For each figure there are three curves, namely, code prediction with realistic heat transfer model, code prediction without heat addition, and the experimental result from our laboratory. Several conclusions can be drawn from the comparisons:

1. In general, the agreement between experimental results and the prediction results are good. For the pressure response, very good agreement has been achieved for $1/4"$ and $1/8"$ break and reasonably good agreement has been achieved for $3/8"$ break. For the carryover response, the agreement in all three cases are all very good. (When blowdown is initiated, because of the upward motion of liquid in the tank there is an uplift force on the tank and therefore a dynamic behavior is observed in the first few seconds. After the water in the pool settles down, the experimental result shows only slight difference from the prediction.)
2. The effect of heat transfer is significant. The transient response, especially the amount of carryover, shows that an adequate heat transfer model is very important when describing the whole transient response.

For some break sizes, the measured pressure is higher than the calculated pressure. The possible reasons are (i) In the experiment, the break is initiated manually, which leads to a time lag before the break is fully open. In the model the break is assumed to be open instantly and therefore a faster depressurization rate is predicted. (ii) The steam may condense inside the blowdown section which decreases the break quality. (iii) The uncertainty associated with the critical flow model.

To get a feeling for the thermal hydraulic behavior in the vessel,

the superficial gas velocity j_g and the superficial liquid velocity j_l for 3/8" break are shown in Fig. 33 and Fig. 34 respectively. Initially, both j_g and j_l are zero. When blowdown begins, the j_g in the upper control volume shows an increasing jump. As time increases the j_g in the top control volume stays almost the same value because of the critical flow restraint while the j_g in the lower control volume increases due to flashing and j_l decreases in the lower control volume due to the effect of gravity. After the mixture water level reaches the upper control volumes, the j_g in the upper control volumes has a reducing jump while the j_l has an increasing jump which makes the upper control volumes behave the same as the lower control volume. The superficial liquid velocities are shown to be positive only at the very beginning of the transient and slightly negative values are calculated throughout the rest of the transient. This indicates that countercurrent flow characterizes the transient response. Another way to show the relationship between j_g , j_l is given in Fig. 35. A pressure of 1000 psi is used to create the constant void lines in Fig. 35. The number of 1 to 8 represents the constant void lines from $\alpha = 0.1$ to $\alpha = 0.8$ respectively. The process of the whole transient faced by the upper, middle and bottom control volumes for 3/8" break are indicated by the arrow and the symbol of U, M, B respectively. To illustrate the flow regimes of the simulated steam generator during the transient, Fig. 35 is replotted as Fig. 36. The description of the flow regime transition criteria in Fig. 36. is given in subsection 2.1.2.

From Fig. 35 and 36, it is found that

1. Ishii's churn-turbulent flow vs. annular flow transition criteria is not important in the empty vessel test.
2. For the bottom control volume and middle control volume, the flow pattern is bubbly flow regime in the very early period which changes into churn-turbulent flow regime later. For upper control volume, the flow pattern is dispersed flow or annular flow in the beginning which passes through churn-turbulent flow regime and back to annular or dispersed flow regime.

During blowdown, liquid droplets will be entrained to the space above the mixture level. We are interested in knowing whether entrainment is important for modeling the system transient response for a MSLB or FLB transient. Specifically, we are interested in the effect of entrainment on the total amount of carryover and the water level propagation during the blowdown.

It is noted that the entrainment from a sharp water-vapor interface into a large diameter tube is similar to the pool entrainment. By applying Ishii's model to our test section with five superficial vapor velocities which are typical values for our blowdown test, namely 10.0, 8.0, 6.0, 4.0, 2.0 ft/sec, the relationship between entrainment and height above mixture level

are observed in Fig. 37, 38. In these figures, the dash lines represent the region where correlation is not available and lower estimate value is given. The entrainment E_{fg} on the y-axis is defined as

$$E_{fg} = \frac{\rho_l j_l}{\rho_v j_v} \quad (2.70)$$

These figures indicate that beyond certain height, that being in deposition controlled region, the entrainment is essentially negligible. Therefore, if entrainment is to be of any significance, it must be in the near surface region or the momentum controlled region. To see the effect of entrainment on break flow rate, an example calculation is made. For the example enclosed, two cases with same given pressure are compared and shown in table 3. For case A, no entrainment is assumed and the upstream condition of a break is given as pure vapor. For case B, some entrainment is assumed. Because of the entrainment some liquid is presented to the break. The amount of liquid being presented to the break is given by

$$\rho_l j_l = E_{fg} \rho_v j_v \quad (4.3)$$

In this way the enthalpy of flow at the upstream of the break becomes:

$$h = \frac{\rho_v j_v h_v + \rho_l j_l h_l}{\rho_v j_v + \rho_l h_l} = \frac{h_v + E_{fg} h_l}{1 + E_{fg}} \quad (4.4)$$

This is different from case A in which $h = h_g$ (saturated vapor enthalpy). Using the E_{fg} value at the near surface region shown in Figs. 37 and 38, the break flow rate for case B is obtained and compared to that for case A in table 3. From this table it is shown that the effect of entrainment on the critical flow rate is not negligible provided the entrainment is large. But this result doesn't imply that entrainment also has large effect on overall carryover. On the contrary, as it will be shown below that the effect of entrainment on overall carryover is negligible.

Before discussing the effect of entrainment on overall carryover, it is helpful to illustrate the water level response and the break mass flow rate during the transient. The whole processes of the water level response is shown in Fig 39 for 1/8" break. Initially, there is a distinct water level in the vessel. When the transient is initiated, the mixture water level goes up due to

flashing, which is the result of fast depressurization. As the mixture level goes up further, it may reach the top of the vessel and the two phase mixture level disappears. This condition will be maintained until two phase mixture level reappears some time later. The break flow rate is determined largely by the water level response. Figures 40 through 43 show the break flow rates for various sizes of breaks. At the beginning of the blowdown, the break mass flow rate is low because the break flow consists of almost pure vapor. Once the water level reaches the break entrance, the break flow rate suddenly increases due to a sudden increase in the fluid density. After water level reappeared (as shown in Fig. 39), the break flow rate returns to the small value because the break flow consists of almost pure steam again.

To evaluate the entrainment effect, we notice that there is no entrainment when there is no mixture level. Also, there is little or no entrainment when there is a large distance between mixture level and the break. This is shown in Fig. 44. Therefore, it is the period when mixture water level is close to but not high enough to reach the break that gives sensible effect to break flow rate as shown in Fig. 40 through 43. The fact that this period is short results in almost identical carryover response for both the no entrainment and the with entrainment calculations.

The effect of entrainment on water level can be figured out by looking at the value of j_l/j_v . From Eq. (2.70)

$$\frac{j_l}{j_v} = E_{fg} \left(\frac{\rho_v}{\rho_l} \right) \quad (4.5)$$

From Figs. 37 and 38, it is found that

$$\begin{array}{ll} \text{at 1000 psi } (E_{fg})_{\max} = 0.095 & (j_l/j_v)_{\max} = 0.45\% \\ \text{at 400 psi } (E_{fg})_{\max} = 0.28 & (j_l/j_v)_{\max} = 0.49\% \end{array}$$

Therefore, in terms of volume, the amount of entrainment is so small that it has almost no effect on water level response.

The time integration of heat transfer from the wall for five break sizes, namely 1/2", 3/8", 1/4", 1/8" and 1/16" diameter, are calculated and shown in Fig. 45, 46. The time scale of 1/16" break is quite different from the other break sizes and therefore is presented separately. The results show that the heat transfer from the largest break size turns out to be the smallest. As we can see the total amount of heat transferred for the 3/8", 1/2" break sizes (the larger break sizes) is smaller than for the other three intermediate or small break sizes. This is because the duration for blowdown is short for large break size and, therefore, in spite of its high heat transfer rate, the cumulative heat transfer becomes smaller for the large break size. This kind of result was anticipated and the calculation demonstrates that it

does, in fact, occur. We also find that the total amount of heat transfer is about the same for 1/4", 1/8" and 1/16" breaks. The time integration of blowdown enthalpy for all break sizes is calculated and shown in Fig. 47, 48. From these figures, it is found that the larger the break size is the faster the blowdown enthalpy increases. This is true because a large break size leads to a large blowdown rate. The results show that when blowdown ended the cumulative blowdown enthalpy is about the same for all break sizes.

The measured and predicted pool temperature is shown in Fig. 49 and Fig. 50. The following results are observed:

1. The rate of pool temperature increase is larger for larger break size. This is because of the larger mass and enthalpy flow rate corresponding to the larger break size.
2. The time at which the pool temperature stops increasing is shorter for the larger break size. This can be explained by the faster depressurization rate corresponding to the larger break size.
3. The predicted pool temperature is higher than the measured pool temperature in the early period of blowdown and it is reversed in the later period of blowdown.

Heat loss may be the reason for overprediction of pool temperature in the early period of blowdown. Before blowdown is initiated, the one inch pipe which connects the blowdown valve and the suppression pool, is cold. When blowdown begins the cold pipe is heated up by either the hot steam or the hot two phase mixture. By the time when blowdown ends, the pipe becomes so hot that it can not be touched. The heating up of the cold pipe provides the evidence of the heat loss. There are other types of heat losses. The heat loss through insulator, the small leakage of steam on the blowdown section, and the heat loss by radiation are typical examples of possible heat loss. Because of these heat losses, the measured pool temperature tends to be somewhat lower than the predicted value. As we can see, the discrepancy is larger in the early period as compared to other periods. This discrepancy occurs for two reasons. First, the heat loss rate is larger when the pipe is cold in the beginning. Second, the predicted depressurization rate is larger than the experimental depressurization rate and therefore the predicted blowdown flow rate is also larger. When the end of blowdown is approached, the chugging instability is observed in the experiment. The chugging phenomena tends to extract more steam out of the vessel and extend the period of blowdown. Consequently, the measured pool temperature tends to be higher at the end of blowdown.

4.4.2.3.2 Initial Pressure of 800 psi

The calculations of transient pressure and carryover for the three middle break sizes (3/8", 1/4", 1/8") are made and compared to the

experimental data. The pressure response is shown in Fig 51 to 53. The prediction successfully reproduces the experimental data. The measured and predicted carryover is shown in Fig 54 to 56. The agreement between the calculated results and the measured data is very good for the 1/4" break. The code overpredicts the carryover for 3/8" break and underpredicts the carryover for the 1/8" break. The reasonable good agreements between the prediction and the data proves the applicability of code for different initial conditions.

4.4.3. Test with Rod Bundles

To simulate the typical tube bundle geometry in the U-tube steam generator, a rod bundle is used. The rod bundle consists of 6 copper rods of 0.63 inches in diameter, arranged in such a way that the pitch to diameter ratio is approximately 1.5. This geometry is very close to the tube bundles in the W model F steam generator in which the steam tubes are 0.688 inches in outside diameter, arranged on a 0.98 inch square pitch. The overall rod height is 4 feet and the total rod bundle surface area is 89.8 square inches. The rod bundle has three support plates as shown in Fig. 57.

4.4.3.1 Test Description

The test procedure is the same as empty vessel test except the vessel is installed with a rod bundle and filled with approximately 9 liters of water. The amount of water is chosen so that the initial liquid to empty space ratio is about the same as that of the empty vessel test. Unlike the empty vessel tests, which are performed with two initial pressure, only tests with initial pressure of 1055 psi is conducted.

4.4.3.2 Computer Code Input Model Description

The input model in this calculation is similiar to that of empty vessel test except the additional modeling of the rod bundle. The stored heat in the rod bundle is modeled by the lumped parameter method which is justified by the high conductivity of the copper rods. The geometrical effect of rod bundle is taken into account by the reduced flow area.

4.4.3.3 Code Prediction and Comparison with Data

The comparison between the predicted and measured pressures are presented in Fig 58 to 61. A slight underprediction of pressure is observed for all the break sizes. The possible reason is already given in subsection 4.4.2.3.1. In spite of this, the comparisons are considered to be good. The comparison between the predicted and measured carryover are illustrated in Figs 62 and 63. After the pool dynamics diminishes, the carryover response is reasonably well predicted.

The comparison between the predicted mixture level and the

measured dryout front are shown in Fig 64 to 67. Large discrepancies exist between the predicted mixture level and the measured dryout front. The high dryout front indicates that a large wet area is sustained between the mixture level and the dryout front. By comparing the pressure-time curve to the dryout front-time curve, it is found that the dryout occurs when the blowdown is almost over. By then the mixture water level is already very small. Therefore, the amount of heat transfer will be greatly underestimated if the mixture level is used to calculate the effective heat transfer area.

The calculated superficial vapor and liquid velocities are shown in Fig 68 through 75. As it is shown in the empty vessel test, the countercurrent flow characterizes the whole transient. The calculated break flow rate is shown in Fig. 76 to 79. The time integrated heat transfer, from both vessel wall and rod bundles, are shown in Fig. 80. The results show that the 1/2" break has the largest integrated heat transfer while the 1/4" break has the lowest integrated heat transfer. The results really depend on the heat transfer rate and the duration of effective heat transfer. The integrated heat transfer is the area below the heat transfer rate curve shown in Fig 81. As is anticipated the heat transfer rate is larger and the duration for the heat transfer is smaller for larger break sizes. If the effect of heat transfer rate outweighs the effect of time duration, the larger the break size the larger the integrated heat transfer and vice versa. Without performing the transient calculation, it is rather difficult to tell which factor will govern. The predicted and measured pool temperature are illustrated in Fig 82 and 83. Reasonable agreement has been obtained. The trend is the same as that for empty vessel test.

The drift flux model constants C_0 , V_{gj} for the transient are shown in Figs. 84 to 91. It is shown that the value of C_0 is roughly 1.18 for the churn turbulent flow regime. As the transition from the churn-turbulent flow regime to annular flow regime occurs, the value of C_0 drops quickly. The weighted mean drift velocity first increases due to pressure drop, bounded by the slug flow correlation, and then decreases when annular flow regime is predicted.

Figures 92 through 95 show the void fraction distribution for various sizes of breaks. The void fraction of the lower control volume, being zero initially, first increases and then decreases as it is shown for control volume 2 in Figs. 94 and 95. The increase of void fraction is because of the flashing resulted from the depressurization while the decrease of void fraction is due to the fall back of liquid resulted from the gravity force outweigh the vapor drag force. The void fraction of the middle control volume increases monotonically partly due to the flash and partly due to the large vapor drag force. The void fraction of the upper control volume, being 1.0 initially, first decreases and then increases. The decrease of void fraction is the result of pool swelling, and the increase of void fraction is the result of

carryover.

The time step size is shown in Fig. 96 to 99. In the early blowdown period, when the transient is more severe, the time step size is smaller while later in the blowdown period, when the blowdown is less severe, the time step size reaches the maximum value. Therefore, a best time step size is indeed automatically selected by the code.

The trajectory of liquid phase or radioactive material which is located at five different elevations at the time the steam line breaks, has been obtained and shown in Fig. 100 to 103. It is found that if radioactive material is initially located below certain elevation, it will be carried up to certain height and then falls back and never leaves the vessel. On the other hand if the initial location is high, i.e. the steam tube rupture occurs at high elevation, the radioactive material will be brought out of the vessel. The results also show that the critical elevation is lower for the larger break size just as it is anticipated. It is concluded that the location of rupture as well as the break size are important to the leakage of radioactive material. As we notice that, this calculation is equivalent to a calculation of steam tube rupture which occurs at the same time that steam line breaks with no flow from the primary side to the secondary side. The restriction on time and flow can be relaxed. If the steam tube rupture occurs with a time delay, it is interesting to see that Figs. 100 to 103 can still be applied. A shift of the curves to right by the amount of time delay is all that is needed. To take into account the flow from the primary side to the secondary side, one simply adds a junction and a boundary condition and repeats the whole calculation.

5. LIQUID HOLD UP EXPERIMENT

When the flow goes through the tube support plate in a steam generator, a much higher velocity is obtained because the flow area is greatly reduced by the tube support plates. As a result, flooding occurs easily once countercurrent flow is established. When the flooding occurs, there is a maximum amount of liquid which is allowed to penetrate down through the tube support plate for a given upward vapor flow rate. The upper limitation of downward liquid flow rate may result in excess liquid above the tube support plate and deficient liquid below the tube support plate. The excess liquid accumulated above the tube support plate results in the liquid hold up. When there are more than one plate, it is important to find out whether the liquid hold up phenomena will occur above each plate and establishes a multi-liquid-levels. If the multi-level hold up occurs the effective heat transfer area is going to increase a lot and the heat transfer from the primary side will increase proportionally. Therefore, it is of interest to find out:

1. Will the multi-level phenomena actually occur?
2. If it does occur, under what conditions will this phenomena occur?
3. What does it look like?
4. Does the phenomena change as the geometry of the tube support plate changes?
5. When the vapor velocity increases, how does the liquid drain?

To answer these questions, an air-water apparatus is set up to run experiments at atmosphere pressure.

5.1 Facility Description

The test section for the multi-level test is a pipe, 4 inches in diameter and 4 ft in height. The pipe is made of plexiglass so that visual observation is possible. A schematic diagram of the test section is shown in Fig. 104. The air enters the test section from the bottom while the water enters from the top so that a counter current flow can be established. A drain line is provided at the bottom to remove the excess water. To prevent the air from leaking to the drain line, the air is injected at a position 6.3 inches higher than the drain hole so that a pool of water be formed above the drain hole. The water is injected into the test section through a bowl shape hemisphere so that the splashing of water is minimized. Three plates of the same type are installed in the vessel to simulate the tube support plates. Monometers are provided to measure the collapsed liquid level above each plate (see Fig. 104). To study the effect of hole size, four different types of plates are used. Type A plate consists of ten 0.5 inch diameter holes, type B plate consists of six 0.5 inch diameter holes and two 1.0 inch diameter holes, type C plate consists of one 0.5 inch diameter hole and one 1.5 inch diameter hole, and type D plate consists of seven 0.5 inch holes

and a cut at the edge of the plate. The cross sections of these four types of plates are illustrated in Fig. 105. Among them, plate A, C and D have the same flow area while plate B has a larger flow area.

5.2 Experimental Procedures and Results

Three kinds of experiments were performed. To distinguish these experiments, we use three letters F, W, T to represent the experiments with Fixed water inventory, the experiment with Water injection from top, and the experiment which is under Transient. We also use four letters A, B, C, D to differential the plates being used so that the test numbers appear to be F-A, F-B, , etc.

5.2.1 Experiment with Fixed Water Inventory (F - Series Experiments)

The purpose of this experiment is to show the effect of tube support plate geometry to the water inventory distribution. Initially, the test section is filled with certain amount of water. After the desired water level is reached the water line is shut off and the air line is opened to initiate the experiment. The experimental results depend largely on the initial amount of water. If the initial water inventory is large, the final mixture water level will also be high. As long as the mixture water level is high enough, the multi-level hold up phenomena can always be observed. Therefore, the observation of multi-level phenomena should not be regarded as the result of flooding. However, it is of interest to compare the results from three different types of plates. For a initial water level of 13.2 inch and gas flow rate of 10.4 CFM, the result from plate A, B, and D (test run F-A1, F-B1, F-D1) can be described as follows:

- (a) After the air flow enters; the water level rises to the bottom plate and water begins to accumulate above the bottom plate.
- (b) As the water level accumulates high enough to reach the middle plate, the water begins to accumulate above the middle plate.
- (c) As the water level accumulate high enough to reach the top plate, no apparent liquid hold up is observed above top plate and a kind steady state is reached. The pictures for this state are shown in Fig. 106, 107, 109.

With the same initial water inventory and same air flow rate, the result from plate C (run number F-C1) is quite different. The developing process is the same as test run F-A1, F-B1, and F-D1 until step (b). After the water level reaches the top plate, it starts to accumulate above the top plate. As this happens, the water already accumulated above bottom and middle plate significantly decreases and when a steady state is achieved, most of the water seems to stay above the top plate with only a tiny amount of water staying above the bottom or middle plate. This is shown in Fig. 108.

To explain the difference between these four runs, we believe that flooding occurs at the top plate of run F-C1 but not in run F-A1, F-B1 or F-D1. In other words, the flooding occurs more easily at the type C plate. This argument is supported by the following W-series run result, in which W-C test has the lowest flooding gas velocity.

5.2.2 Countercurrent Flow Experiment (W-Serial Tests)

The purpose of this experiment is to study the effect of the plate geometry on the onset of flooding. In running the experiment, a constant air and water flow rate is supplied to the test section from bottom and top of the test section respectively. The flow in the drain line is controlled by a valve on the drain line so that the pool water level is always lower than the location where air is injected and higher than the drain hole.

Observation of the experiment shows that the onset of flooding (defined by the continuous water accumulation above a plate) can occur at the bottom plate or the top plate. If the flooding first occurs at the top plate, no water level accumulation is observed above the bottom or the middle plate. If the flooding first occurs at the bottom plate, the same phenomena in test run F-C1 (fixed water inventory with plate C) is observed. Water accumulates from bottom, through the developing process, and a final top flooding phenomena is maintained. This phenomena are observed for almost all the tests (shown in Fig 110 through 113) except one particular observation. For a liquid flow rate of 0.6 gpm (superficial velocity of 0.1 ft/sec) and a gas flow rate of 55.64 gpm (superficial velocity of 9.1 ft/sec), a steady liquid hold up above the bottom plate is observed as it is shown in Fig. 114. A slightly increase of gas velocity then leads to the top plate flooding as it is shown in Fig. 115. Although this exception provides the evidence that a steady liquid hold up above the bottom plate can occur, all the other observations show a strong tendency of liquid hold up above the top plate. Therefore, we believe that should liquid hold up phenomena occur, it is most likely to occur above the top plate. This can be explained by the pressure drop along the flow path. Because of the pressure drop, the pressure faced by the bottom plate is higher than that by the top plate. For a given liquid flow rate, the required gas velocity for flooding varies with gas density:

$$(j_g)_{\text{flooding}} \propto (\rho_g)^{-0.5} \quad (5.1)$$

with other parameters not very sensitive to the pressure. For a steady state flow, the mass conservation requires

$$(\rho_g j_g A) = \text{Constant} \quad (5.2)$$

$$(j_g) \propto (\rho_g)^{-1} \quad (5.3)$$

Therefore,

$$\frac{j_g}{(j_g)_{\text{flooding}}} \propto (\rho_g)^{-0.5} \quad (5.4)$$

At the top plate, the pressure is lower, the gas density is smaller, and, therefore, the potential for flooding, i.e. $(j_g)/(j_g)_{\text{flooding}}$ is larger. This also implies that the drain capability is smaller for a plate at a higher location. For a given intermediate plate, the amount of drain from the next higher plate is less than the amount of drain from the plate in question. With less input and more output, it is not very likely for water to accumulate above an intermediate plate.

A flooding curve for three types of plates are presented on Fig. 116. On the same figure, the Wallis flooding criteria⁽¹⁵⁾

$$j_g^{*1/2} + m j_l^{*1/2} = C \quad (5.5)$$

where

$$j_g^* = j_g \left(\frac{\rho_g}{gD(\Delta\rho)} \right)^{1/2}$$

$$j_l^* = j_l \left(\frac{\rho_l}{gD(\Delta\rho)} \right)^{1/2}$$

with $m=1.0$, $c=0.775$ for 1/2", 1", and 3/2" tubes are compared. It is found that a sizable geometry effect exists for different hole size distributions. If the geometry effect is governed by the large size hole, then for a given liquid flow rate the flooding gas velocity for plate C (which has 3/2" hole on it) should be higher than that for plate A (only 1/2" hole on it). The experimental results do not show this kind of trend. Therefore, we conclude that the flooding phenomena is not governed by the large size hole.

5.2.3 Transient Experiment (T-serial Tests)

The purpose of this experiment is to simulate the conditions occurring in the steam generator blowdown. In the later period of steam generator blowdown, the vapor flow rate decreases with time because the break flow rate decreases with time.

To simulate this transient condition, a flooding above the top plate is established either by a F-type experiment followed by an opening of the drain line or by a W-type experiment. The vapor flow rate is then gradually decreased. The experimental results show that it takes a long time to drain out the water above the

top plate while most of the time there is no accumulation of water above the middle or bottom plate during the transient. Occasionally, there is a small accumulation of water above the middle plate but it drains out very quickly (within a few seconds).

5.3 CONCLUSION

From the description of the above experimental observations, we find out that one plate (top plate) flooding phenomena is more likely to occur than multi-level phenomena. This has been explained by the effect of pressure drop in subsection 5.2.2. For a steam generator blowdown, the tendency of top plate flooding is further enhanced by the heat transfer from the hot surface and the flashing. The steam velocity increases with the elevation due to the generation of steam from the heat transfer, the flashing, and due to the expansion resulting from the pressure dropping. Consequently, we would only expect to find a pool of liquid in the bottom of the steam generator or on top of the tube bundle, provided that flooding occurs. This expectation is indeed confirmed by the blowdown experiment done by Dane⁽³⁹⁾. The dryout front in Fig. 122 shows a discontinuity across the top support plate while no discontinuity is observed across the intermediate support plate.

6. SUMMARY AND RECOMMENDATIONS

6.1 Summary

A computer program, called SIT-SG, has been developed to predict the heat transfer on the secondary side of a steam generator, the pressure, the carryover, the mixture water level, the flow rate distribution, and the void fraction distribution during the steam generator blowdown. This computer program is developed for best estimate predictions with a fast running capability.

Flow regime dependent drift flow model constants are used to take into account the difference between the liquid velocity and the vapor velocity. The correlations used for the various flow regimes are connected with a smoothing scheme. As far as the mixture level is concerned, the drift flux constants in the churn-turbulent flow regime is most important. The following drift flux constants in the churn-turbulent flow regime are recommended. The flow and void fraction distribution parameter C_0 is selected from Ishii's correlation and its value as function of pressure and void fraction is shown in Fig. 117. The weighted mean drift velocity being selected is originated from the equation proposed by Zuber with the coefficient given by Bertodano. This correlation is used in conjunction with the upper limitations provide by the slug flow regime correlation and a constant value of 3 ft/sec, which is the maximum drift velocity having been observed. The weighted mean drift velocity so obtained is plotted, in terms of pressure and vessel diameter, in Fig. 118. The recommended drift flux constants for the other flow regimes include: (i) V_{gj} and C_0 from Wallis correlation for bubbly flow regime (ii) V_{gj} and C_0 from Ishii correlation for annular flow regime. For bubbly flow regime, the recommended C_0 is 1.0 while the V_{gj} is shown in Fig. 119. For annular flow regime, the recommended C_0 is shown in Fig. 120 and the V_{gj} , with $D=0.34$ ft, is shown in Fig. 121.

A simple slip equilibrium critical flow model proposed by Fauske is selected for the calculation of two phase critical flow rate. This model is shown to be good for the venturi nozzle as well as for the blowdown pipe with L/D equals 20.

The water level propagation models and the water level reappearance criteria are shown to exhibit a reasonable mixture level behavior.

6.2 Recommendations

Several areas require further investigation are described as the followings:

- In SIT-SG, the effect of the separator to the blowdown is ignored. During a steam line break or a combined steam line break plus tube rupture, the behavior of the separator is unknown at present. It is expected that as the flashing

occurs, the water level swells and the flow direction in the drain line of the separator may reverse. The exact conditions which lead to flow reversal in the drain line have not been delineated. It is also expected that the separator may have large effects on the amount of radioactive material released in the combined steam line break plus tube rupture. Therefore, a study of the performance of separator during blowdown is recommended.

- . The calculation results show that large discrepancies exist between the calculated mixture level and the measured dryout front. It is suspected that the large discrepancy is a result of the low heat flux on the rod bundle surface. In a real steam generator, the difference may be smaller due to the higher surface heat flux in which a little bit of spray won't be able to keep the tube wet. It is recommended to study the effect of heat flux on the discrepancies between the predicted mixture level and the measured dryout front.

- . From our liquid hold up experiment, it is concluded that the potential for liquid hold up is greatest for the top tube support plate. Consequently, we would expect to find two mixture water levels, one in the bottom of the steam generator and one above the top tube support plate (provided that flooding occurs). To prove this conclusion in the steam generator blowdown experiment further investigations are recommended.

7. CONCLUSIONS

From the computer code calculations, the key parameters in the transient can be identified and a better understanding of the transient process has been obtained. With respect to the transient process and the computer code modeling, the following conclusions can be drawn.

- . For the blowdown process in steam line break, there are three periods can be identified: (i)pool swelling period (ii)water level disappearance period (iii)water level reappearance period. Because the characteristic behavior is different for each period, computer modeling should be able to distinguish these periods and simulate them appropriately.
- . As far as the break flow is concerned, the critical flow model is the only model which is important for determining the amount of outgoing flow in the pool swelling period and the water level reappearance period. The drift flux model is as important as the critical flow model in the water level disappearance period.
- . The heat transfer during the transient is very important to the transient response in steam generator secondary side. For the heat transfer calculation, it is very important to know whether the tube is dry or wet. If the tube is wet, the heat transfer is excellent. The secondary side heat transfer coefficient for the wet surface itself is, however, not important because the wall conduction, the primary heat transfer coefficient and the fouling factor are the real limits.
- . The pool entrainment phenomena has a small effect on both the total amount of outgoing fluid and the transient water level response.
- . In general, the thermal hydraulic properties in a control volume can be considered as homogeneous. However, special attention should be focused on the modeling of the node which contains the sharp water-vapor interface. Interpretation of node average quantities can be misleading under many circumstances. For example, using the node average void fraction to determine flow regime can result in significant error. In addition to void fraction, the knowledge of flow developing history and velocity level are also important for determining the flow regime in a control volume.
- . During the transient, the flow regime in the bottom control volume is bubbly flow initially. It changes into churn-turbulent flow regime after a very short period and

stays on churn-turbulent flow regime thereafter. The period for which the bubbly flow regime prevails is so short that the modeling of bubbly flow regime can be ignored. This conclusion is drawn from the calculations for our experiment. This experiment is equivalent to a break without feedwater. When this is applied to a real steam generator, the flow rate and the temperature of both the feedwater and auxiliary feedwater will have some effect on this conclusion due to the additional overcooling. These effects are, however, not expected to be very large because the feedwater has high temperature and the auxiliary feedwater has low flow rate. For the control volumes above the initial water level, the flow regime changes from the annular or liquid dispersed flow regime to churn-turbulent flow regime and back to annular or liquid dispersed flow regime. Because the flow regime in a fixed space is changing as the transient proceeds, we do not recommend a fixed drift flux constant for a certain given space. Instead, we recommend a set of correlations which can be used to calculate the drift flux constants for different flow regimes.

SIT-SG has been used to perform the pressure and the mixture level calculation for the Battelle-Frankfurt blowdown experiment, the G.E. small vessel, and the G.E. large vessel blowdown test. SIT-SG has also been used to predict the pressure, the water level, the carryover, the pool temperature, and the heat transfer from the hot wall for the M.I.T. steam generator simulator. The comparisons between the code prediction and the experimental data give rise to the following conclusions:

- . Good agreement is observed between the code prediction and experimental data for the pressure, the total amount of outgoing fluid and the suppression pool temperature response. These results justify our assumption in the code: (i) The pressure distribution is not important inside the secondary vessel and no momentum equation is required (ii) The behavior of the fluid in the vessel is basically one dimensional and one dimensional equation is capable of describing the system response (iii) Drift flux model is an adequate model for predicting the two-phase flow under blowdown conditions (iv) Thermal equilibrium exists between vapor and liquid phases.
- . Good agreement has been achieved by comparing the predicted pressure response with the experimental data measured in GE large vessel blowdown test, M.I.T. empty vessel test, and M.I.T. tests with internals. The original Henry-Fauske model is for a sharp-edged entrance. The break in the GE large vessel test is simulated by the venturi nozzles and the break geometry in M.I.T. experiment has a rounded entrance with L/D ratio equal to 20.0. This implies that the Henry-Fauskes critical flow model can be applied to a wide range of operating conditions when an L/D=20 nozzle or

a venturi nozzle is chosen. Short L/D nozzles were'nt tested.

- . Various drift flux models has been studied and a large discrepancy has been found for current available drift flux model constants. These discrepancies have a large effect on the water level prediction. The best drift flux model constants for this problem have been selected and shown in Chapter 6.
- . The measured dryout front is much higher than the predicted mixture water level. Consequently, the calculated effective heat transfer area is much smaller than the measured effective heat transfer area. The heat transfer rate from steam generator primary side to secondary side and the duration of effective heat transfer will be underpredicted if the dryout front is regared as the mixture level. However, it should be pointed out that in our experiment, the heat flux is quite low which leads to a reduced evaporation rate of liquid film and consequently results in a larger difference between dryout front and mixture level. Further study on the relation between dryout front and mixture level as function of entrainment rate, deposition rate, evaporation rate is recommended.
- . Our model is developed under the assumption of thermal equilibrium. This assumption is quite good for our empty vessel experiment which shows that the vapor temperature stays at the saturated temperature throughout the whole blowdown. For the experiment installed with rod bundle, superheat of vapor temperature is observed. Although the assumption isn't consistent with the real vapor state, the pressure and the carryover show the same degree of agreement as the empty vessel experiment. This suggests the effect of vapor superheat is insignificant on the pressure and the total amount of outgoing fluid.
- . From the liquid hold up experiment, we find that flooding can occur at the tube support plates, where the flow area is minimum. The potential for the liquid hold up due to flooding is largest for the top tube support plate. When this is applied to the blowdown in the steam generator secondary side, we would expect to find two mixture level, one in the bottom of the steam generator and one above the top tube support plate, provided that flooding occurs.

TABLE 1
CRITERIA FOR FLOW REGIME DETERMINATION

Bubbly Flow	$j_L > 2.34 - 1.07 \frac{[g\Delta\rho\sigma]}{\rho_f^{1/2}}$ and $\alpha < 0.1$
Churn-turbulent	$ j_v < \left(\frac{\Delta\rho g D}{\rho_g}\right)^{0.5} \cdot \left(\frac{1}{C_o} - 0.1\right)$ and $\alpha < 0.8$
Annular	$ j_v > \left(\frac{\Delta\rho g D}{\rho_g}\right)^{0.5} \cdot \left(\frac{1}{C_o} - 0.1\right)$ or $\alpha > 0.8$

TABLE 2
DRIFT FLUX MODEL CONSTANT V_{gj} USED IN FIGURE 3 AND 4

Key	Name of Model	Expression of V_{gj}	Applicable Regime
2	Wallis Model	Equation (2.7)	Bubbly Flow
3	Ishii Model	Equation (2.10) ^a	Churn-Turbulent
4	Zuber Model	Equation (2.10)	Churn-Turbulent
5	Zuber Model ^b	Equation (2.12)	Churn-Turbulent
6	Ishii Model	Equation (2.21)	Annular Flow
7	Ishii Model	Equation (2.23)	Liquid Dispersed
8	Wilson Model	Equation (2.18) Equation (2.19)	Lower Void Fraction higher Void Fraction
9		Equation (2.20)	Slug Flow
10	Wallis Model	Equation (2.32)	Annular Flow

a : The coefficient in Eq.(2.10) is replaeed by 1.414

b : The coefficient is given by Bertodanoi

TABLE 3

EFFECT OF POOL ENTRAINMENT MODEL
ON THE CRITICAL FLOW RATE

P (psi)	A	B		$\frac{G'_c - G_c}{G_c} \times 100\%$
	Critical flow rate G_c (lbm/ft ² -sec)	Assumed entrainment E_{fg}	Critical flow rate G'_c (lbm/ft ² sec)	
1000	1834.09	0.09	1939.5	5.0%
		0.05	1894.6	3.3%
400	762.49	0.30	926.2	21.0%
		0.10	815.8	7.0%

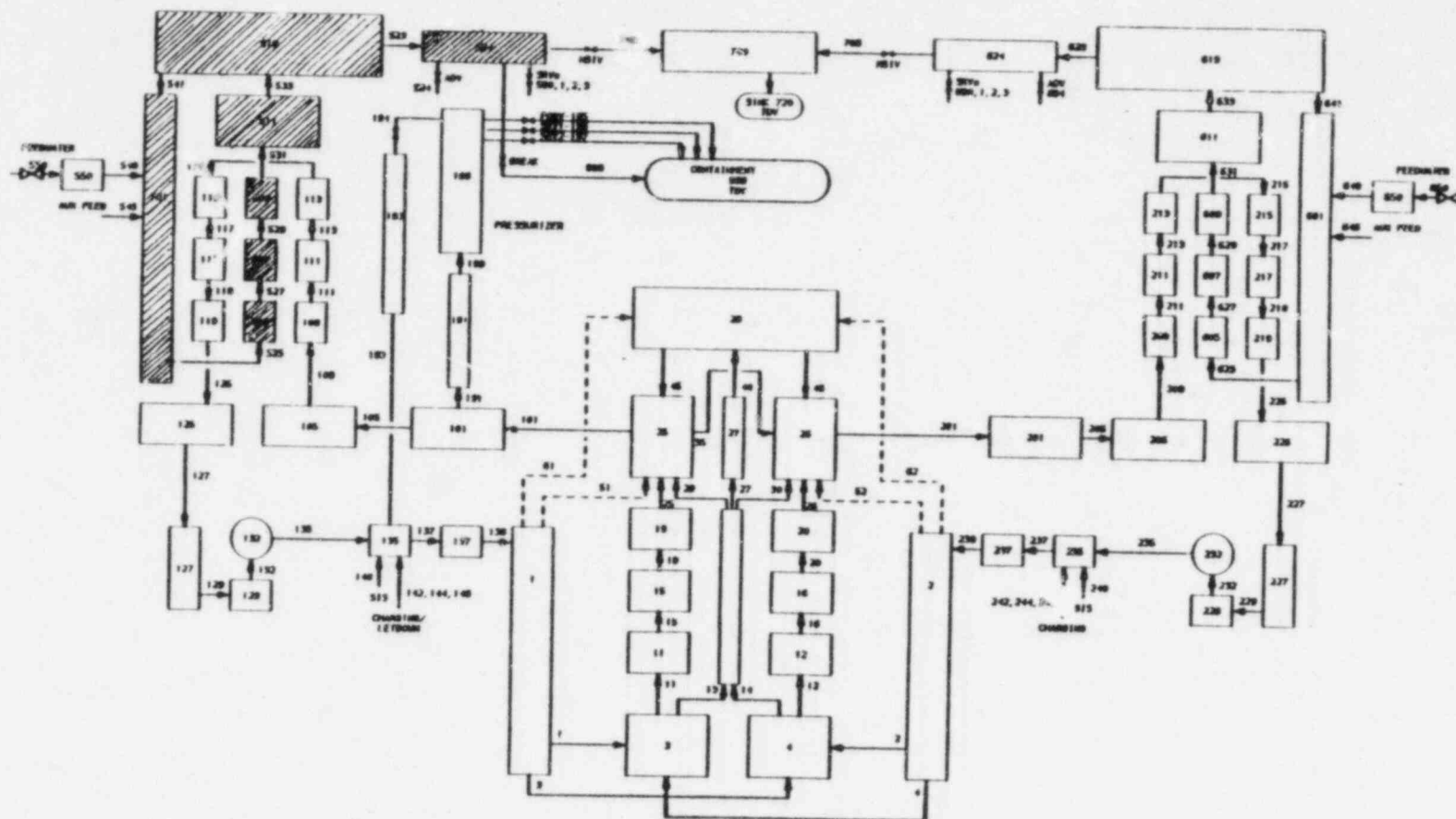
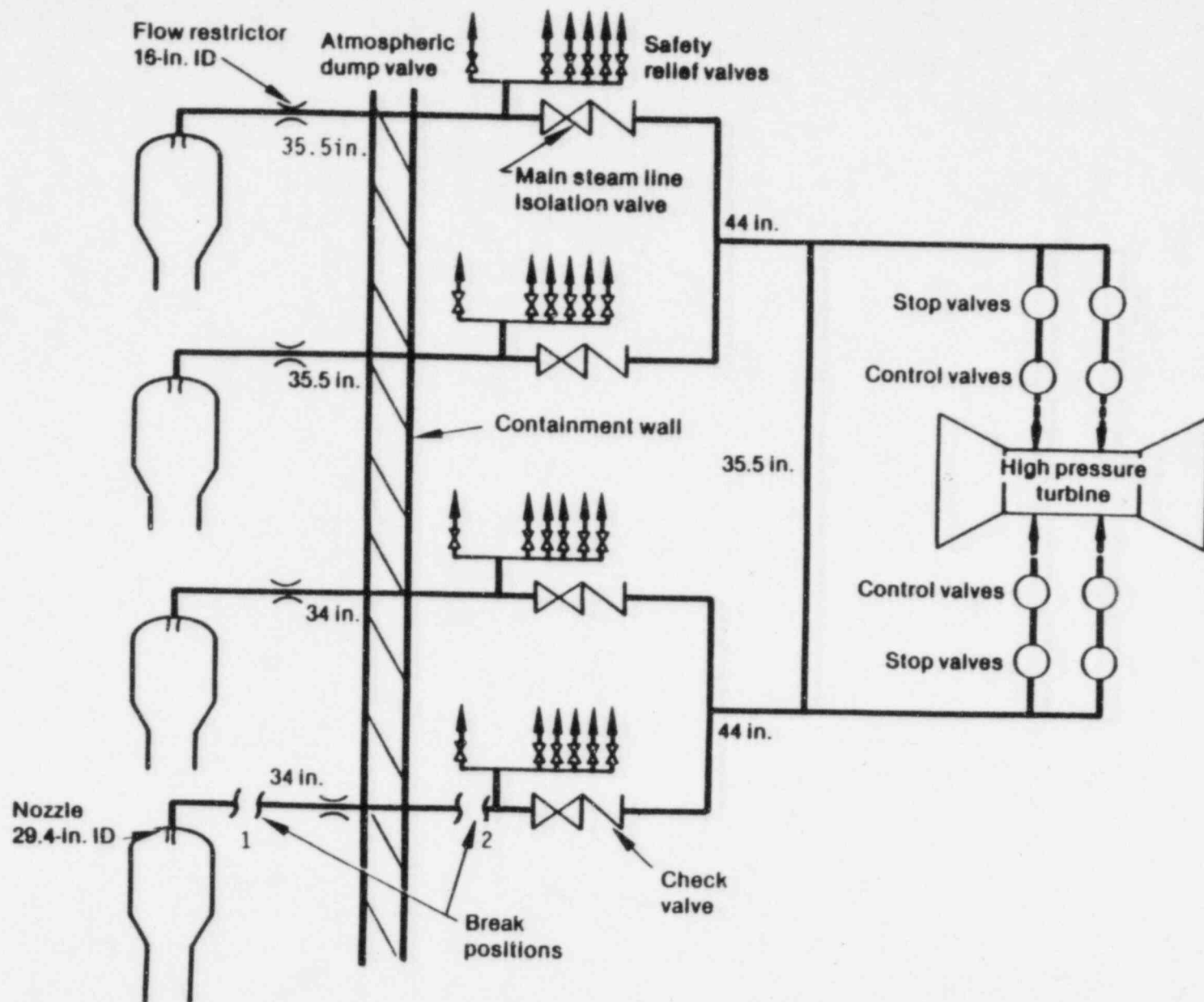


Figure 1. Typical Nodalization for Steam Line Break

Figure 2. Schematic of Four Loop Steam Line Break



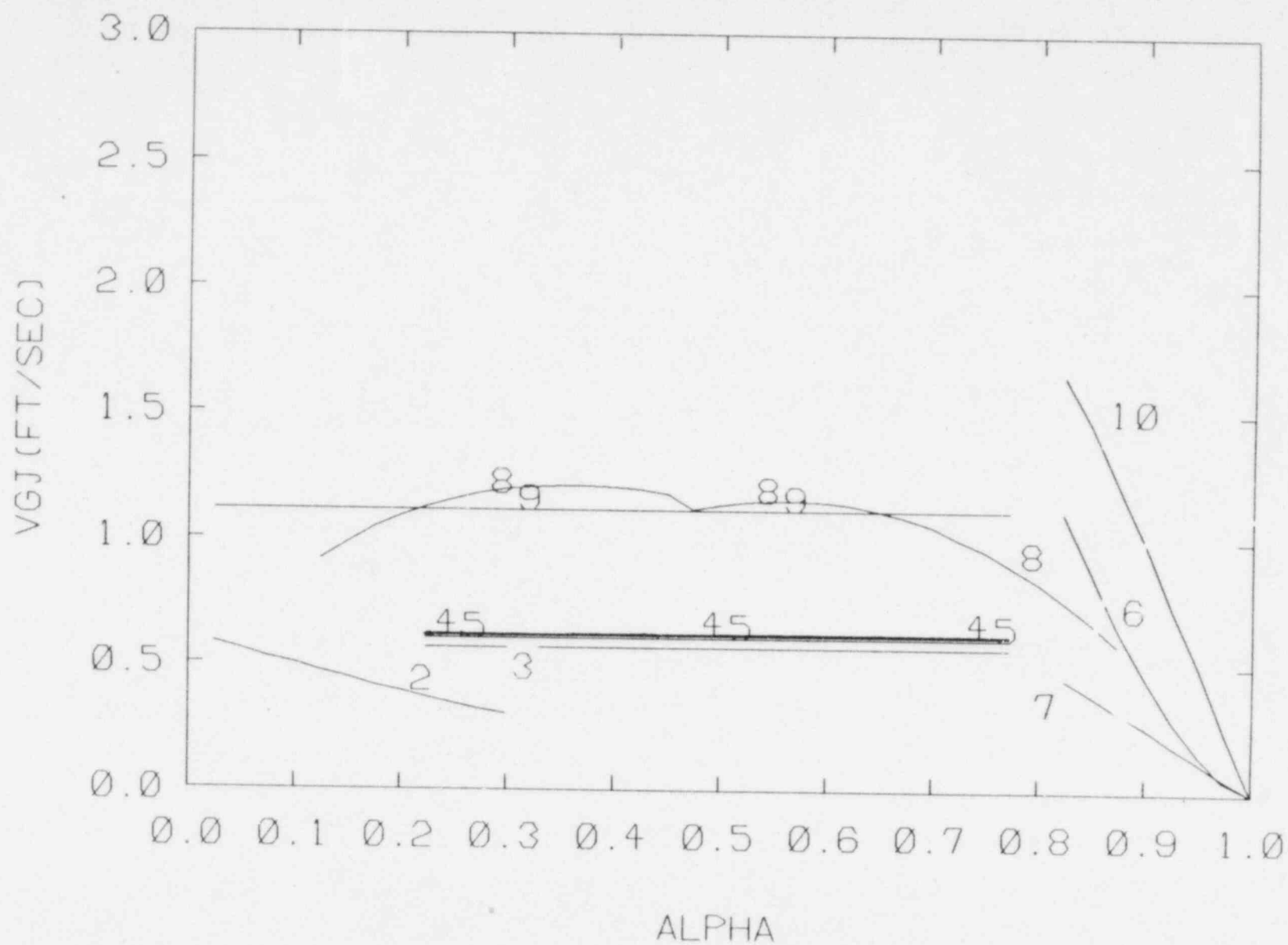


Figure 3. Comparison of Various Weighted Mean Drift Velocities as Function of Void Fraction at a Pressure of 1000 psi

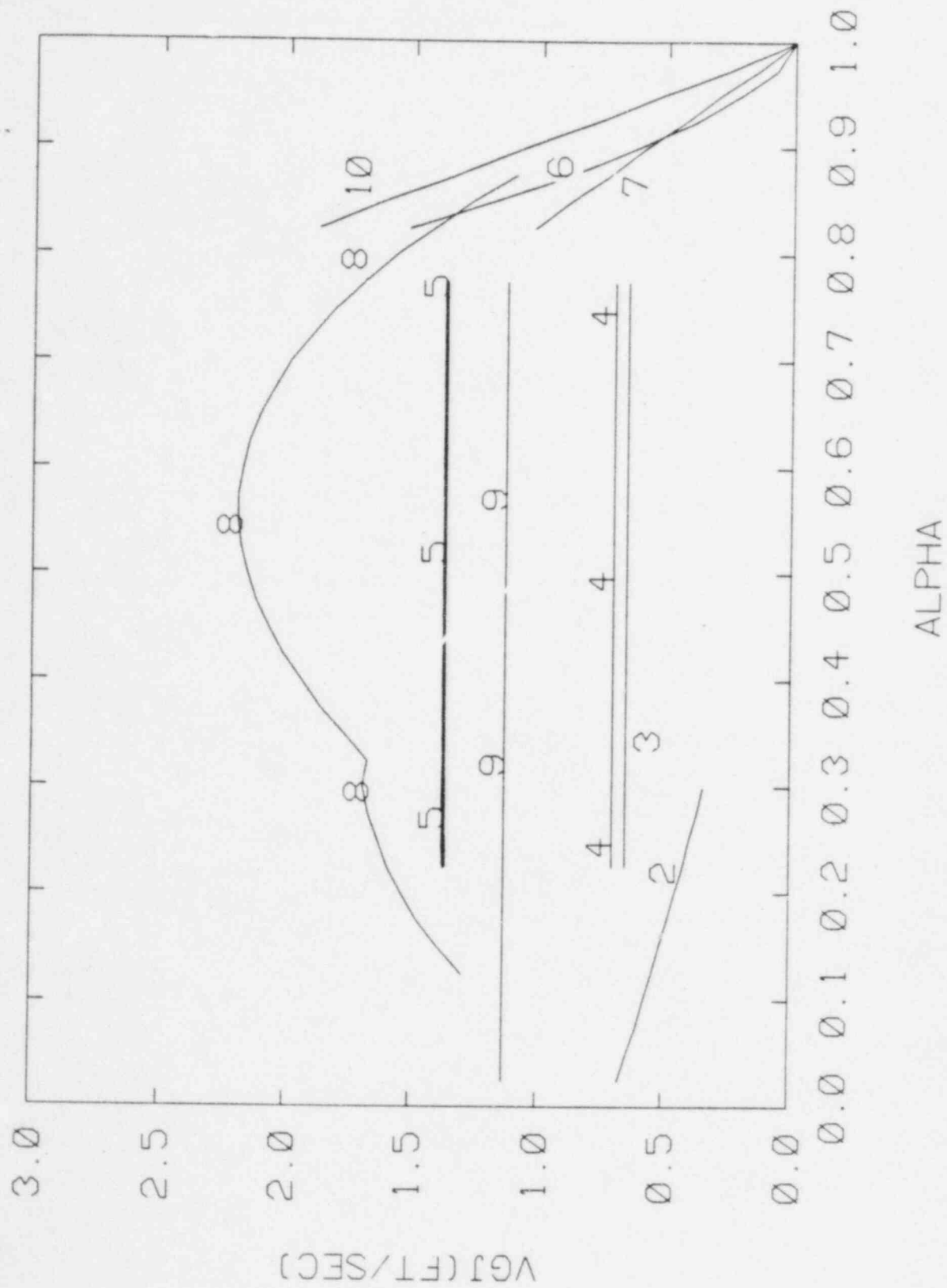
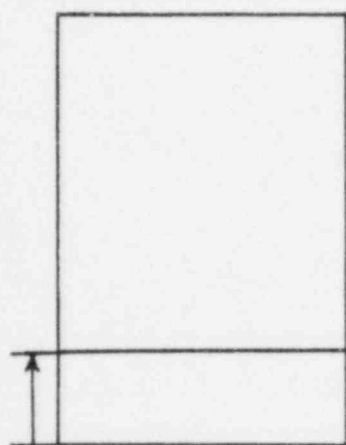
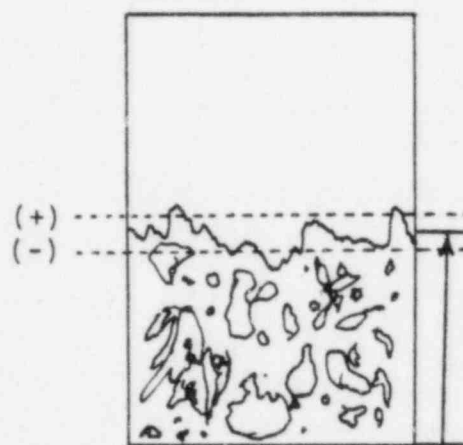


Figure 4. Comparison of Various Weighted Mean Drift Velocities as Function of Void Fraction at a Pressure of 300 psi



(a) Collapsed Water Level



(b) mixture Water Level

Figure 5. Collapsed Water Level and the Mixture Water Level

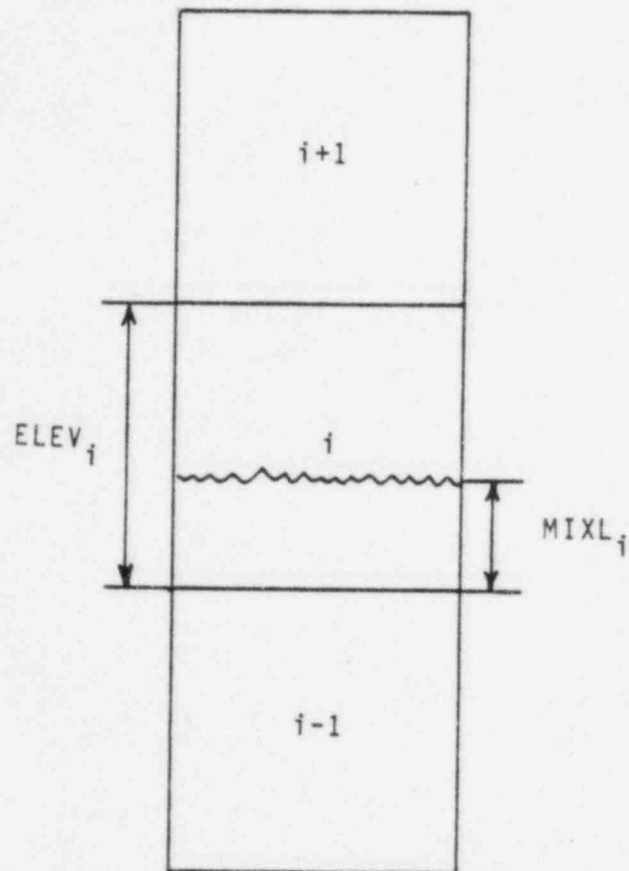
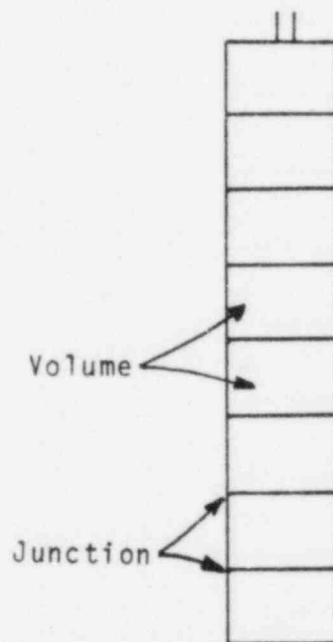


Figure 6. The Mixture Level and the Void Fraction Distribution

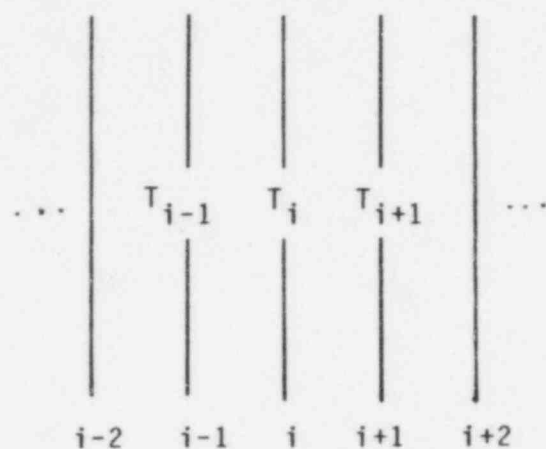


(a) Global Vessel System

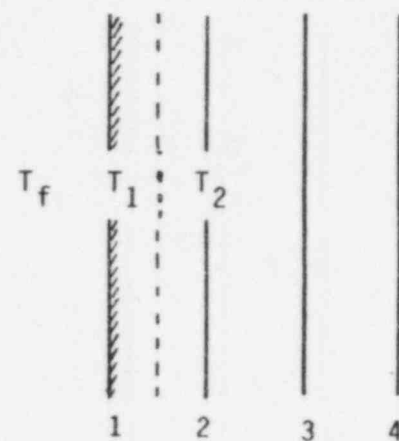


(b) Local Control Volume System

Figure 7. Schematic of the Global Vessel System and the Local Control Volume System



(a) Nodalization for Interior Temperature Calculation



(b) Nodalization for Surface Temperature Calculation

Figure 8. Nodalization for Heat Conduction Model

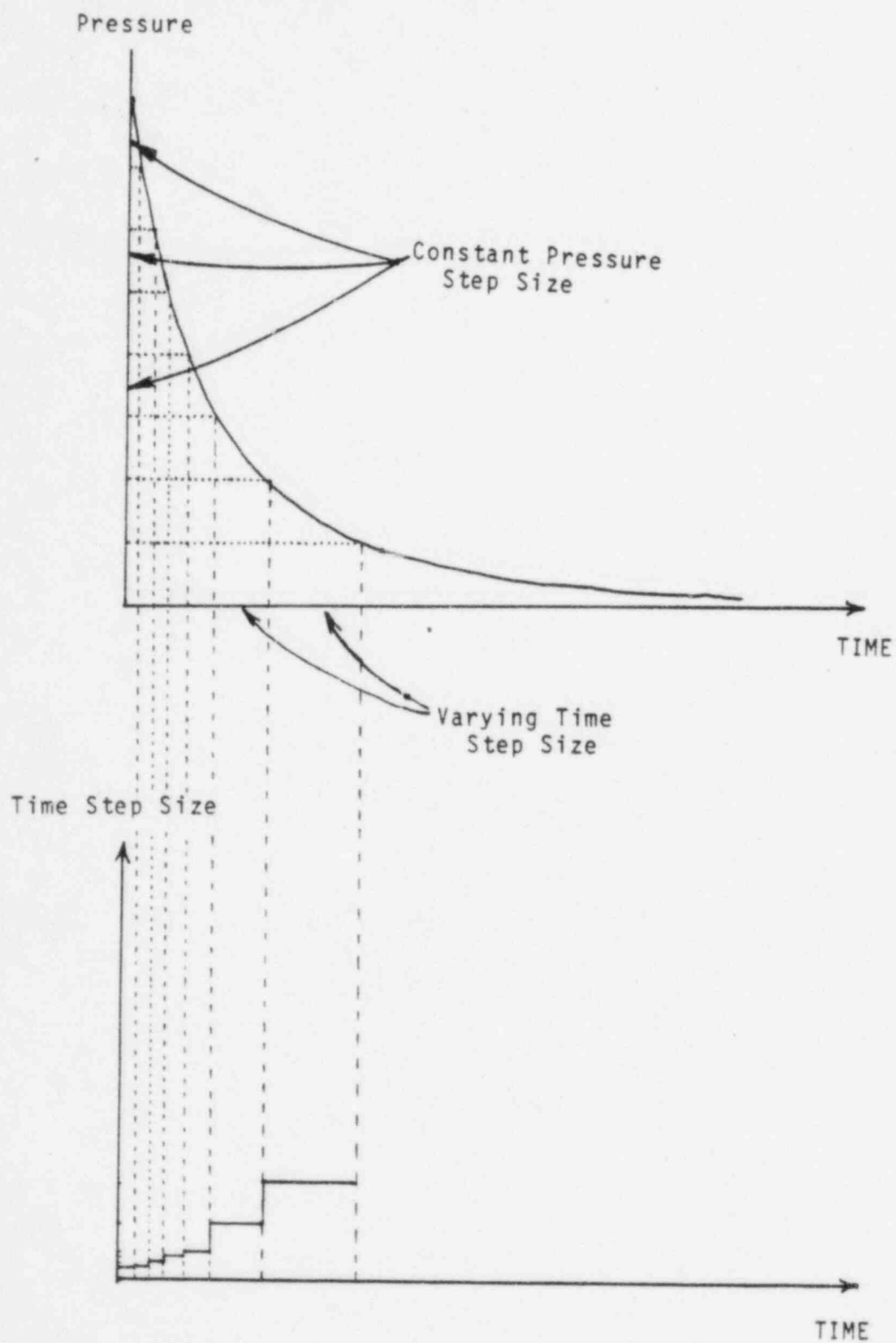
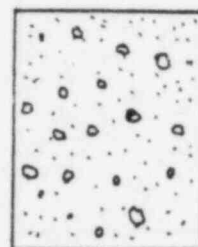
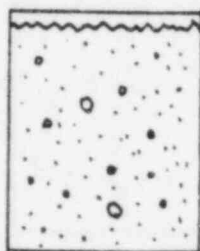


Figure 9. Comparison Between the Pressure Step Size and the Time Step Size

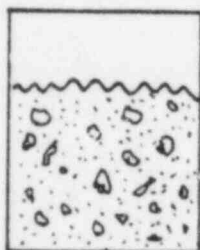
a : Low Void Fraction
 b : Intermediate Void Fraction
 c : High Void Fraction



10.c3: High vapor velocity

(10.a1)

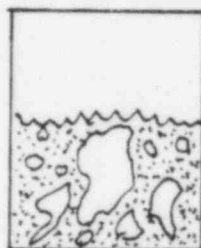
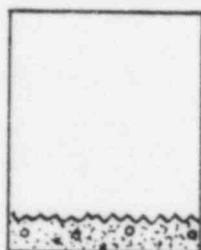
(10.a2)



(10.b1)

(10.b2)

(10.b3)



(10.c1)

(10.c2)

(10.c3)

Figure 10. Various Void Fraction Distributions in a Control Volume

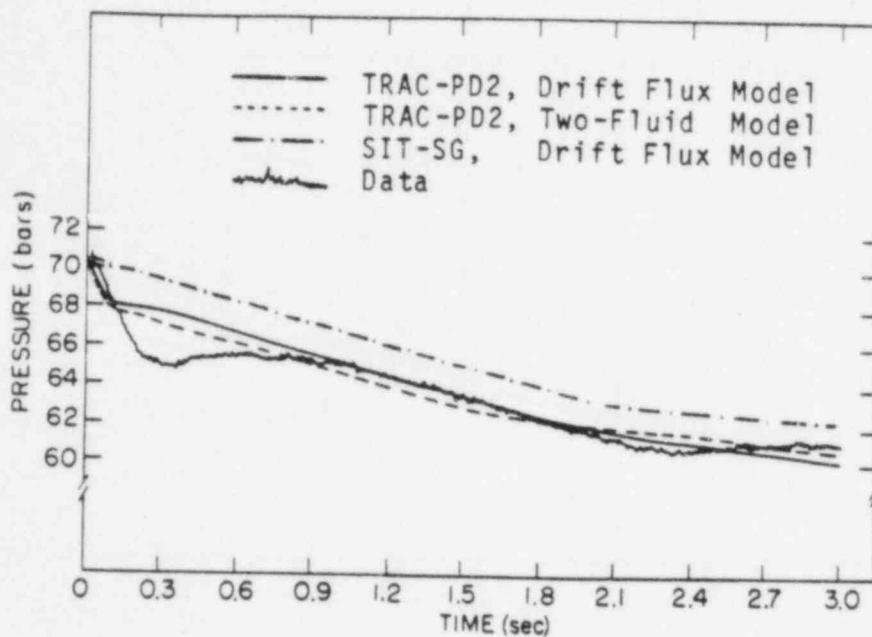


Figure 11. Comparison Between the Measured and Predicted Pressure for Battelle-Frankfurt Blowdown Test SWR-2R

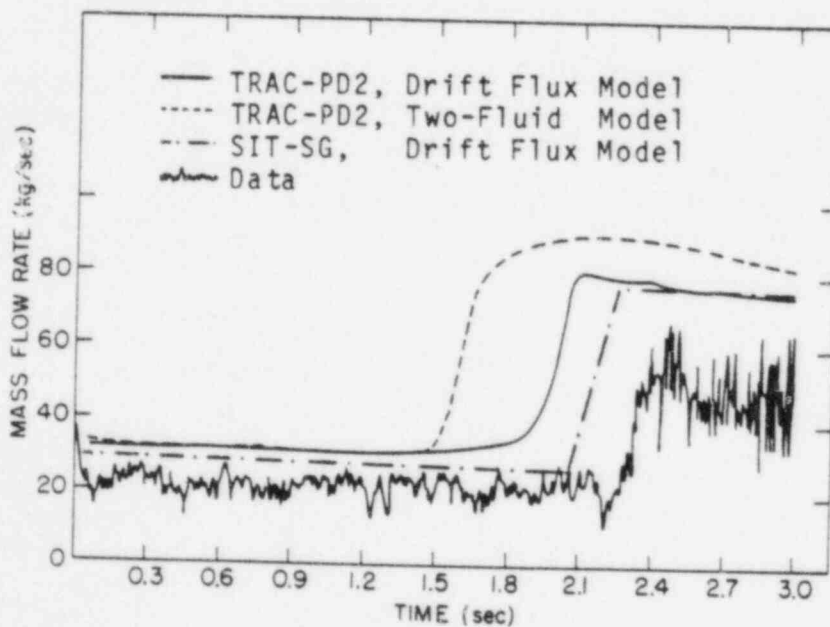


Figure 12. Comparison Between the Measured and Predicted Break Mass Flow Rate for Battelle-Frankfurt Test SWR-2R

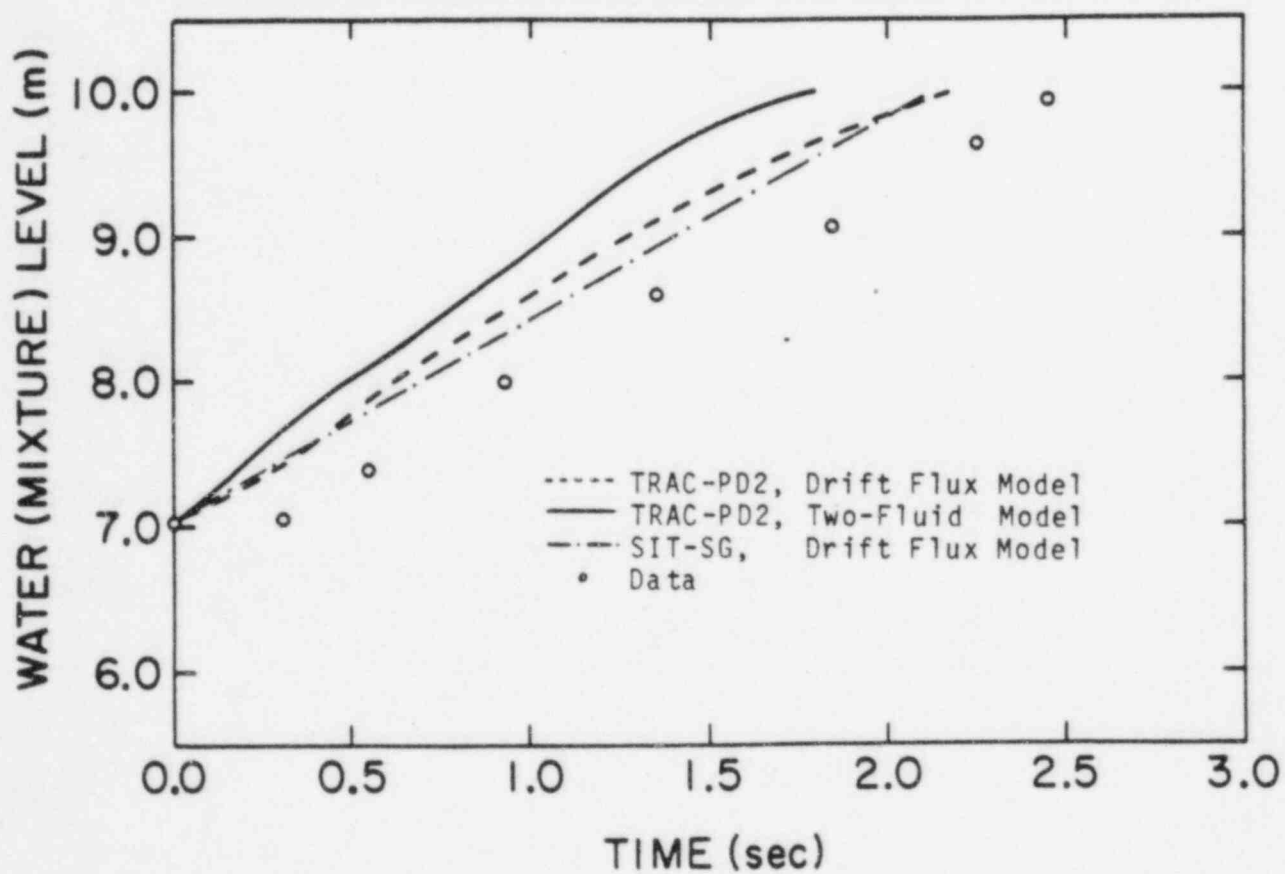


Figure 13. Comparison Between the Measured and Predicted Mixture Level for Battelle-Frankfurt Test SWR-2R

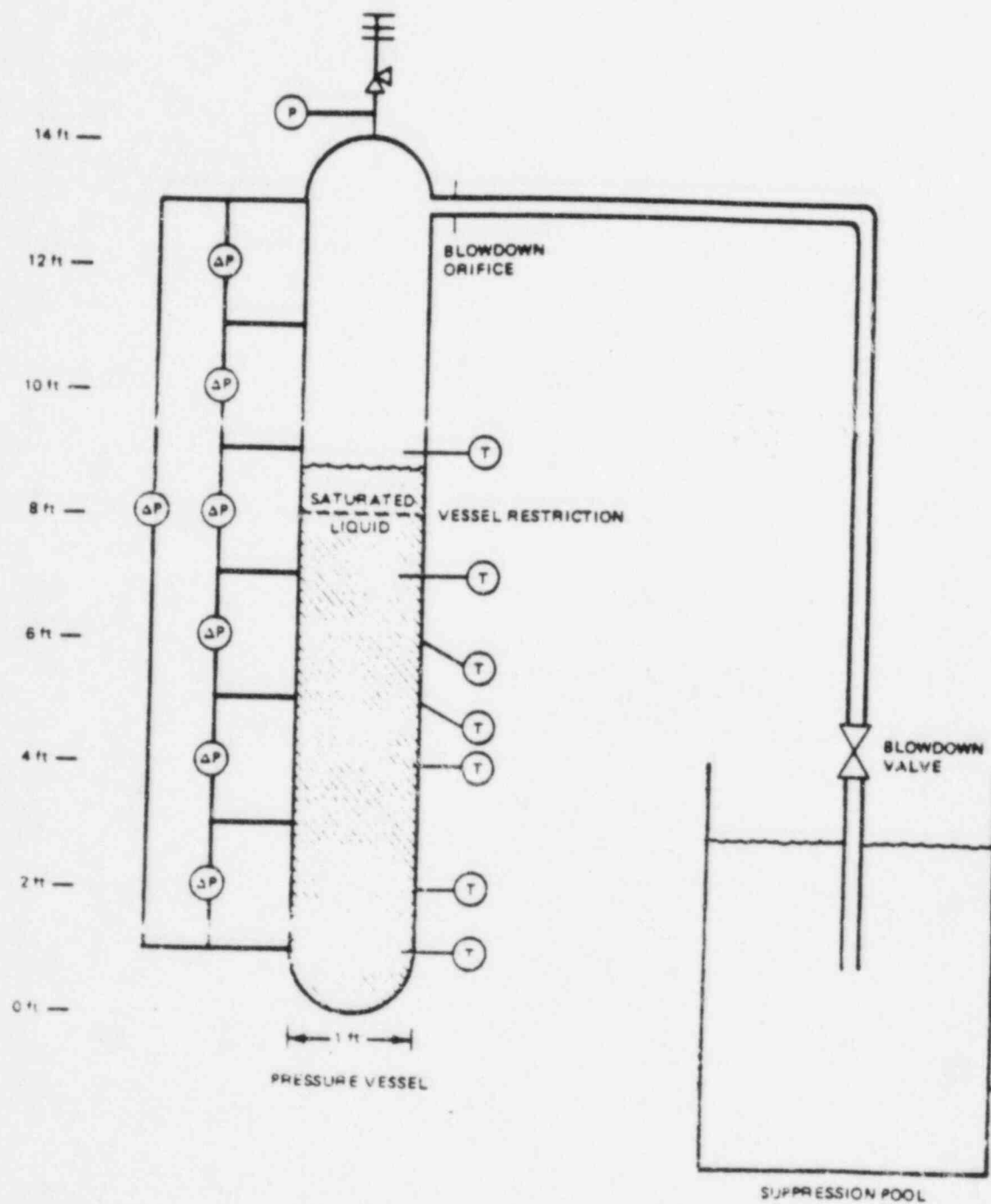


Figure 14. Instrumentation for G.E. Small Vessel Blowdown Test

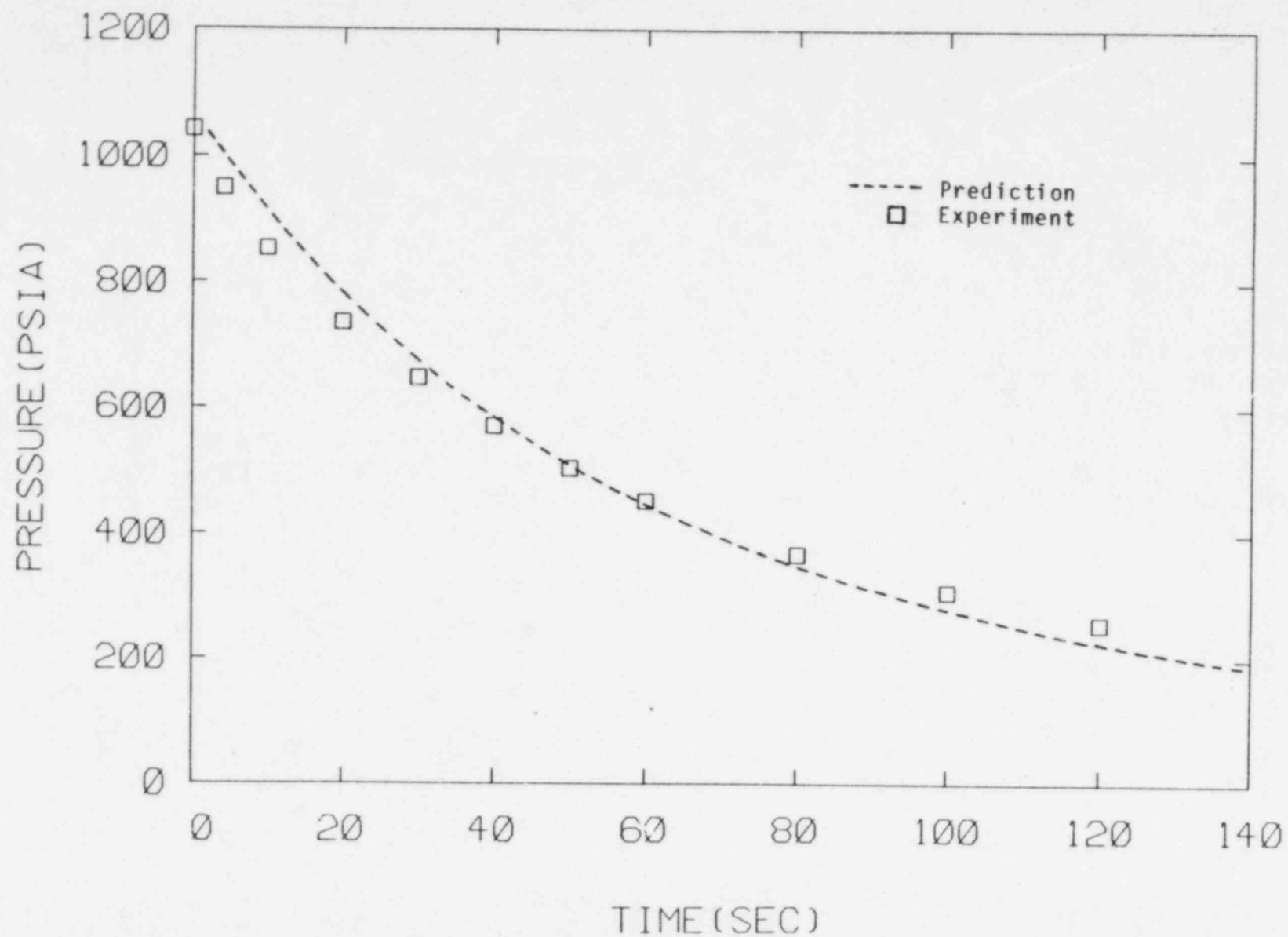


Figure 15. Comparison Between the Measured and Predicted Pressure for Level Swell Test

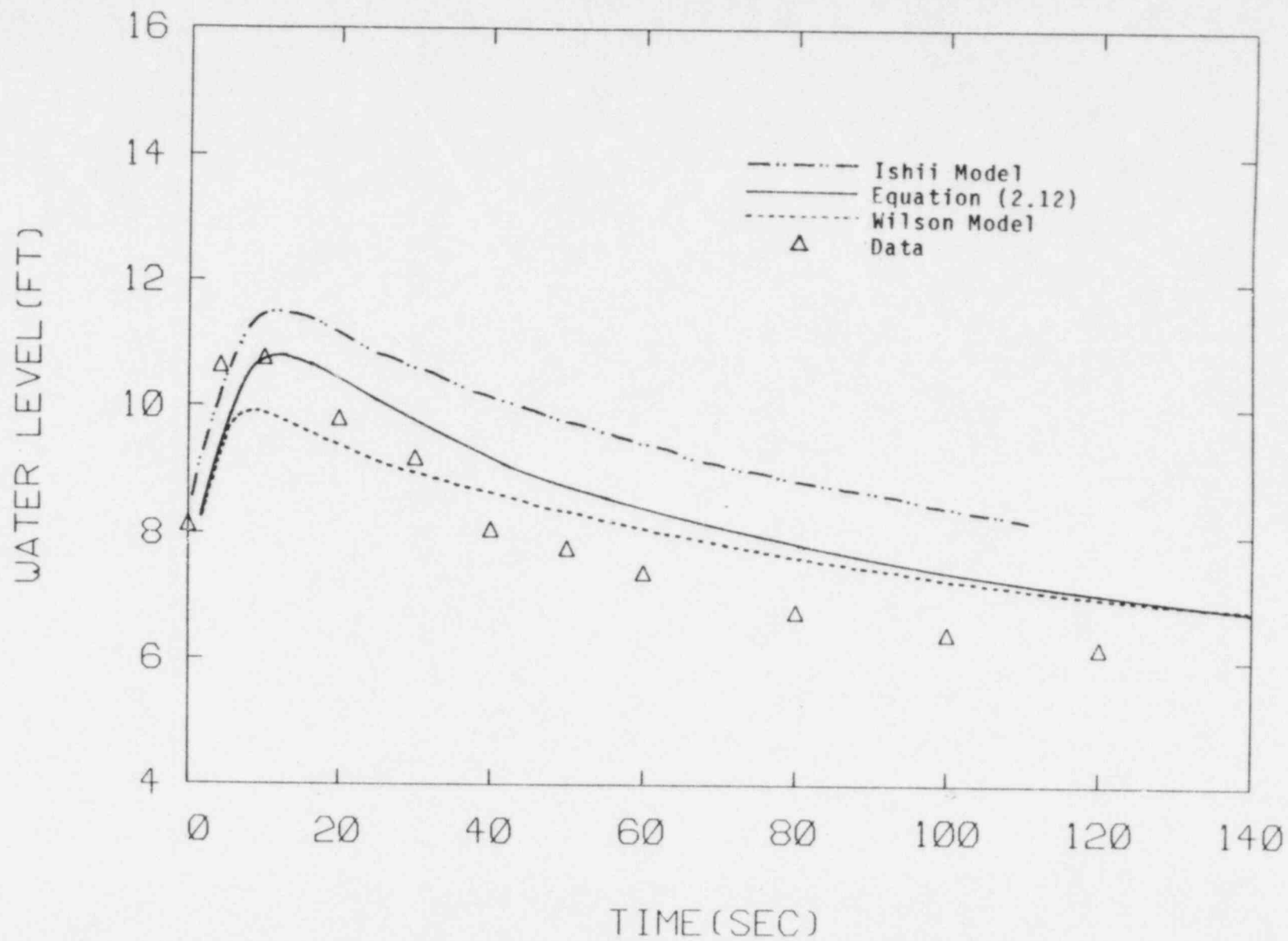


Figure 16. Comparison Between the Measured and Predicted Mixture Level for Level Swell Test

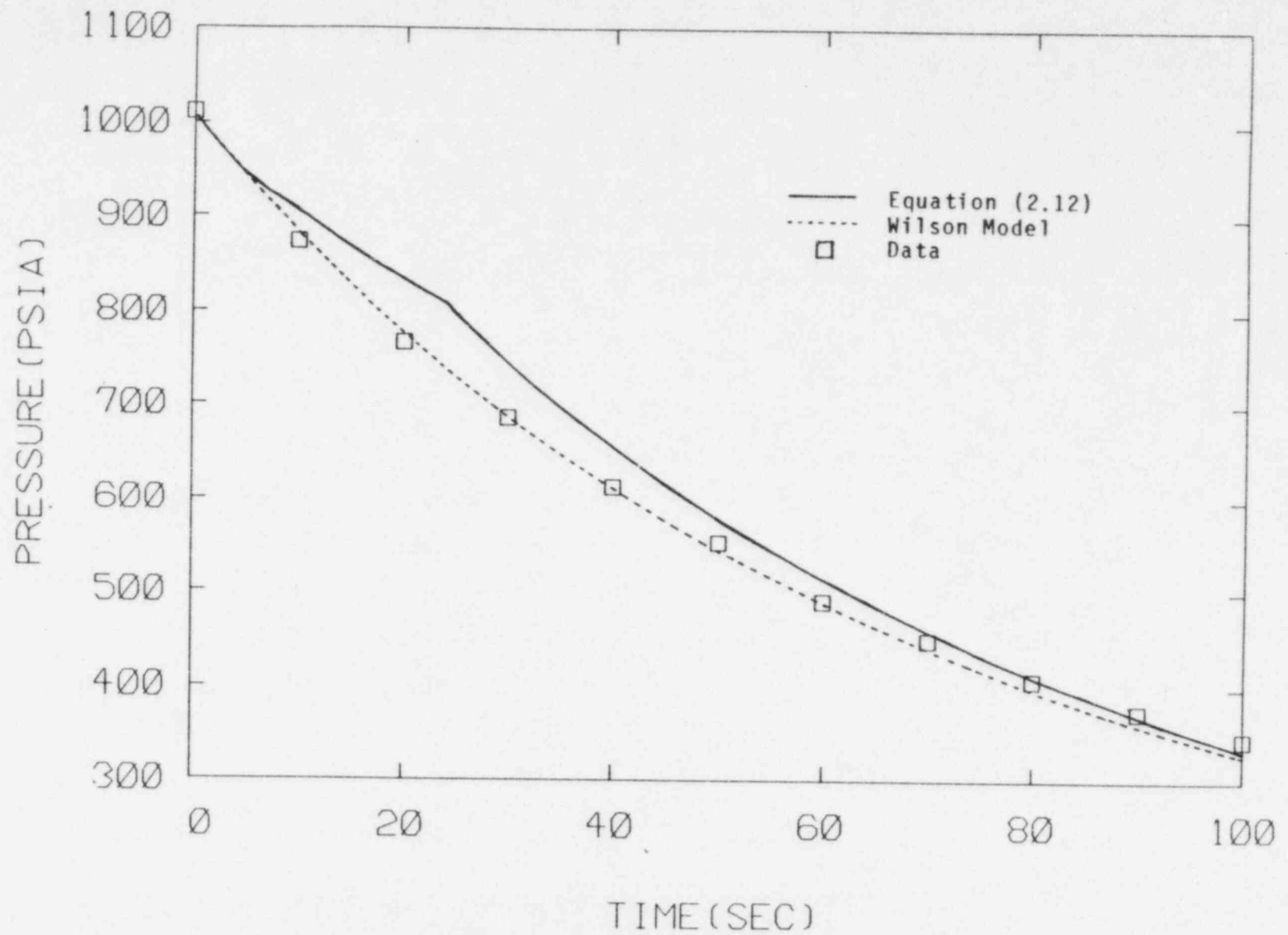


Figure 17. Comparison Between the Measured and Predicted Pressure for G.E. Small Vessel Test 1004-3

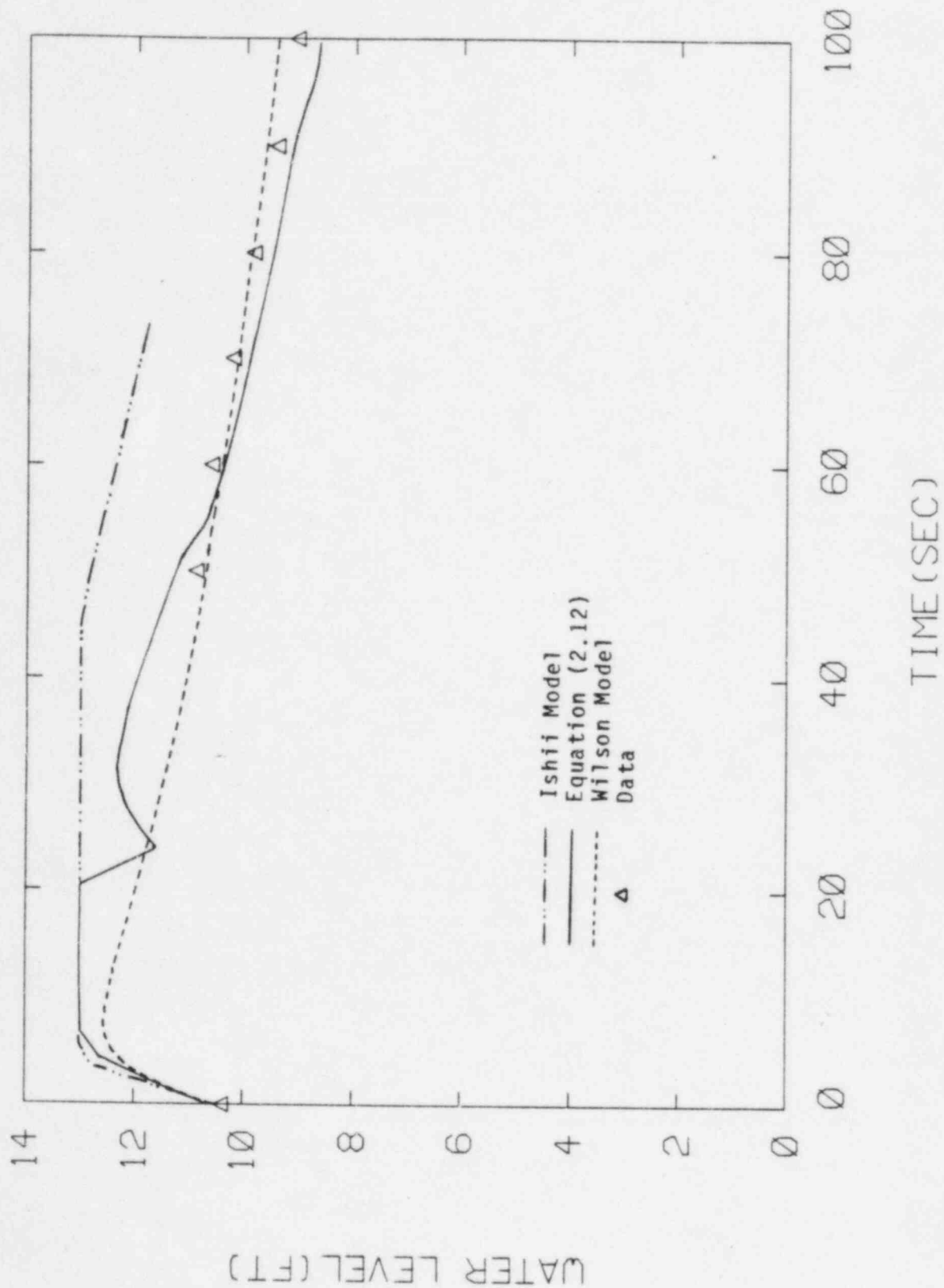


Figure 18. Comparison Between the Measured and Predicted Mixture Level for G.E.Small Vessel Test 1004-3

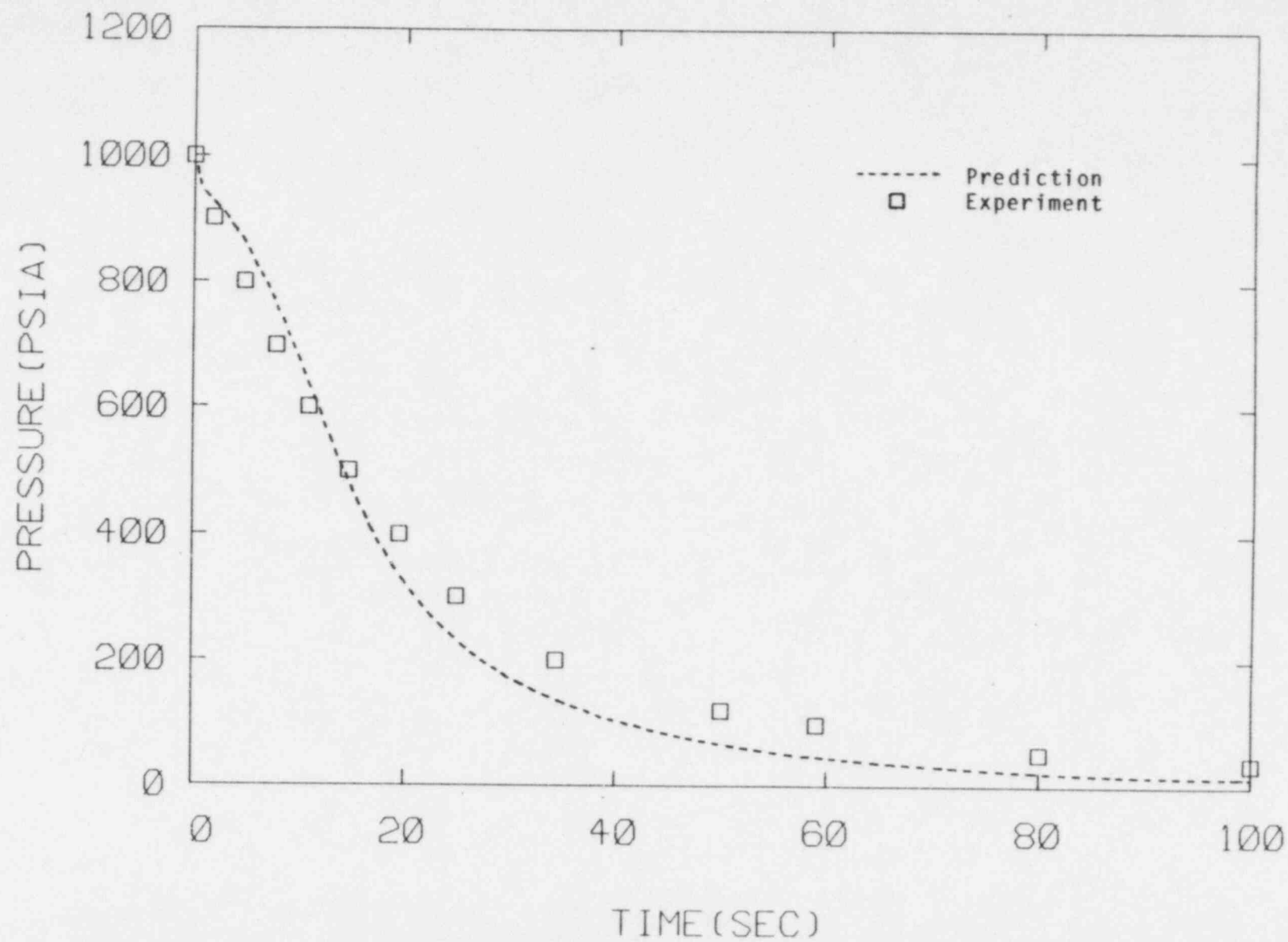


Figure 19. Comparison Between the Measured and Predicted Pressure for G.E. Small Vessel Test 1004-2

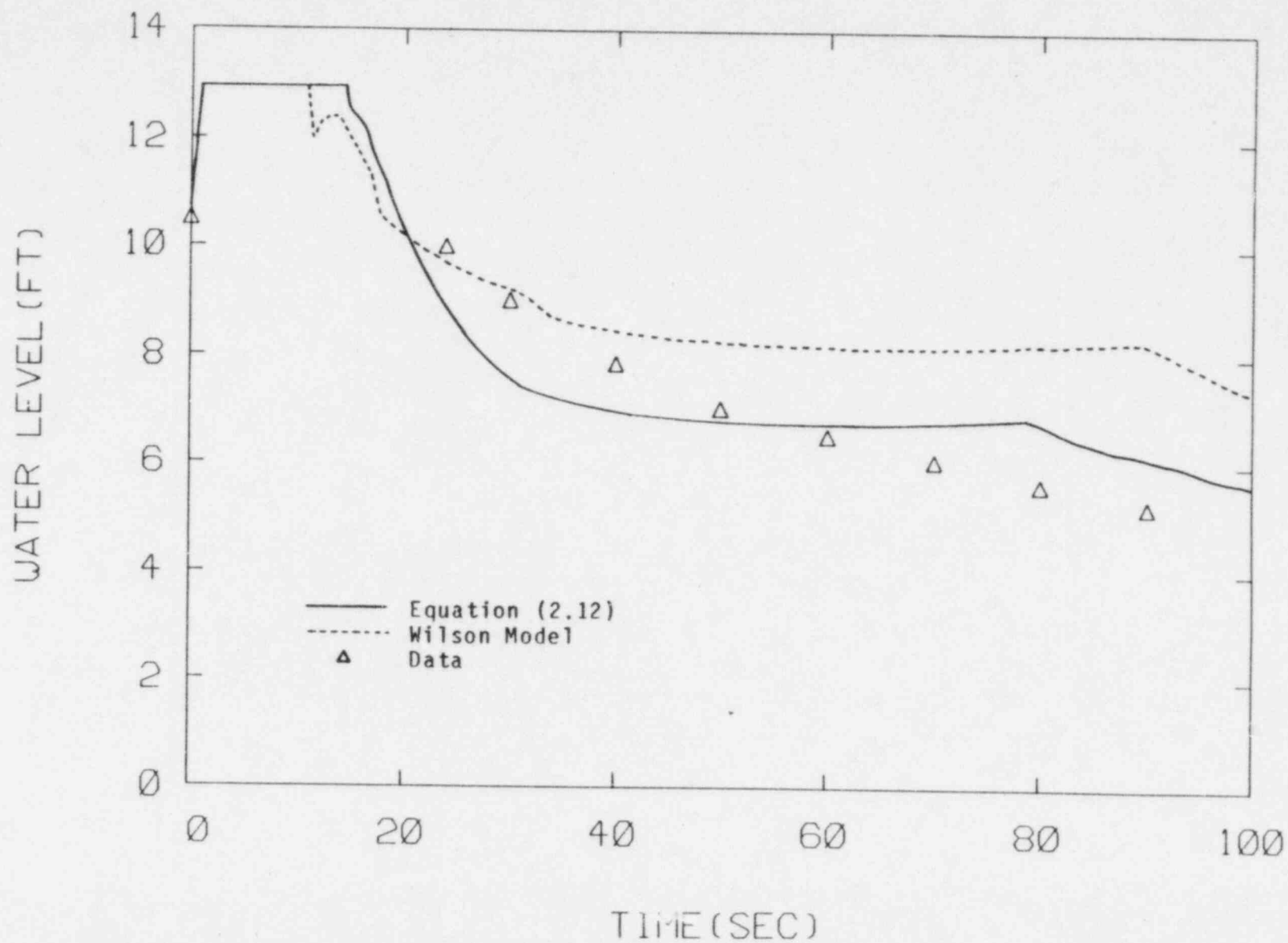


Figure 20. Comparison Between the Measured and Predicted Mixture Level for G.E. Small Vessel Test 1004-2

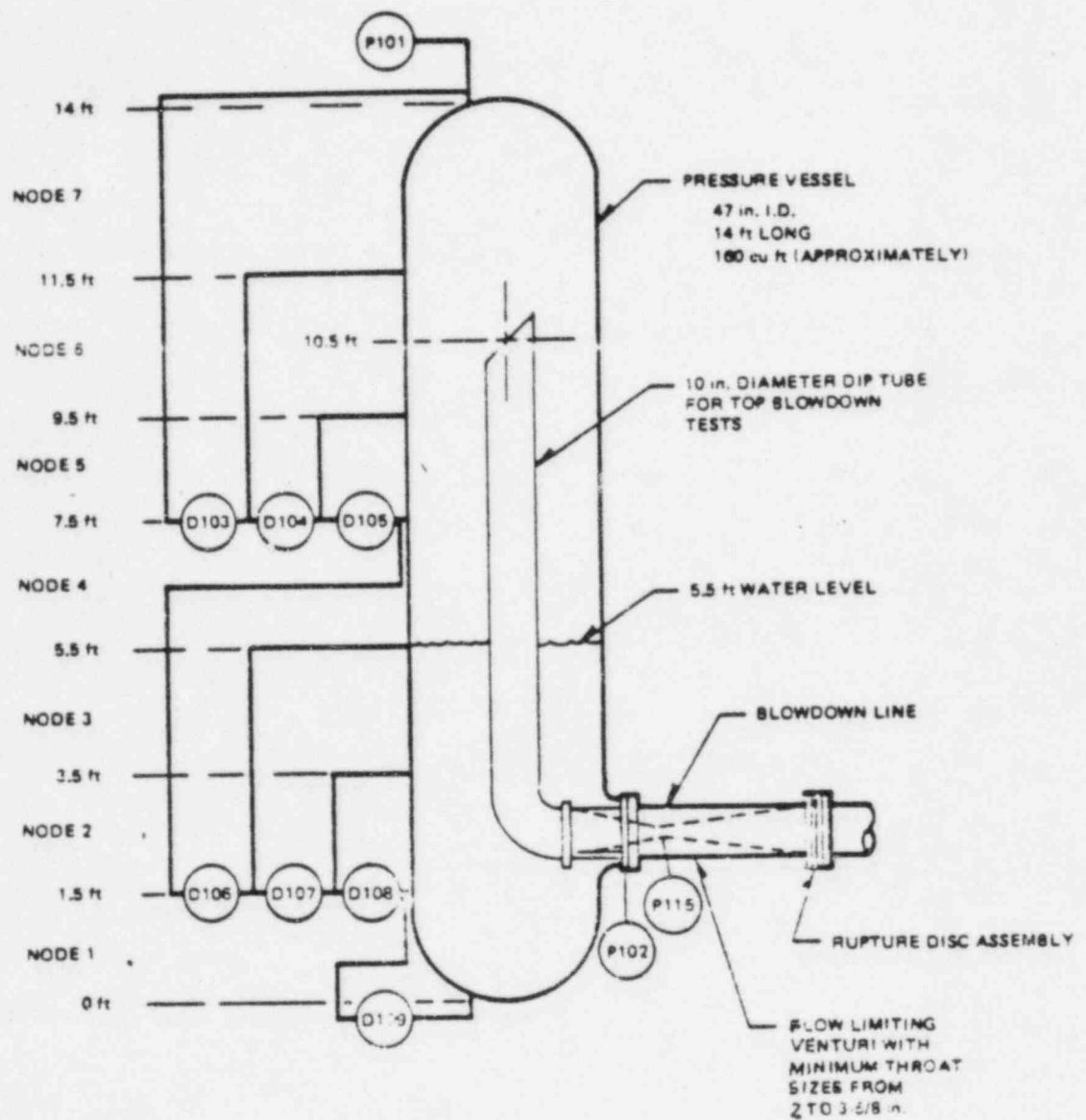


Figure 21. Schematic of G.E. Large Vessel Blowdown Test Facility

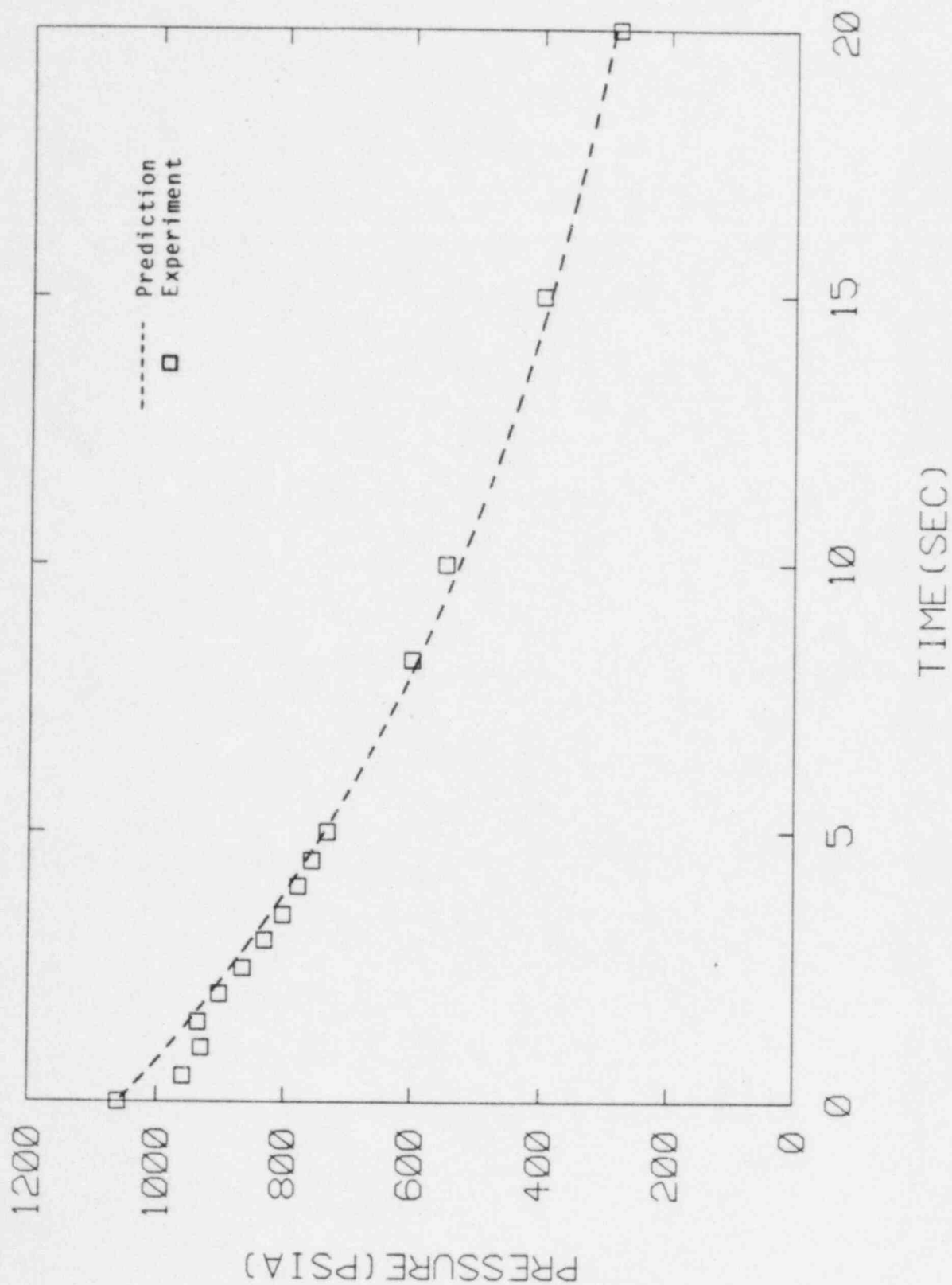


Figure 22. Comparison Between the Measured and Predicted Pressure for G.E. Large Vessel Test 5801-15

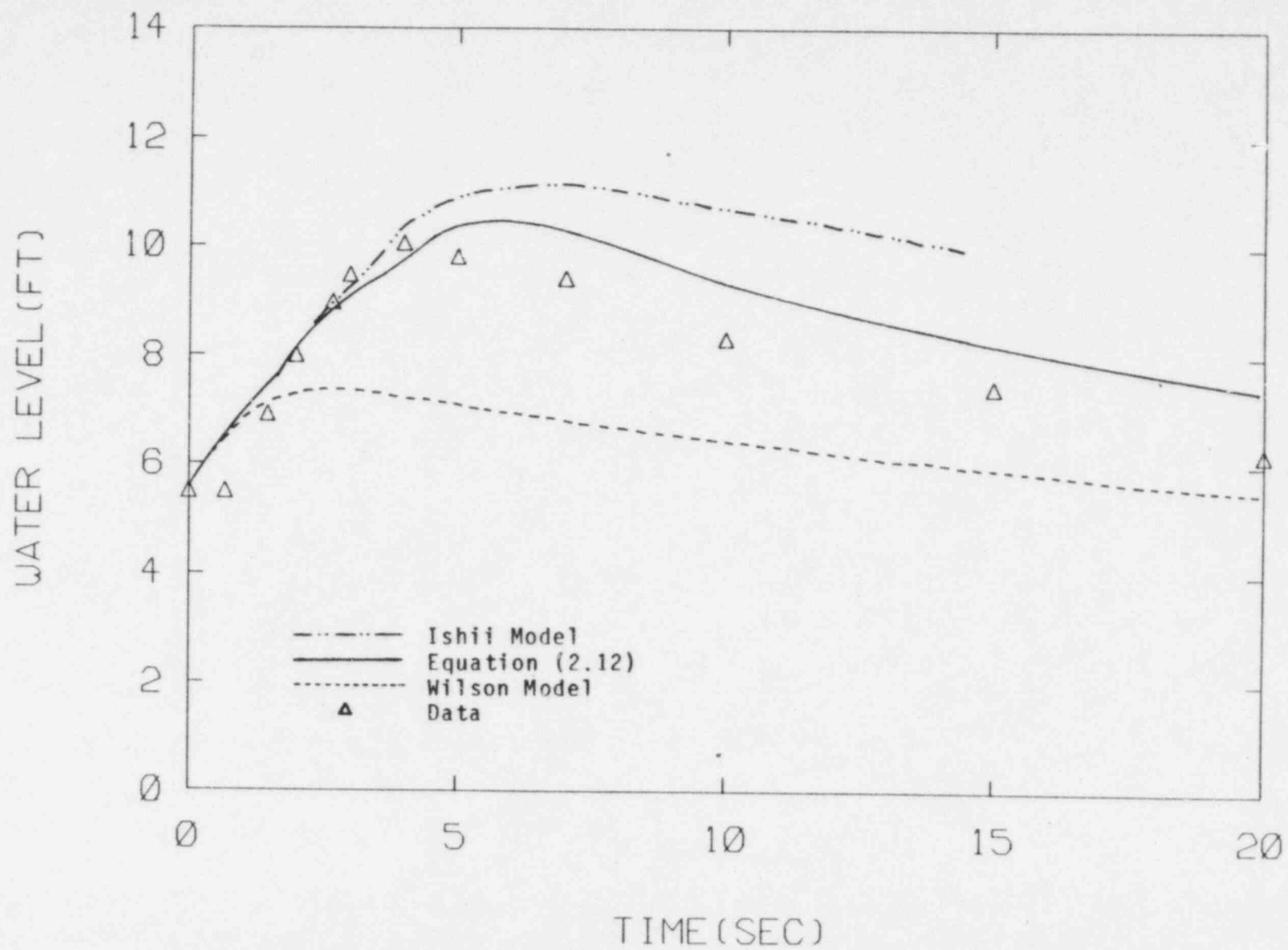


Figure 23. Comparison Between the Measured and Predicted Mixture Level for G.E. Large Vessel Test 5801-15

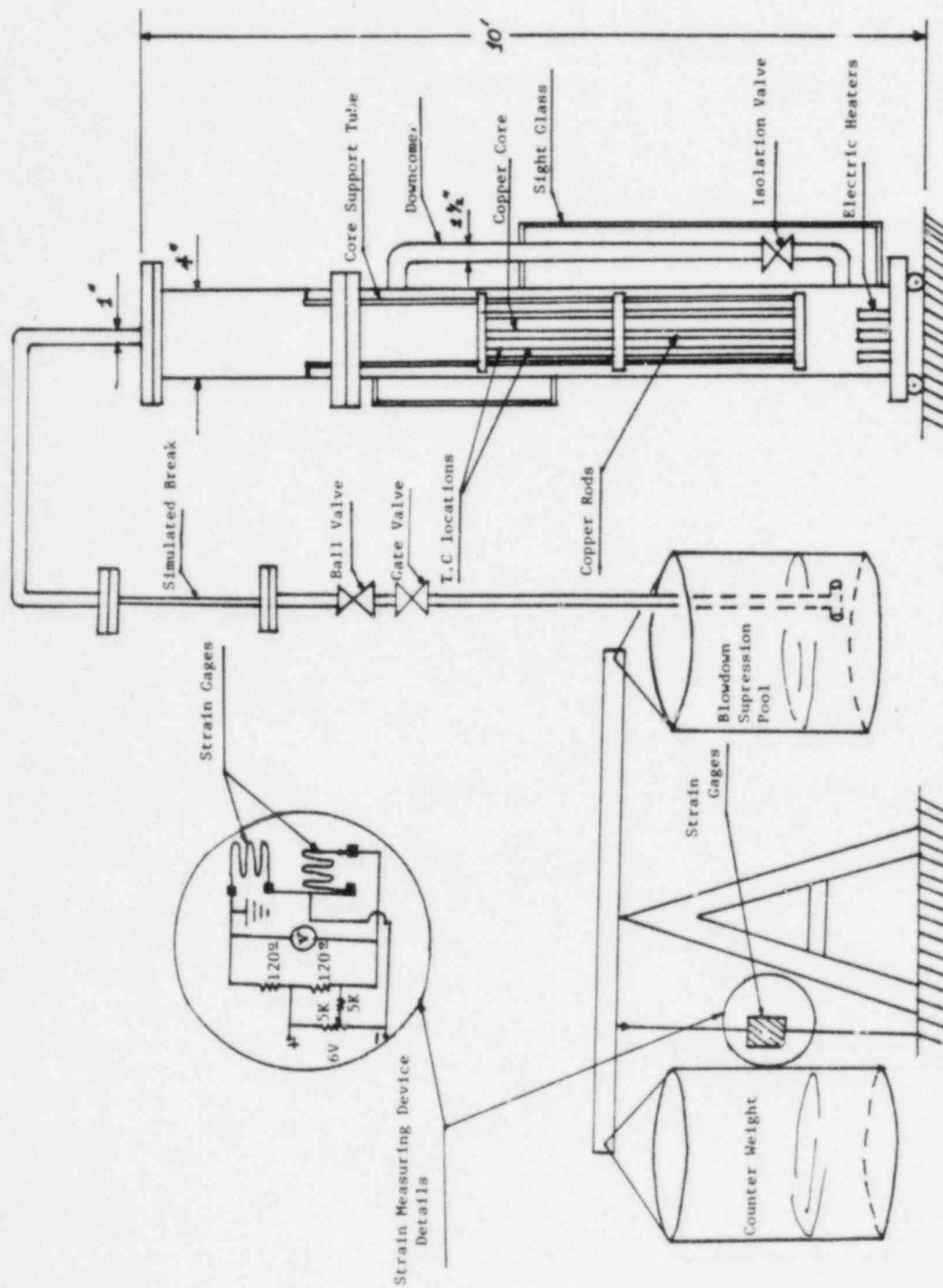


Figure 24. Schematic of Steam Generator Simulator Test Facility

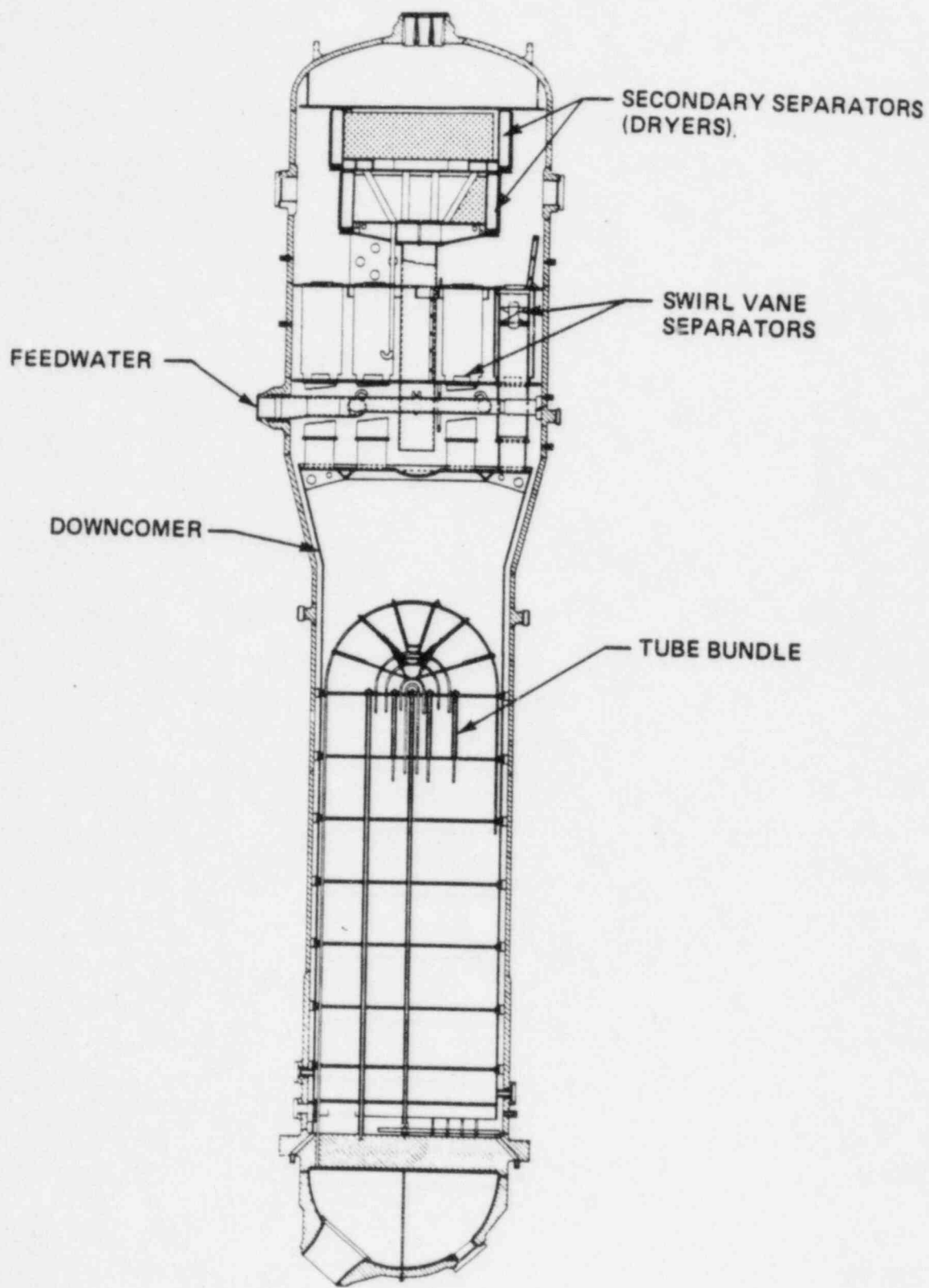


Figure 25. Schematic of U-tube Steam Generator

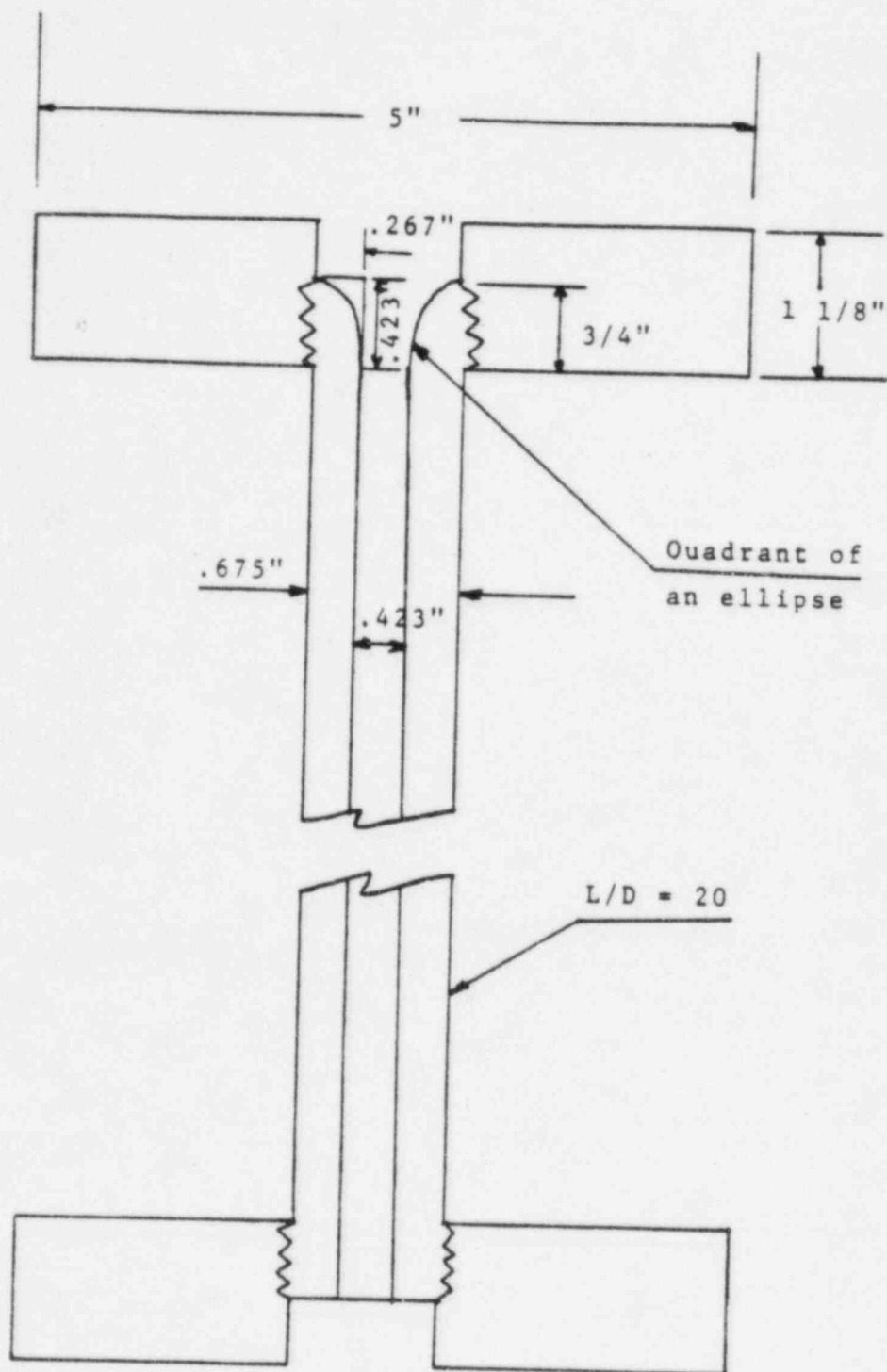


Figure 26. Break Geometry (3/8" Case)

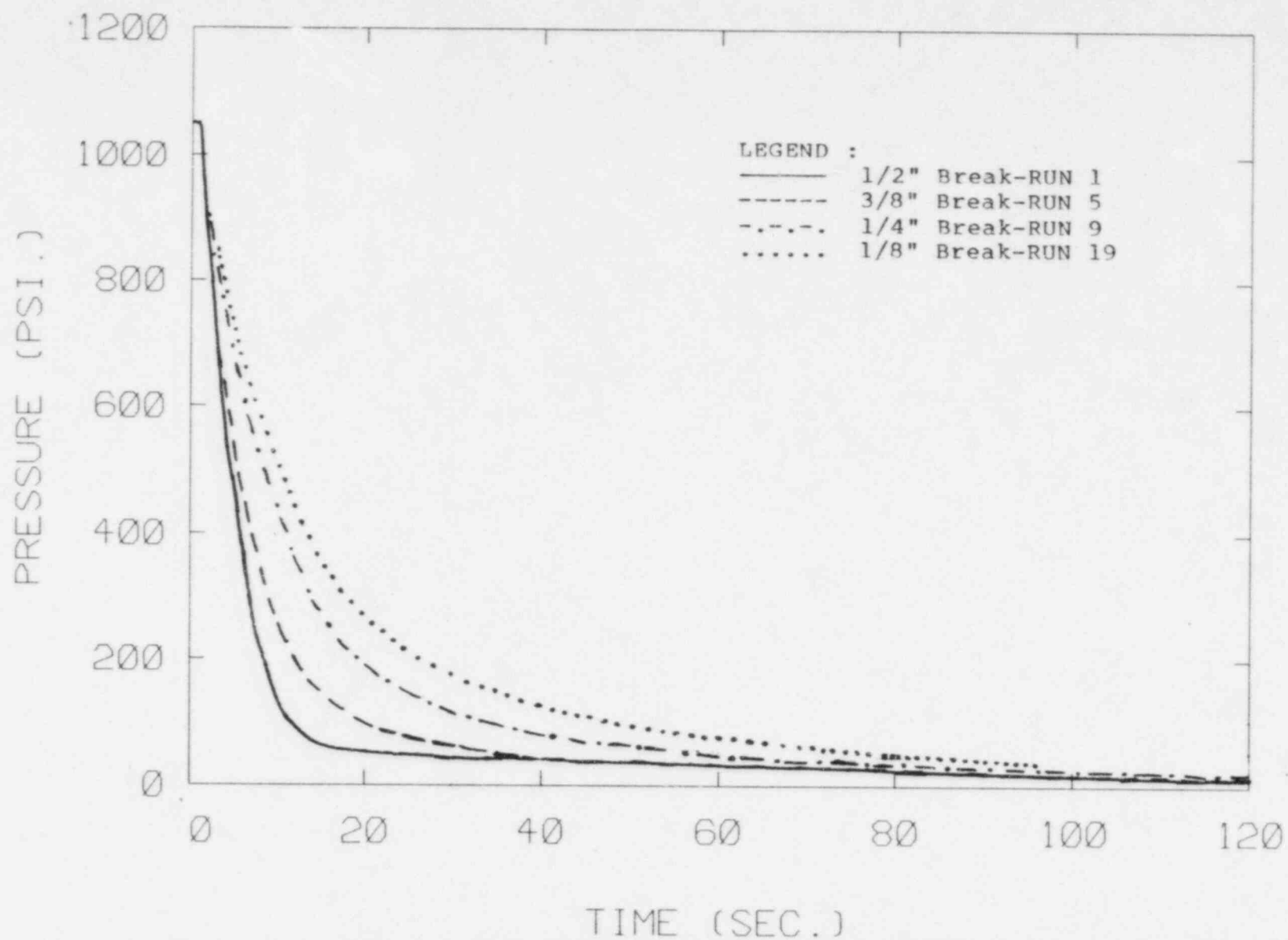


Figure 26a. Pressure transients with downcomer valve open and initial pressure 1055 psi. No generator internals.

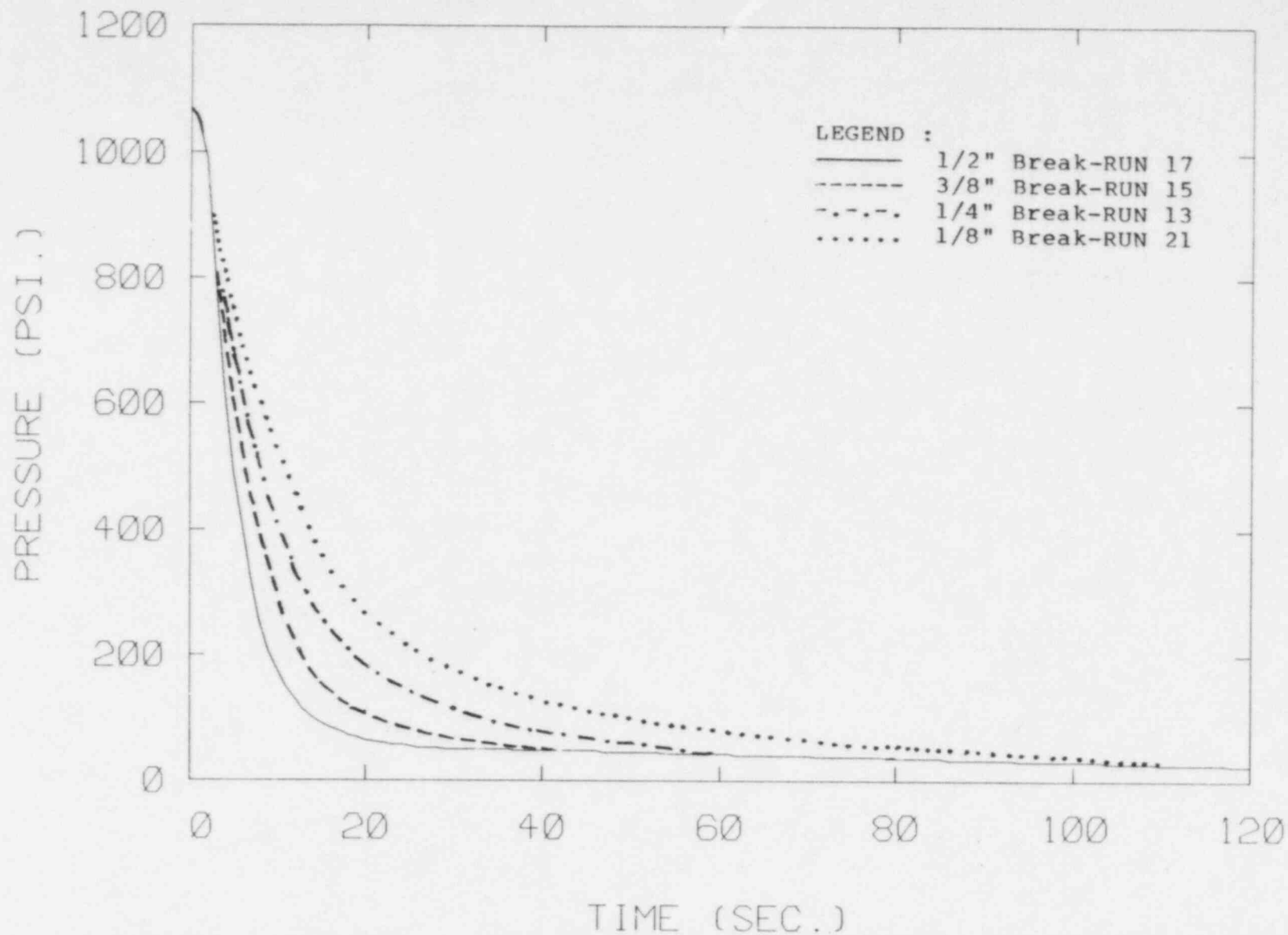


Figure 26b. Pressure transients with downcomer temperature 20°F lower than the vessel and initial pressure 1055 psi.
No generator internals.

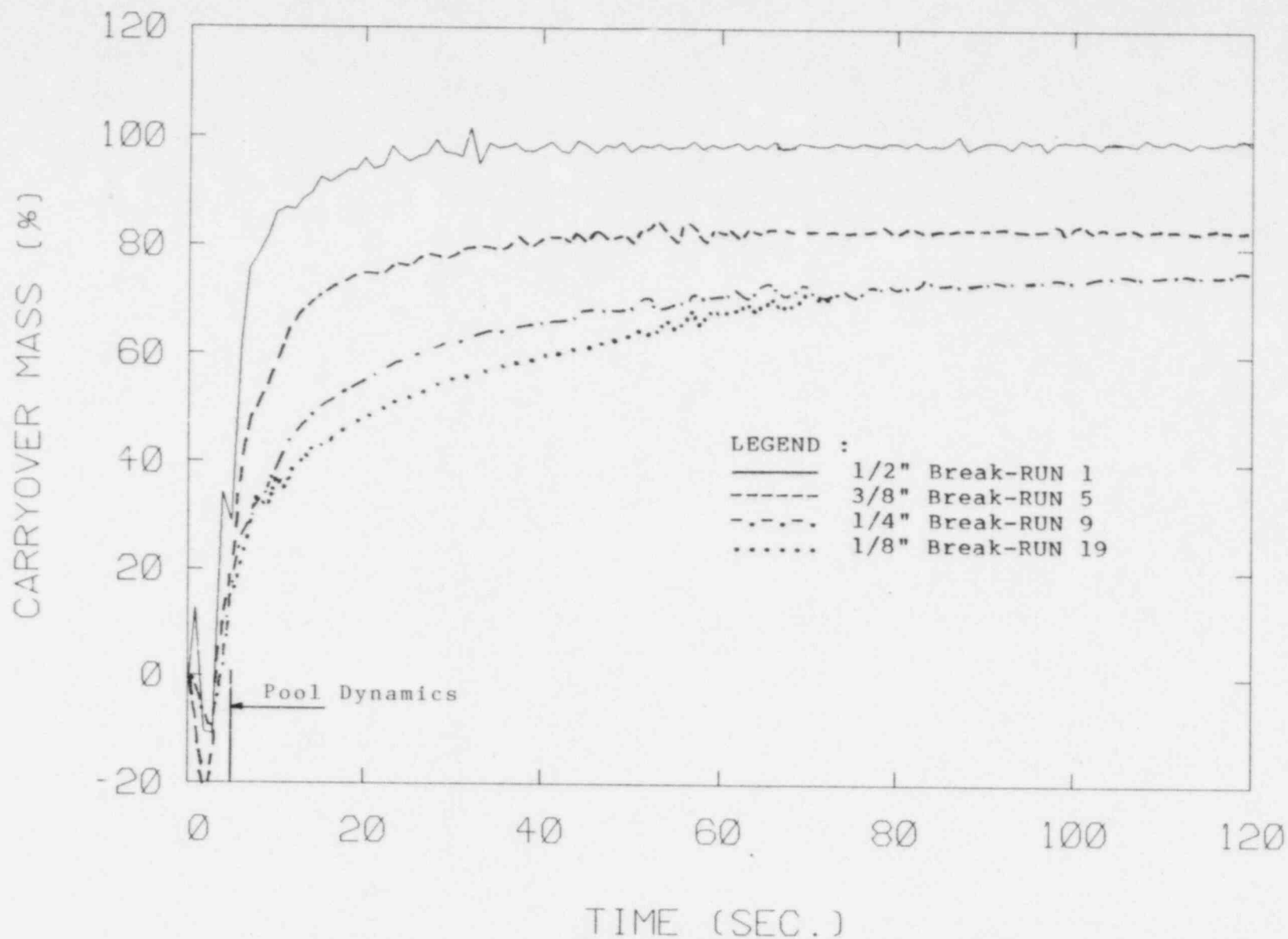


Figure 26c. Carryover mass transients with downcomer valve open and initial pressure 1055 psi. No generator internals. The effect of pool dynamics is evident in the first 5 seconds of the transient.

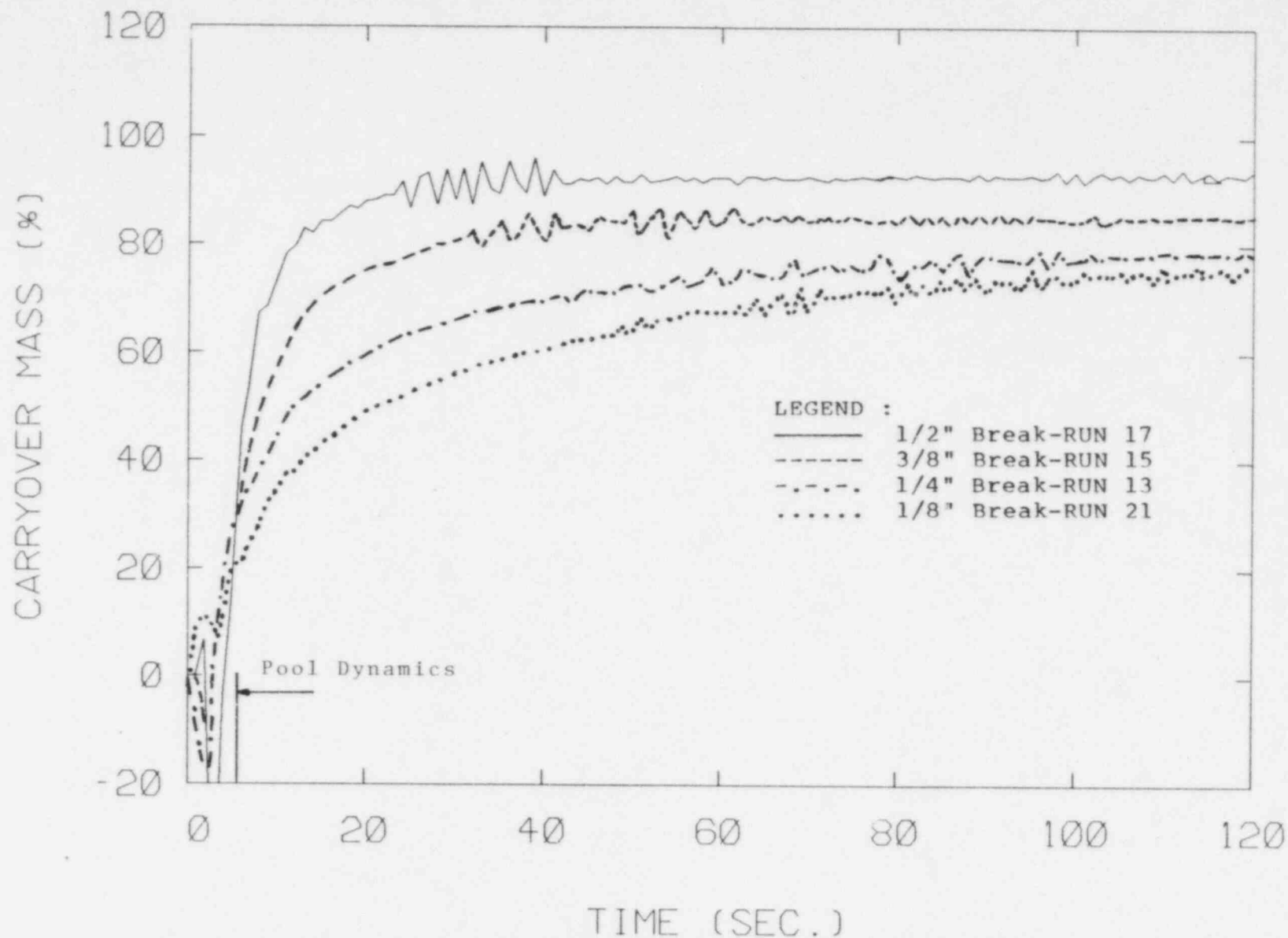


Figure 26d. Carryover mass transients with downcomer temperature 20°F lower than the vessel and initial pressure 1055 psi.

No generator internals.

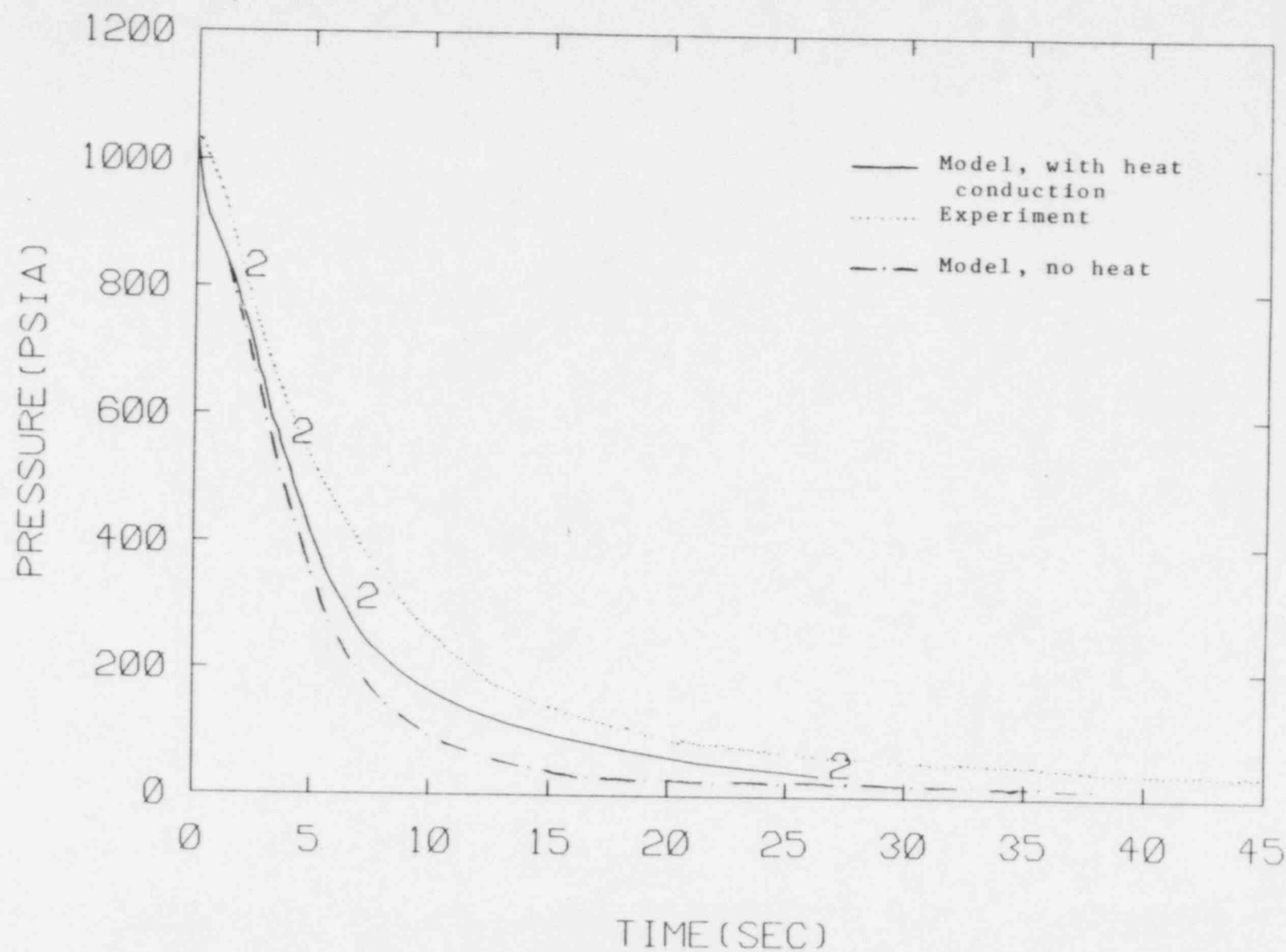


Figure 27. Comparison Between the Measured and Predicted pressure for MIT Test Run 5, 3/8" break

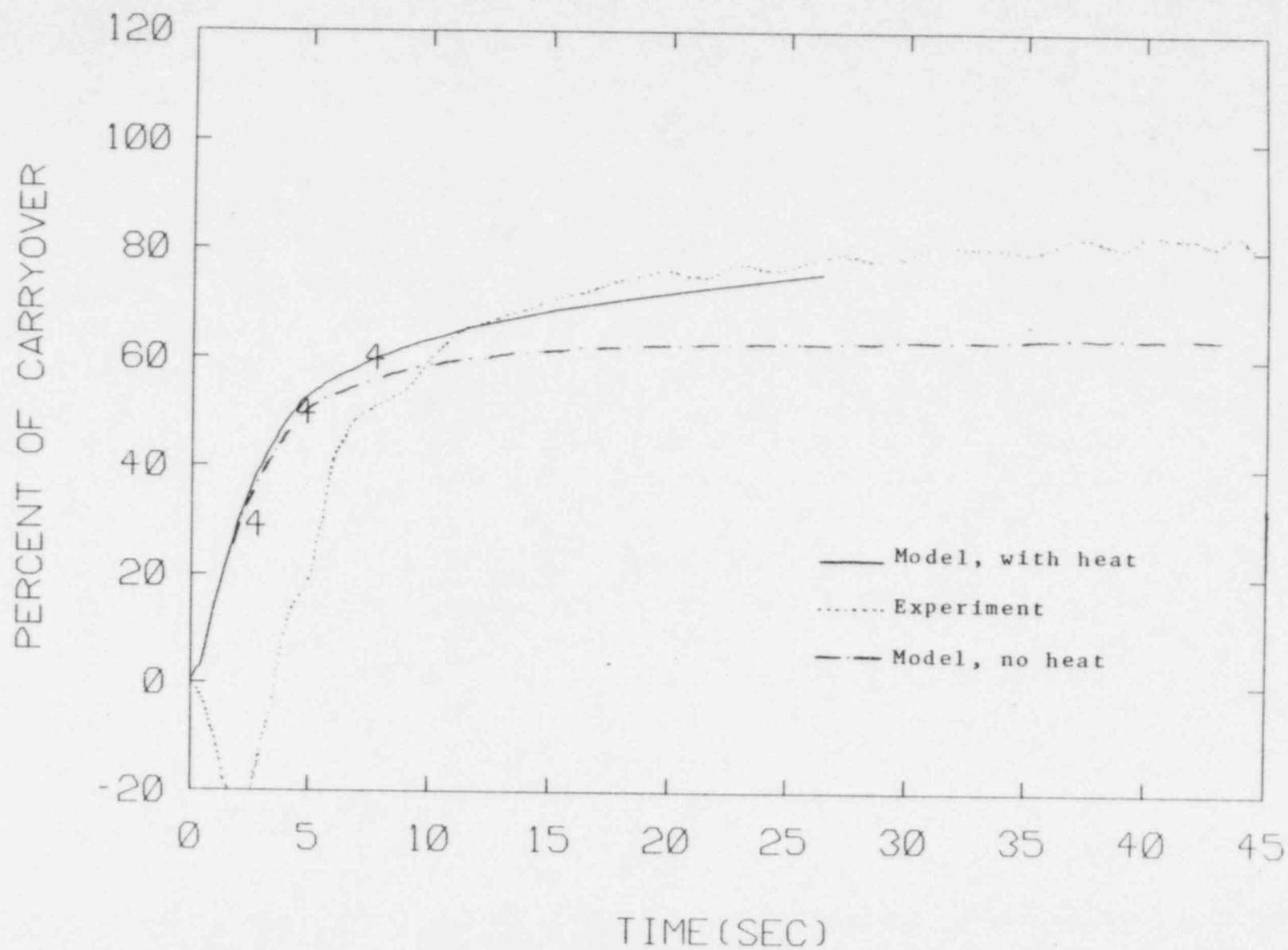


Figure 28. Comparison Between the Measured and Predicted Carryover for MIT Test Run 5, 3/8" break

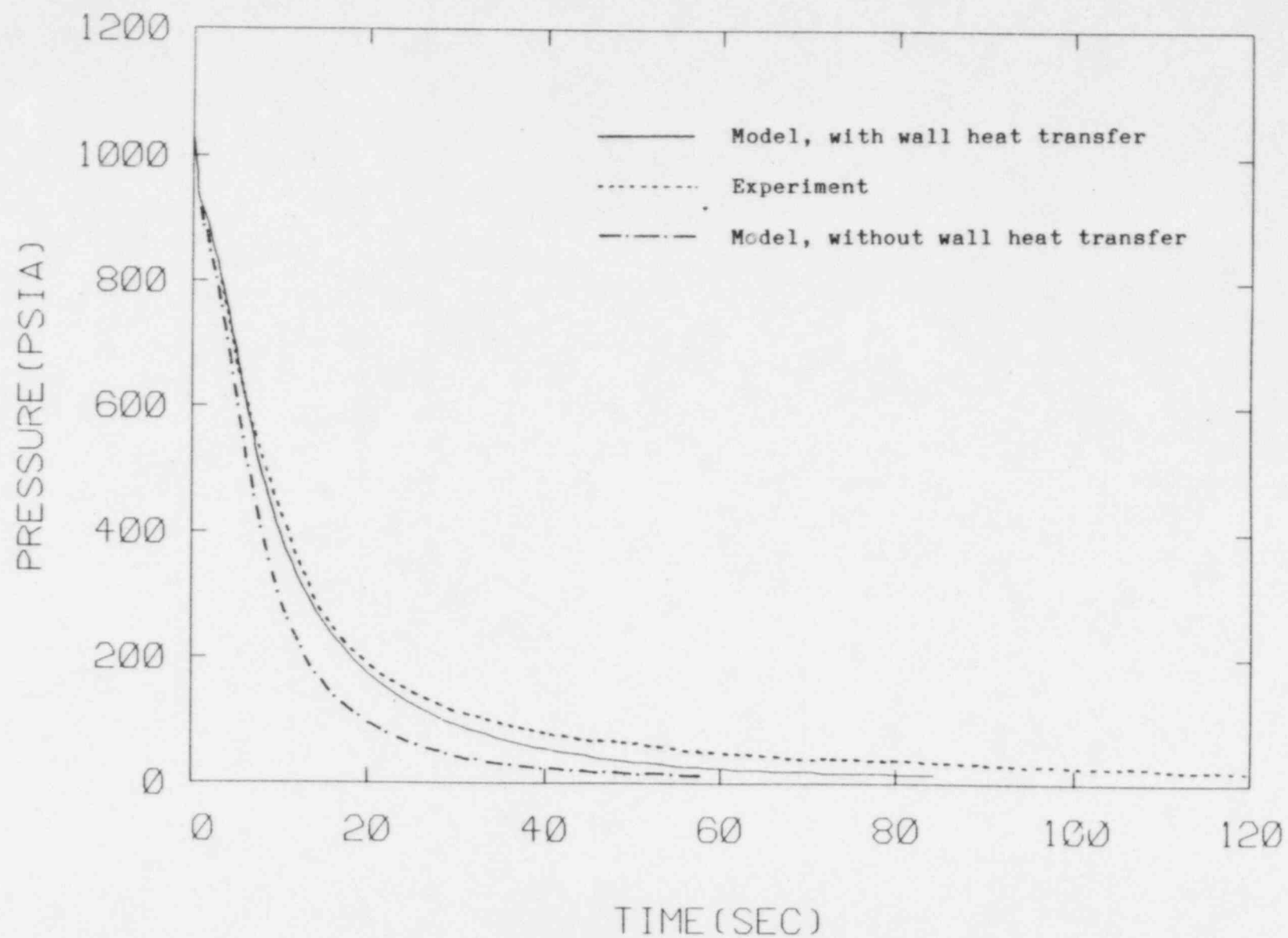


Figure 29. Comparison Between the Measured and Predicted Pressure for MIT Test Run 9, 1/4" break

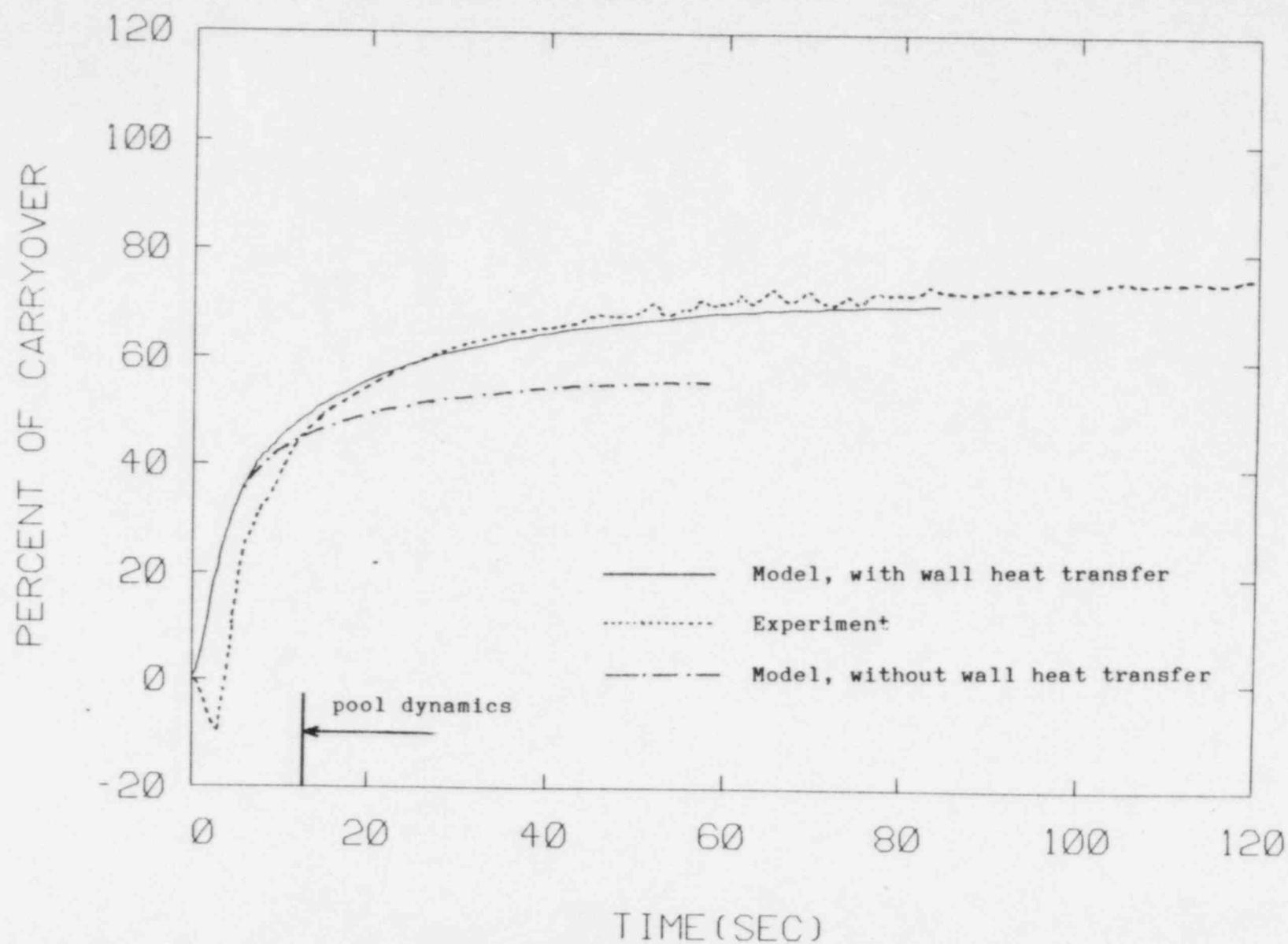


Figure 30. Comparison Between the Measured and Predicted Carryover for MIT Test Run 9, 1/4" break

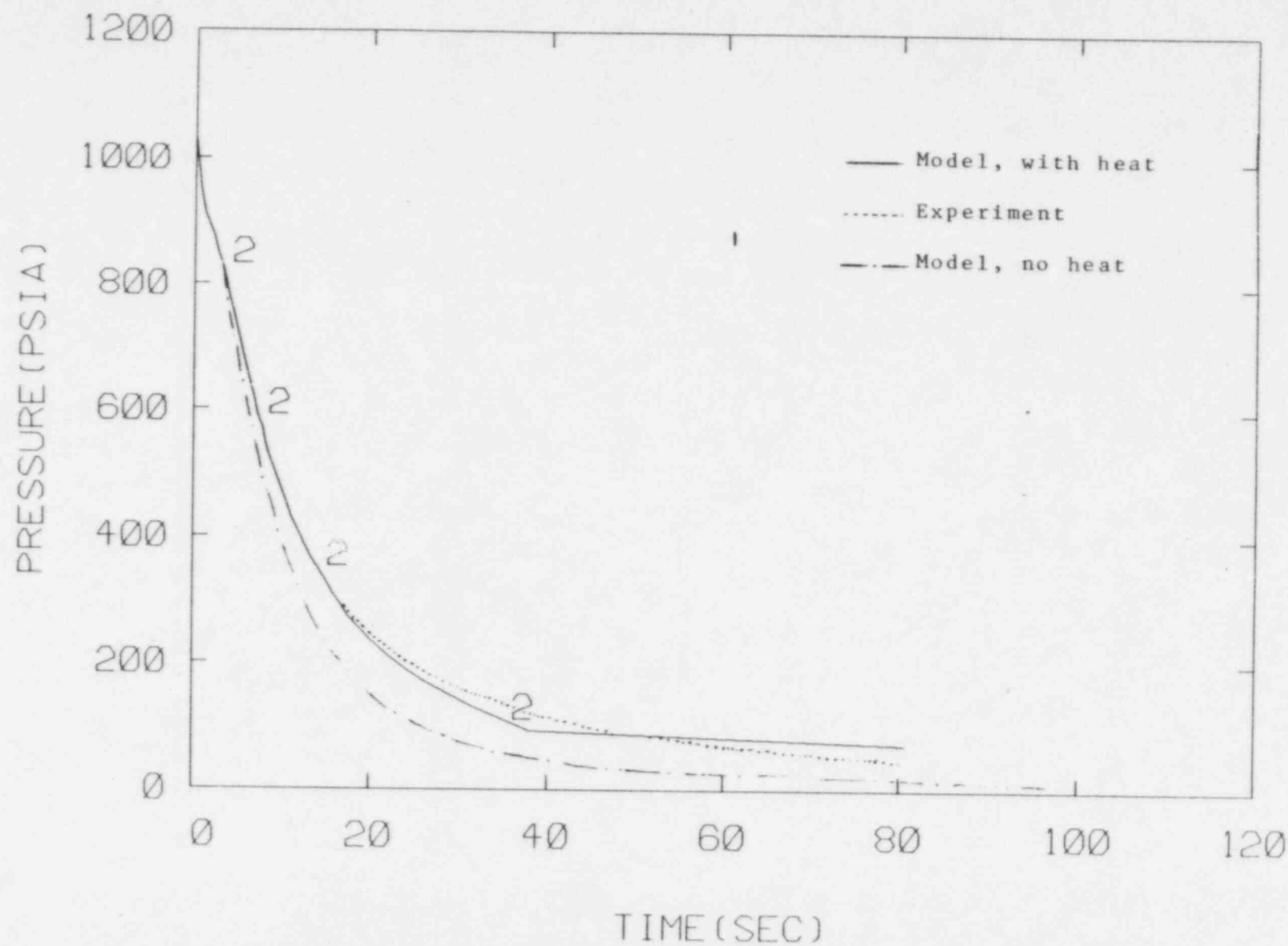


Figure 31. Comparison Between the Measured and Predicted Pressure for MIT Test Run 19, 1/8" break

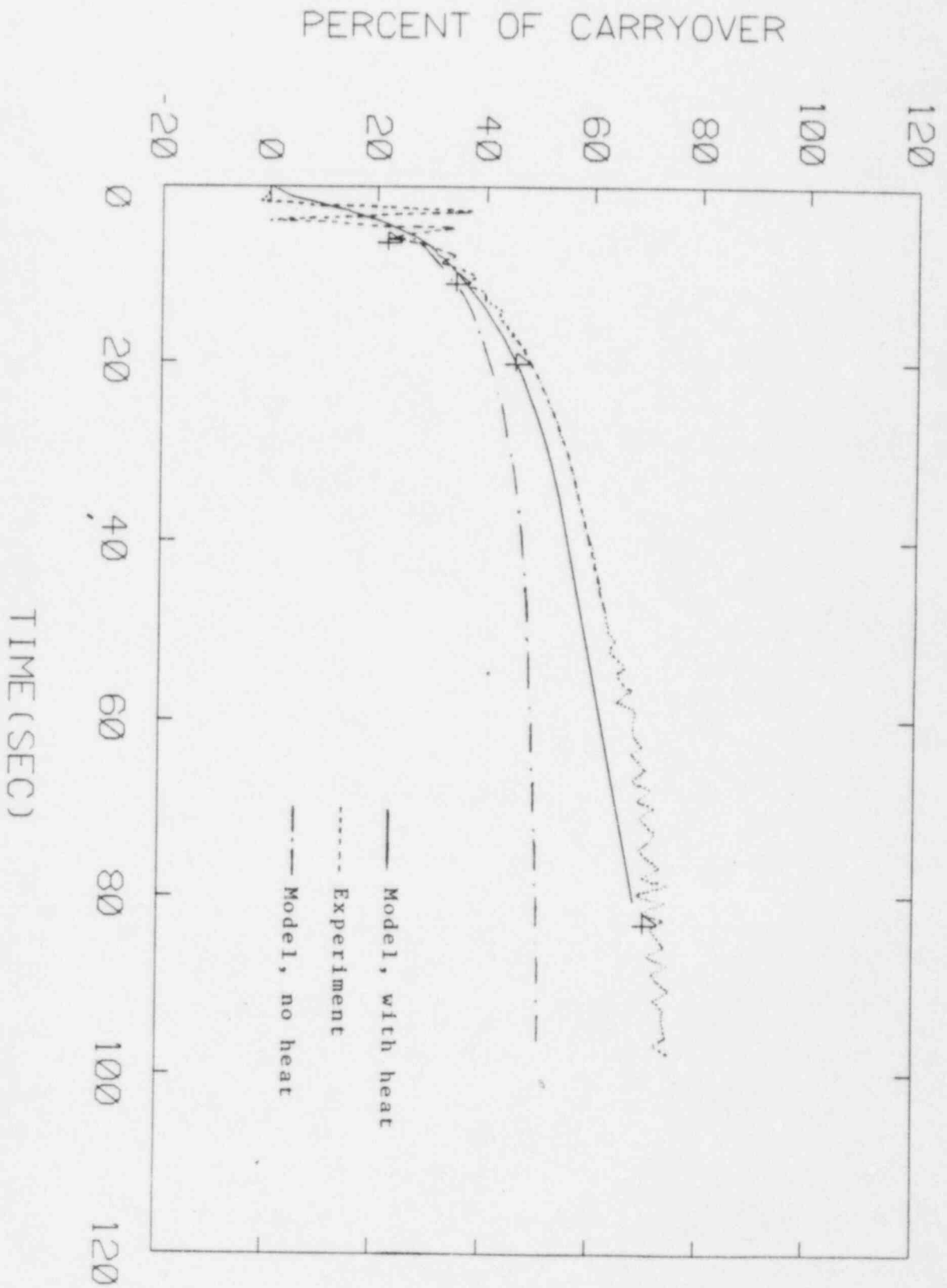


Figure 32. Comparison Between the Measured and Predicted Carryover for MIT Test Run 19, 1/8" break

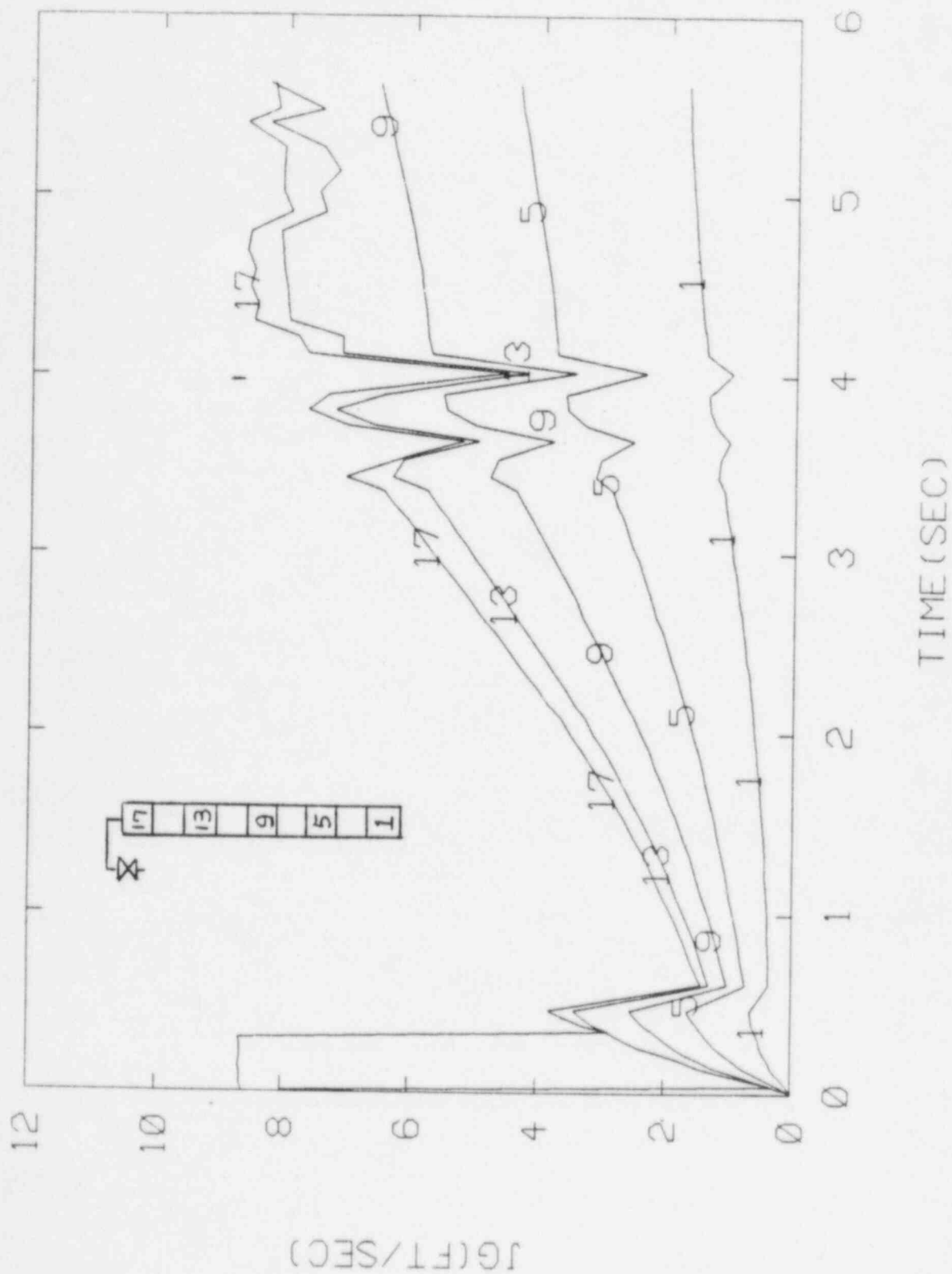


Figure 33. Predicted Superficial Vapor Velocity for MIT Test Run 5, 3/8" Break

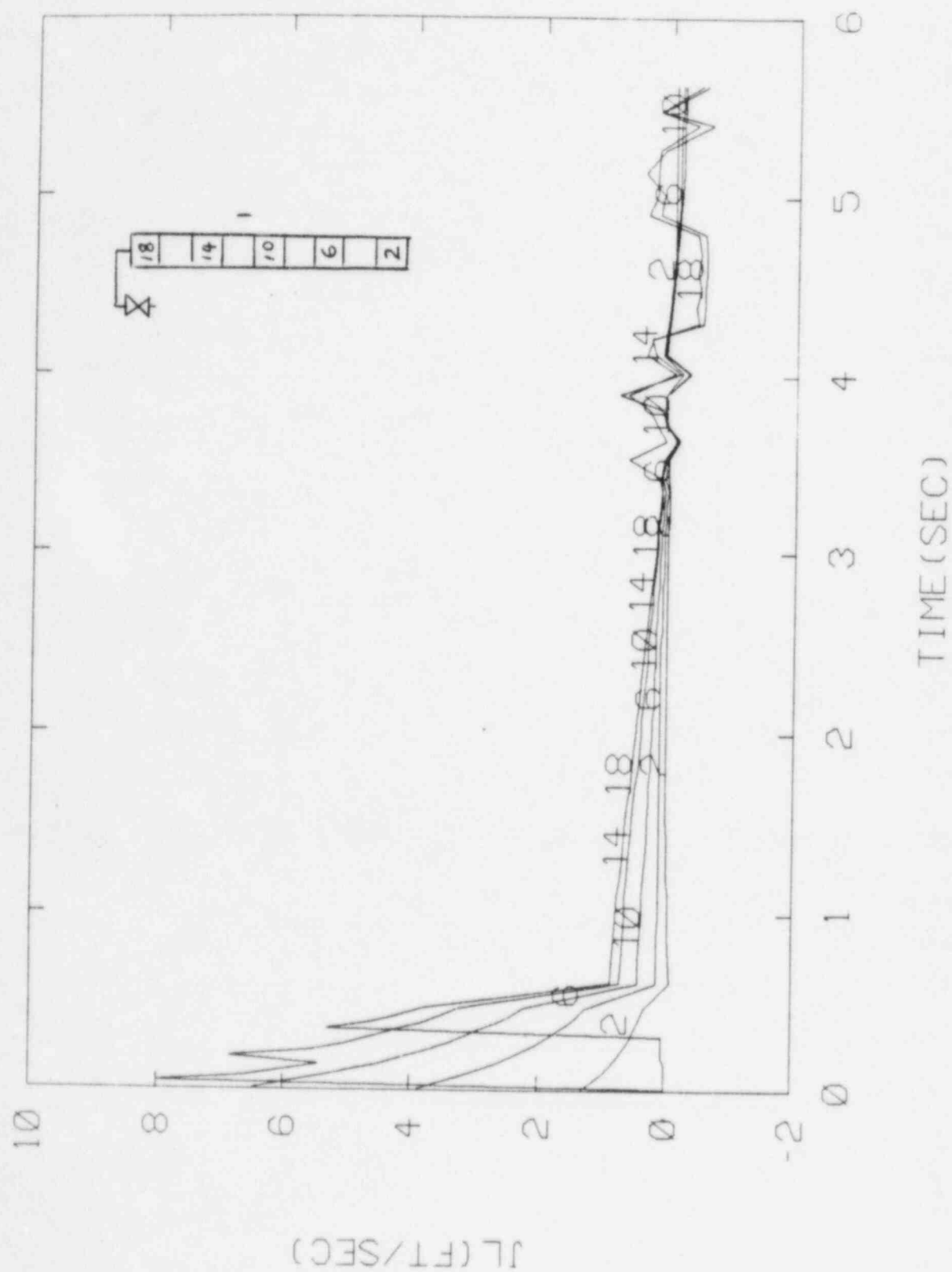


Figure 34. Predicted Superficial Liquid Velocity for MIT Test Run 5, 3/8" Break

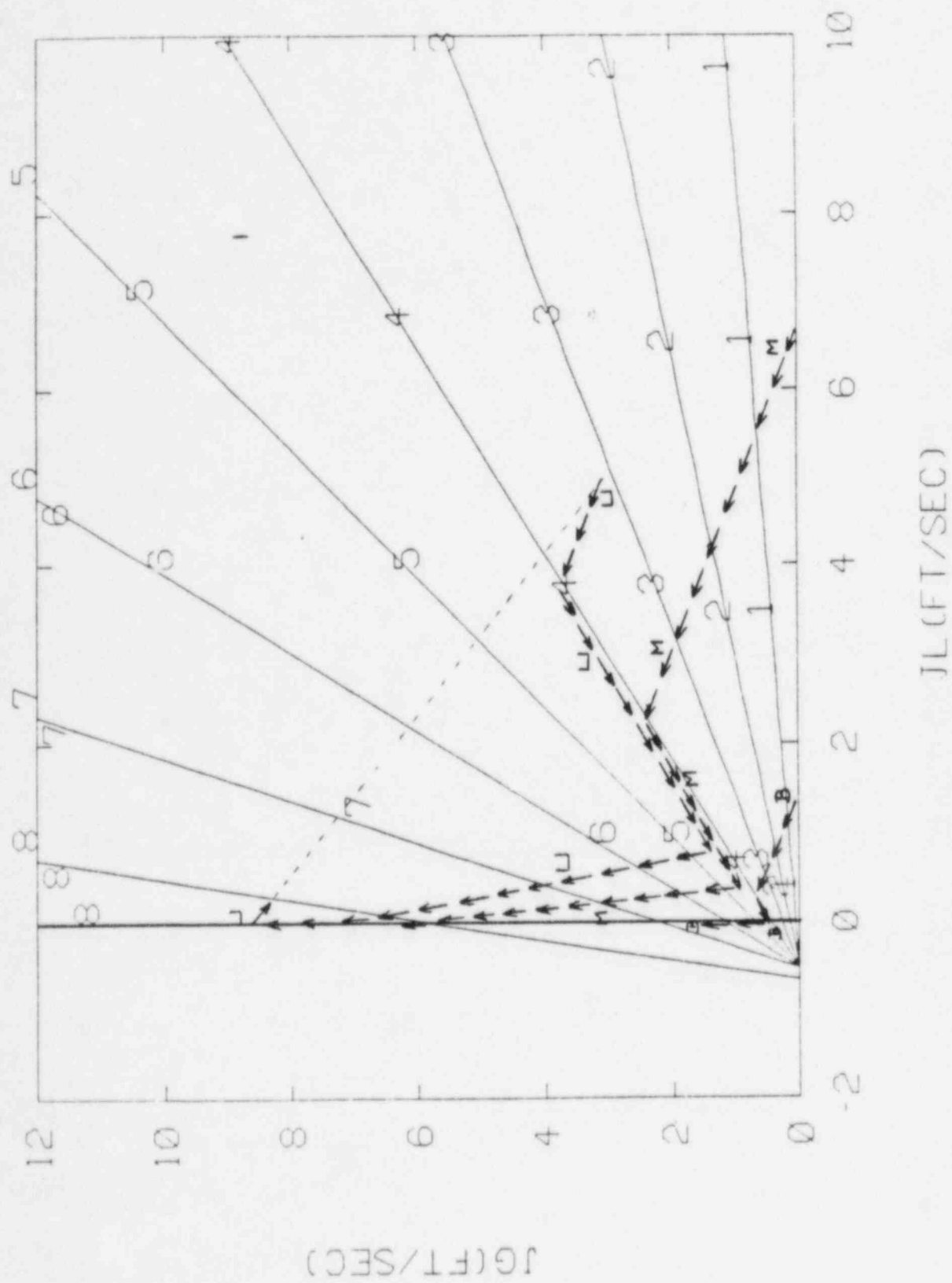


Figure 35. Trajectory of States for MIT Test Run 5, 3/8" Break, with
Lines of Constant Void Fraction

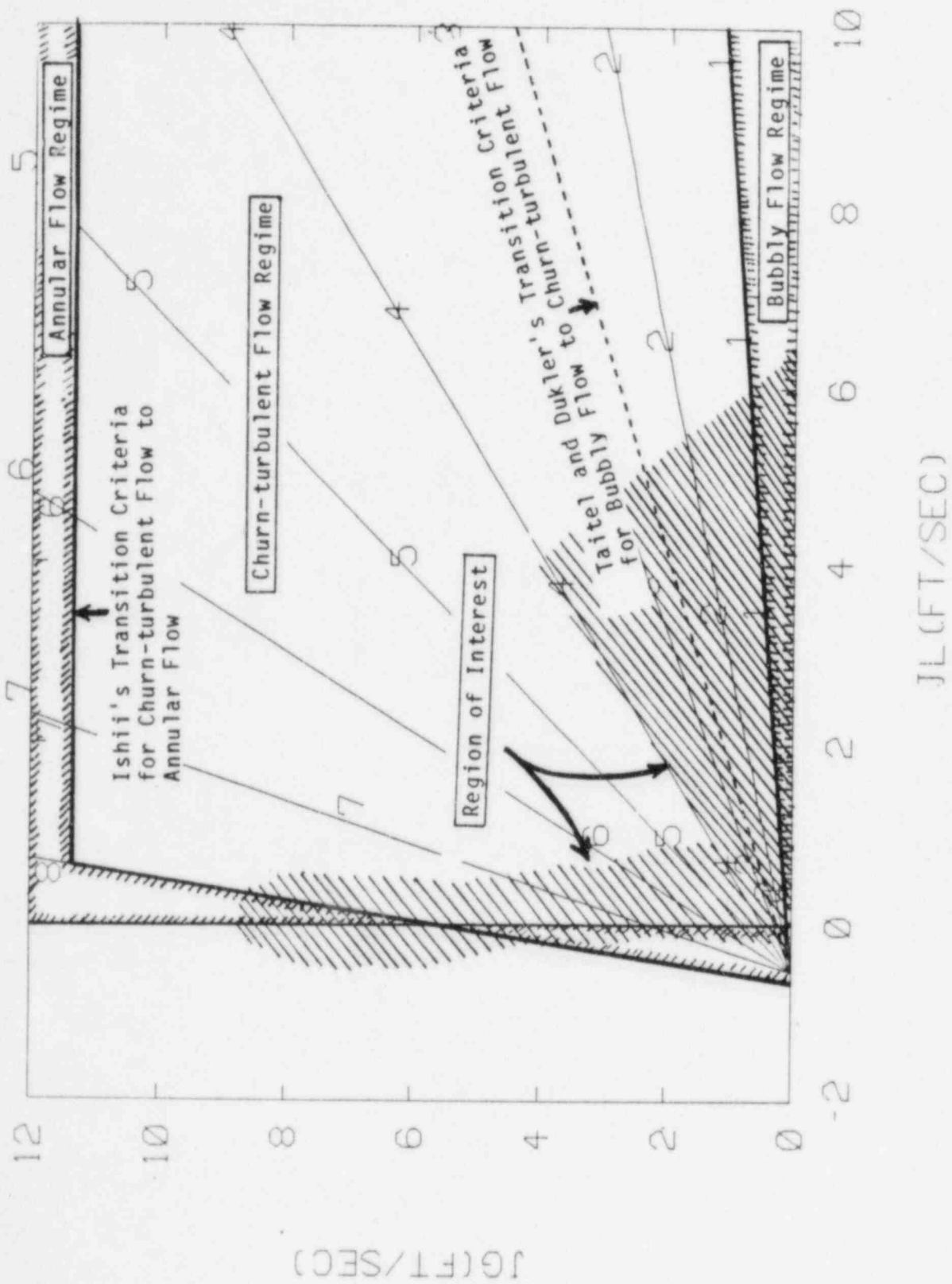


Figure 36. Region of Interest and the Flow Regime Boundary for MIT
Test Run 5, 3/8" Break

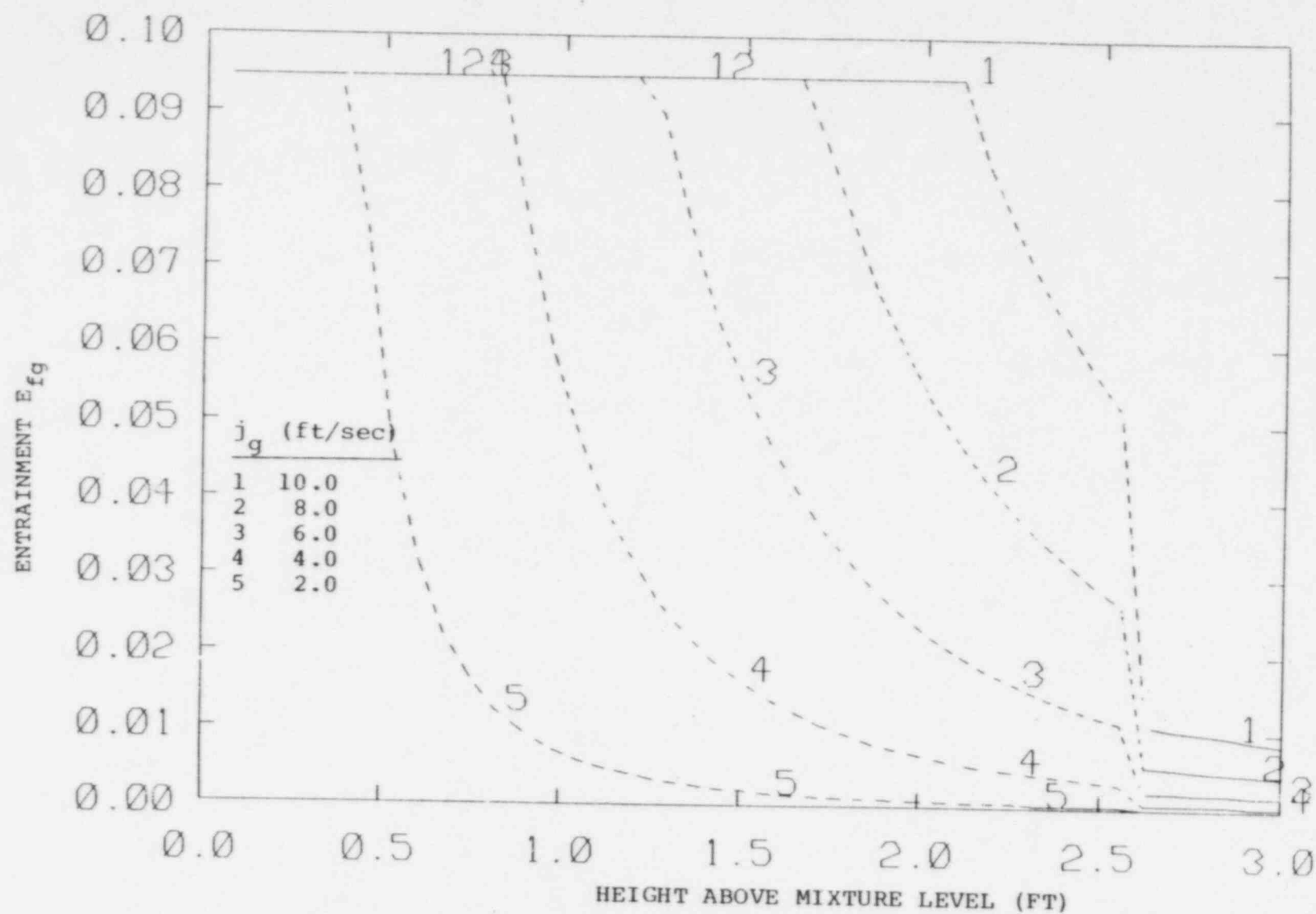


Figure 37. Pool Entrainment for a Pressure of 1000 psi

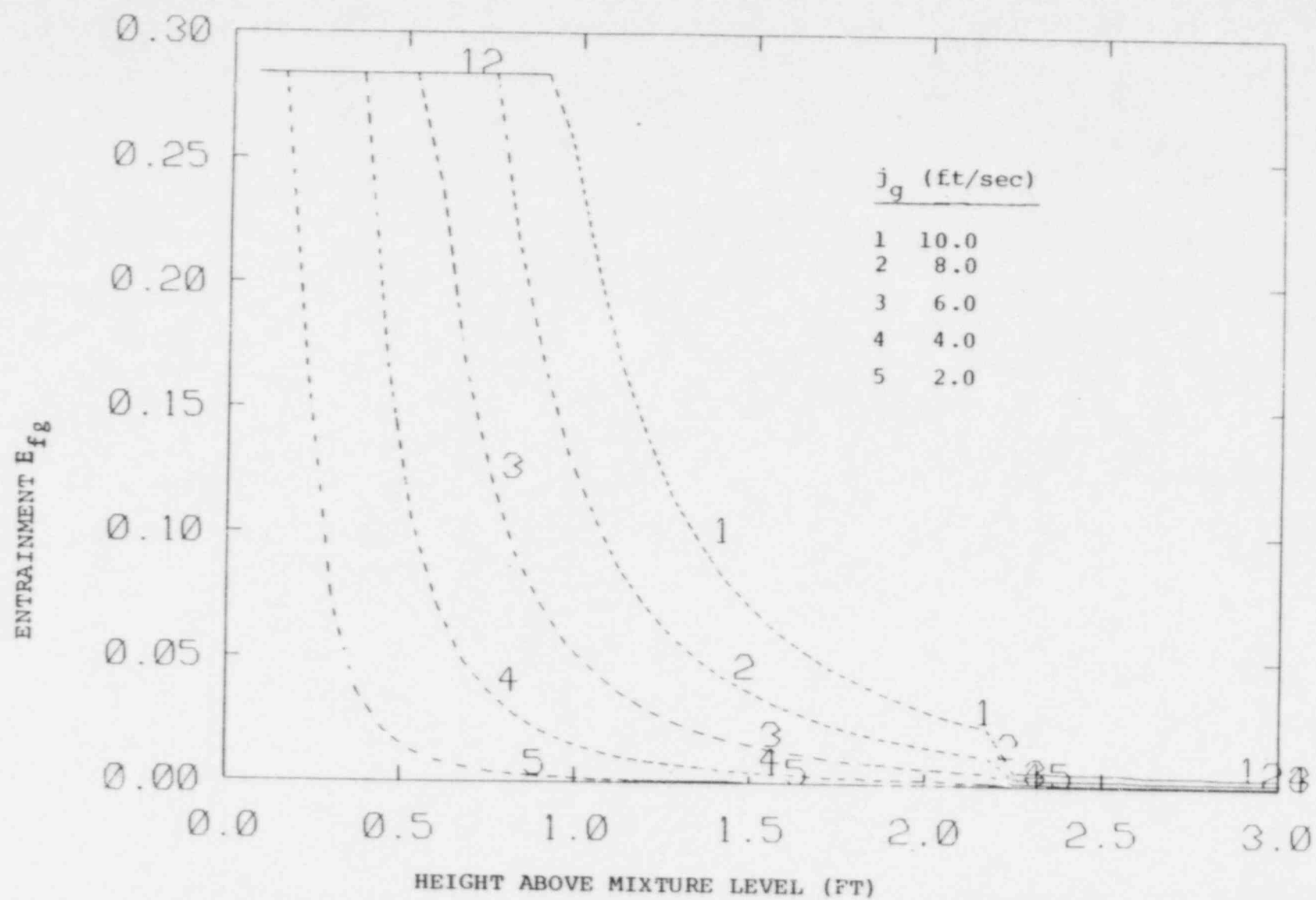
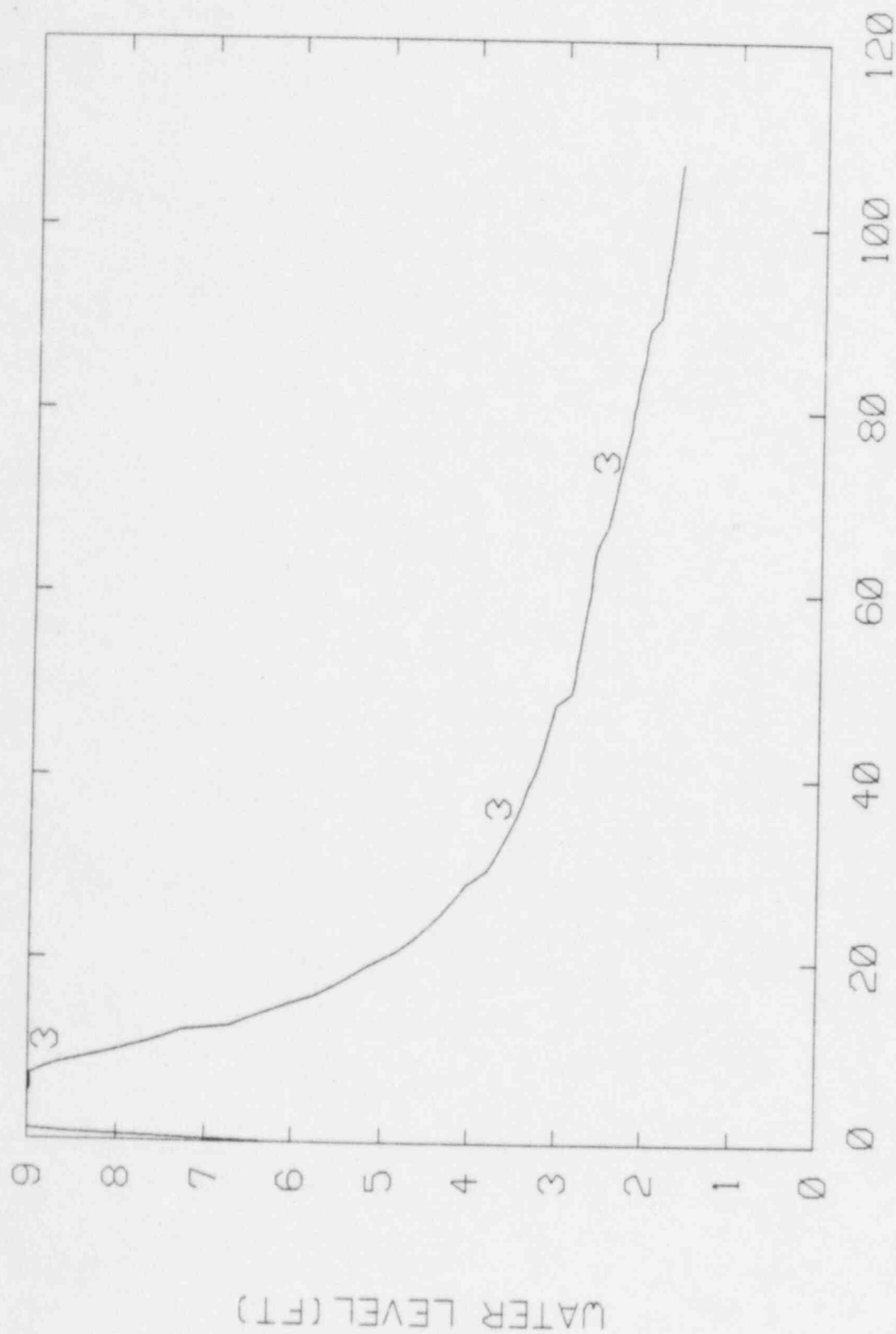


Figure 38. Pool Entrainment for a Pressure of 400 psi



TIME (SEC)

Figure 39. Predicted Mixture Water Level for MIT Test Run 19, 1/8" Break

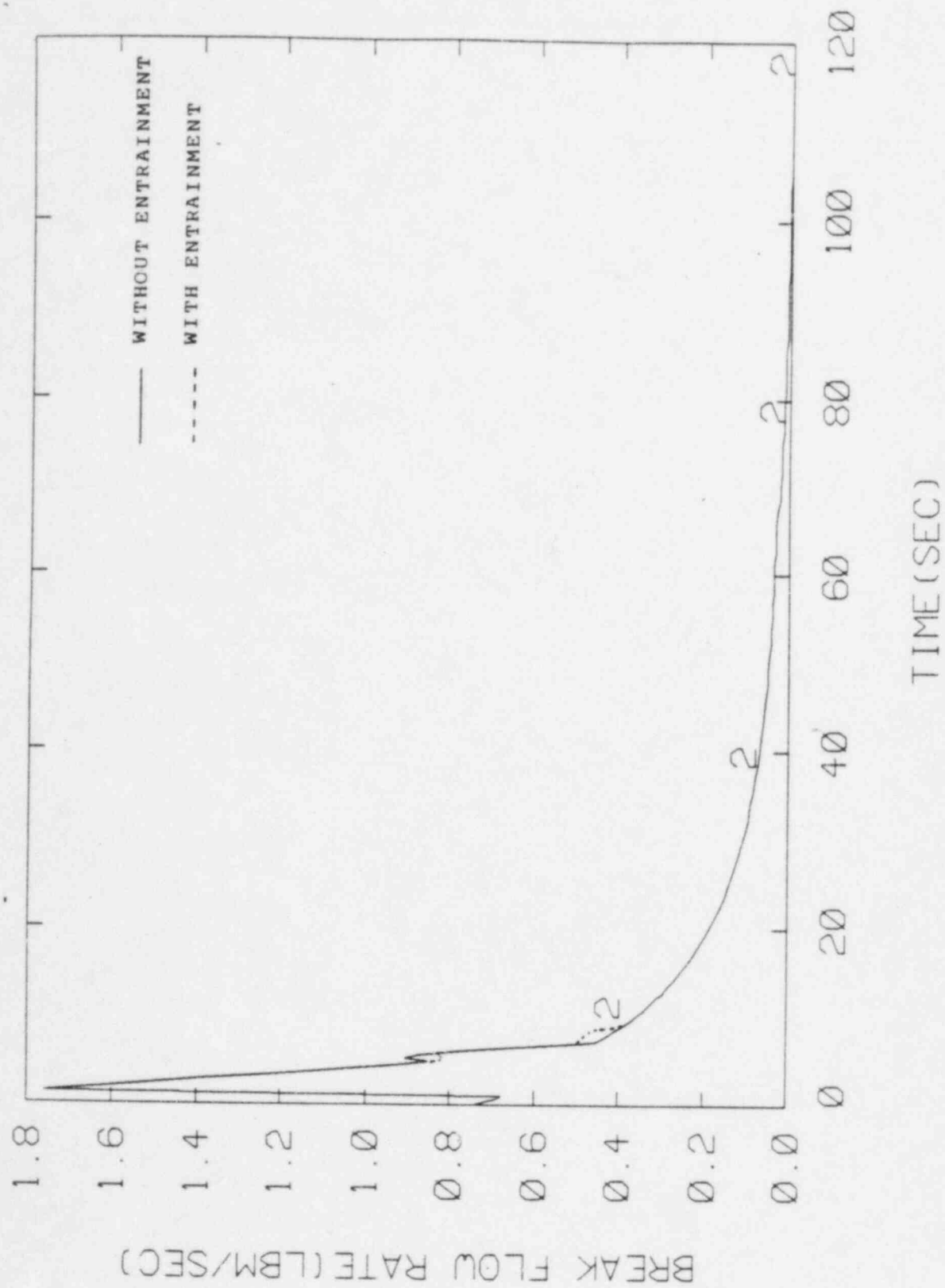


Figure 40. Predicted Break Flow Rate for MIT Test Run 19,
1/8"Break

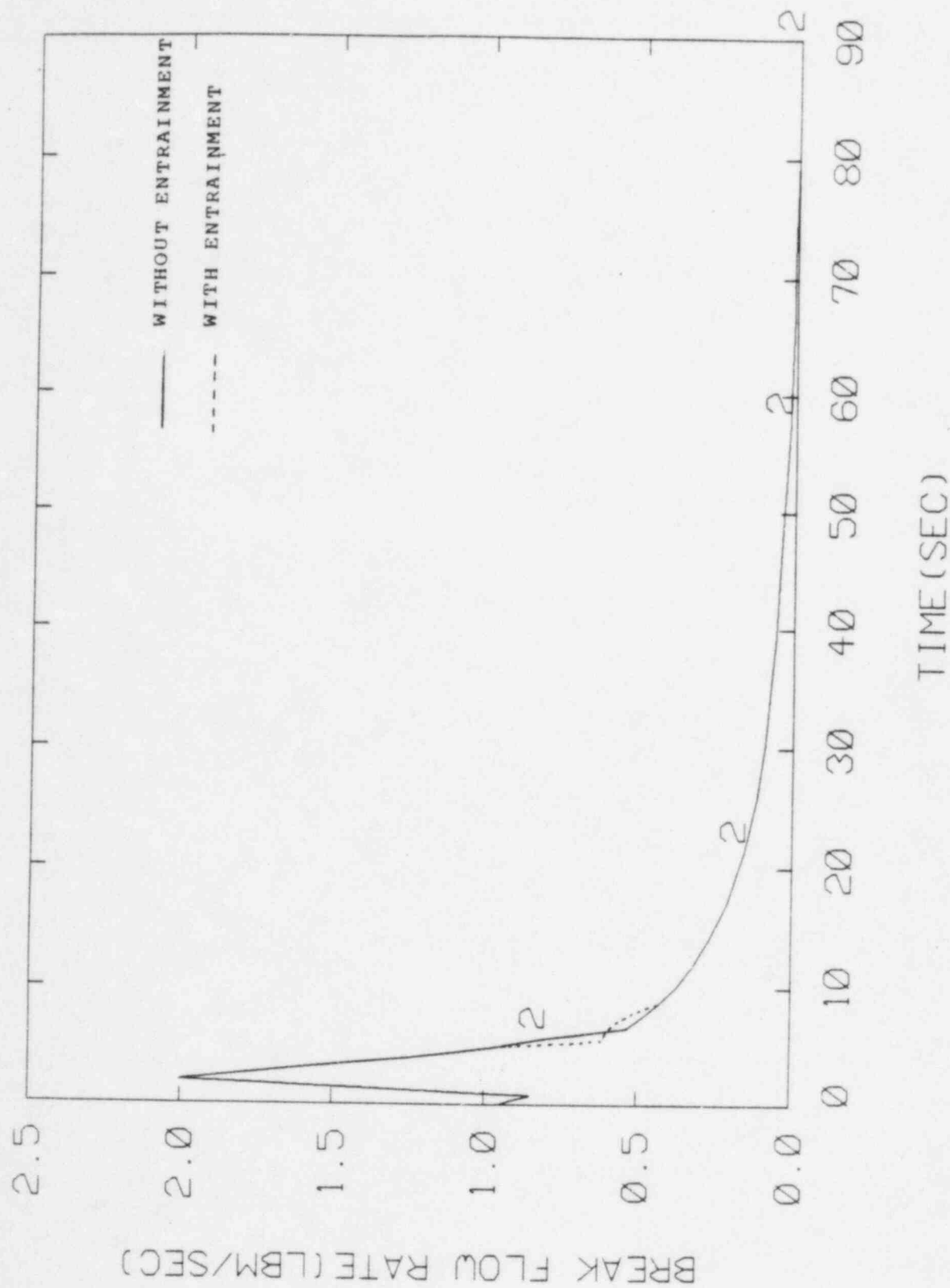


Figure 41. Predicted Break Flow Rate for MIT Test Run 9, 1/4" Break

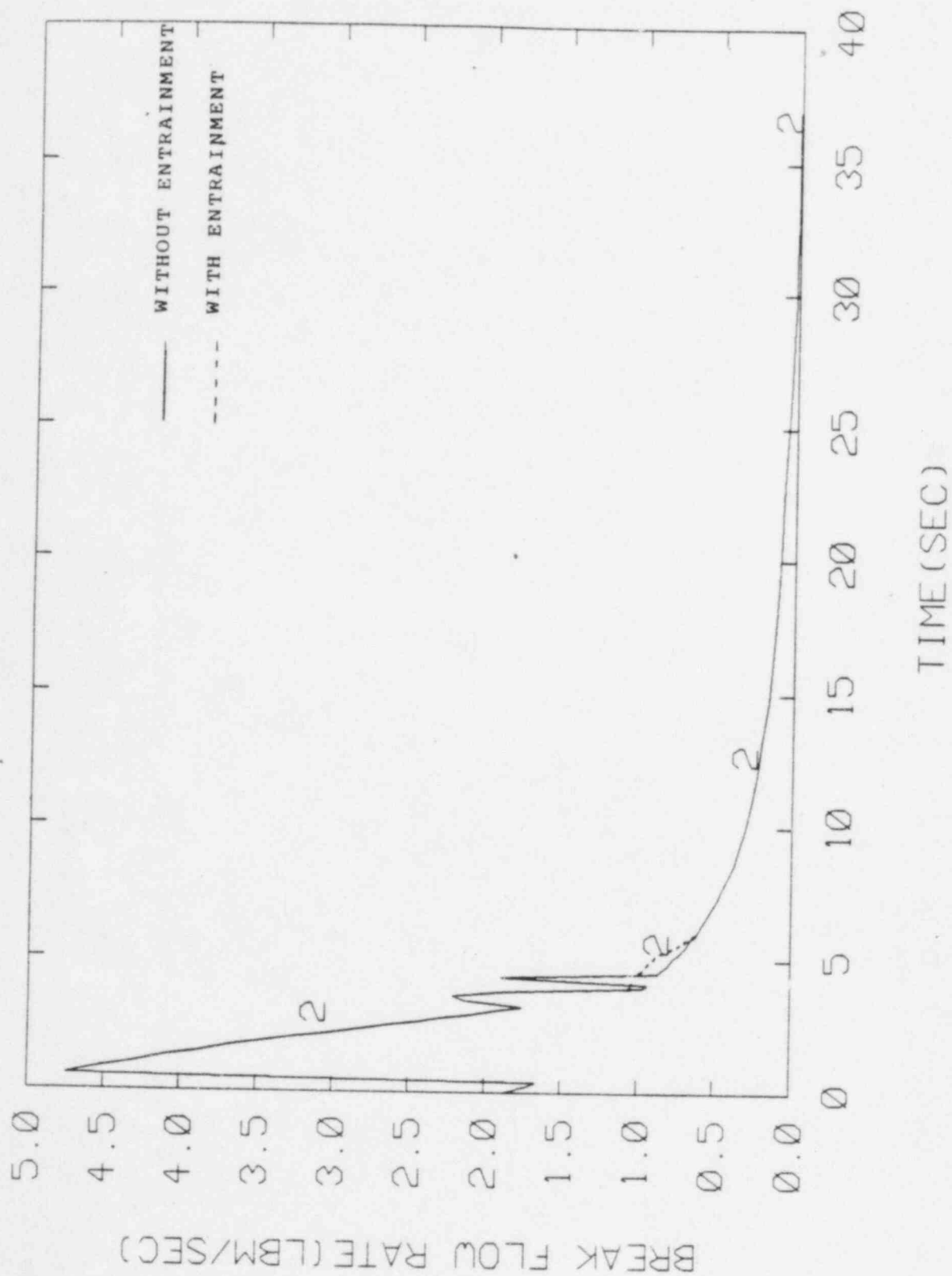


Figure 42. Predicted Break Flow Rate for MIT Test Run 5, 3/8" Break

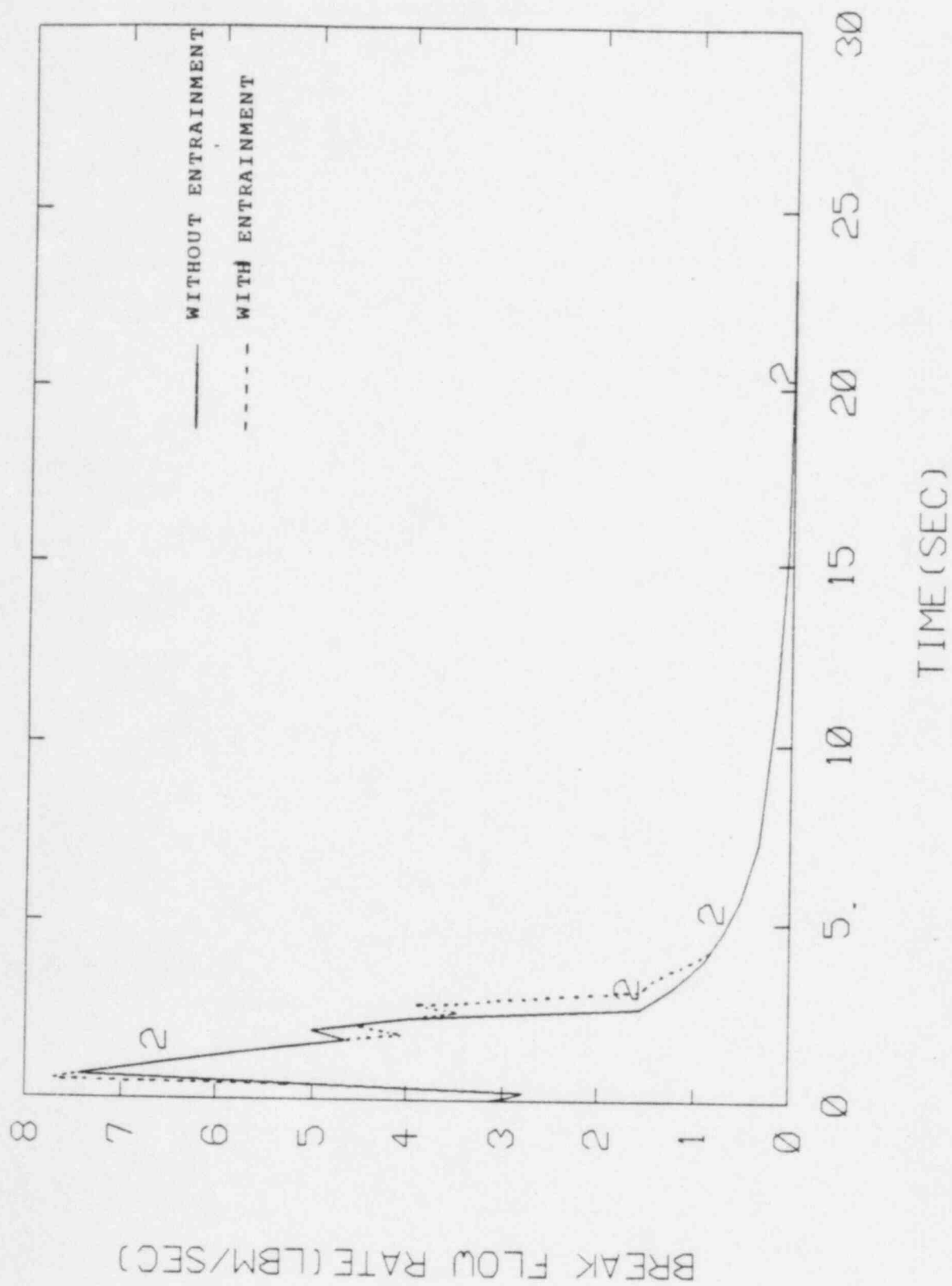


Figure 43. Predicted Break Flow Rate for MIT Test Run 1, 1/2" Break

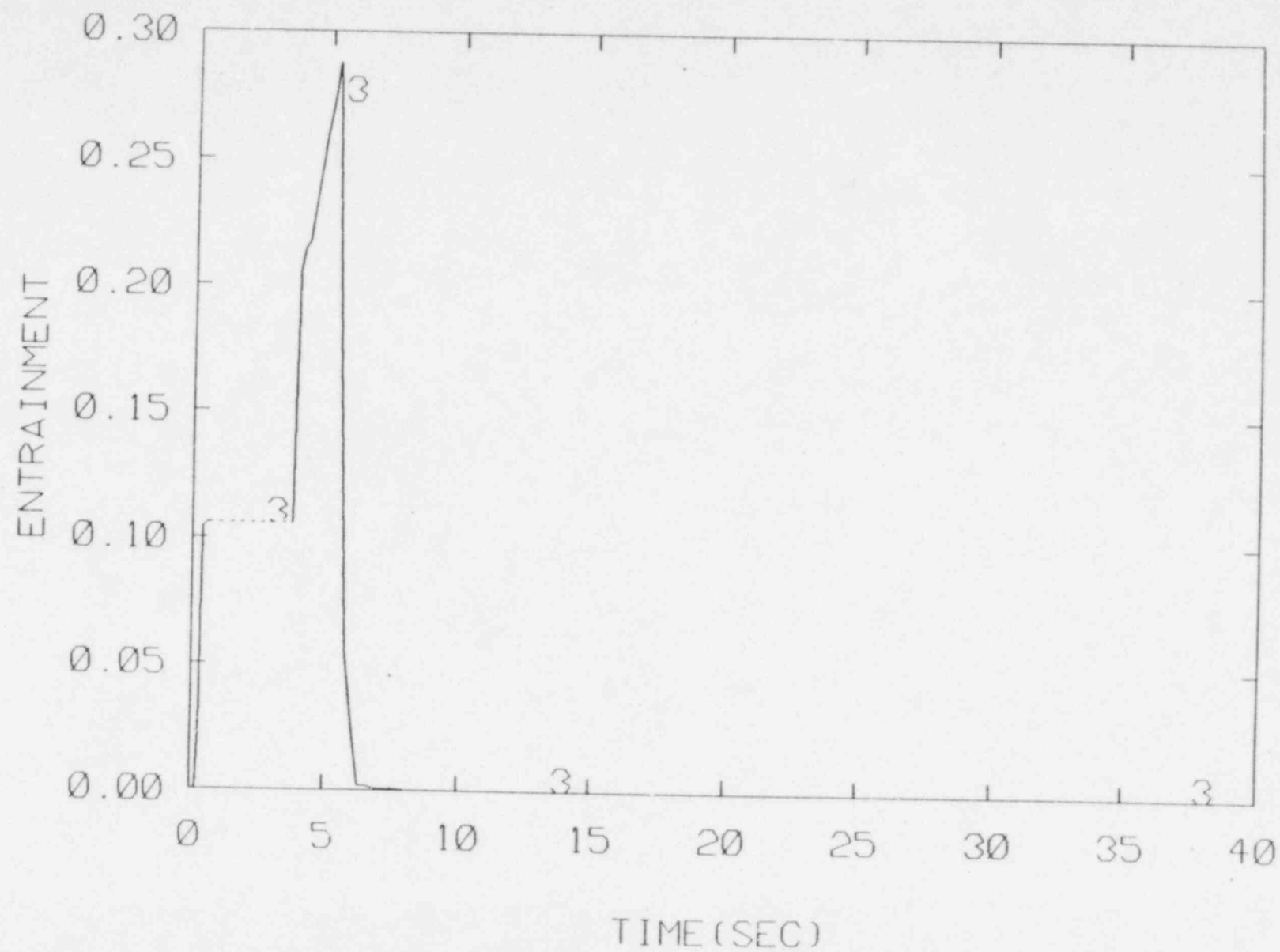


Figure 44. Predicted entrainment for MIT Test Run 5, 3/8" Break

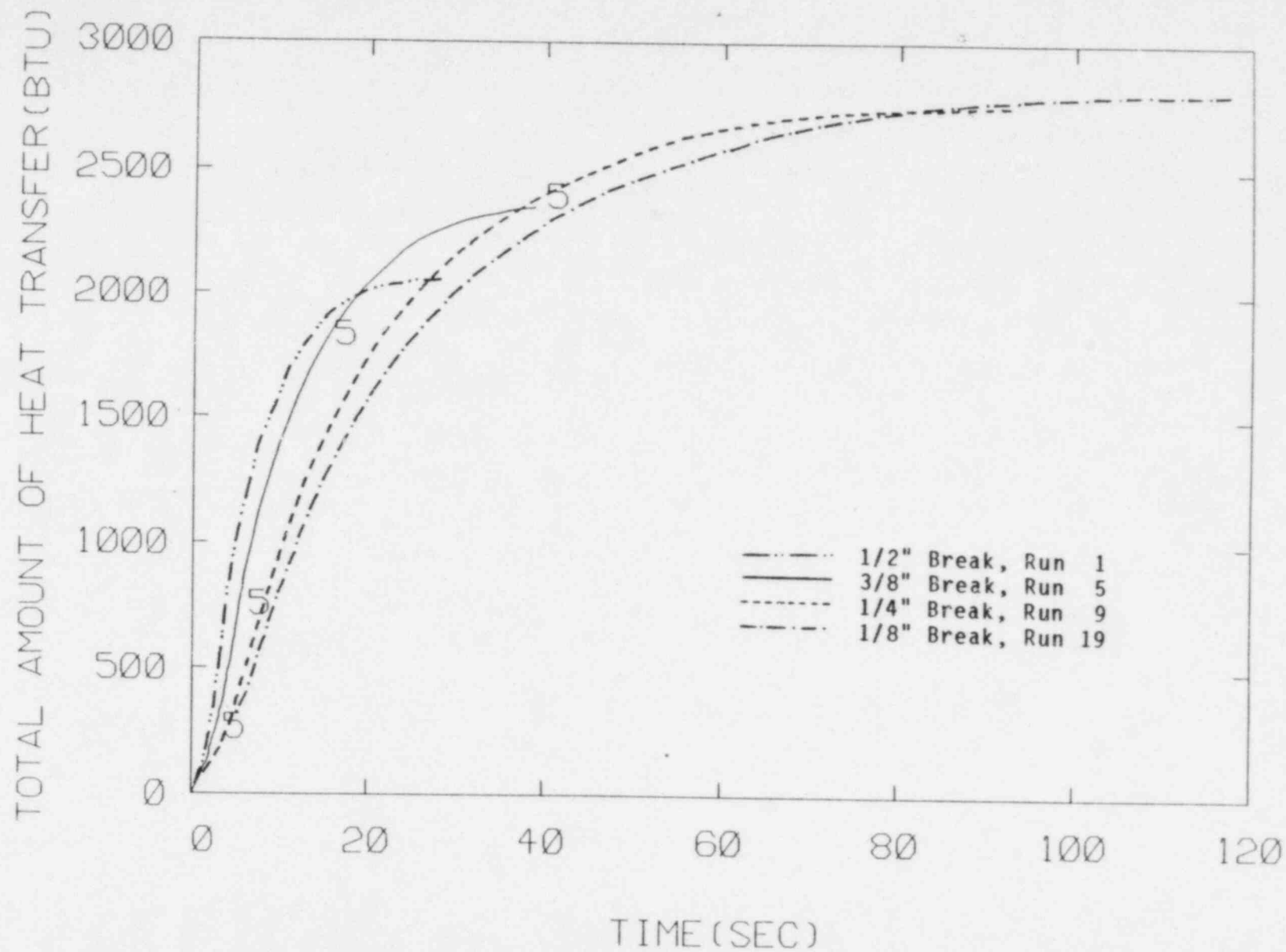


Figure 45. Predicted Time Integration of Heat Transfer for MIT Test Run 1,5,9,19

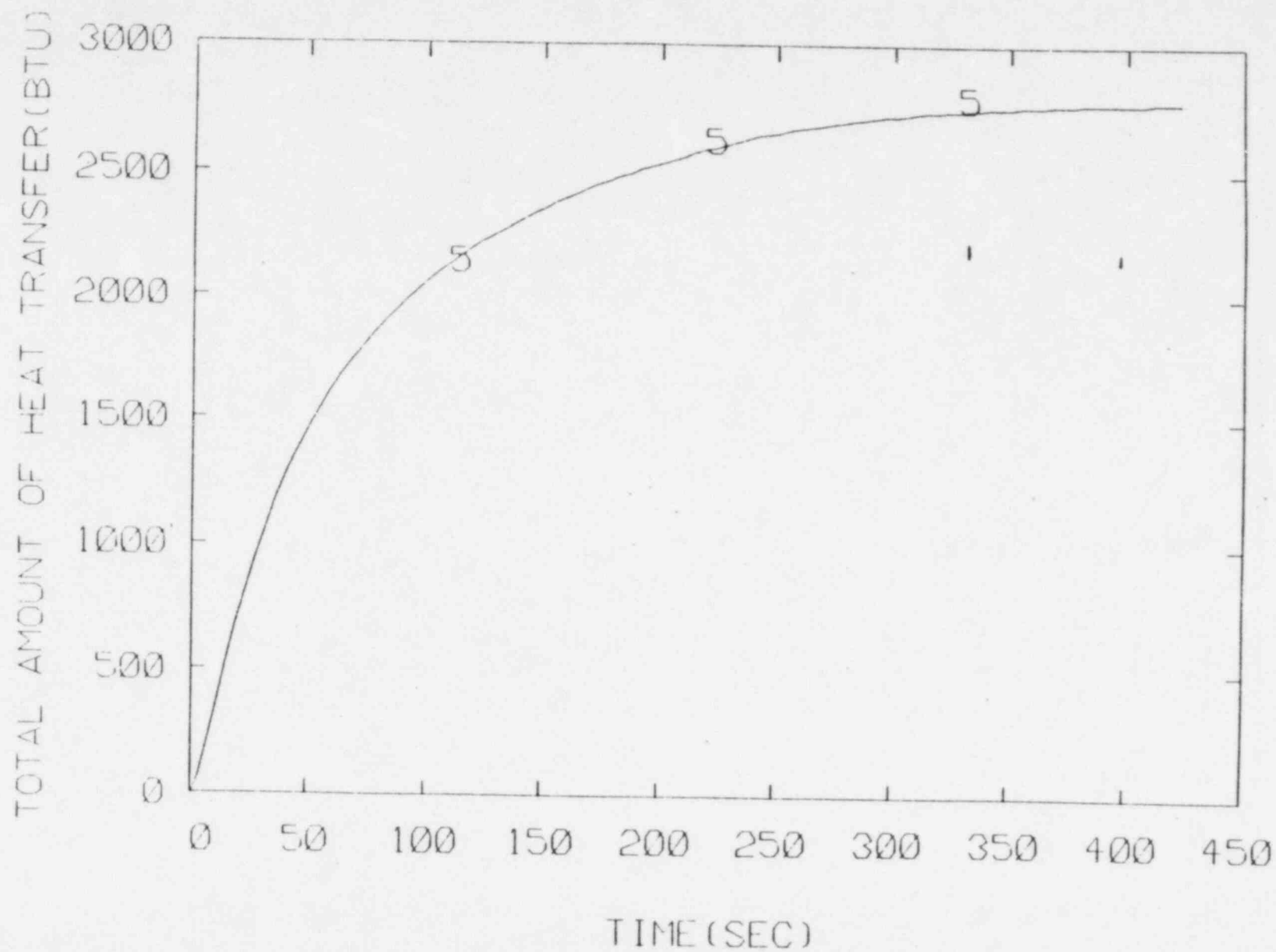


Figure 46. Predicted Time Integration of Heat Transfer for MIT Test Run 25, 1/16" Break

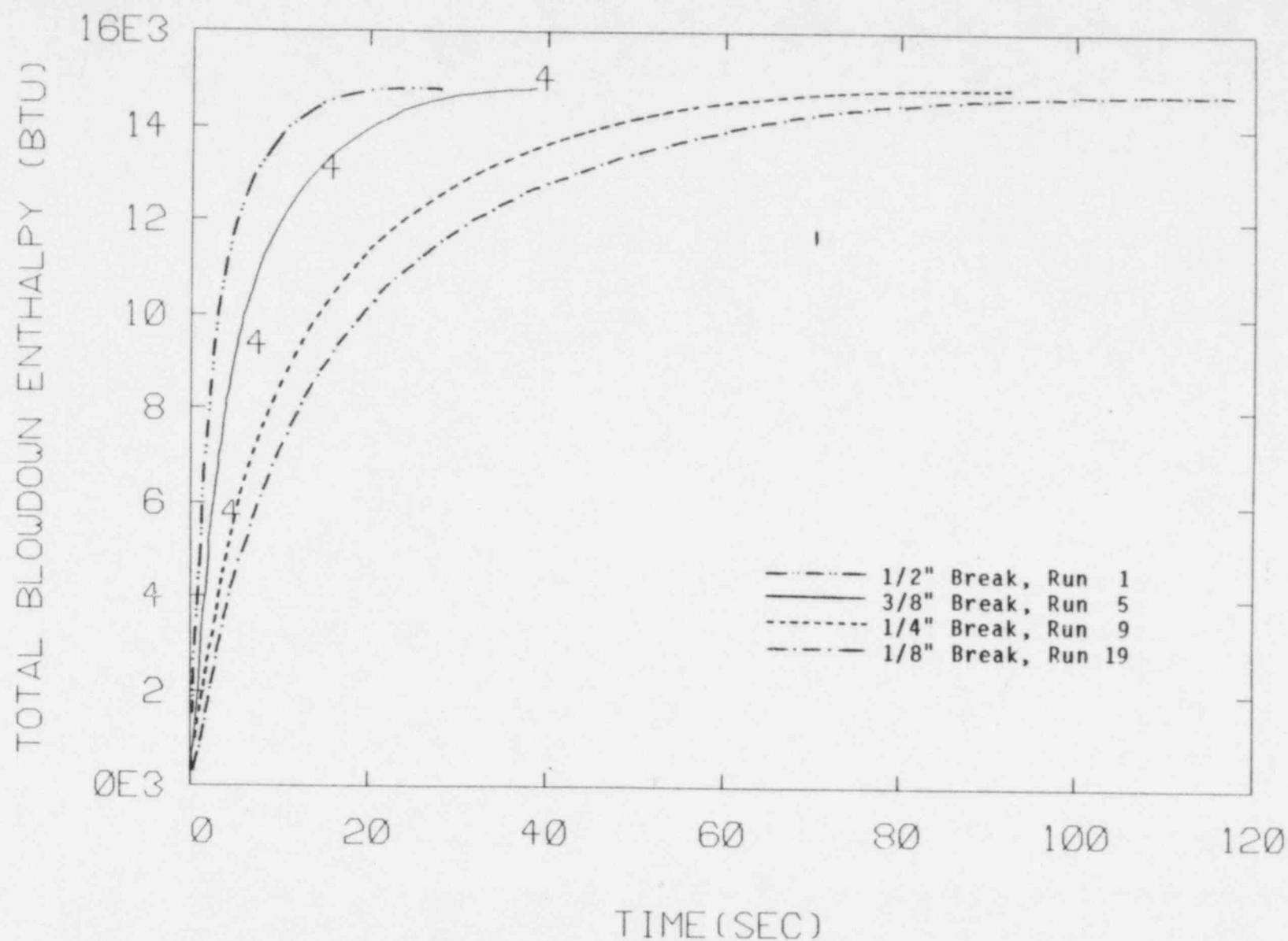


Figure 47. Predicted Time Integration of Blowdown Energy for MIT Test Run 1,5,9,19

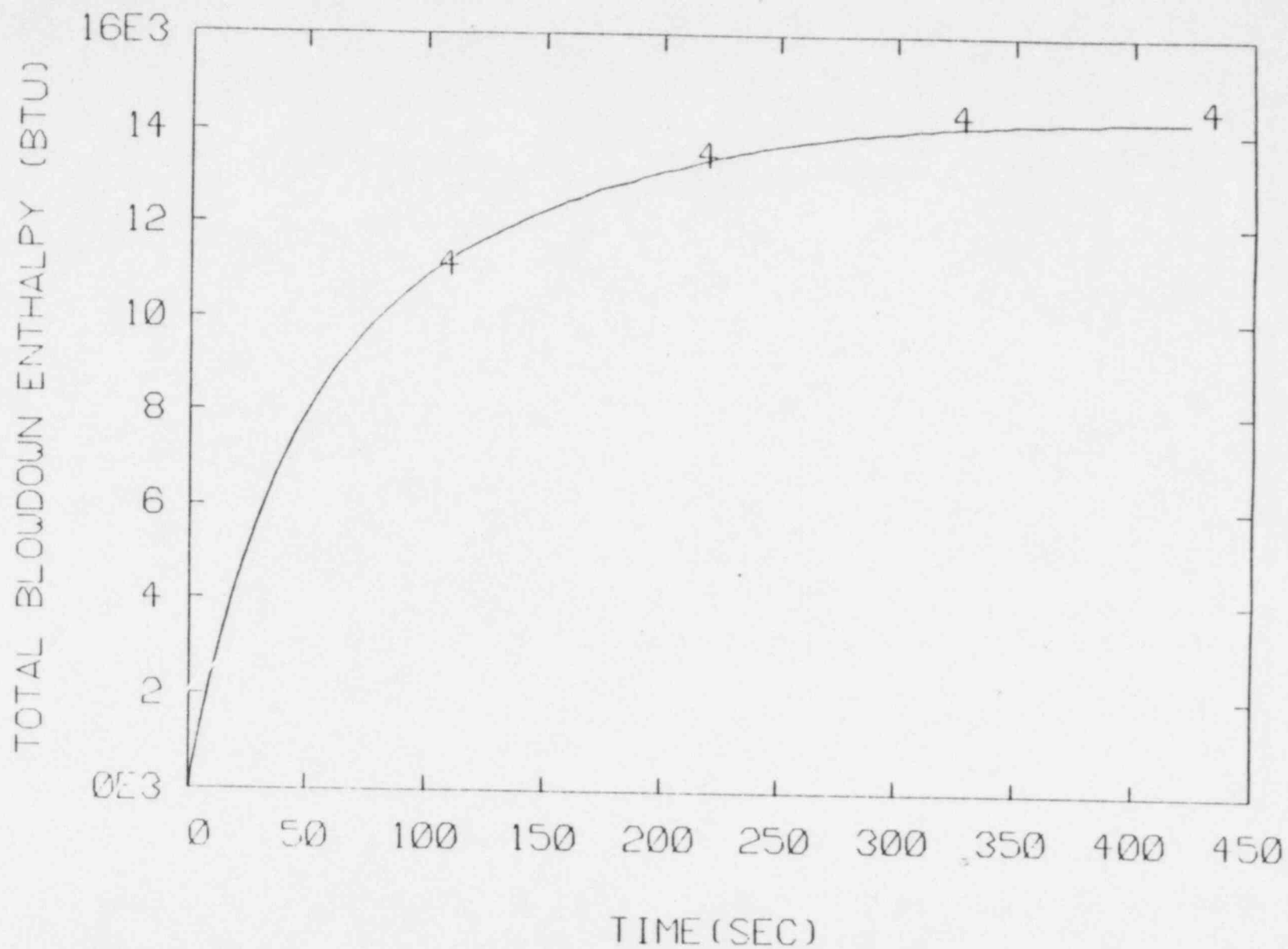


Figure 48. Predicted Time Integration of Blowdown Energy for MIT
Test Run 25, 1/16" Break

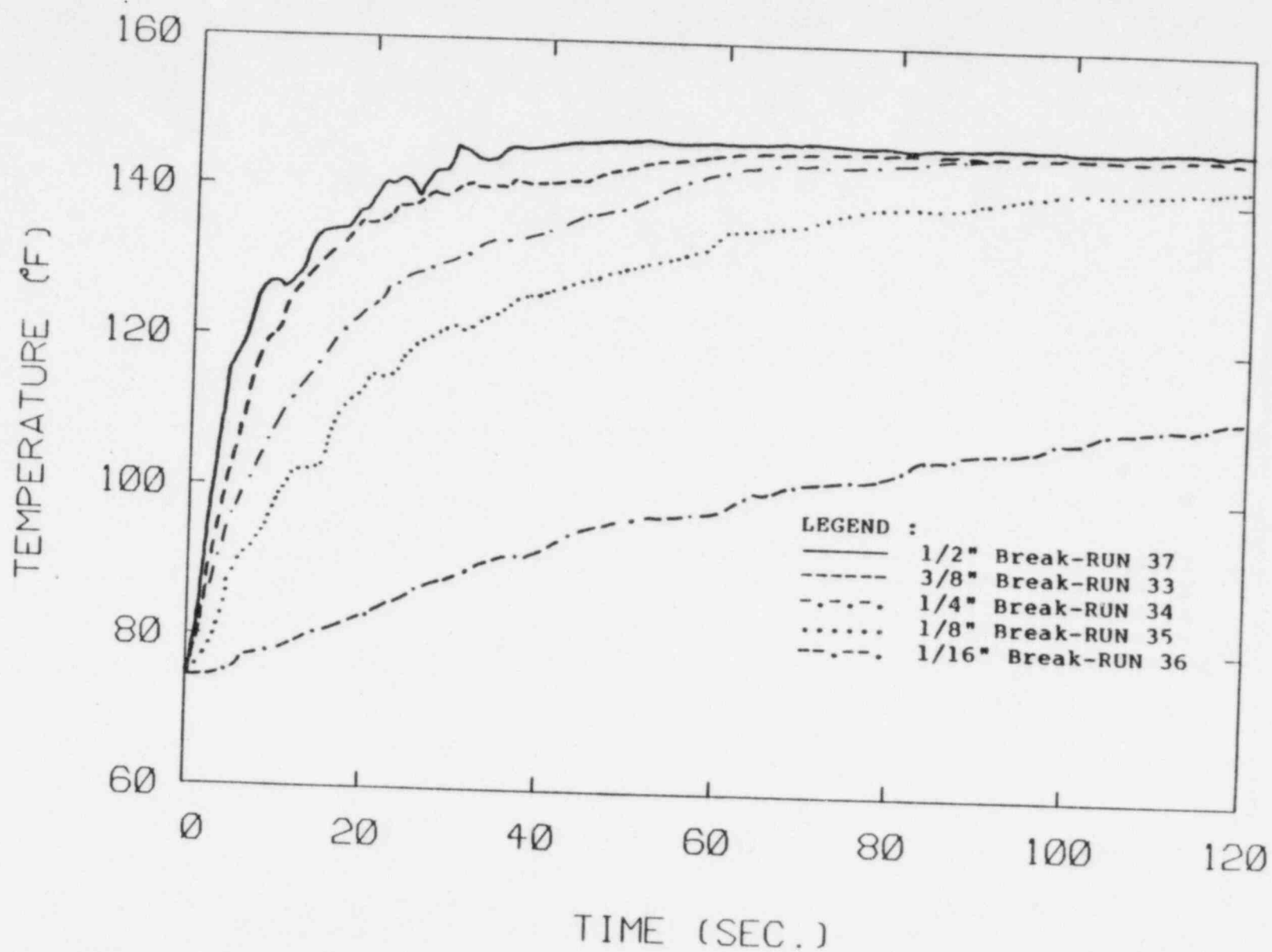


Figure 49. The Measured Pool Temperature for MIT Test Run 33,34,35,36,37

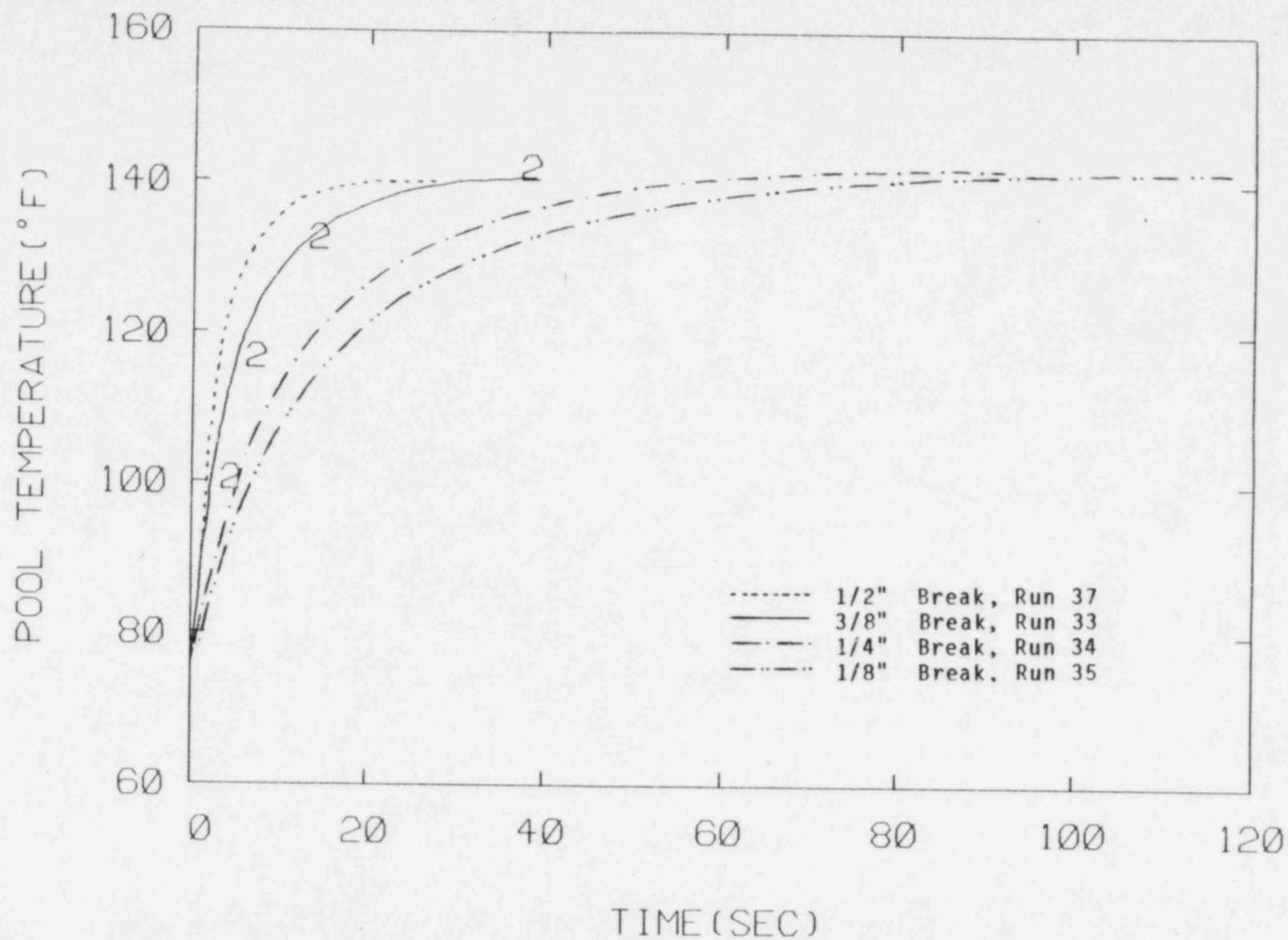


Figure 50. The Predicted Pool Temperature for MIT Test Run 33,34,35,37

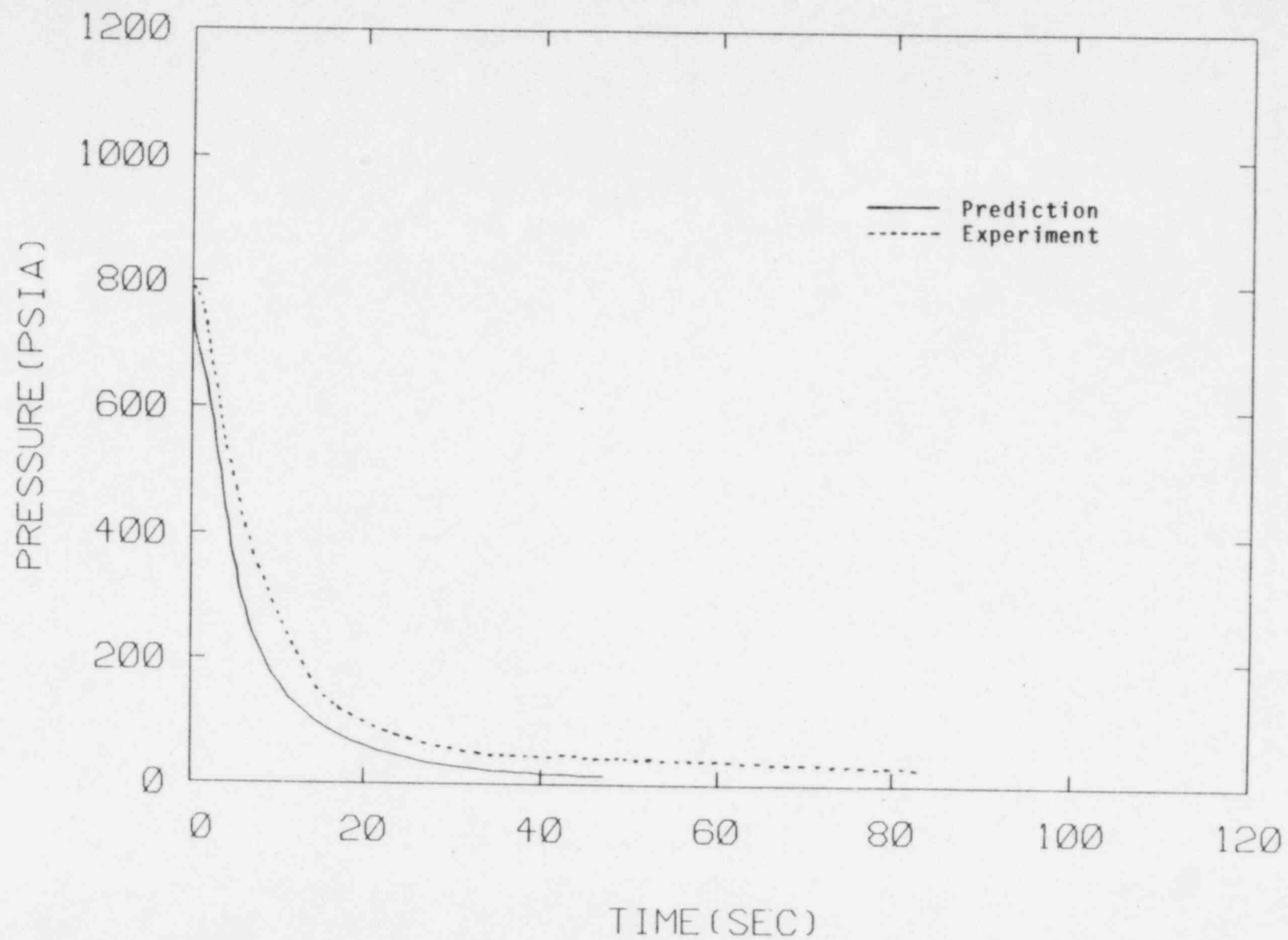


Figure 51. Comparison Between the Measured and Predicted Pressure for MIT Test Run 7, 3/8" Break

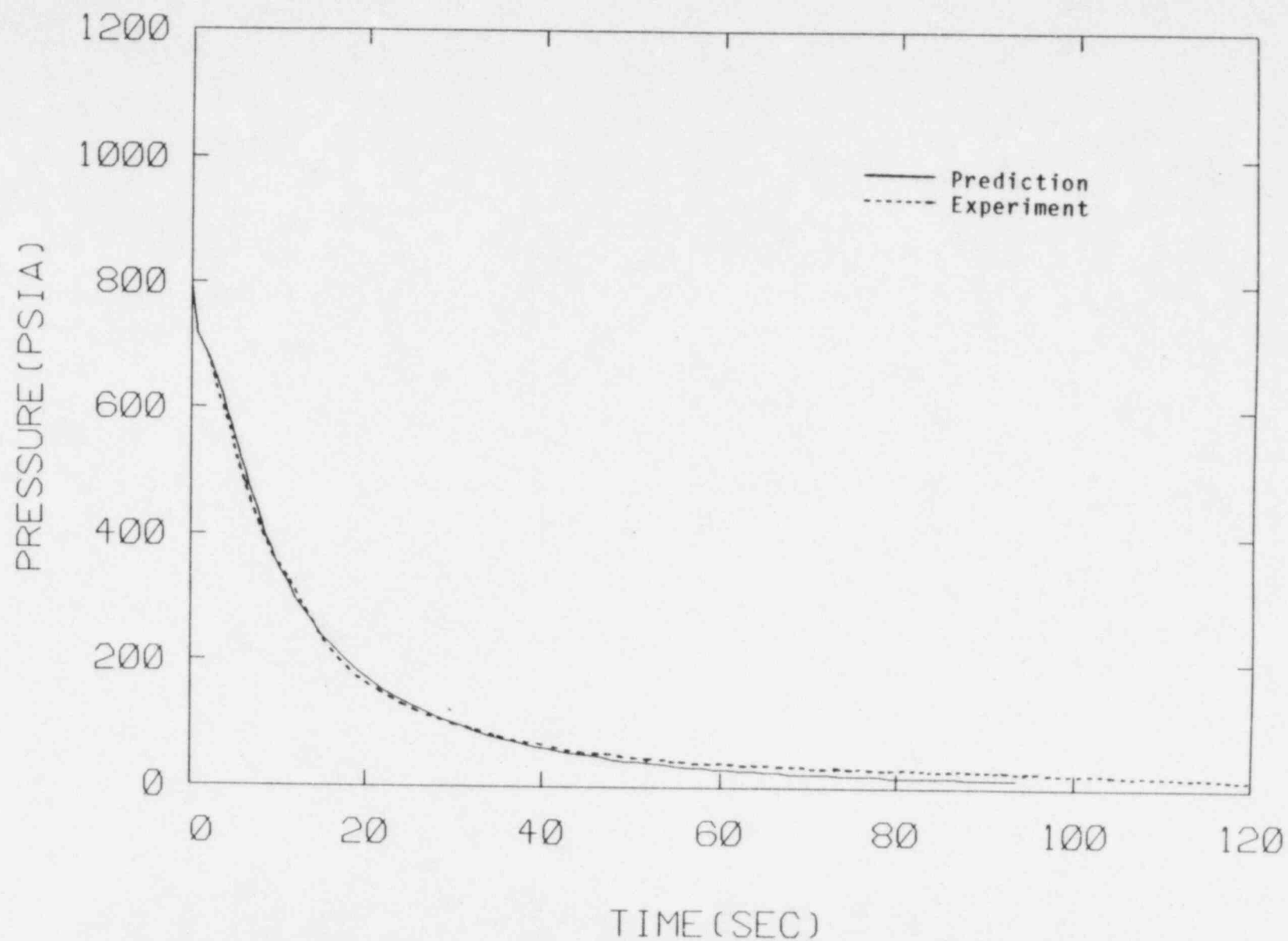


Figure 52. Comparison Between the Measured and Predicted Pressure for MIT Test Run 11, 1/4" Break

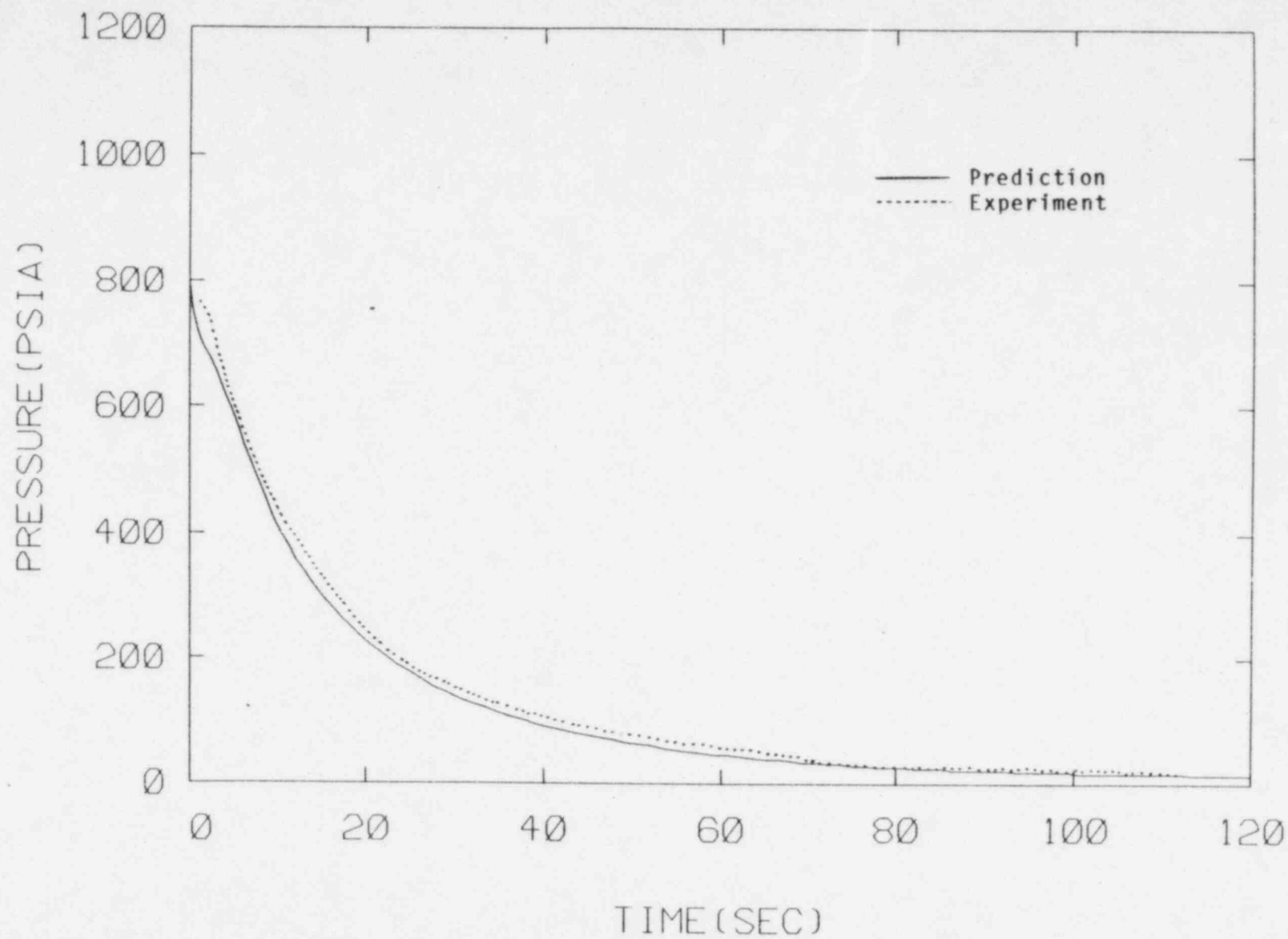


Figure 53. Comparison Between the Measured and Predicted Pressure for MIT Test Run 22, 1/8" Break

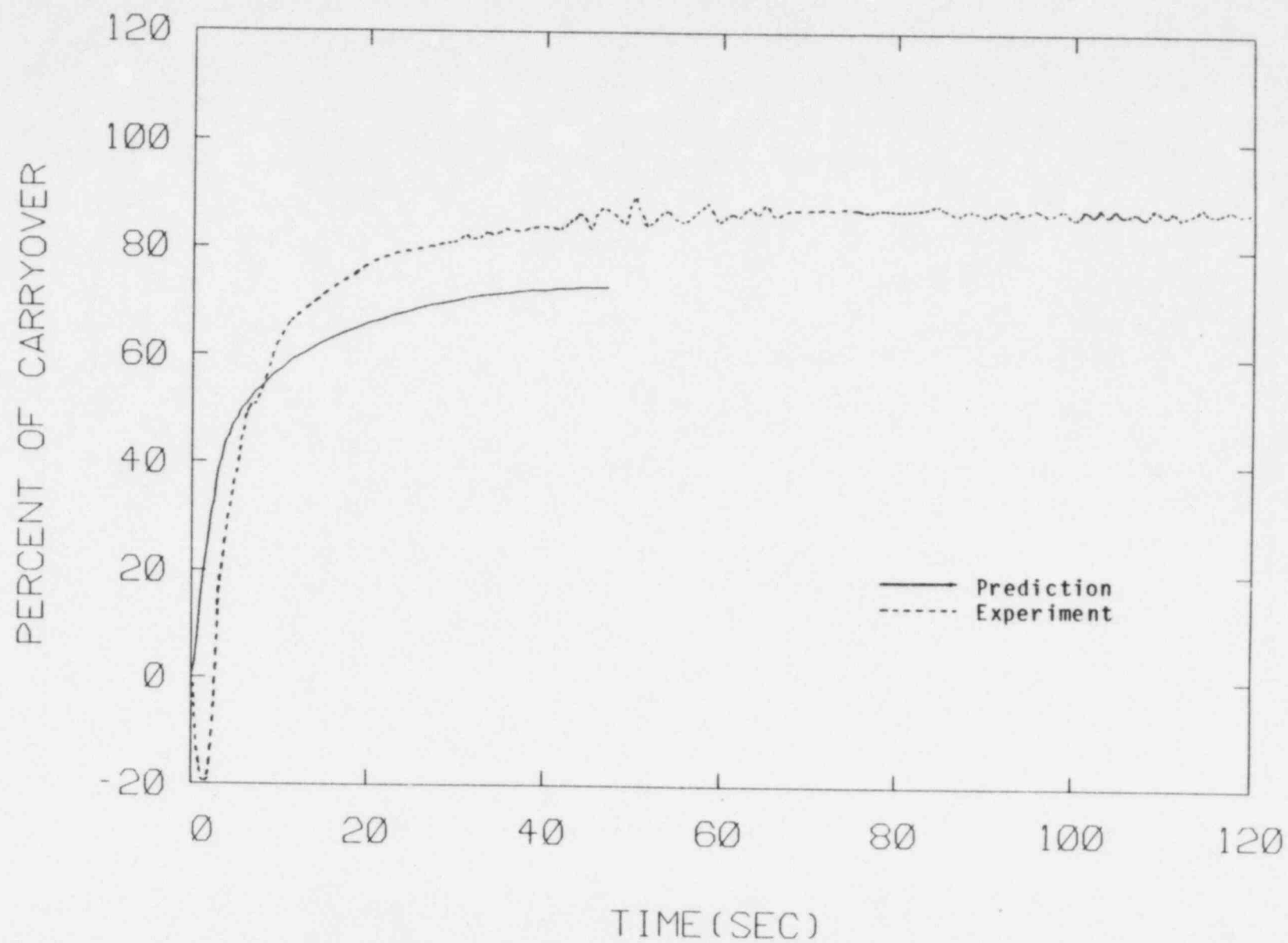


Figure 54. Comparison Between the Measured and Predicted Carryover for MIT Test Run 7, 3/8" Break

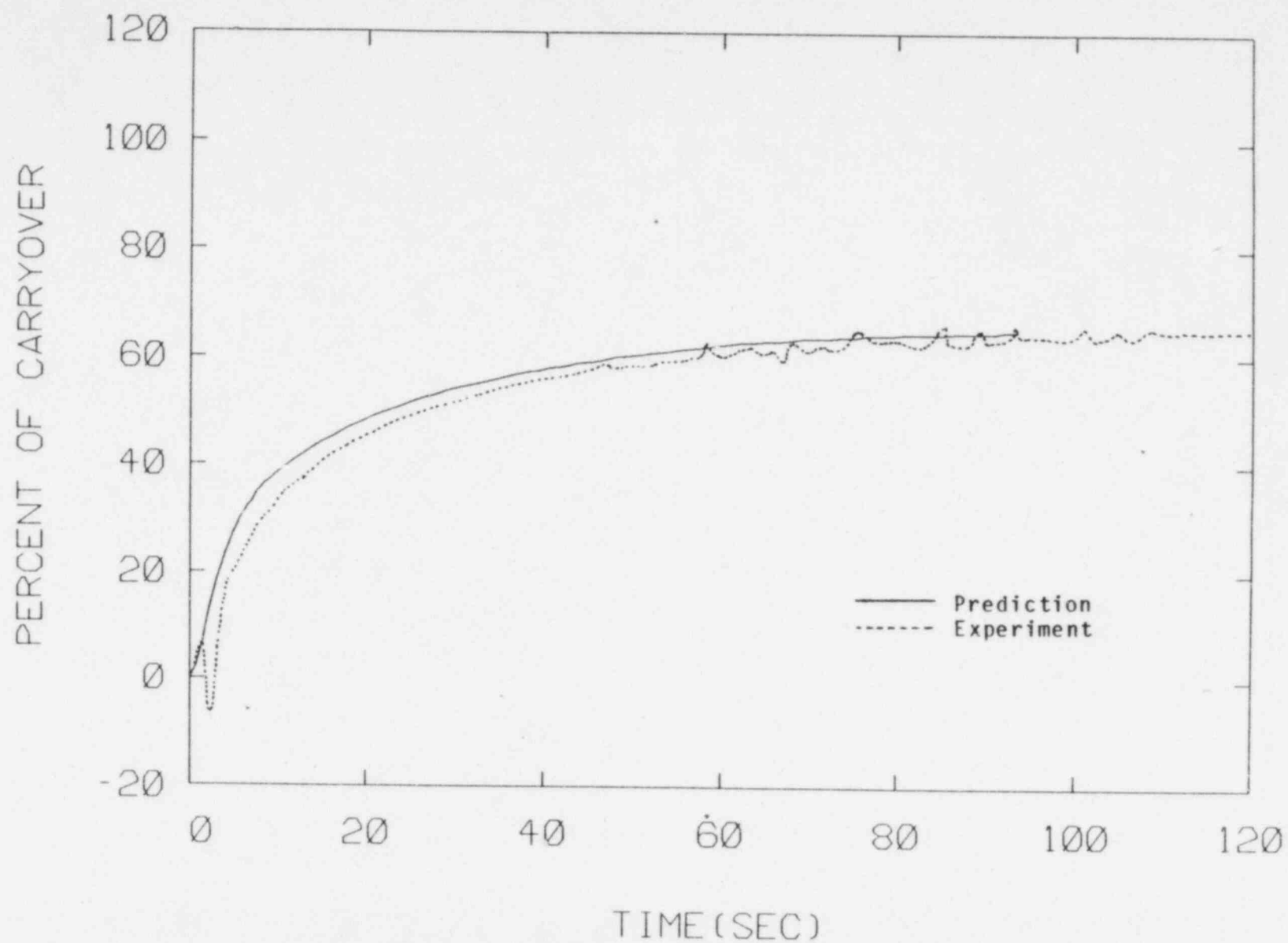


Figure 55. Comparison Between the Measured and Predicted Carryover for MIT Test Run 11, 1/4" Break

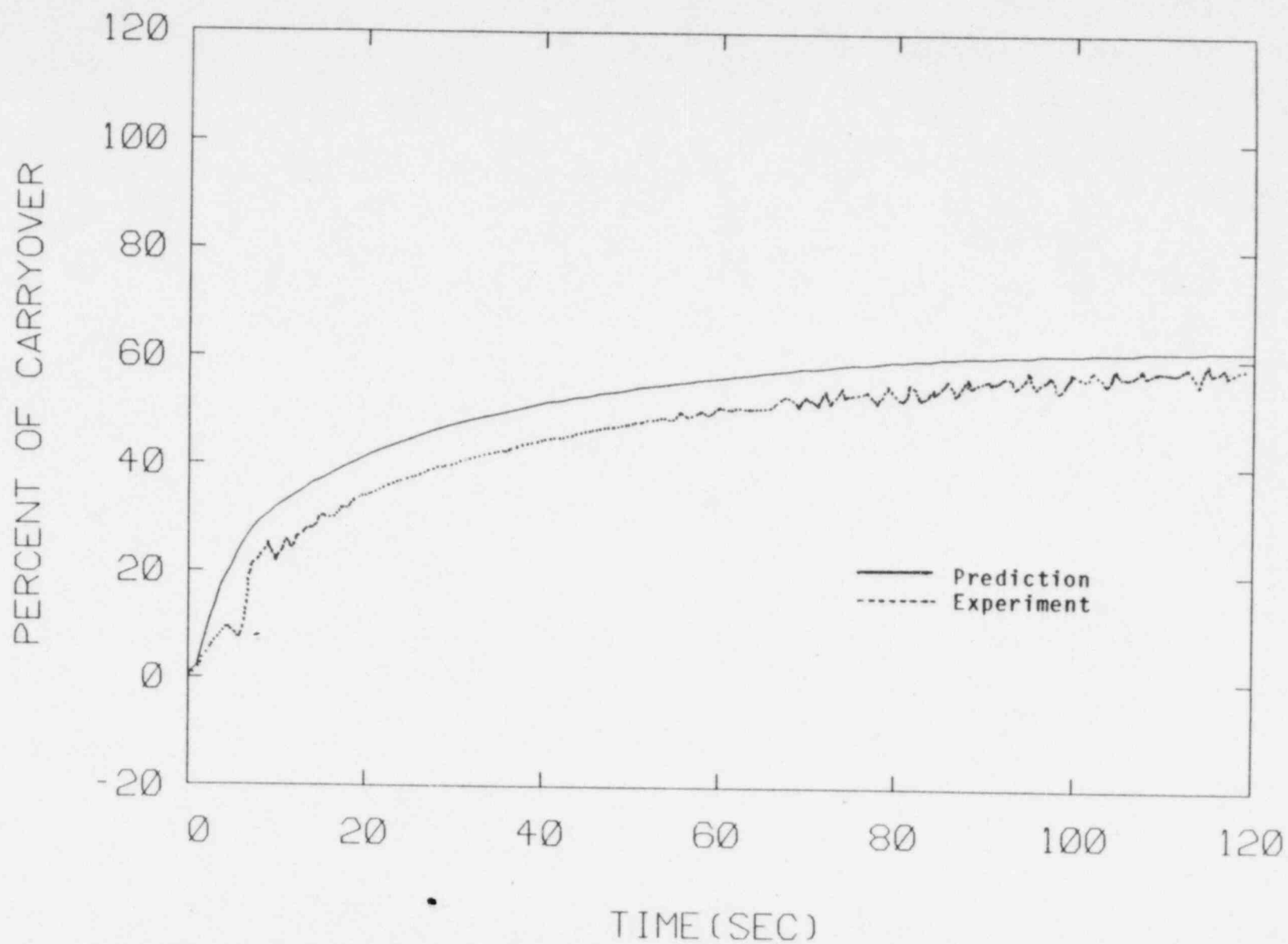


Figure 56. Comparison Between the Measured and Predicted Carryover for MIT Test Run 22, 1/8" Break

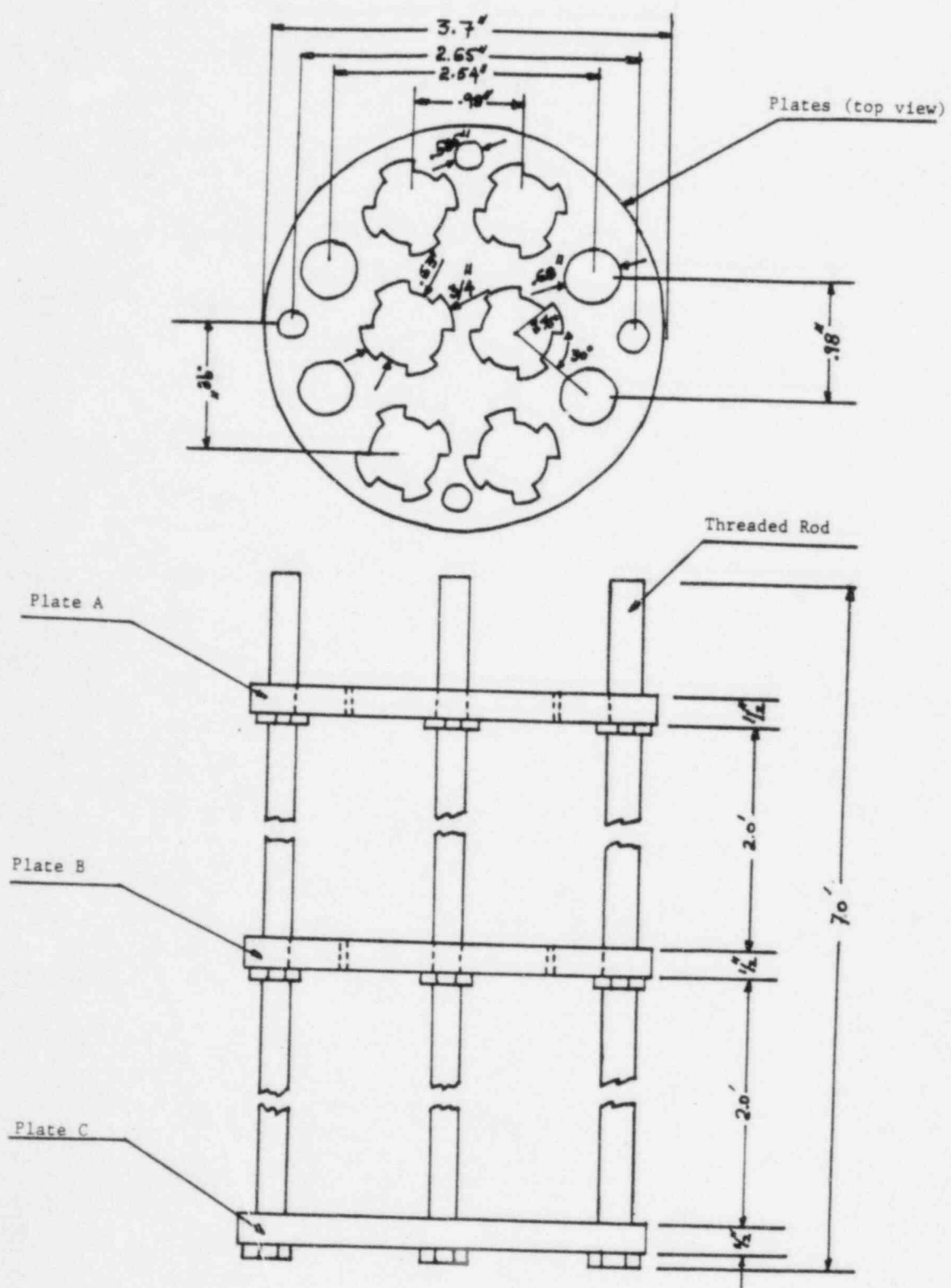


Figure 57. Schematic of the Tube Support Plates

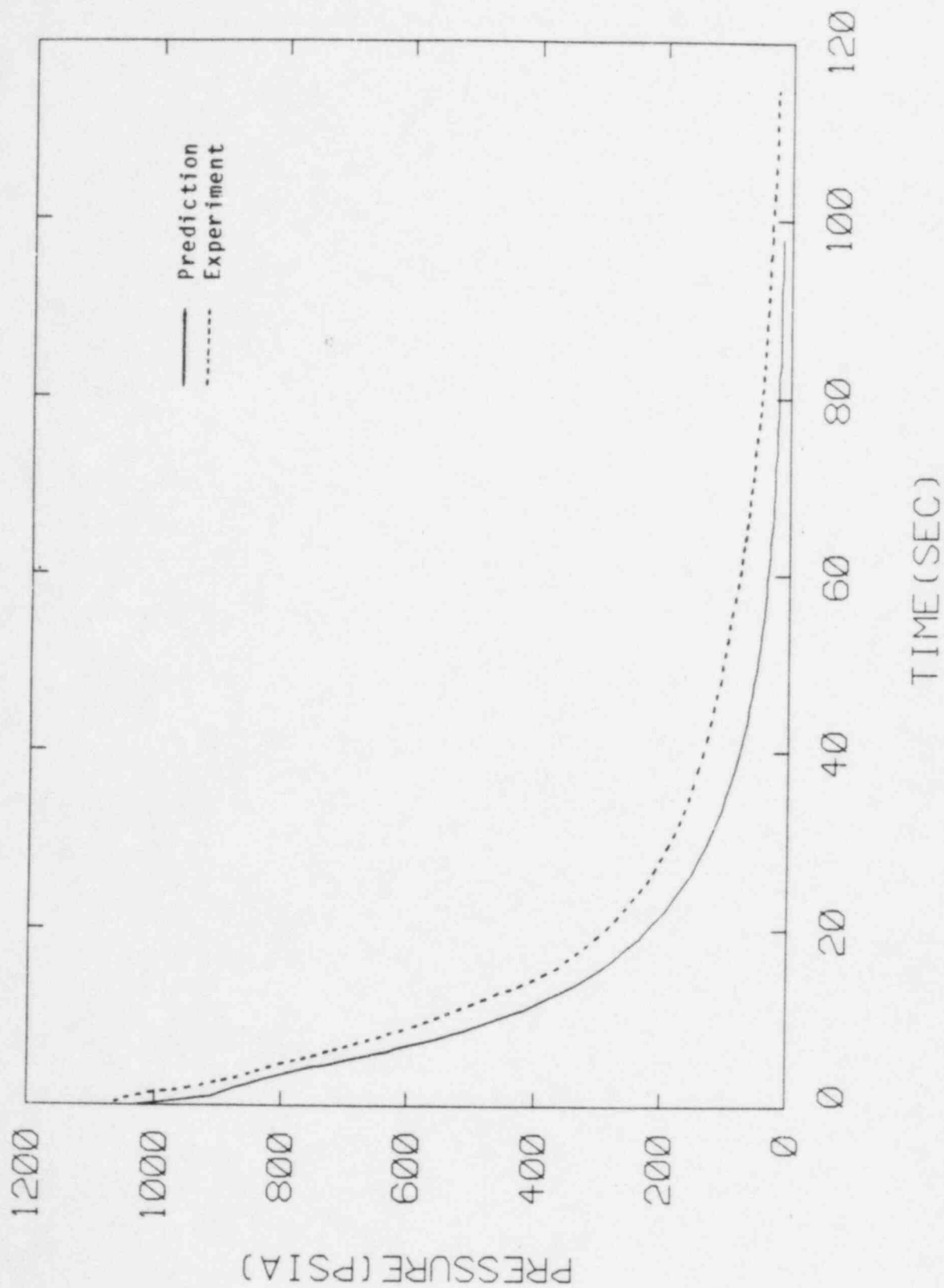


Figure 58. Comparison Between the Measured and Predicted Pressure for MIT Test Run 48, 1/8" Break

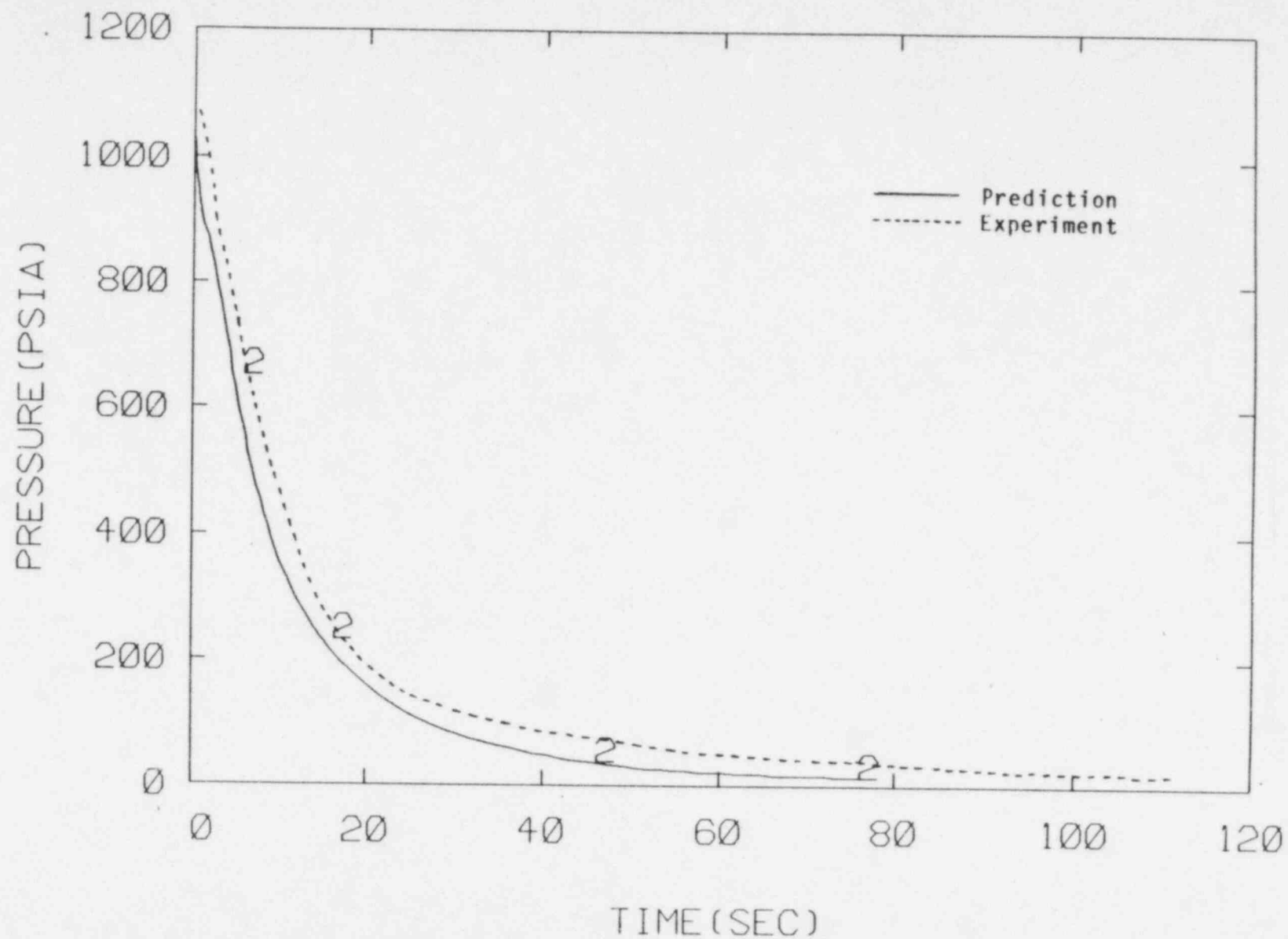


Figure 59. Comparison Between the Measured and Predicted Pressure for MIT Test Run 49, 1/4" Break

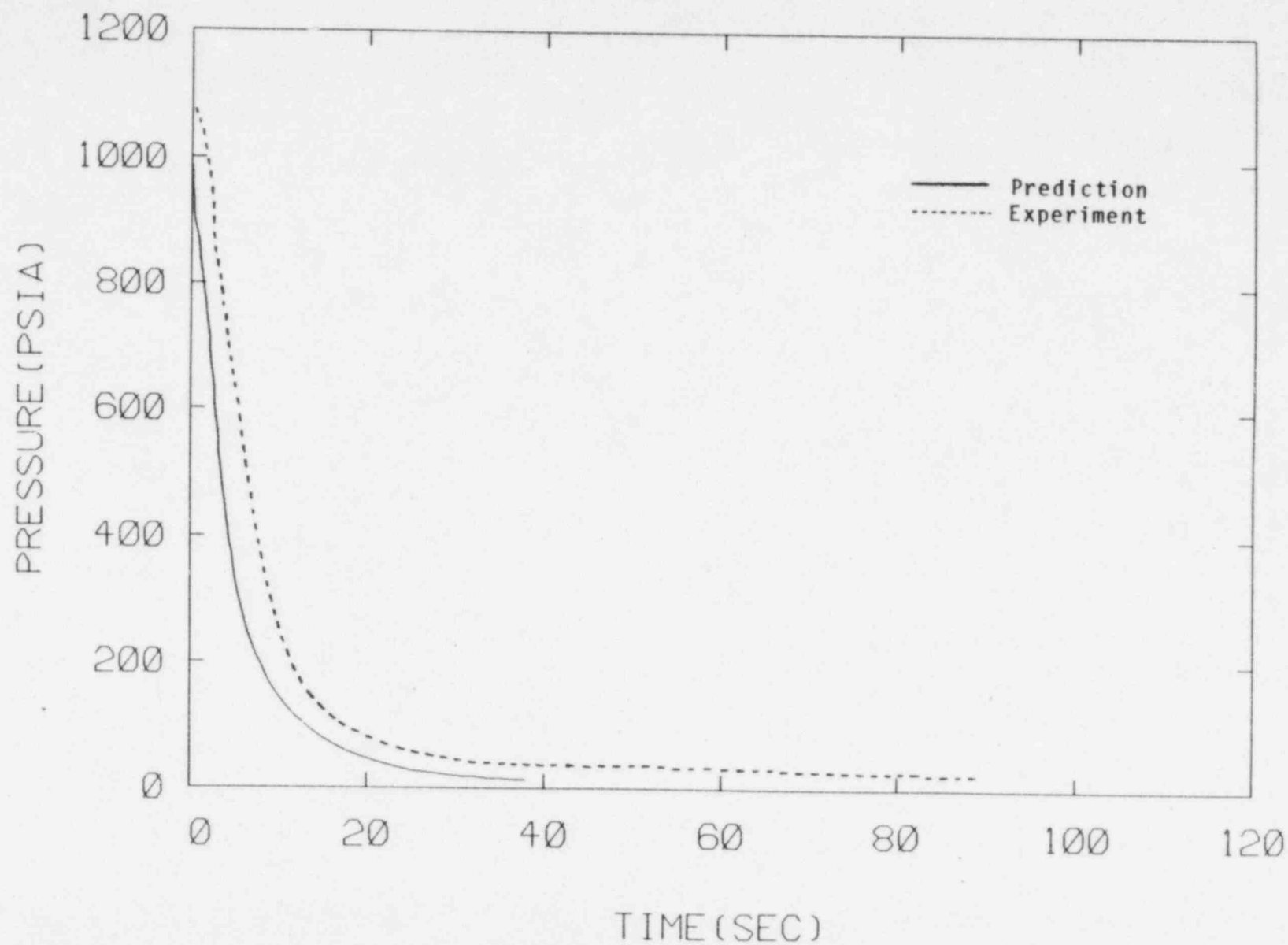


Figure 60. Comparison Between the Measured and Predicted Pressure for MIT Test Run 50, 3/8" Break

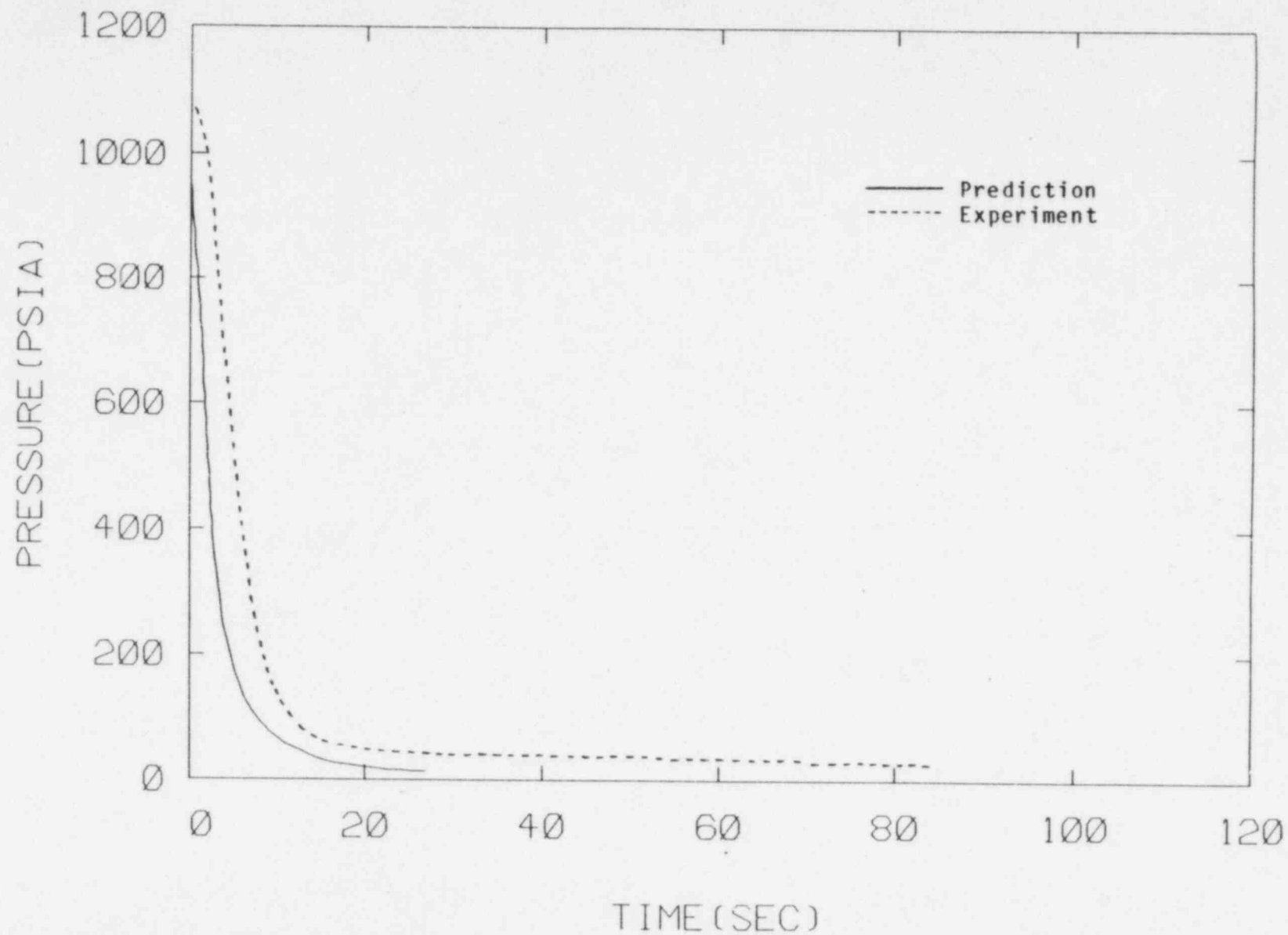


Figure 61. Comparison Between the Measured and Predicted Pressure for MIT Test Run 51, 1/2" Break

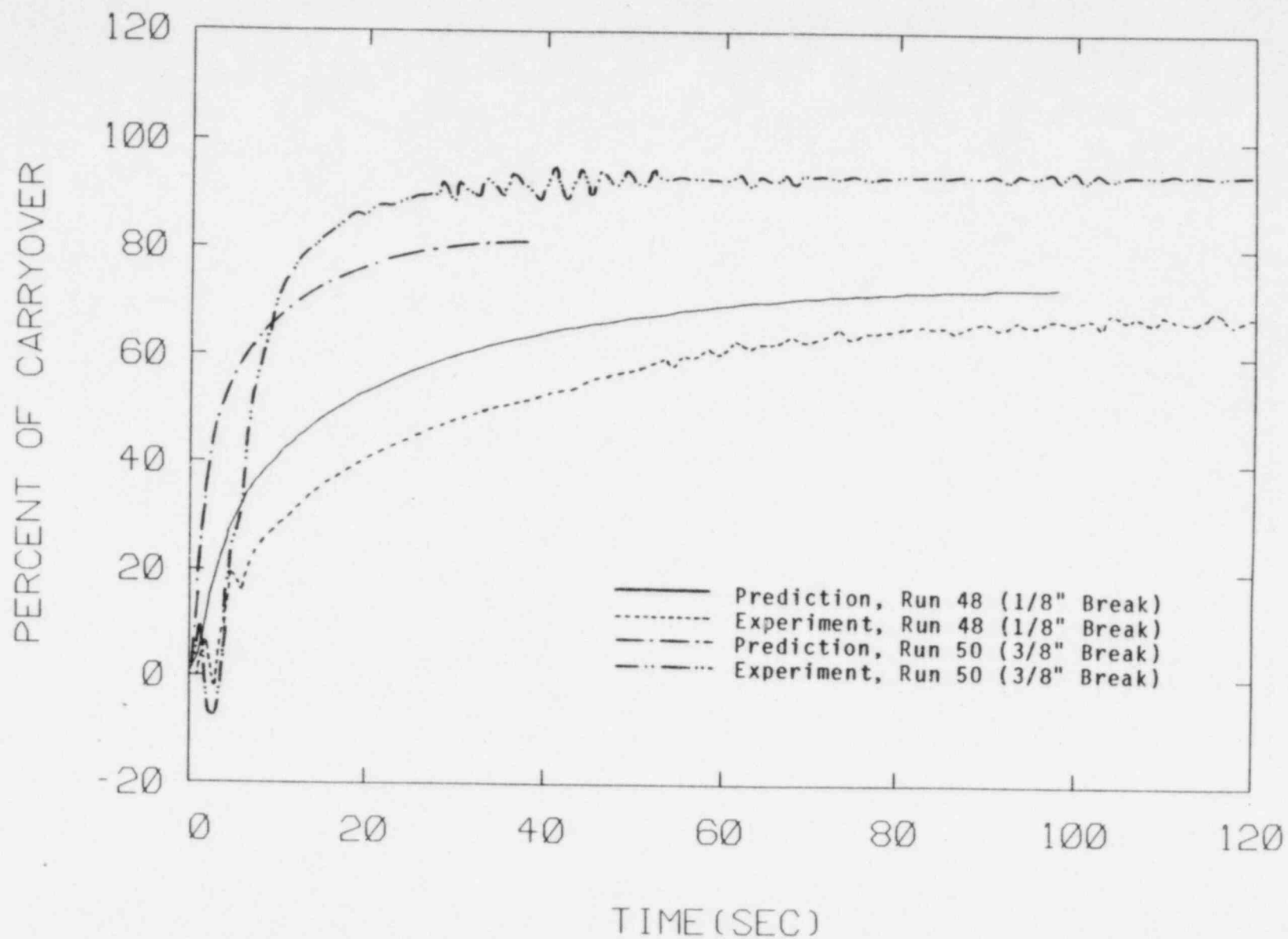


Figure 62. Comparison Between the Measured and Predicted Carryover for MIT Test Run 48,50

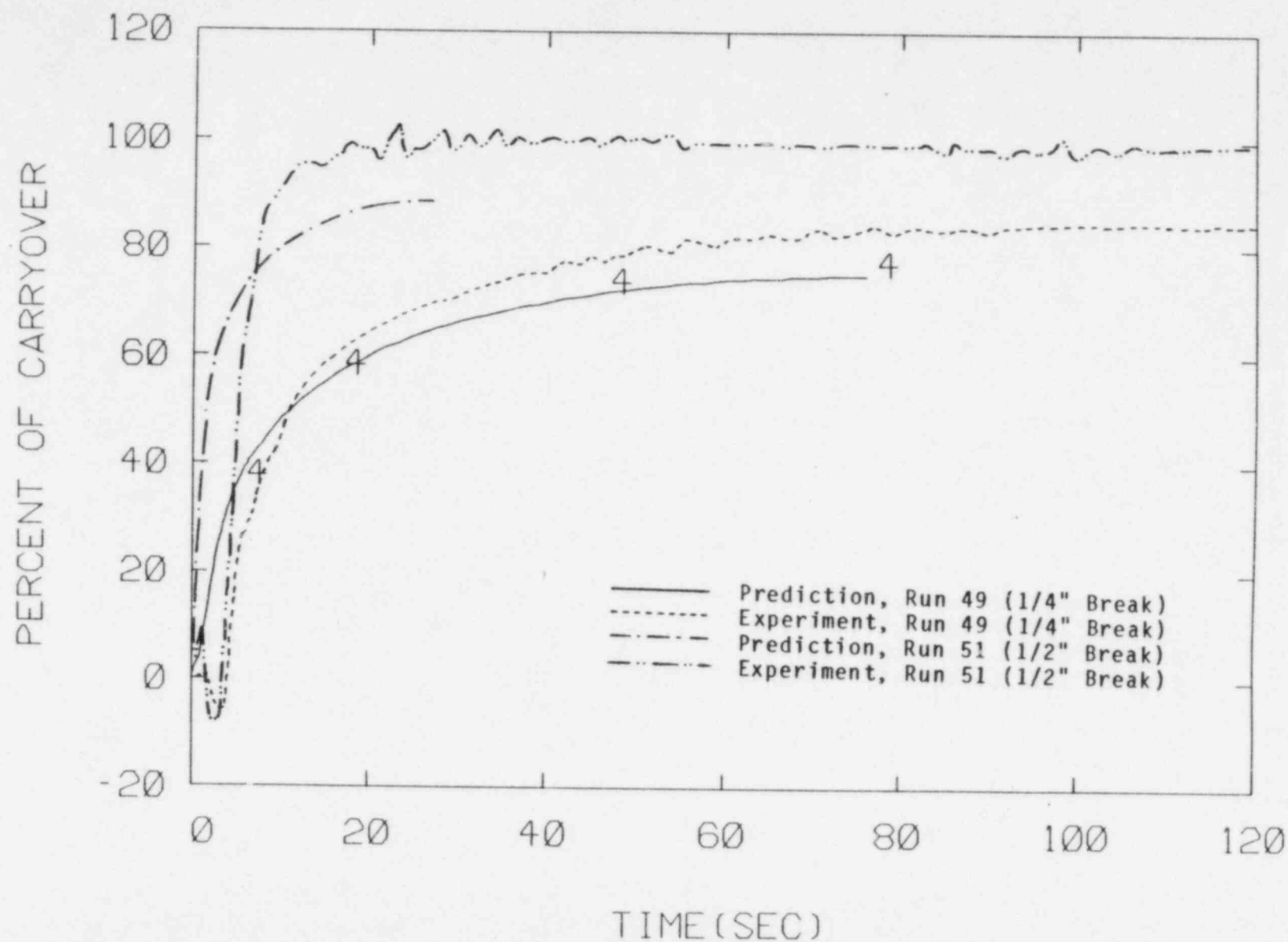


Figure 63. Comparison Between the Measured and Predicted Carryover for MIT Test Run 49,51

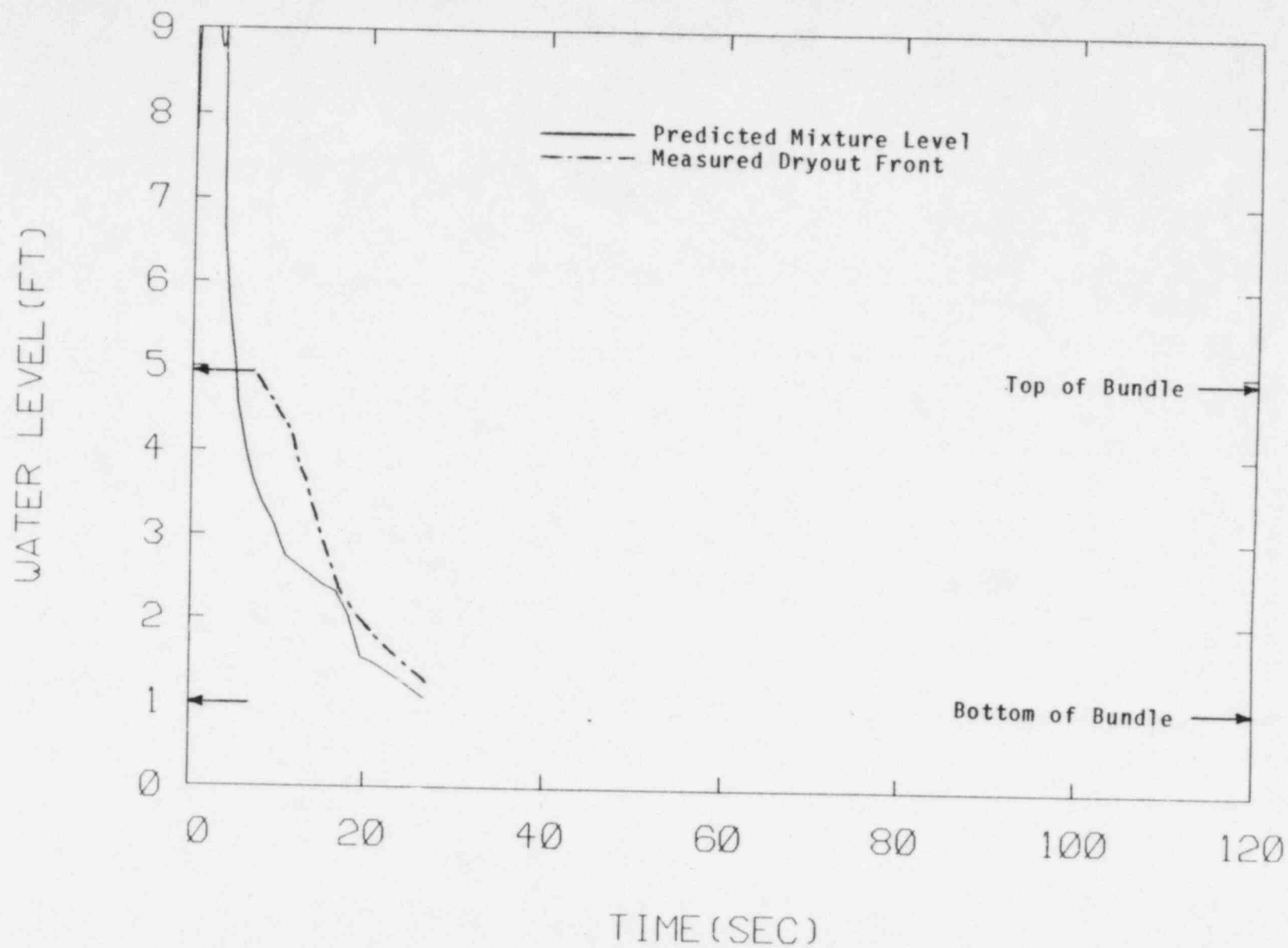


Figure 64. Comparison Between the Predicted Mixture Level and the Measured Dryout Front for MIT Test Run 51, 1/2" Break

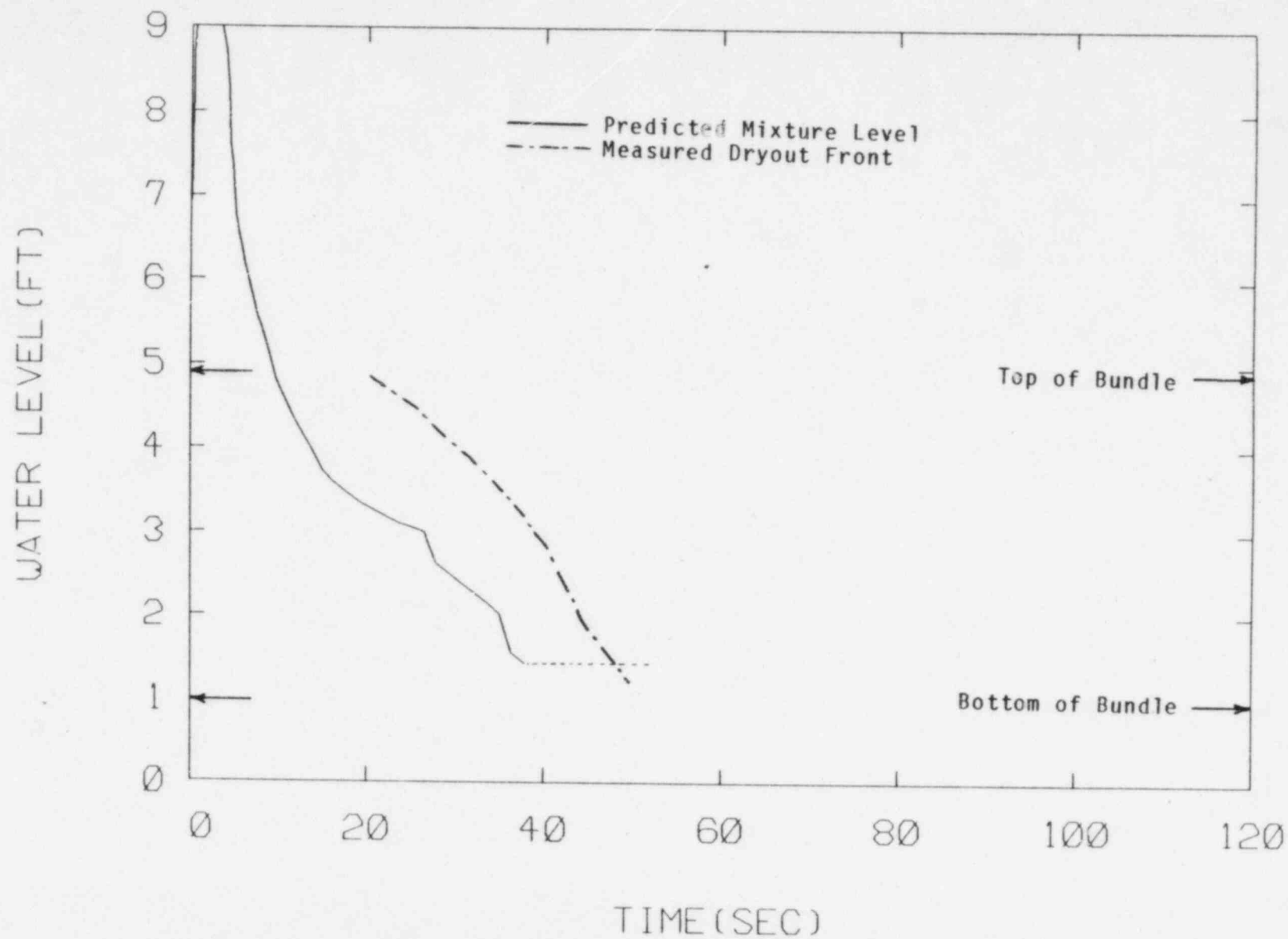


Figure 65. Comparison Between the Predicted Mixture Level and the Measured Dryout Front for MIT Test Run 50, 3/8" Break

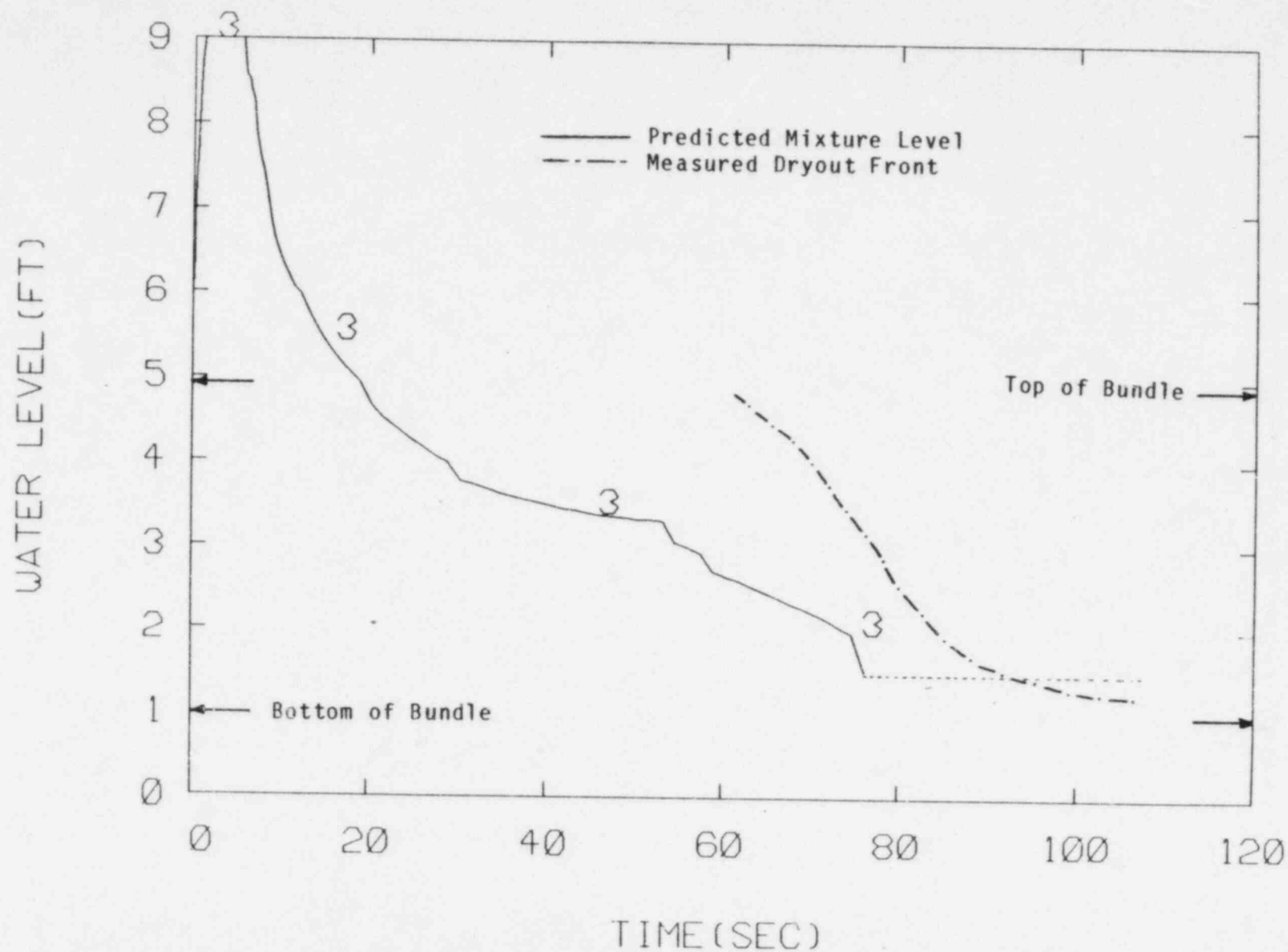


Figure 66. Comparison Between the Predicted Mixture Level and the Measured Dryout Front for MIT Test Run 49, 1/4" Break

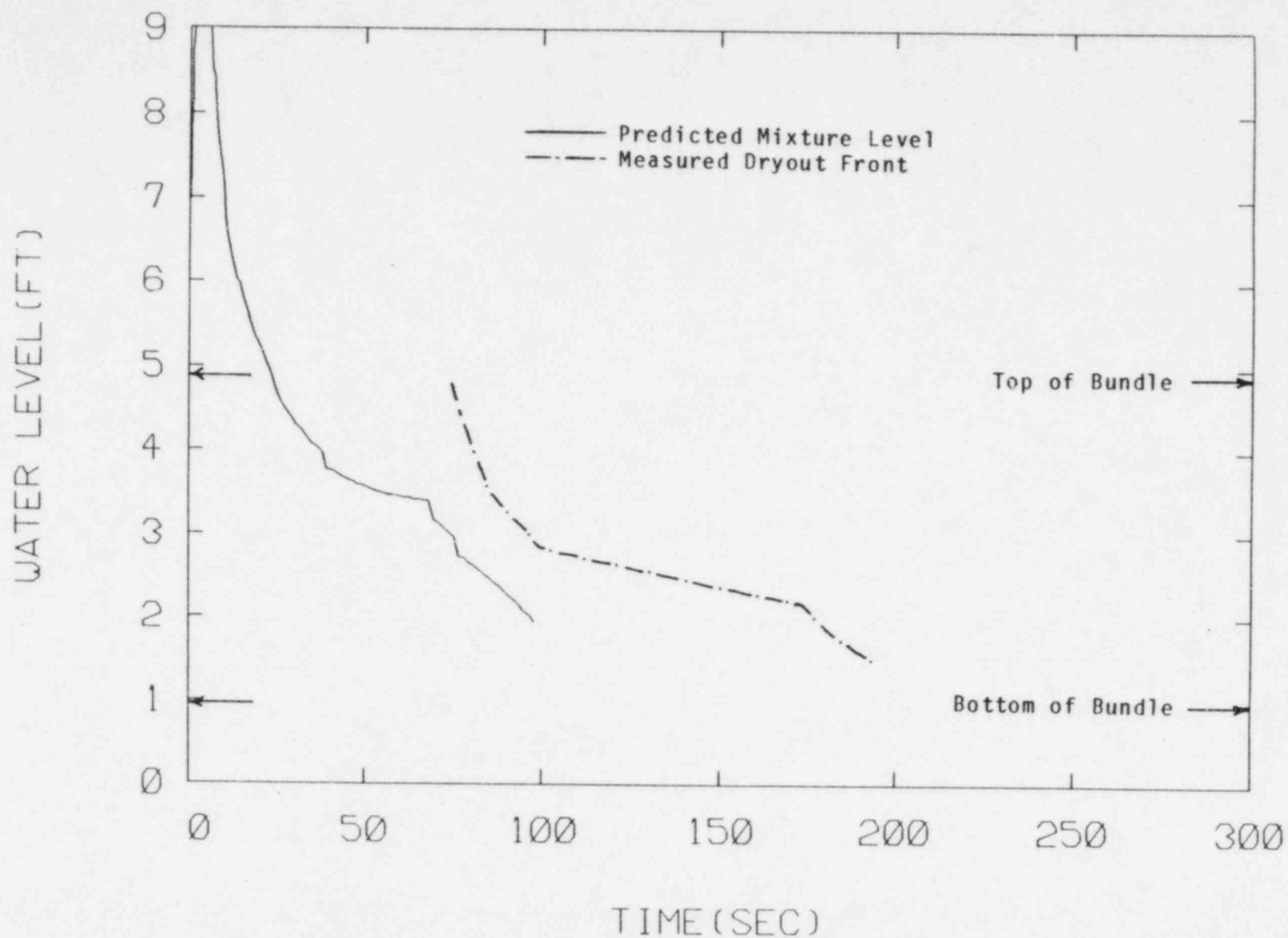


Figure 67. Comparison Between the Predicted Mixture Level and the Measured Dryout Front for MIT Test Run 48, 1/8" Break

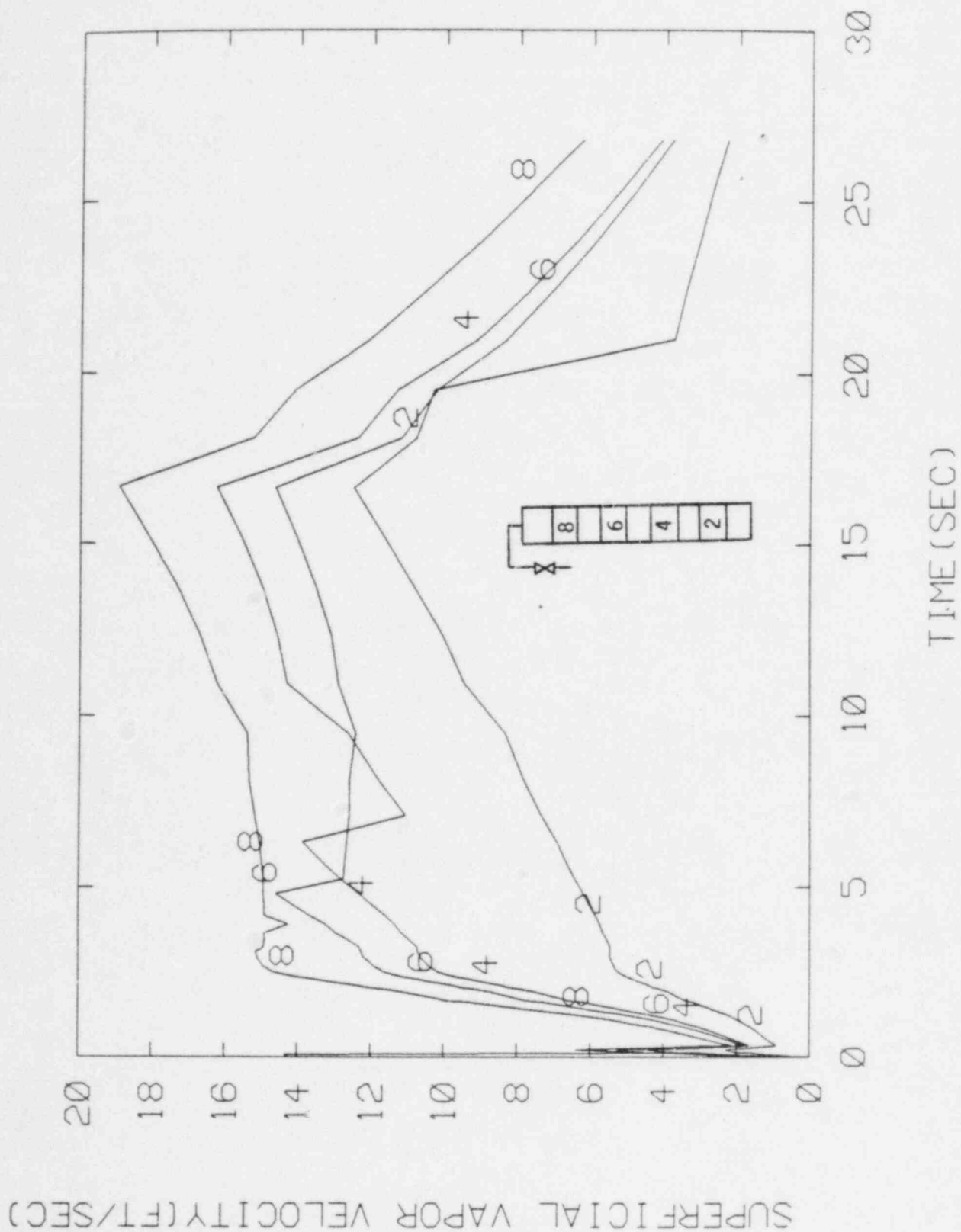


Figure 68. The Calculated Superficial Vapor Velocity for MIT Test Run 51, 1 1/2" Break

SUPERFICIAL VAPOR VELOCITY (FT/SEC)

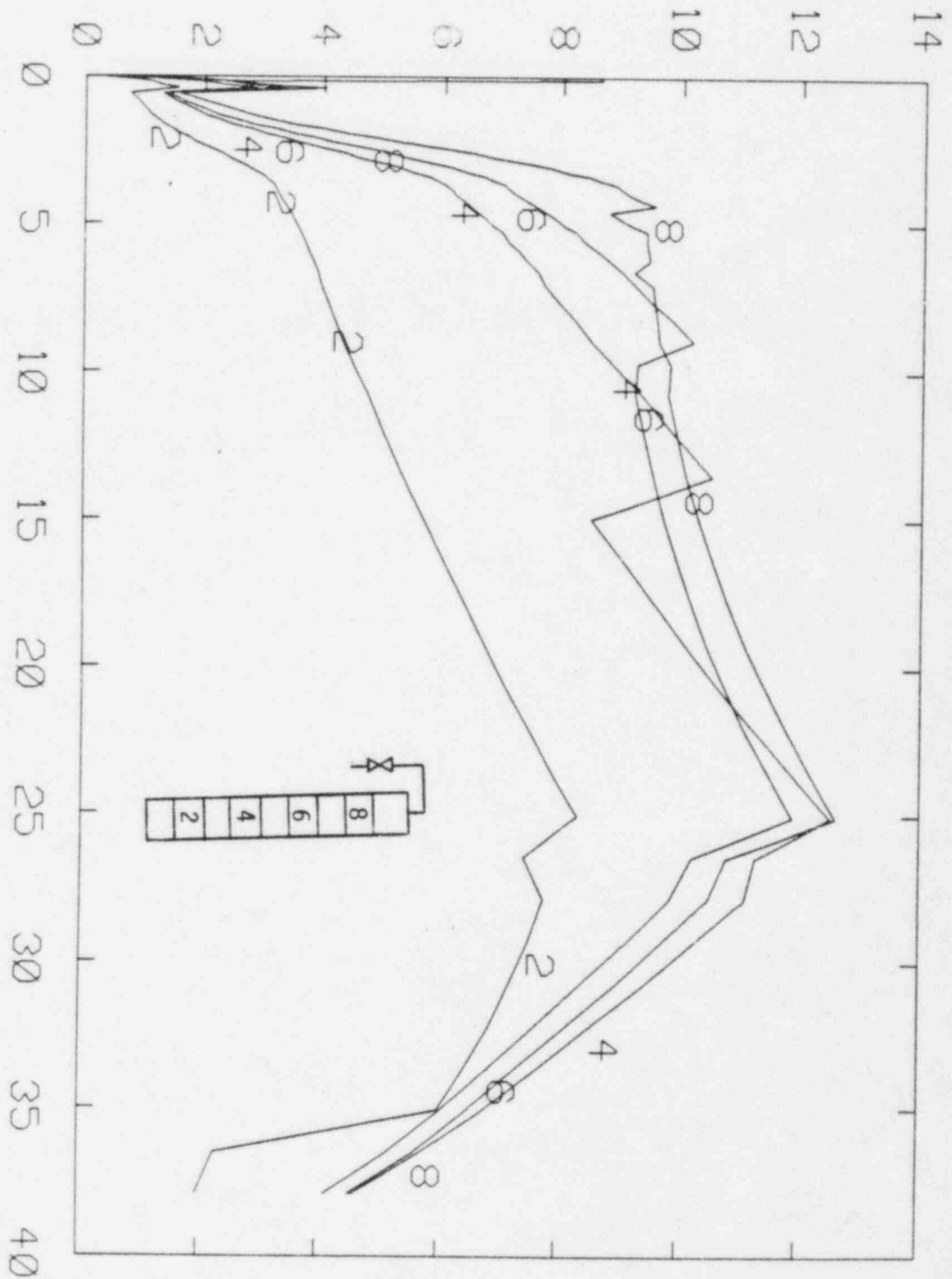


Figure 69. The Calculated Superficial Vapor Velocity for MIT Test Run 50, 3/8" Break

SUPERFICIAL VAPOR VELOCITY (FT/SEC)

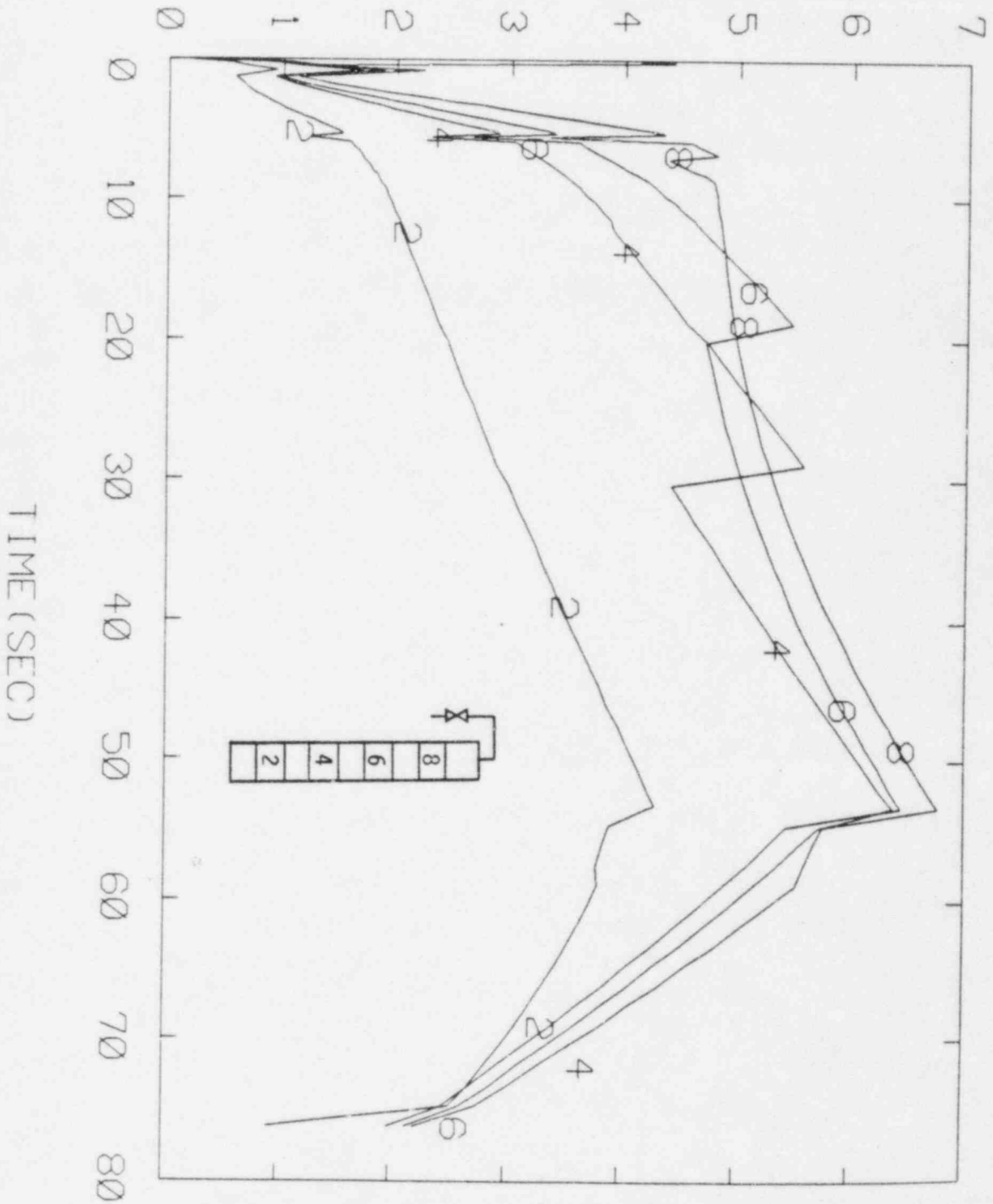


Figure 70. The Calculated Superficial Vapor Velocity for MIT Test Run 49, 1/4" Break

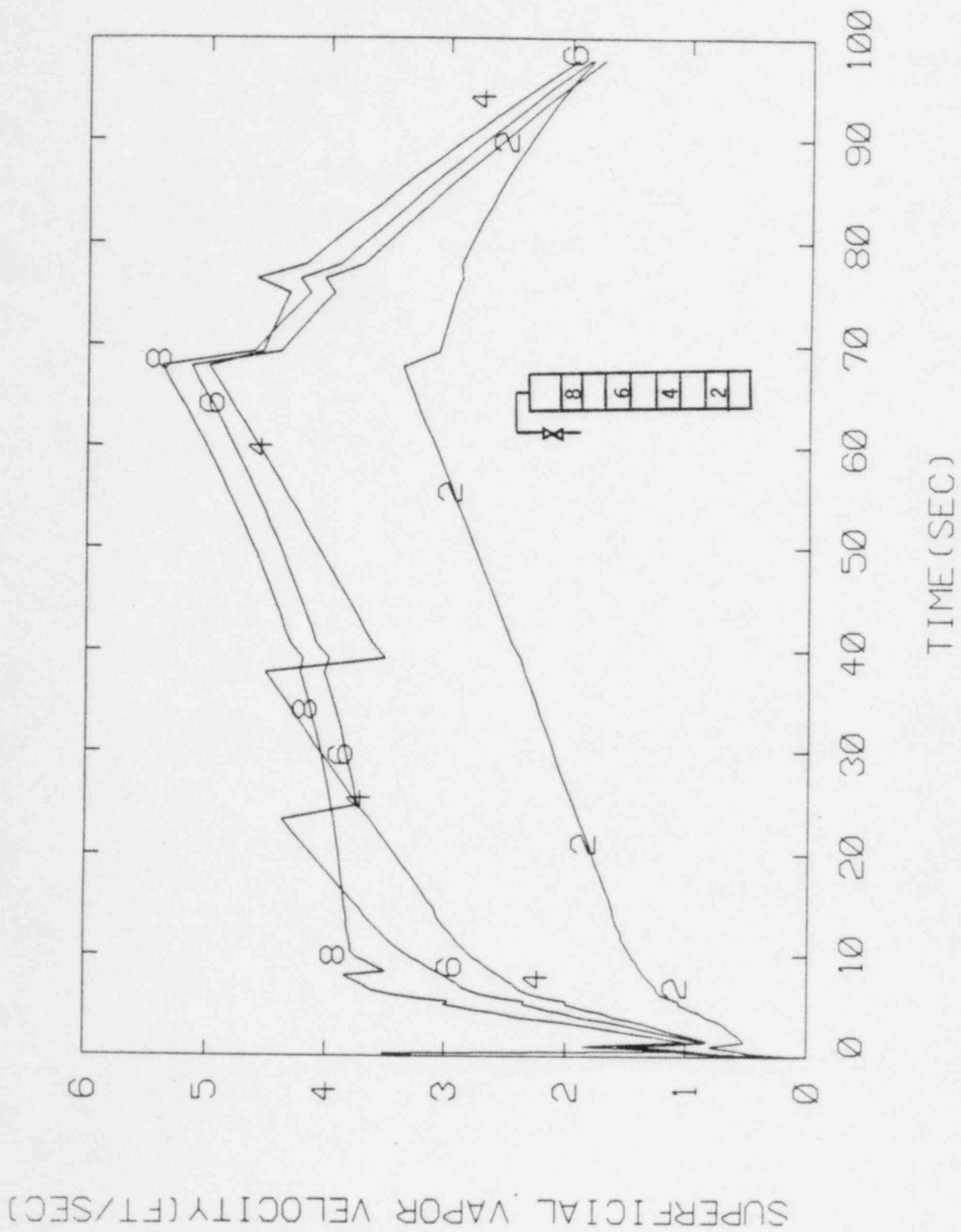


Figure 71. The Calculated Superficial Vapor Velocity for MIT Test Run 48, 1/8" Break

SUPERFICIAL LIQUID VELOCITY

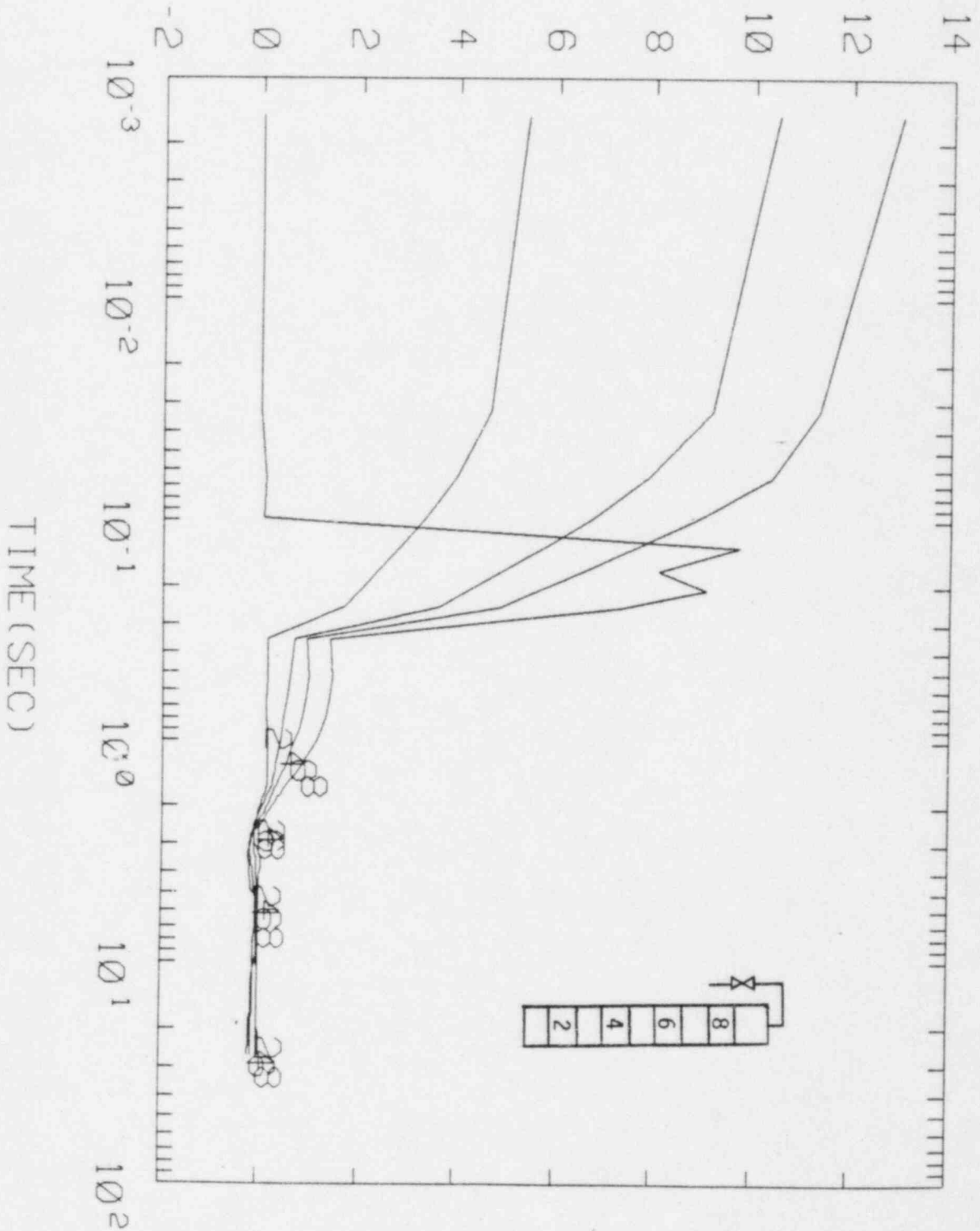


Figure 72. The Calculated Superficial Liquid Velocity for MIT Test Run 51, 1/2" Break

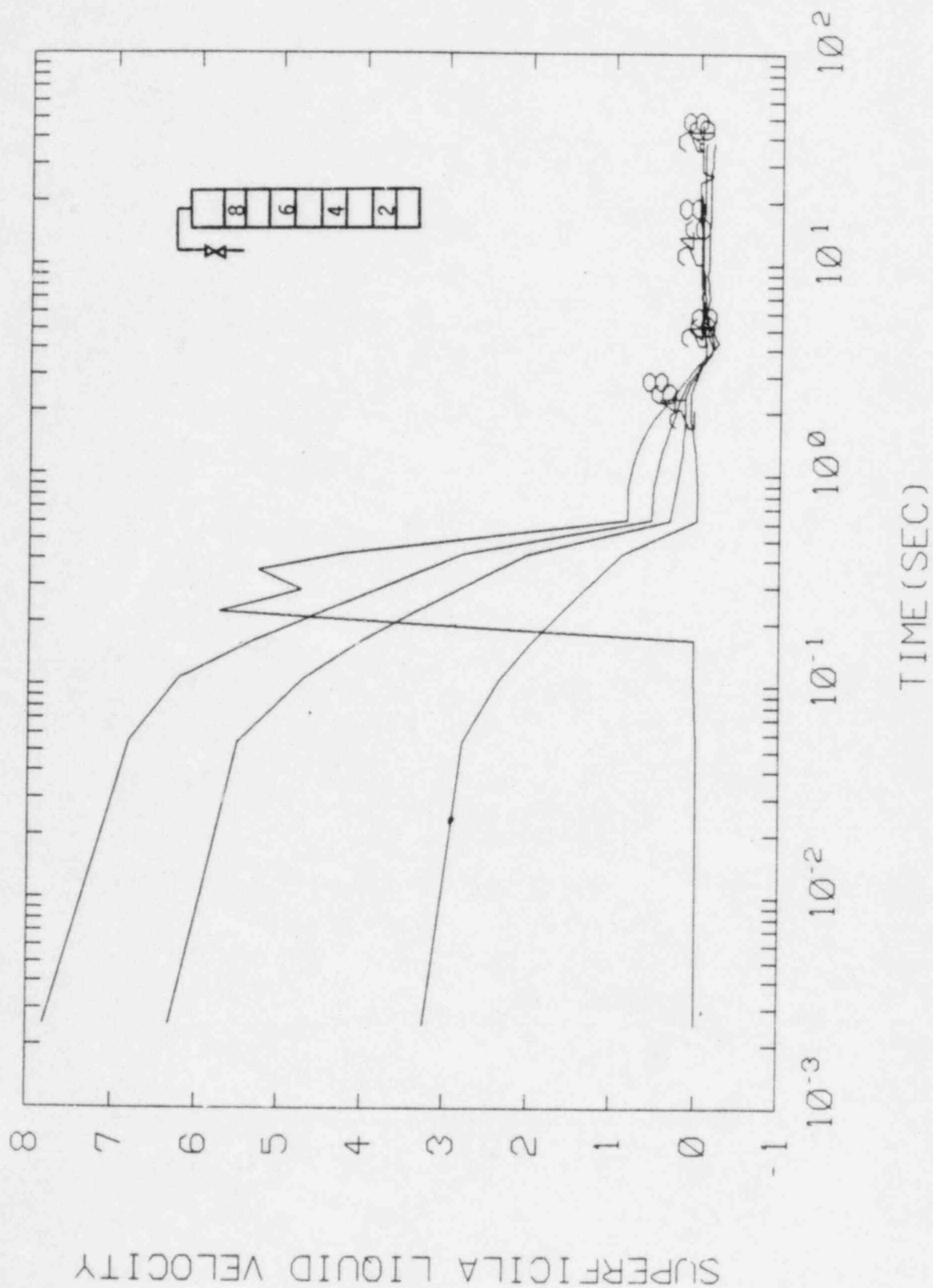


Figure 73. The Calculated Superficial Liquid Velocity for MIT Test Run 50, 3/8" Break

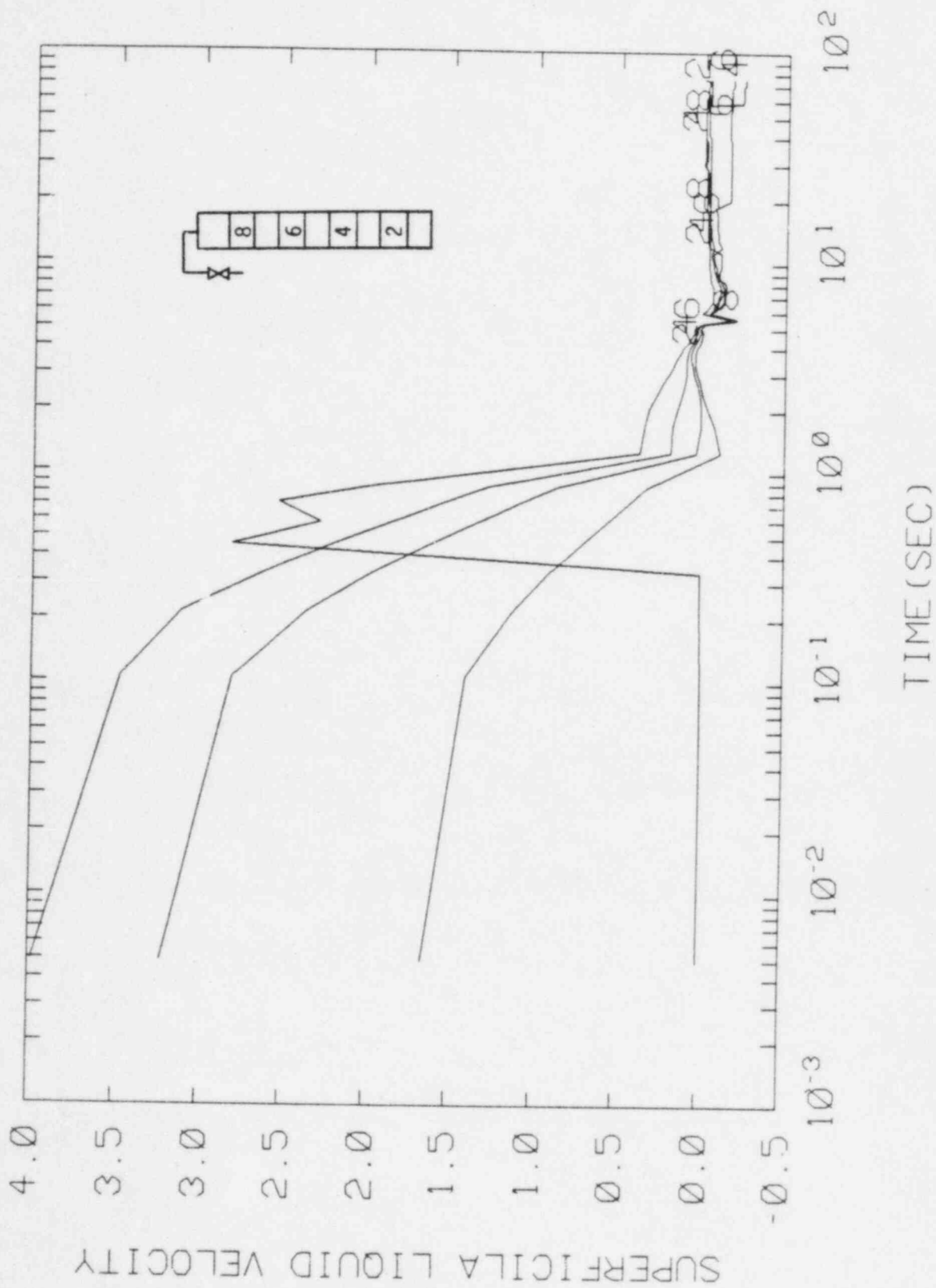


Figure 74. The Calculated Superficial Liquid Velocity for MIT Test Run 49, 1/4" Break

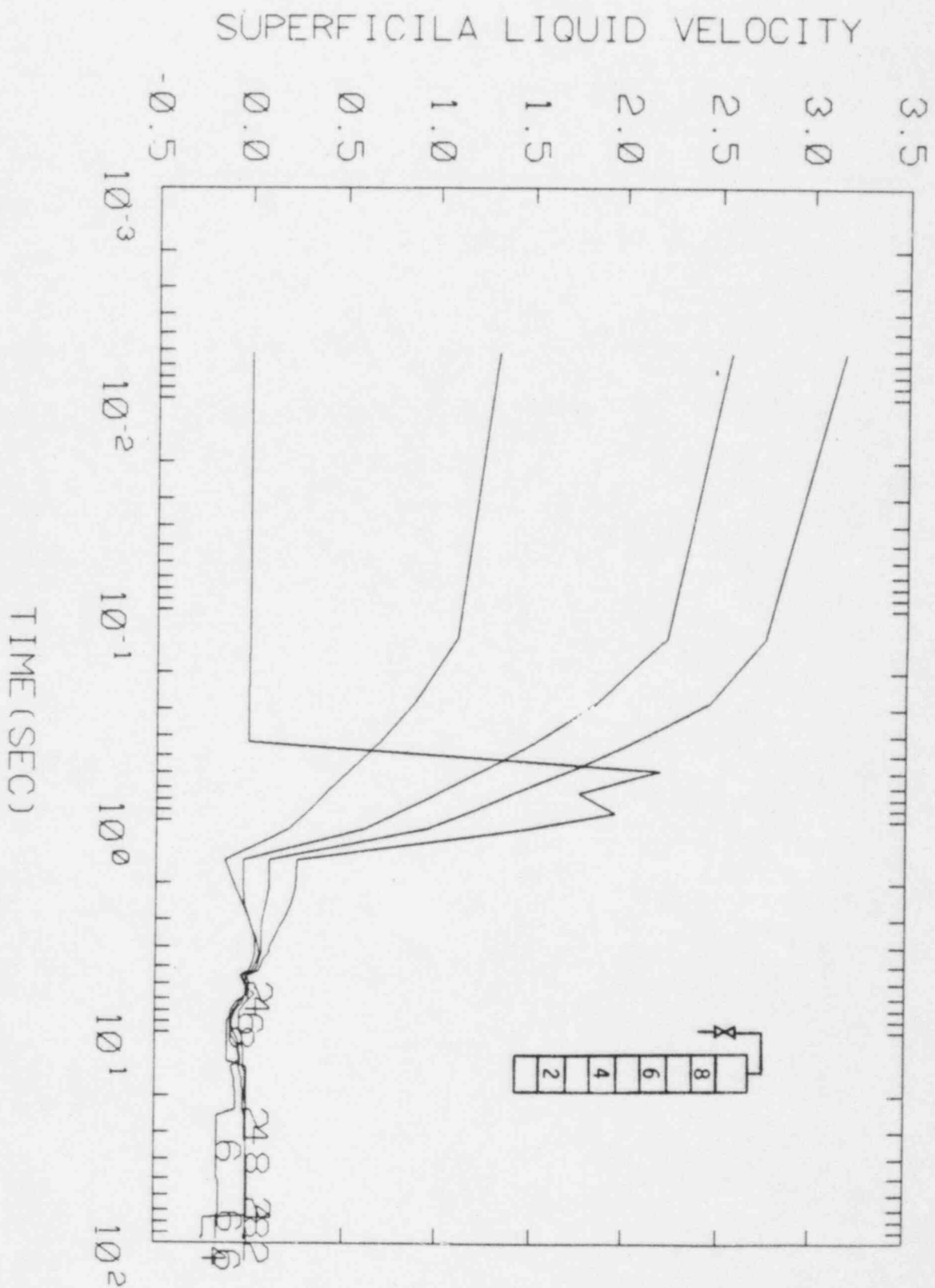


Figure 75. The Calculated Superficial Liquid Velocity for MIT Test Run 48, 1/8" Break

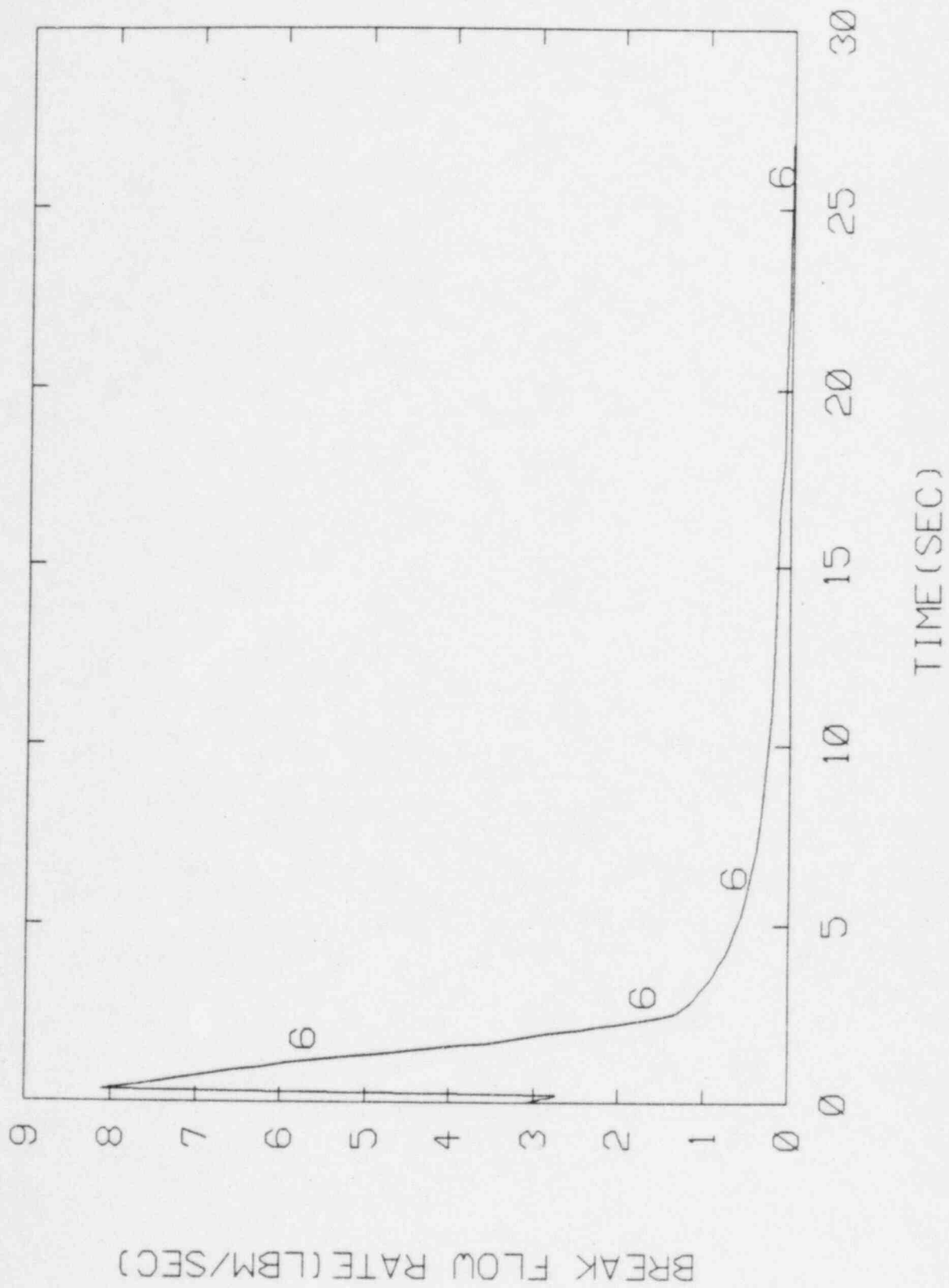


Figure 76. Calculated Break Flow Rate for MIT Test Run 51,
1/2" Break

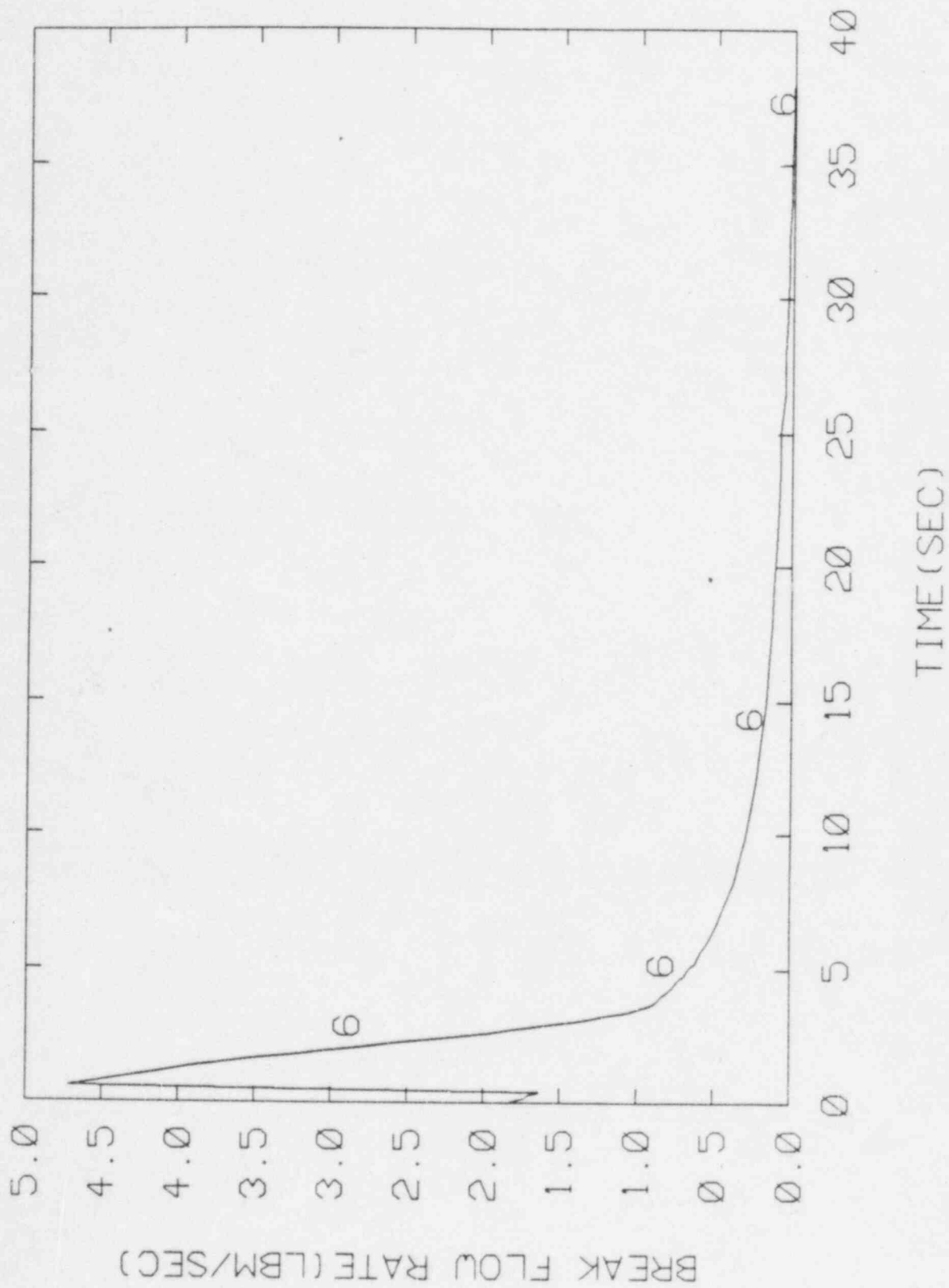


Figure 77. Calculated Break Flow Rate for MIT Test Run 50,
3/8" Break

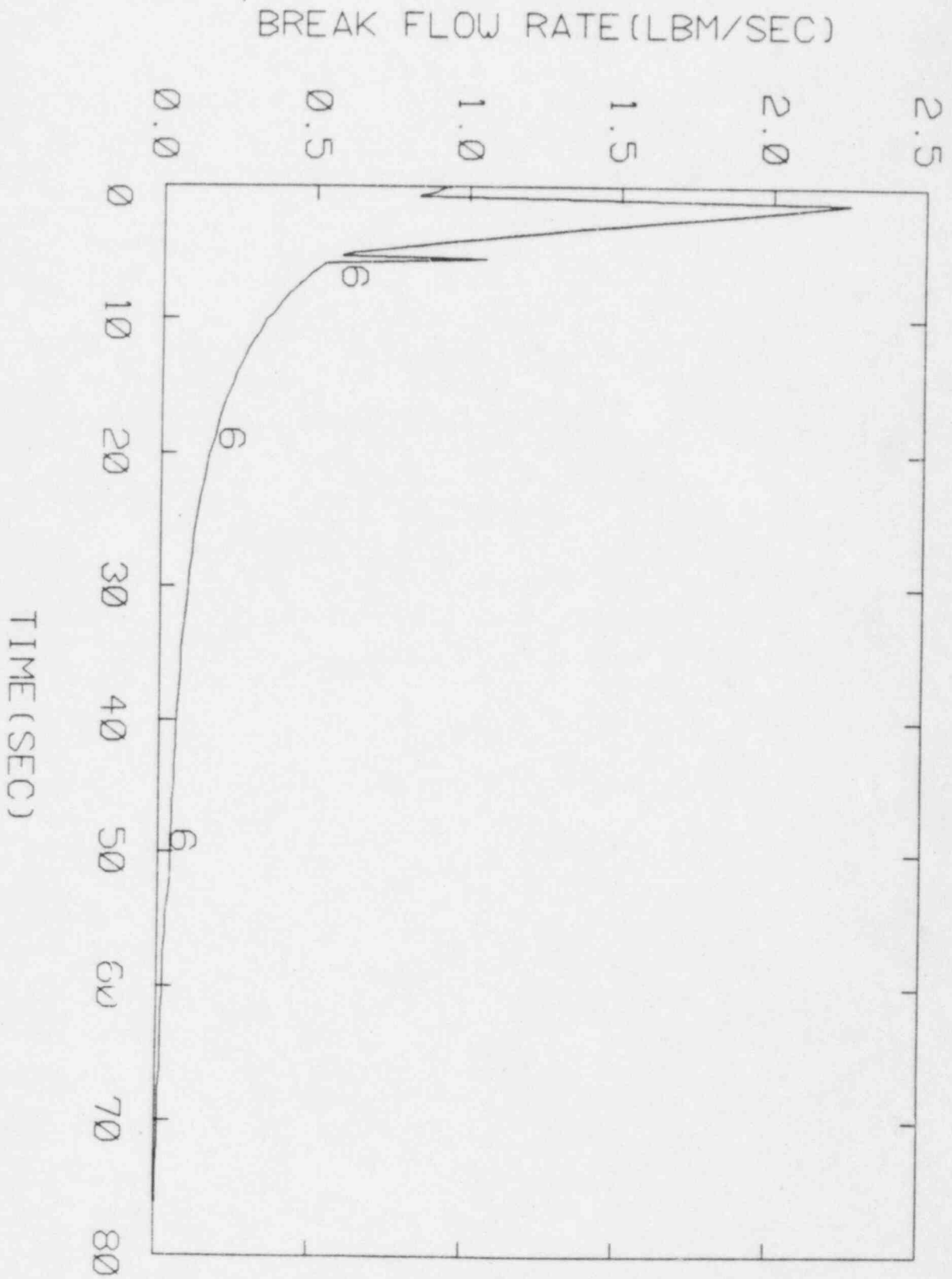


Figure 78. Calculated Break Flow Rate for MIT Test Run 49,
1/4" Break

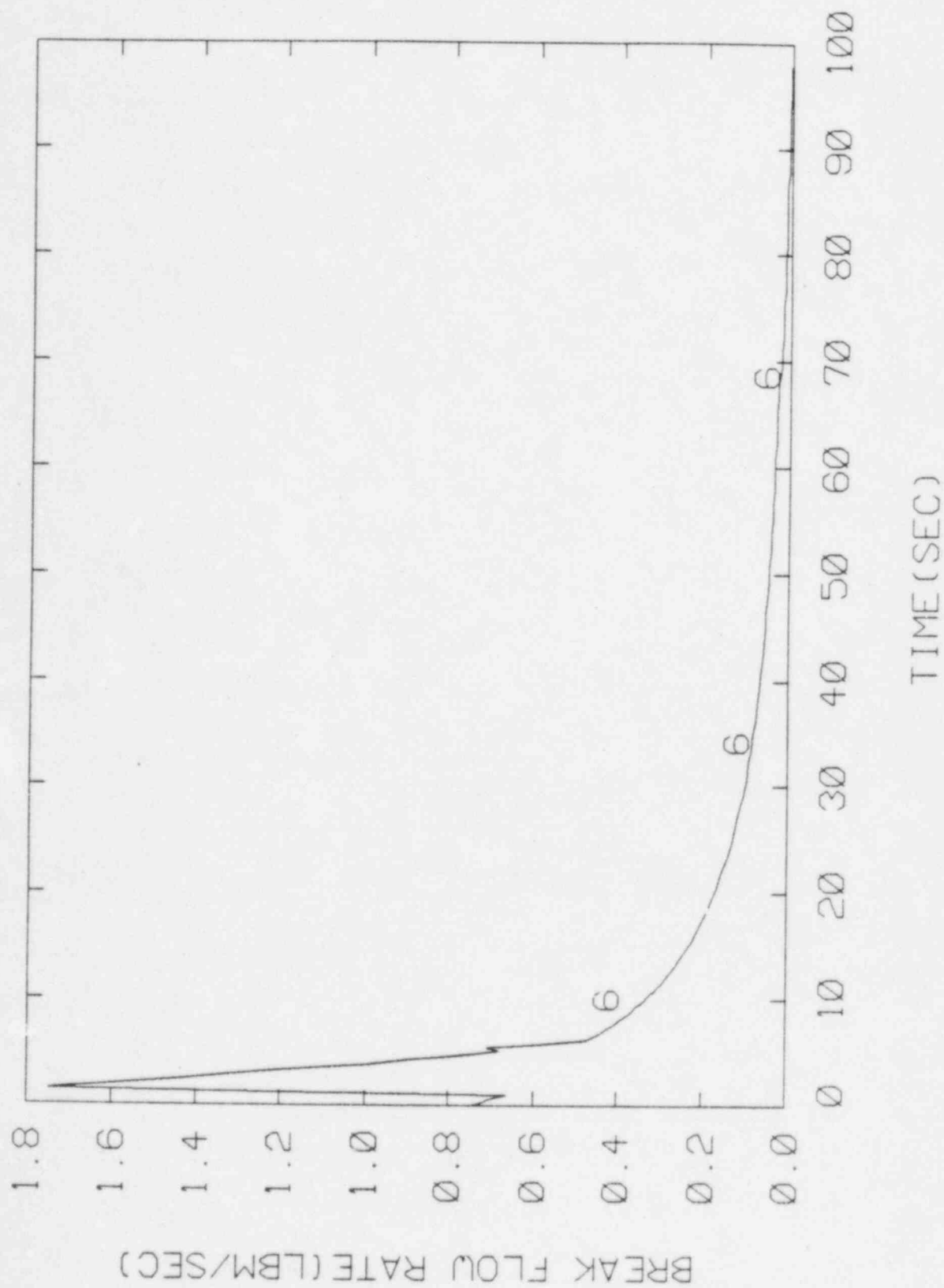


Figure 79. Calculated Break Flow Rate for MIT Test Run 48,
1/8" Break

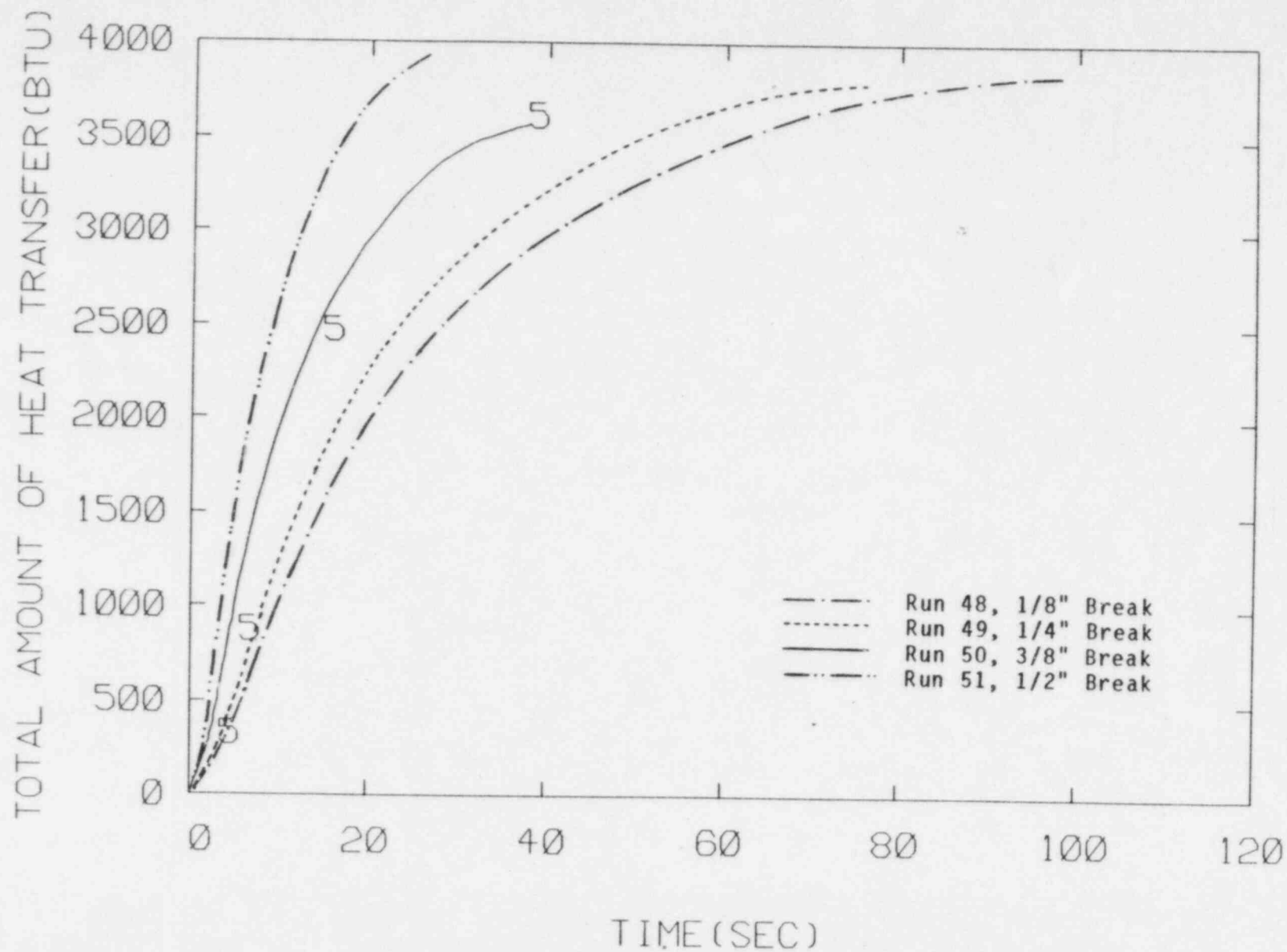


Figure 80. Calculated Time Integrated Heat Transfer for MIT Test Run 48 to 51

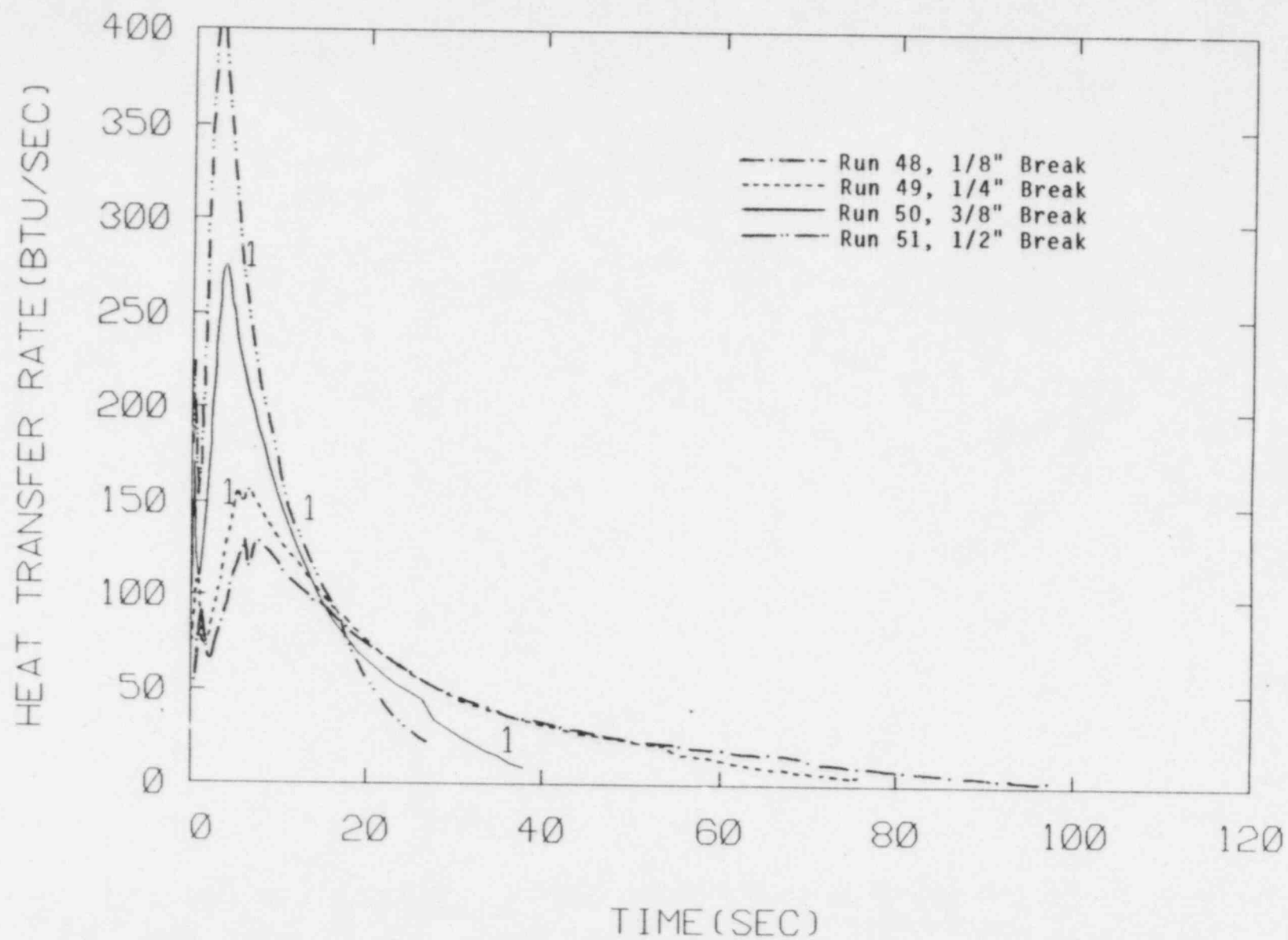


Figure 81. Calculated Heat Transfer Rate for MIT Test Run 48 to 51

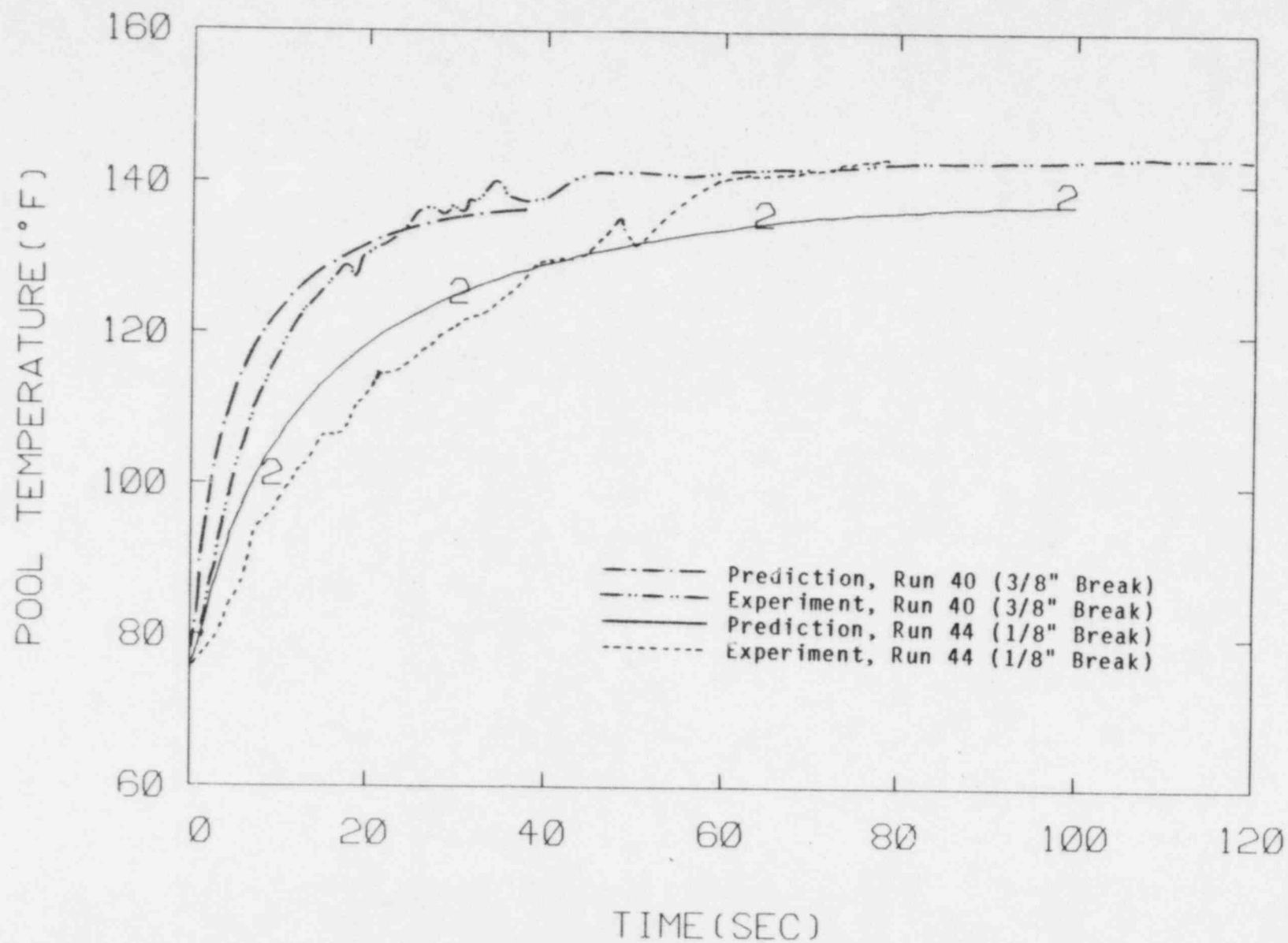


Figure 82. Comparison Between the Predicted and Measured Pool Temperature for MIT Test Run 40,44

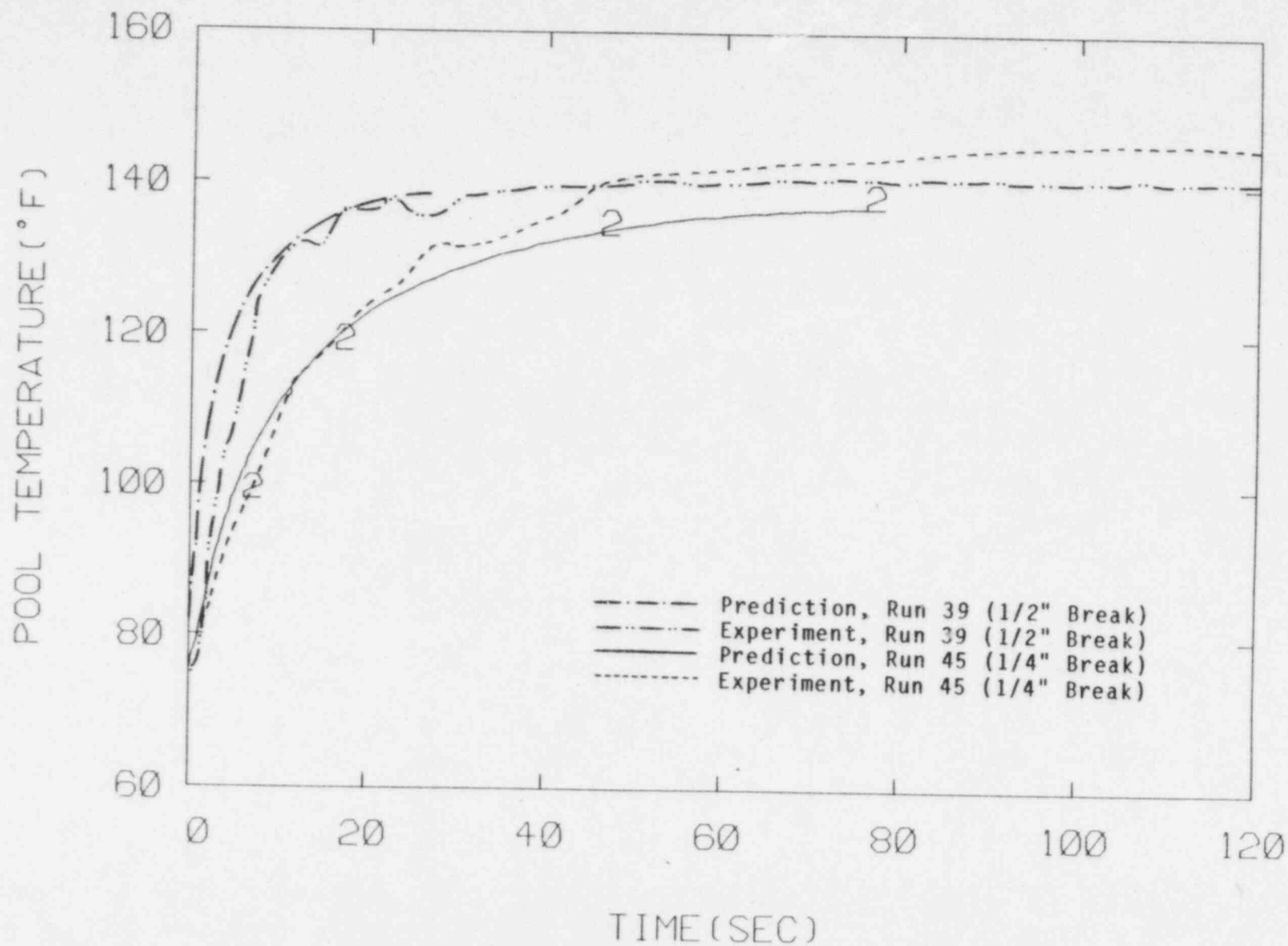


Figure 83. Comparison Between The Predicted and Measured Pool Temperature for MIT Test Run 39,45

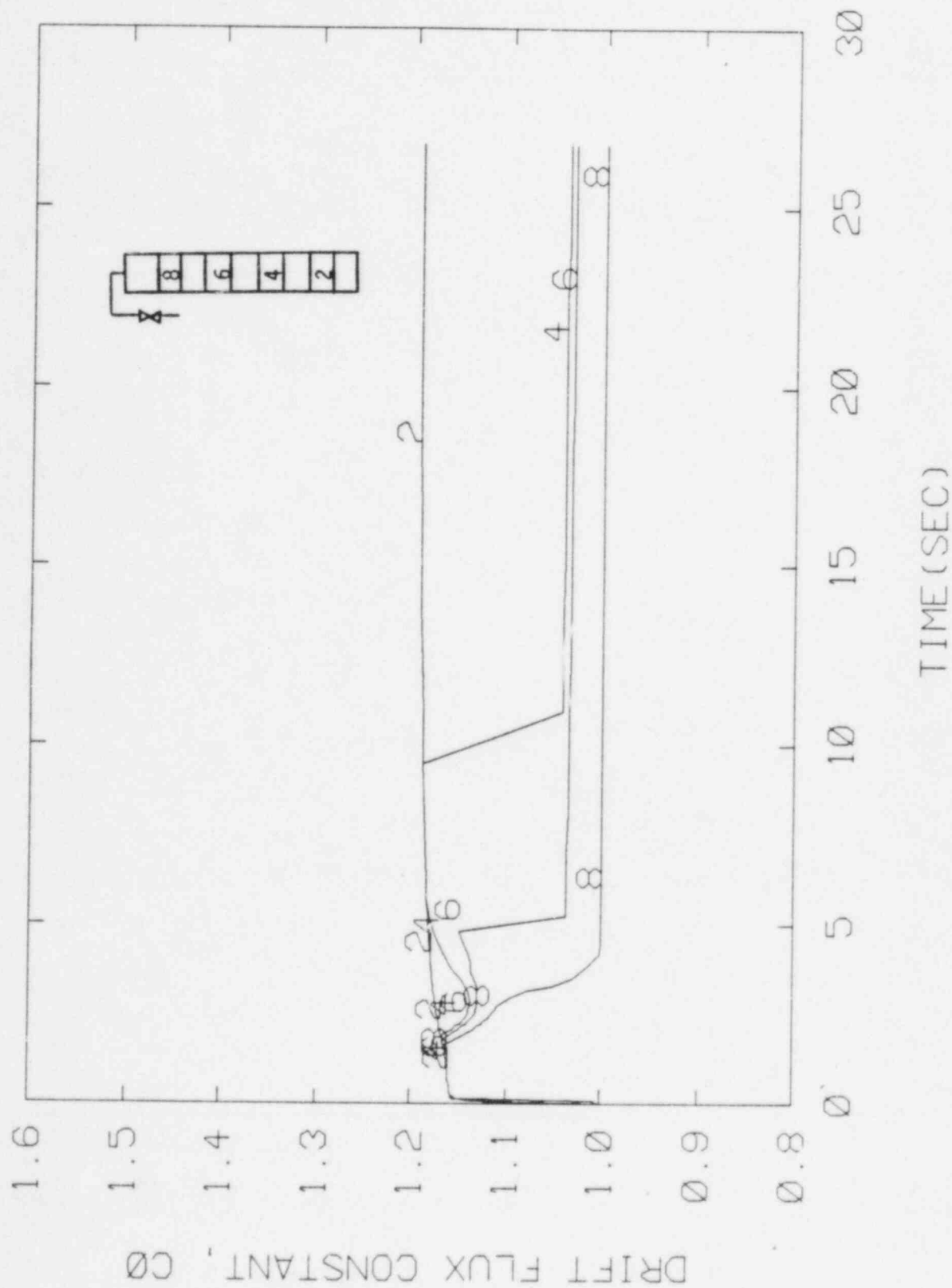


Figure 84. Flow and Void Fraction Distribution Parameter, C_0 , for MIT Test Run 51, 1 1/2" Break

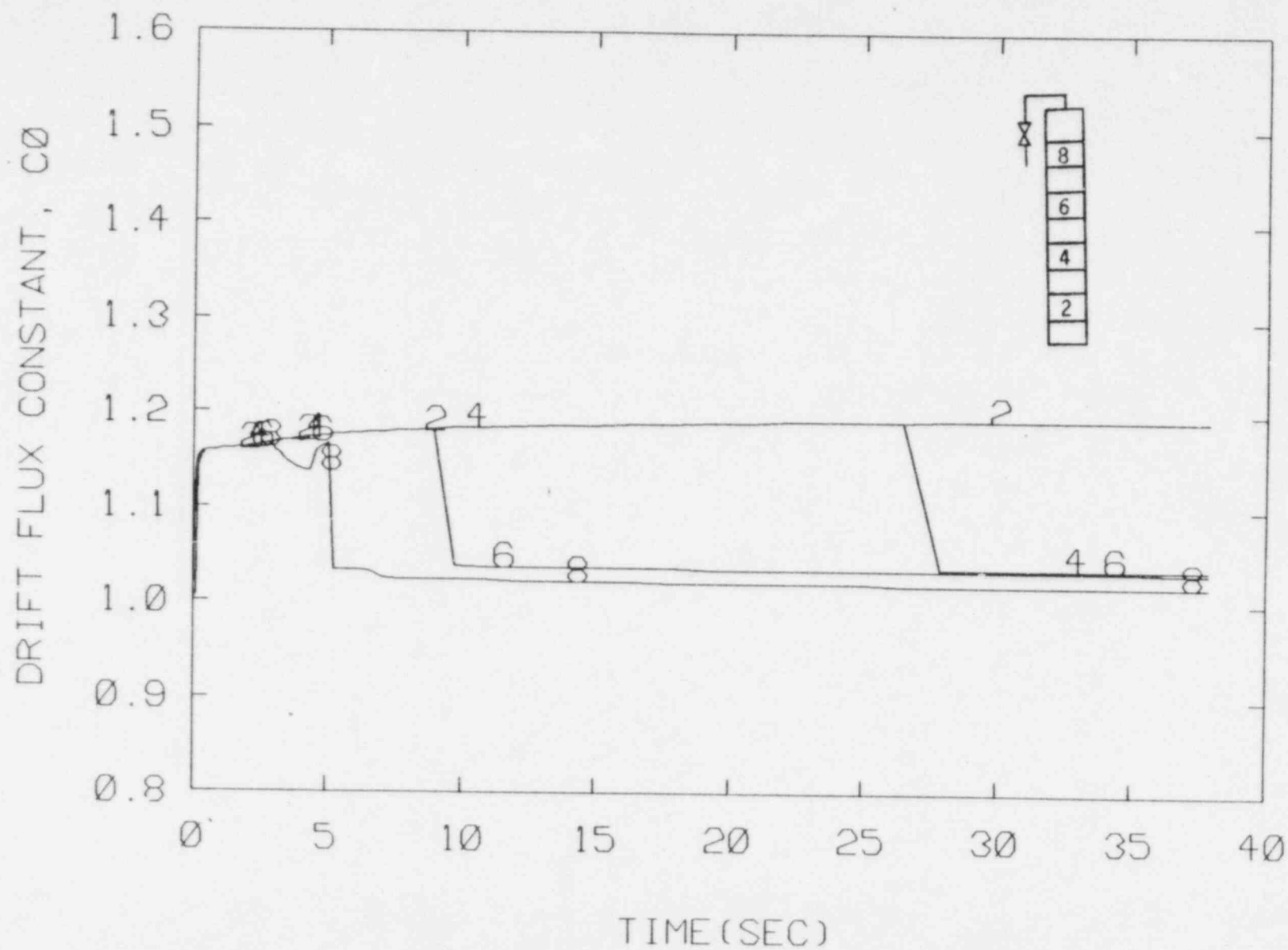


Figure 85. Flow and Void Fraction Distribution Parameter, C_0 , for MIT Test Run 50, 3/8" Break

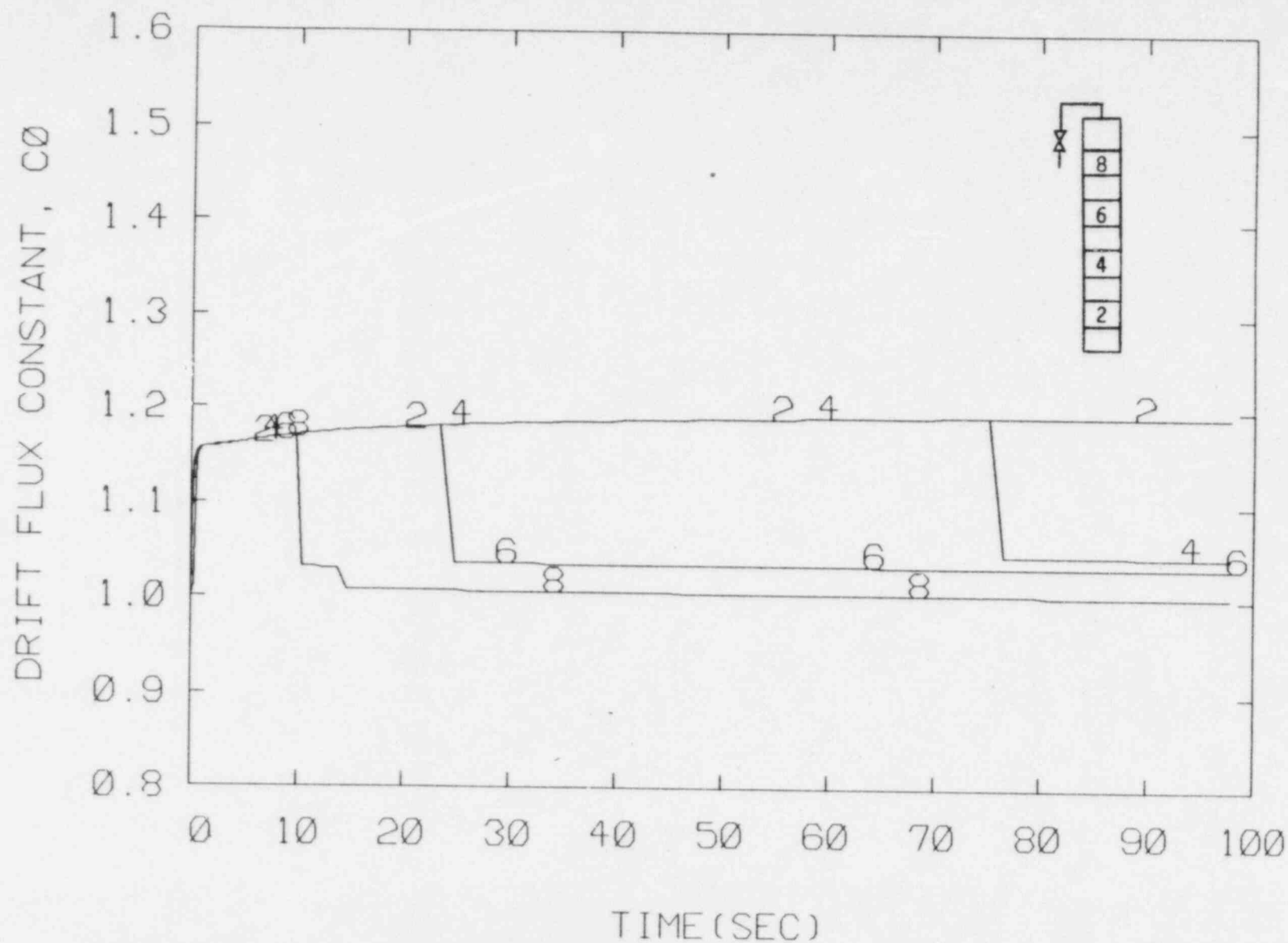


Figure 87. Flow and Void Fraction Distribution Parameter, C_0 , for MIT Test Run 48, 1/8" Break

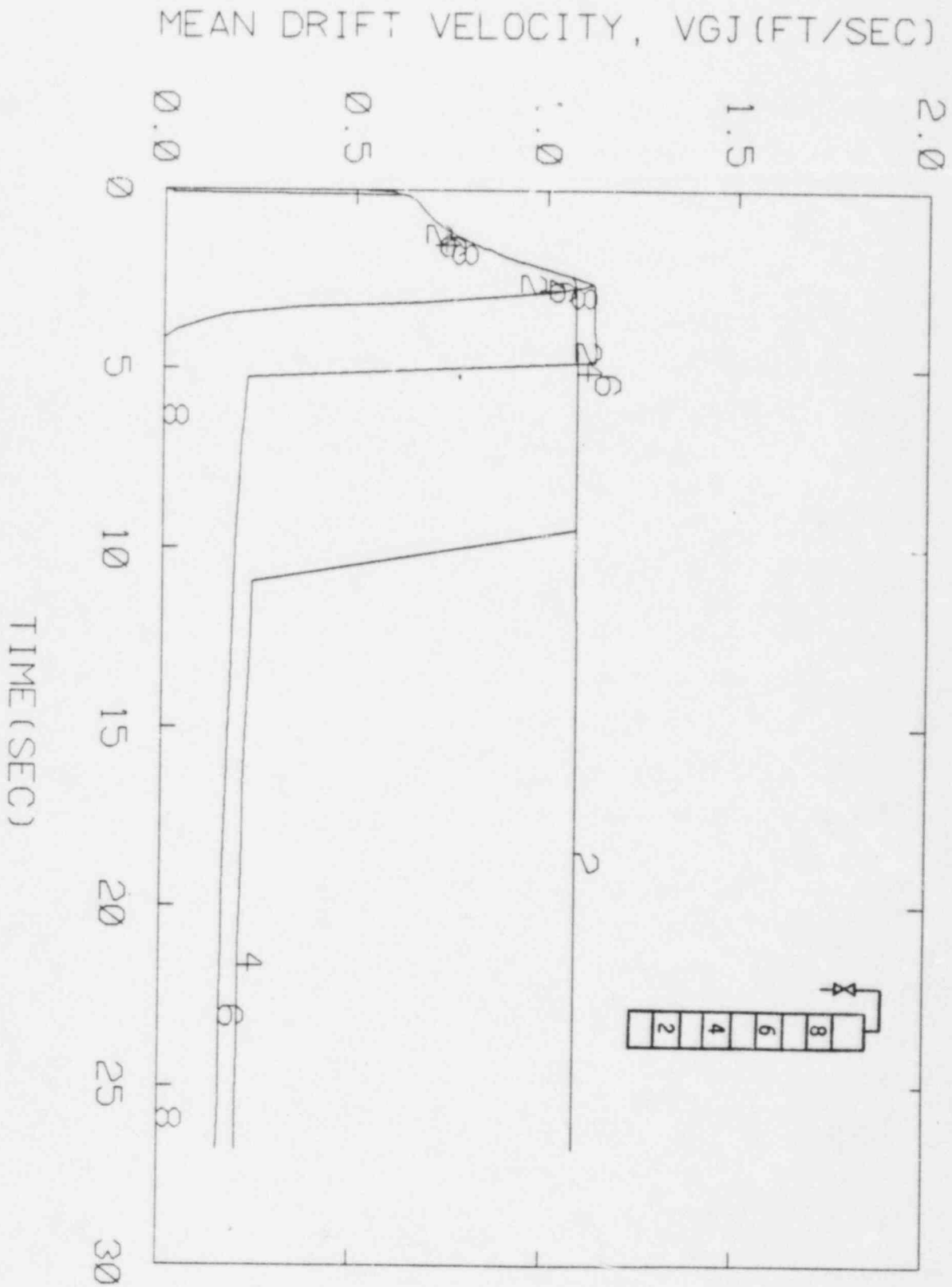


Figure 88. The Weighted Mean Drift Velocity, V_{gj} , for MIT Test Run 51, 1/2" Break

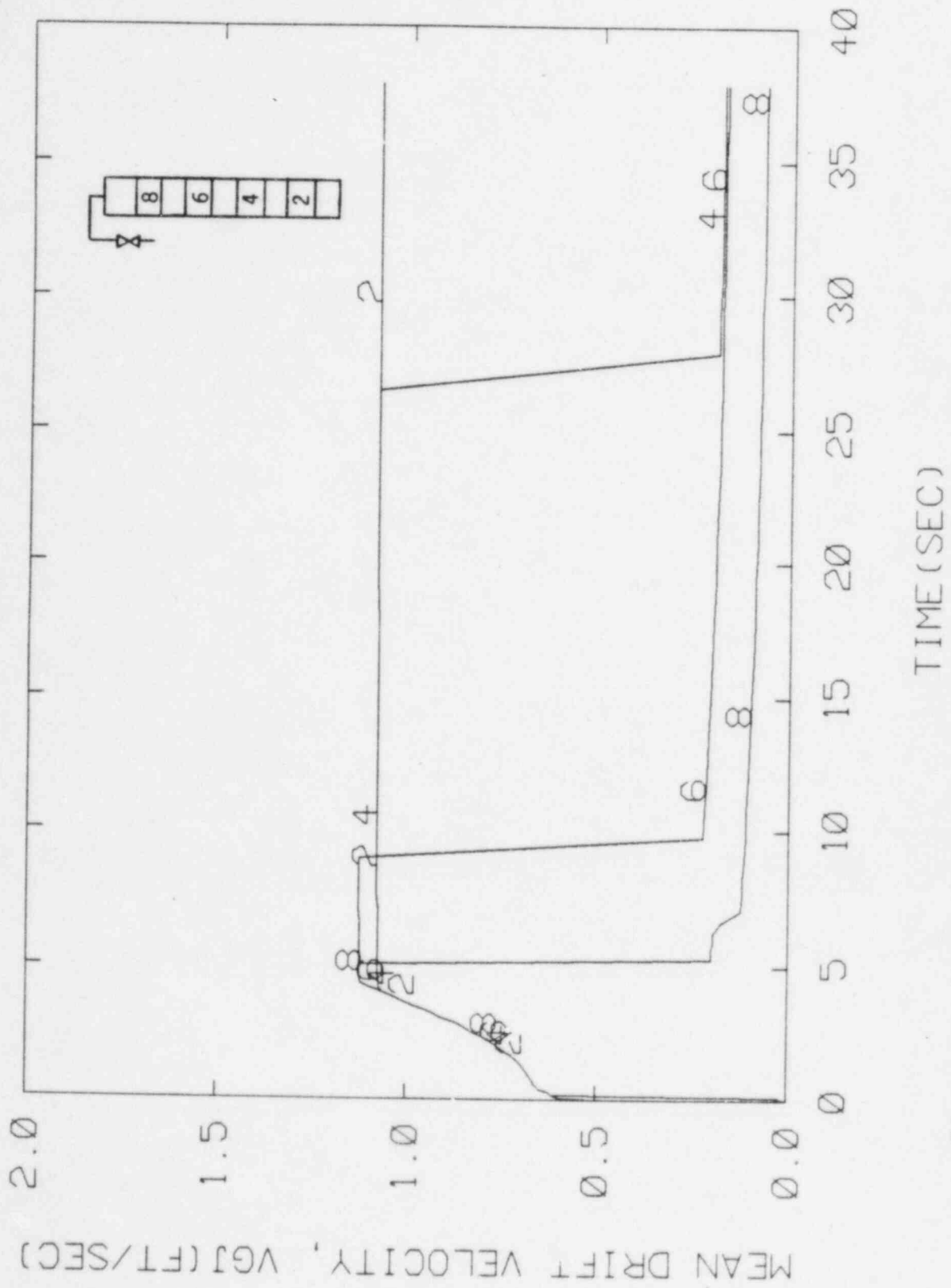


Figure 89. The Weighted Mean Drift Velocity, V_{gj} , for MIT Test Run 50, 3/8" Break

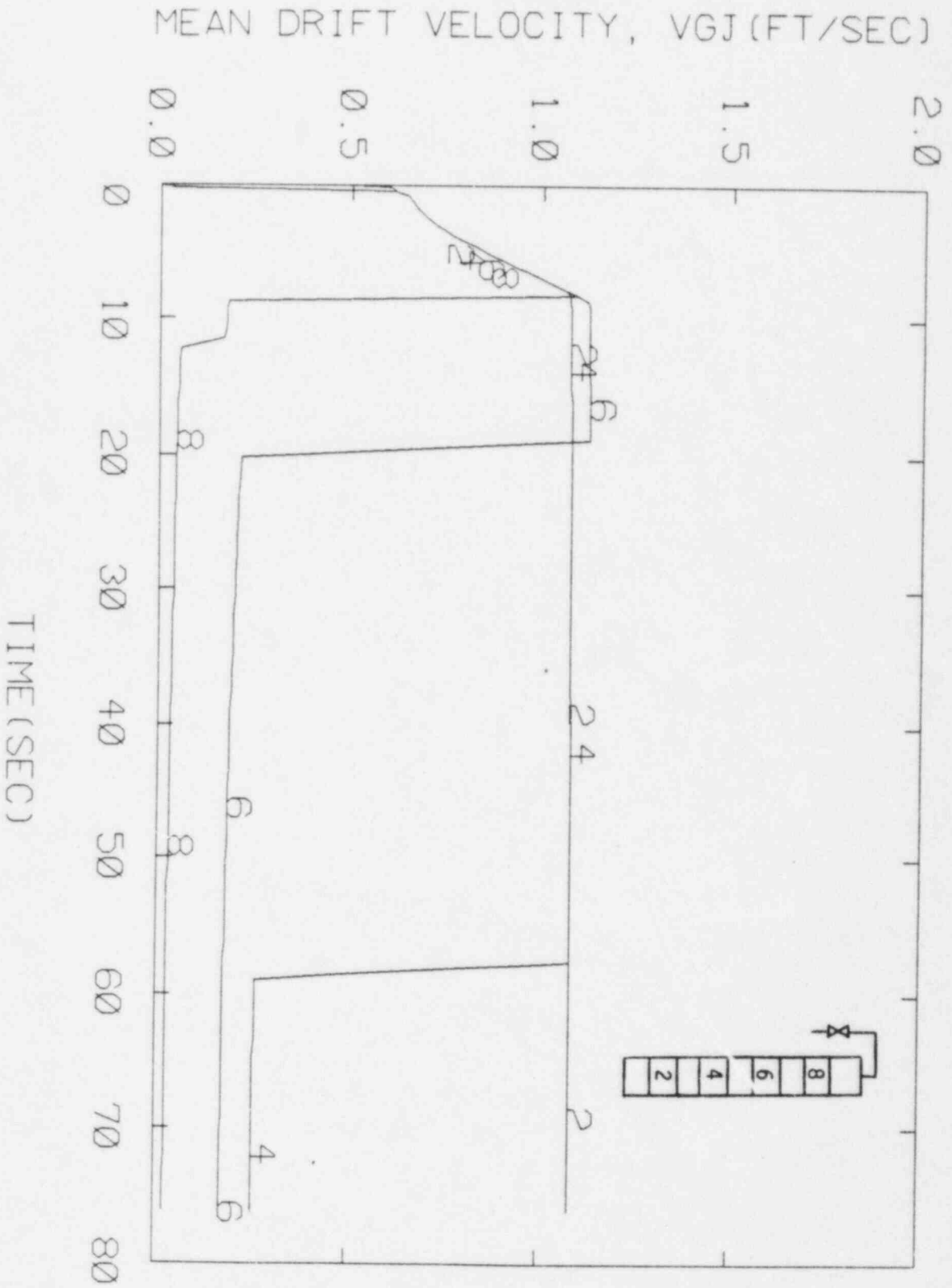
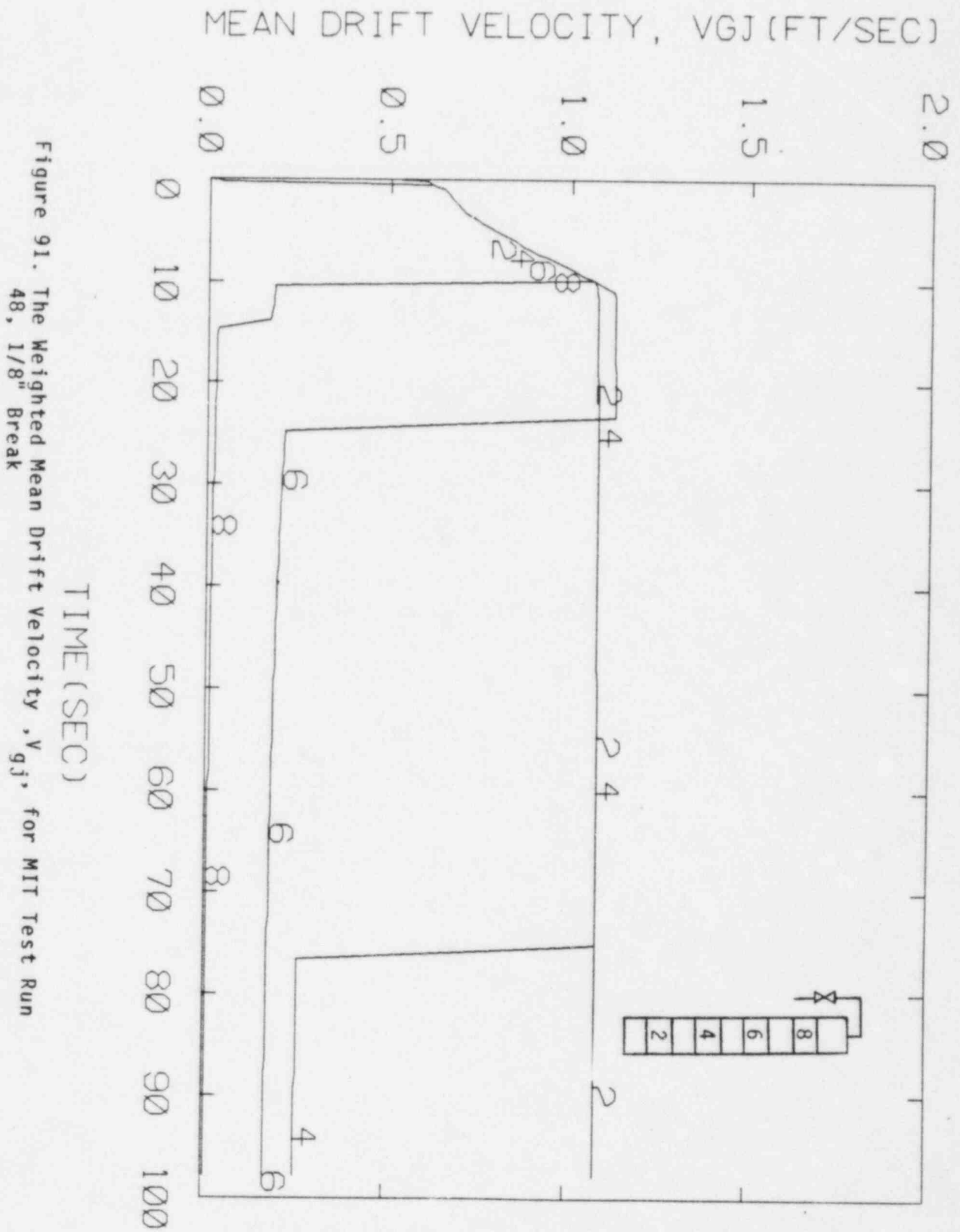


Figure 90. The Weighted Mean Drift Velocity, V_{gj} , for MIT Test Run 49, 1/4" Break



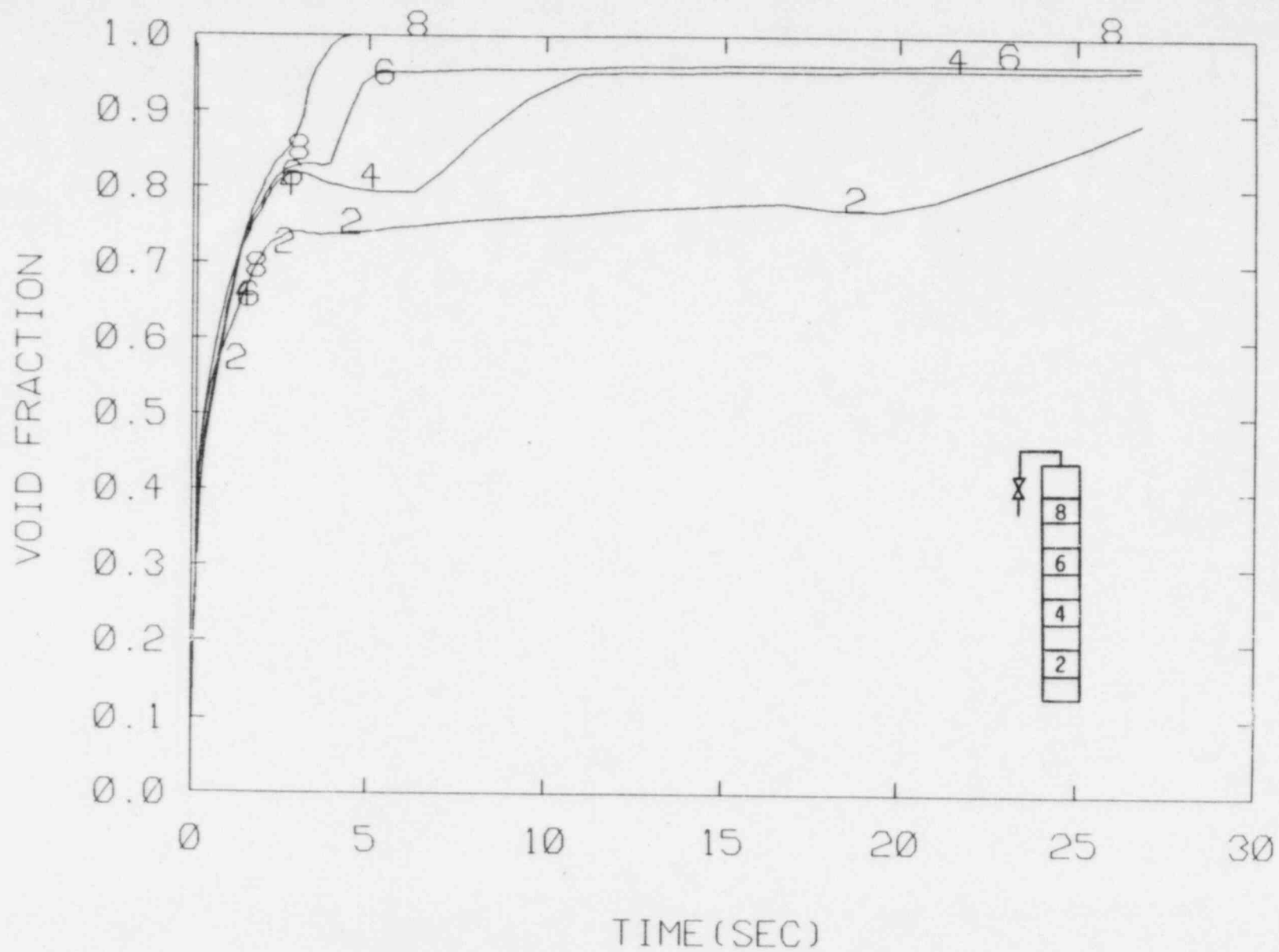


Figure 92. The Predicted Void Fraction Distribution for MIT Test Run 51, 1/2" Break

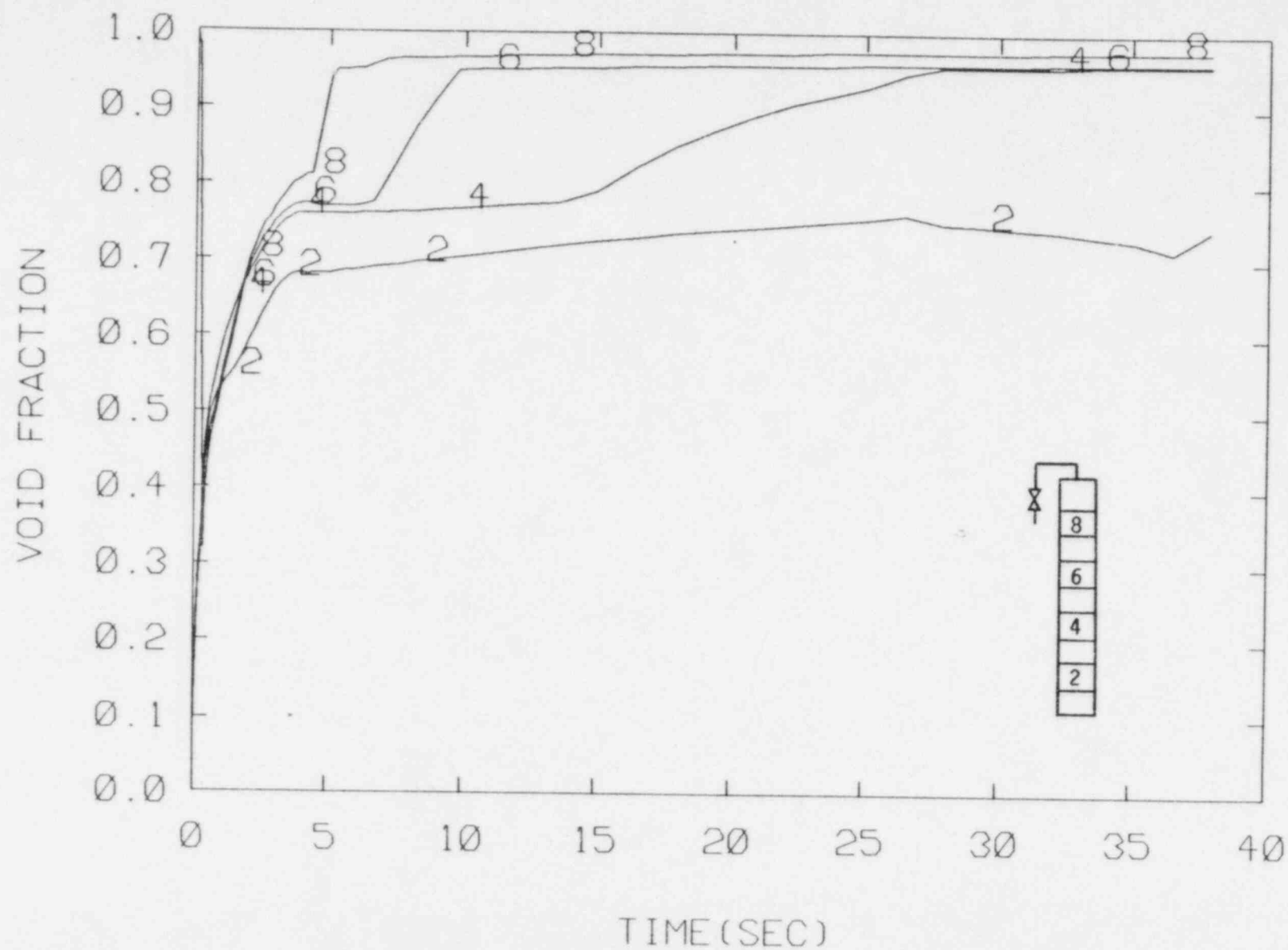


Figure 93. The Predicted Void Fraction Distribution for MIT Test Run 50, 3/8" Break

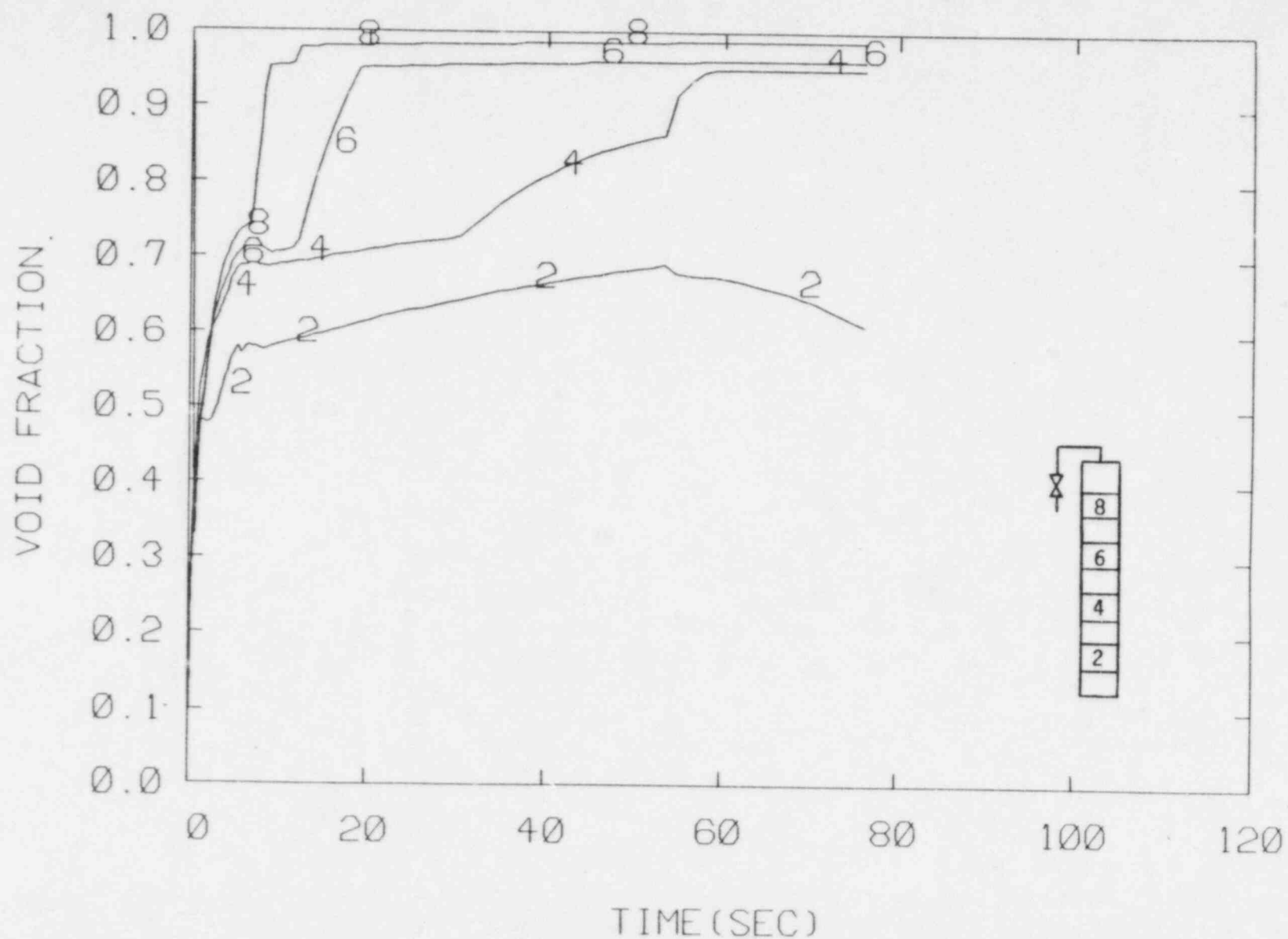


Figure 94. The Predicted Void Fraction Distribution for MIT Test Run 49, 1/4" Break

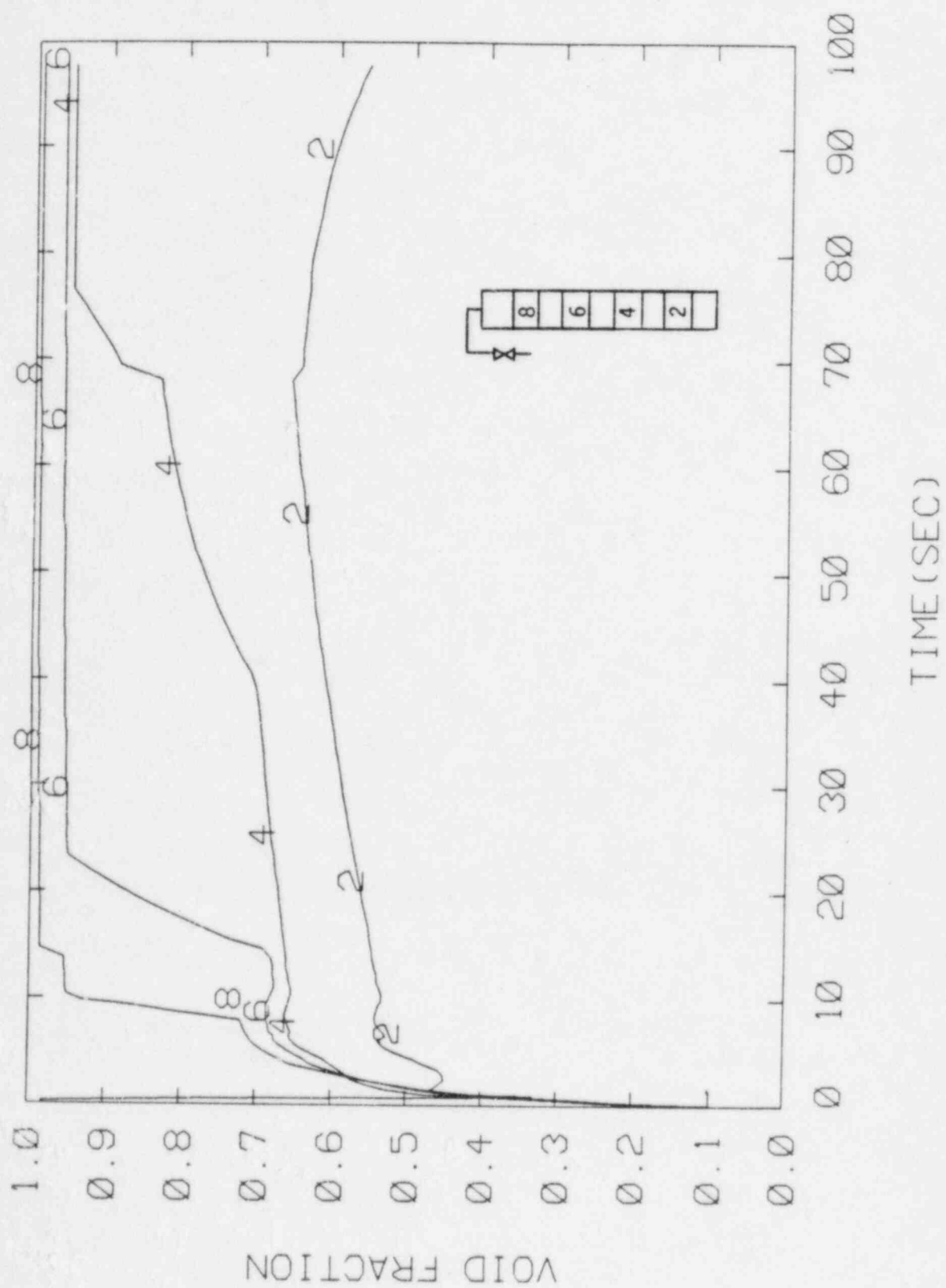


Figure 95. The Predicted Void Fraction Distribution for MIT Test Run 48, 1/8" Break

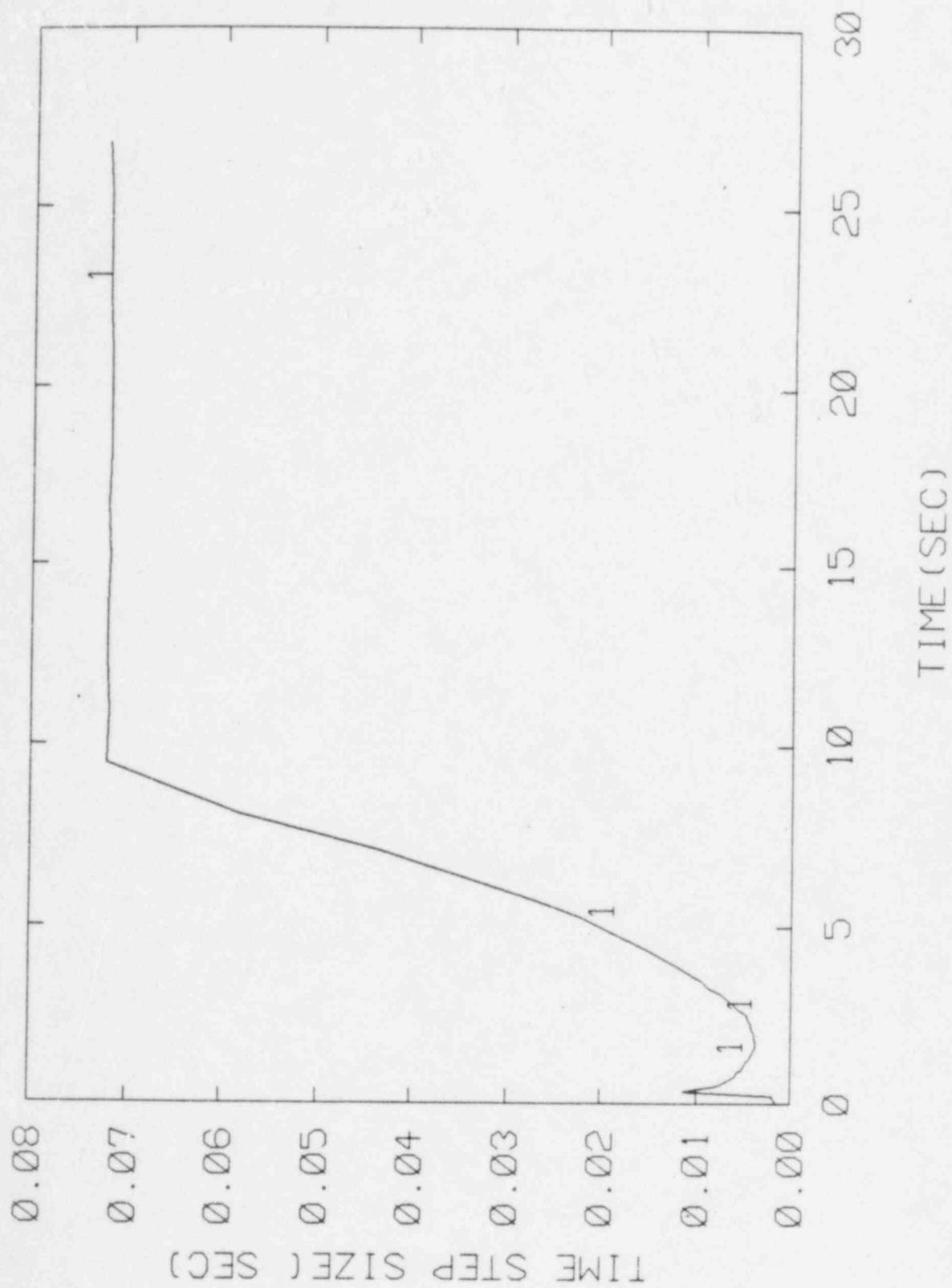


Figure 96. The Time Step Size for MIT Test Run 51, 1/2" Break

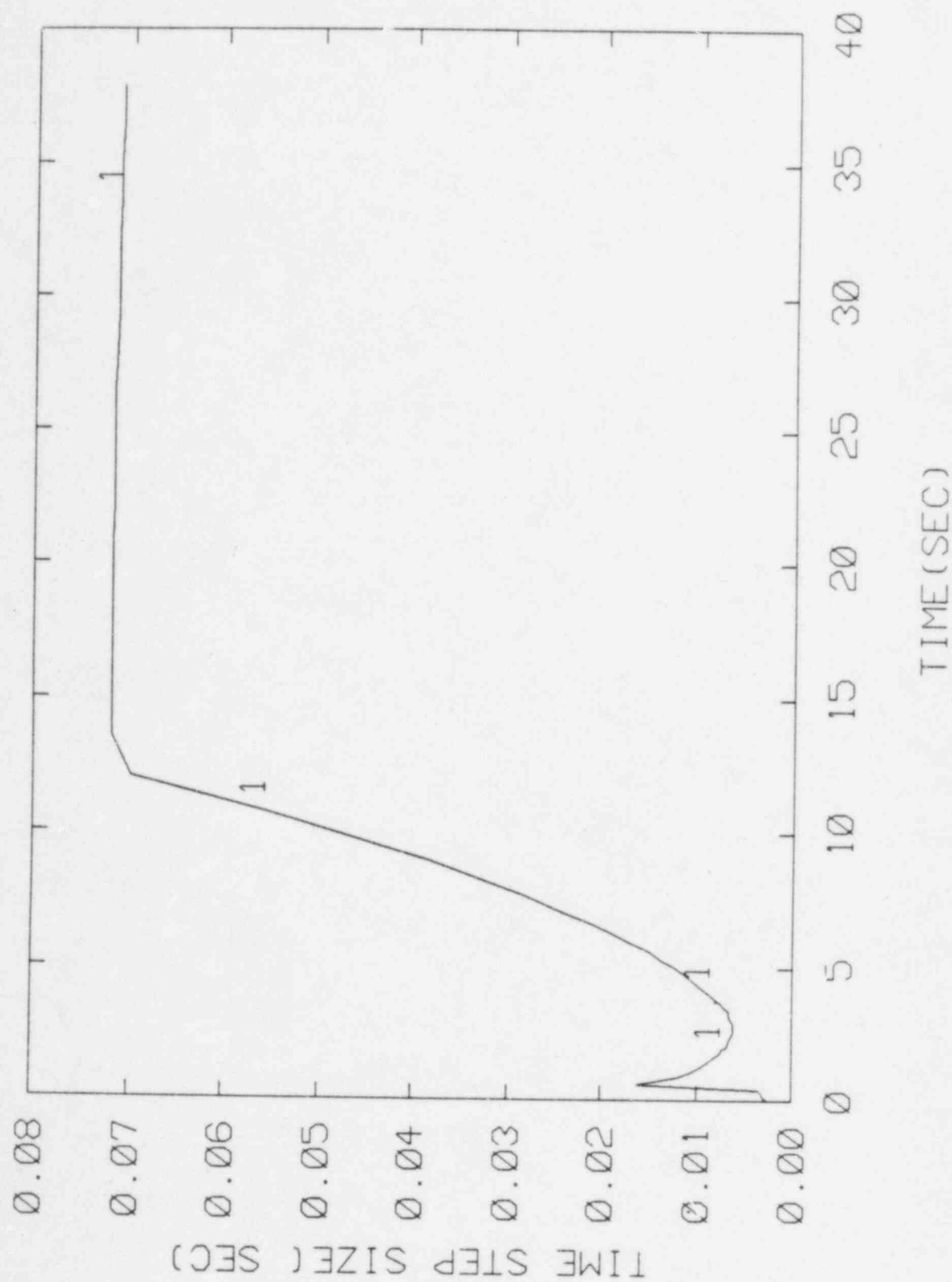


Figure 97 . The Time Step Size for MIT Test Run 50, 3/8" Break

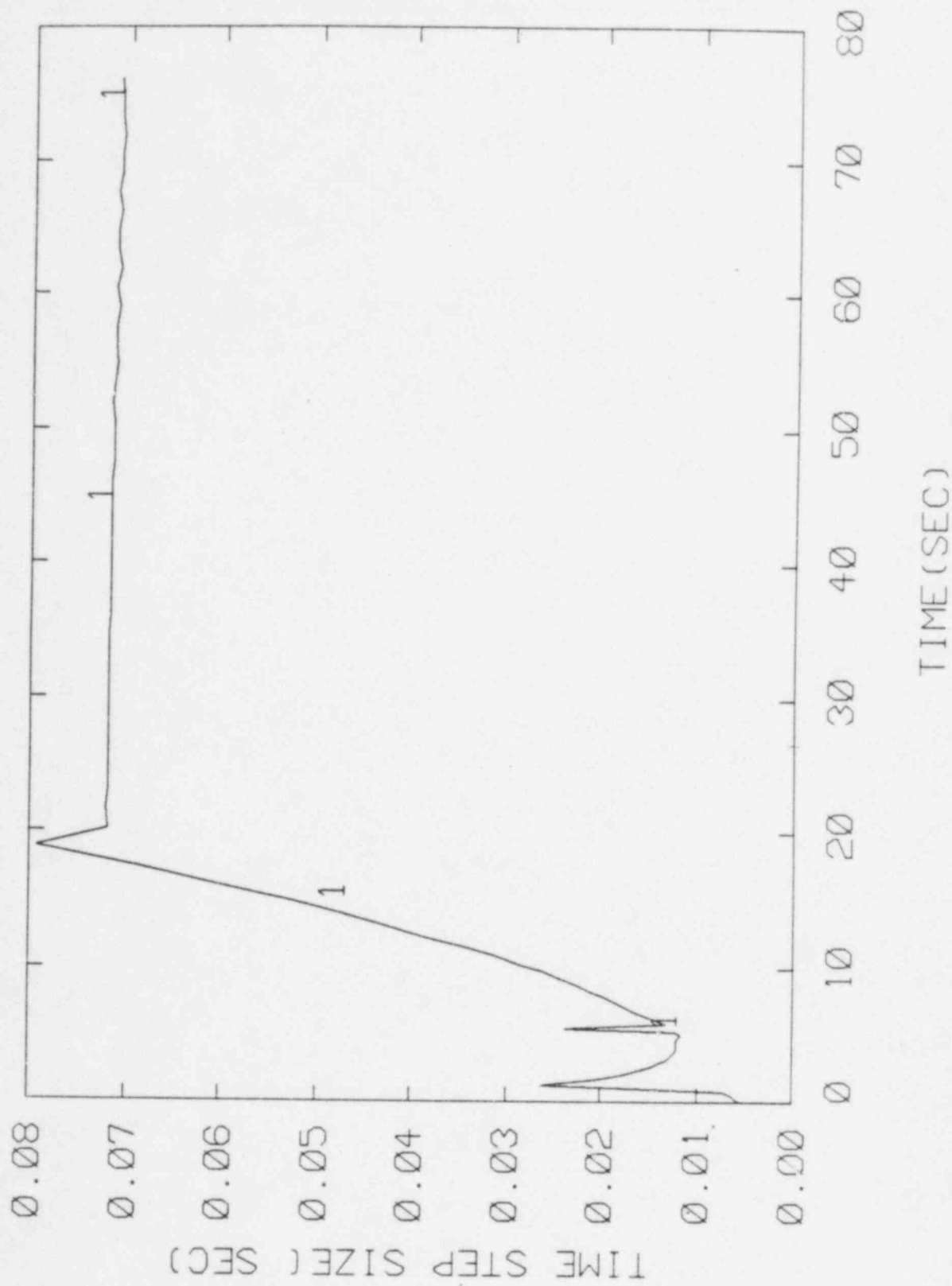


Figure 98. The Time Step Size for MIT Test Run 49, 1/4" Break

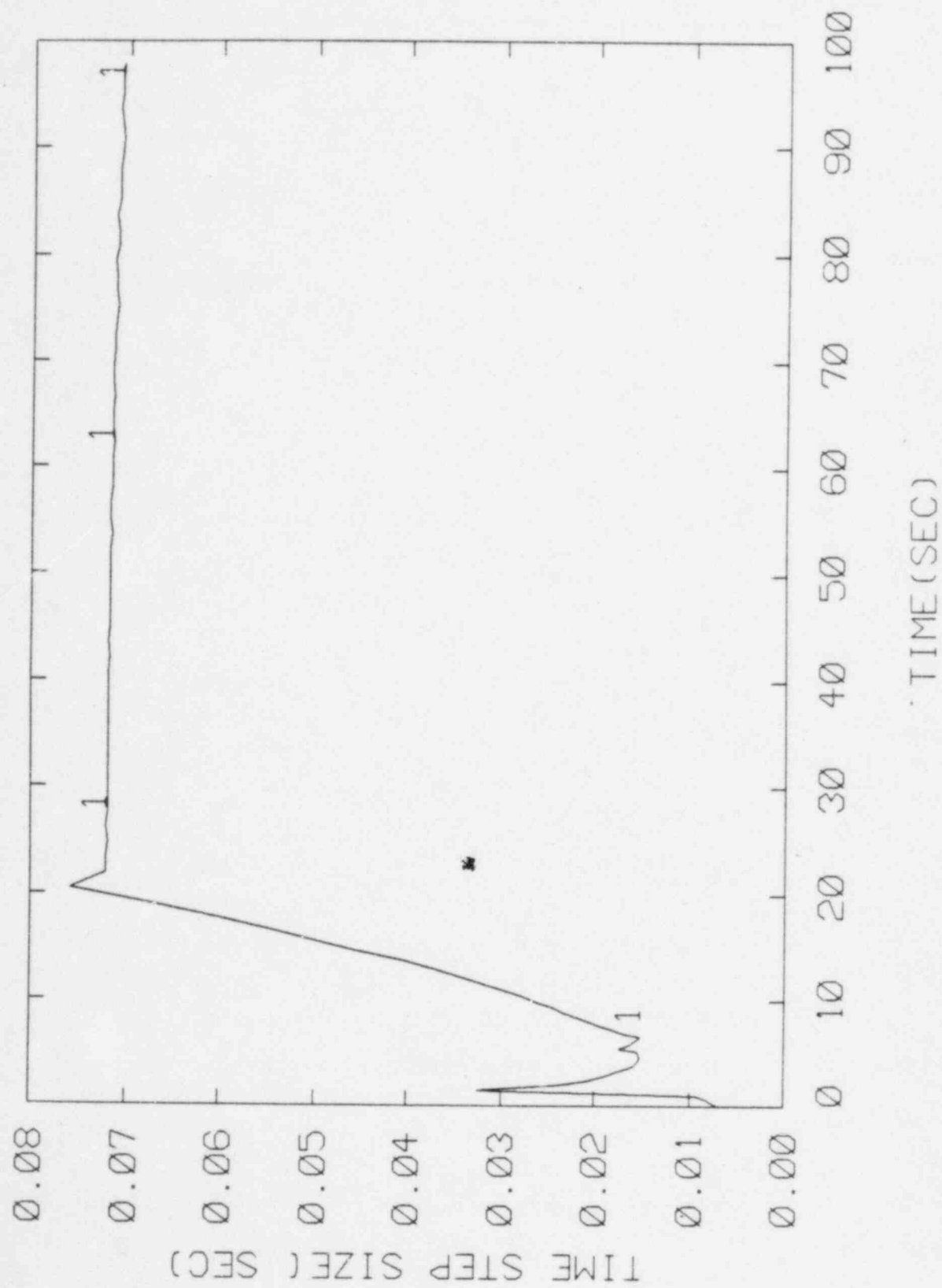


Figure 99. The Time Step Size for MIT Test Run 48, 1/8" Break

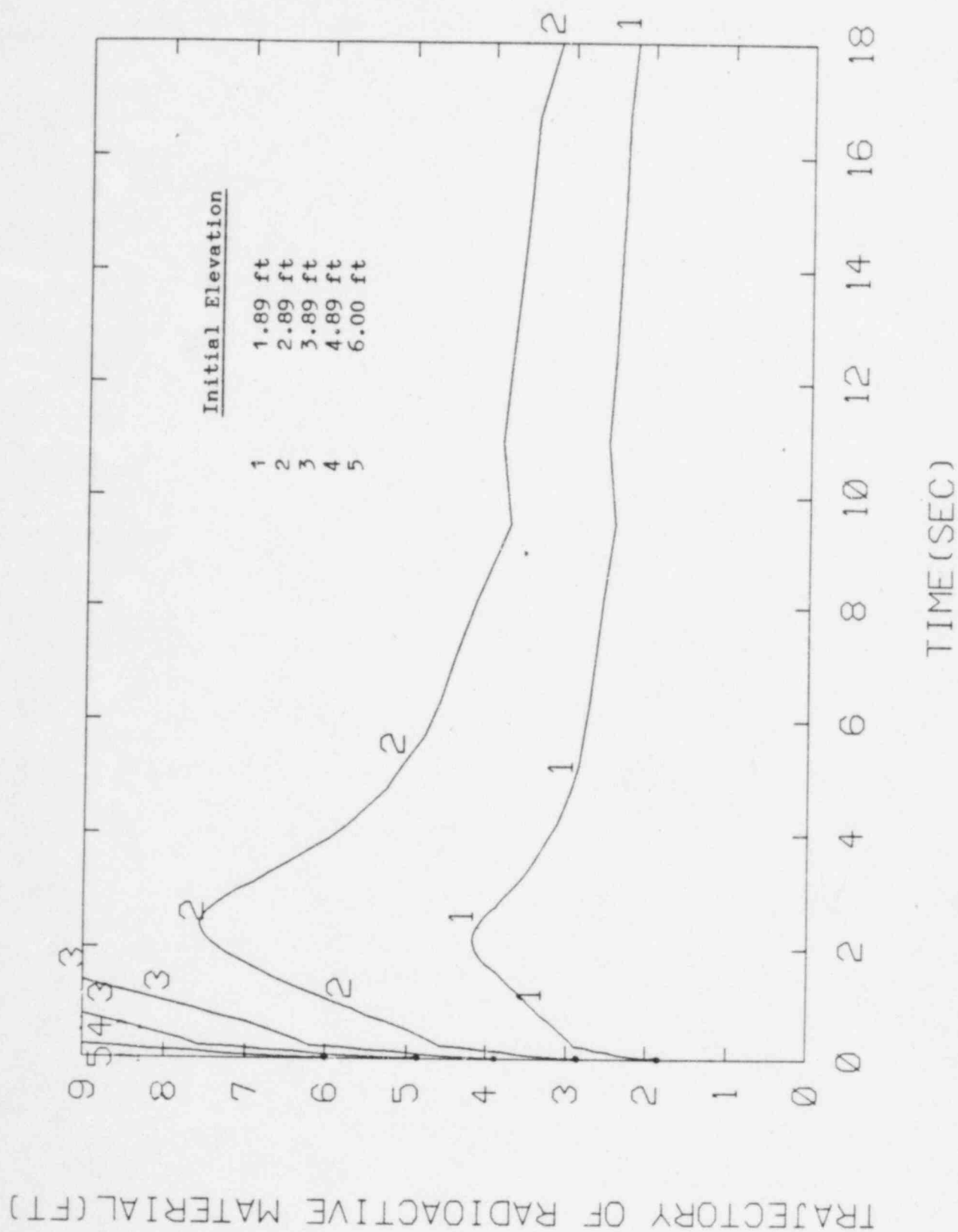


Figure 100. The Trajectory of Radioactive Material for MIT Test Run 51, 1 1/2" Break

TRAJECTORY OF RADIOACTIVE MATERIAL (FT)

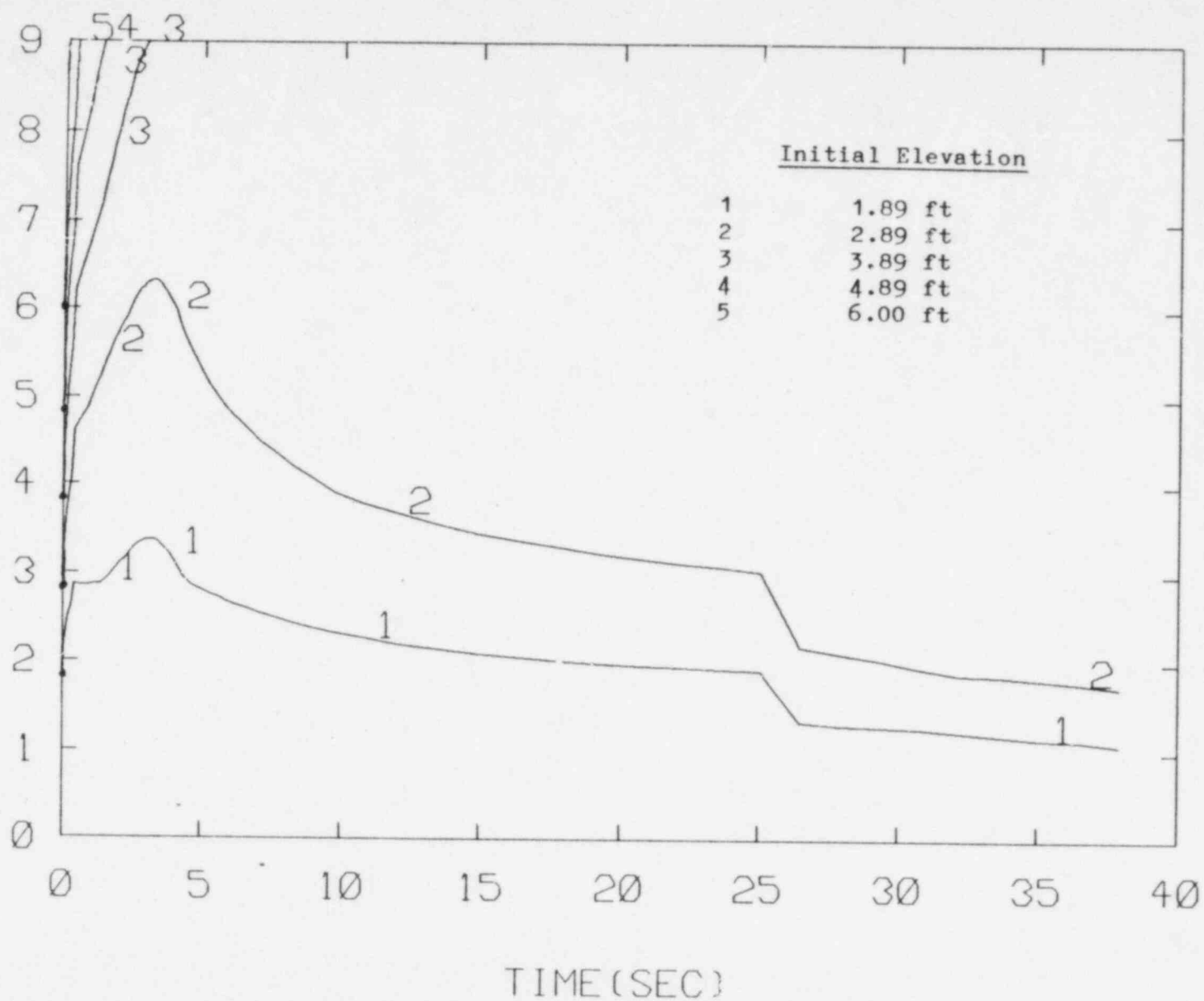


Figure 101. The Trajectory of Radioactive Material for MIT Test Run 50, 3/8" Break

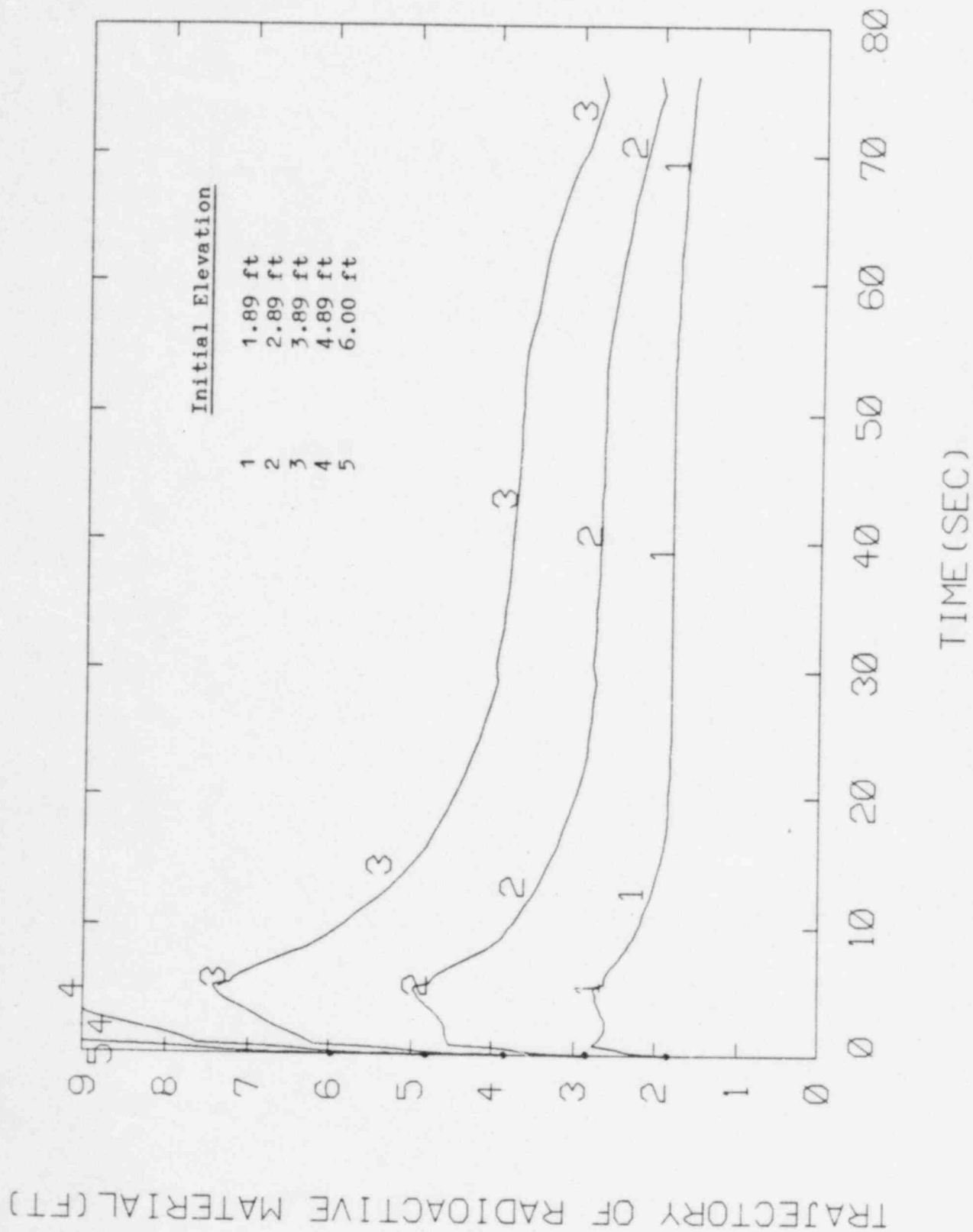
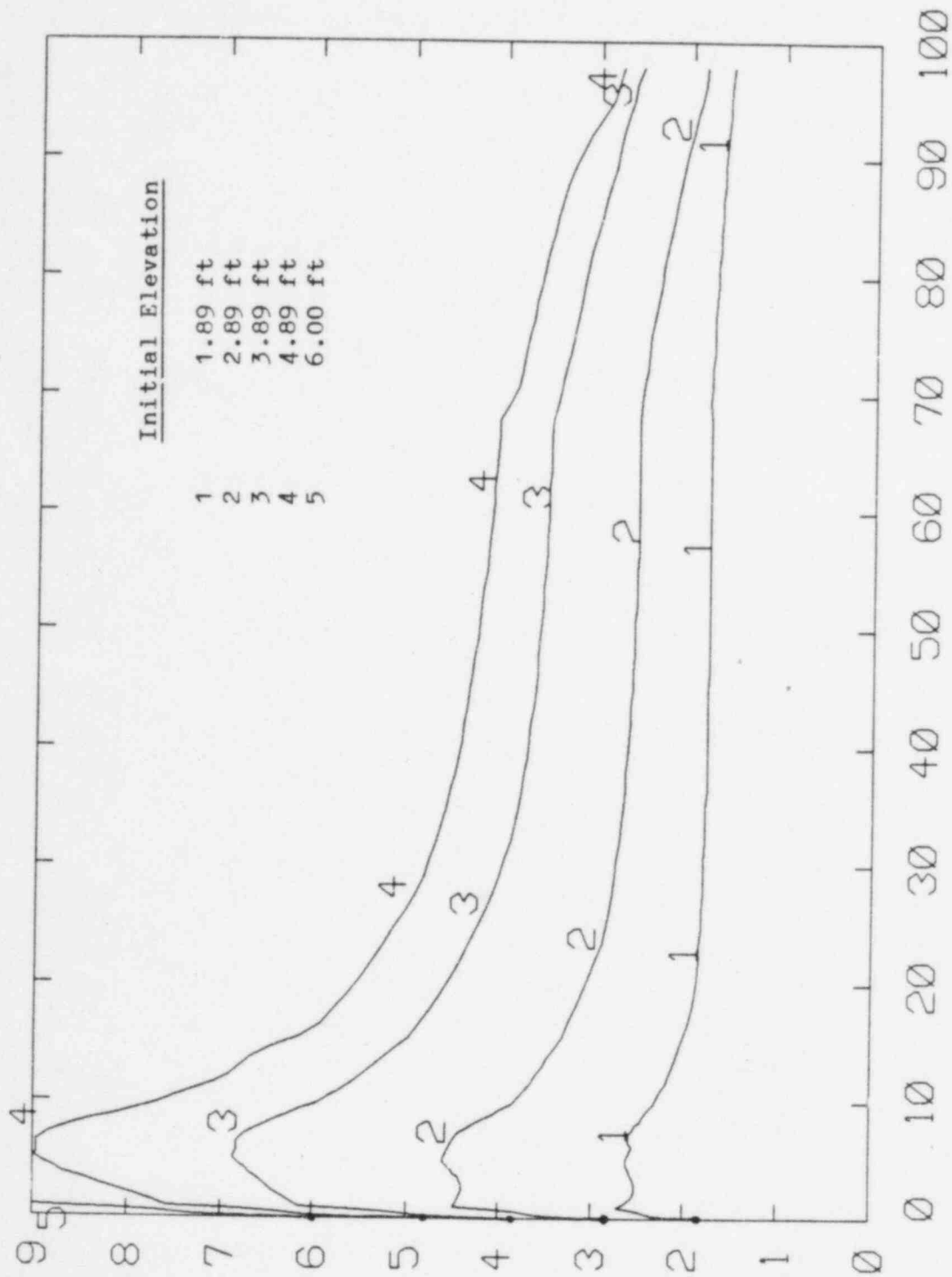


Figure 102. The Trajectory of Radioactive Material for MIT Test Run 49, 1/4" Break

TRAJECTORY OF RADIOACTIVE MATERIAL (FT)



TIME (SEC)

Figure 103. The Trajectory of Radioactive Material for MIT Test Run 48, 1/8" Break

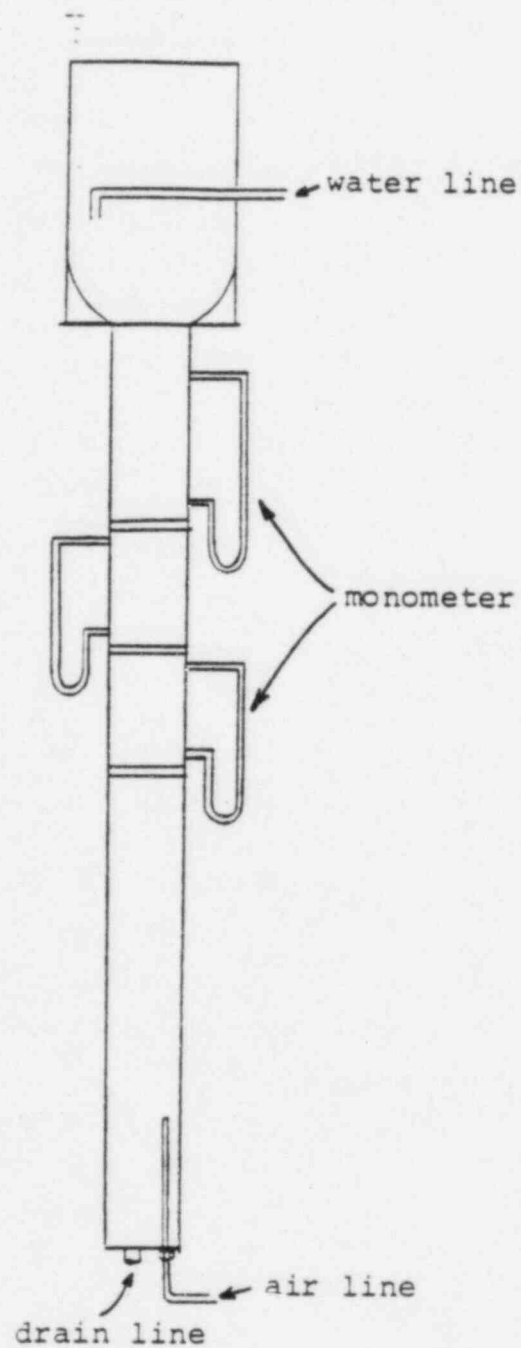
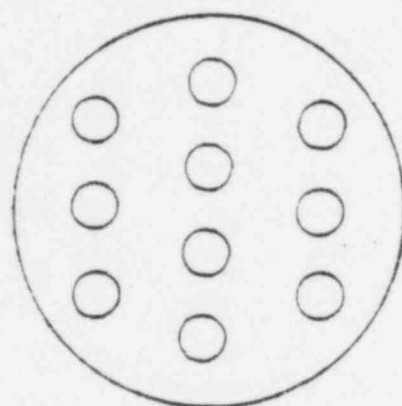
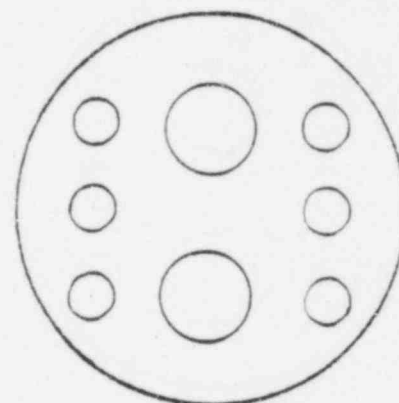


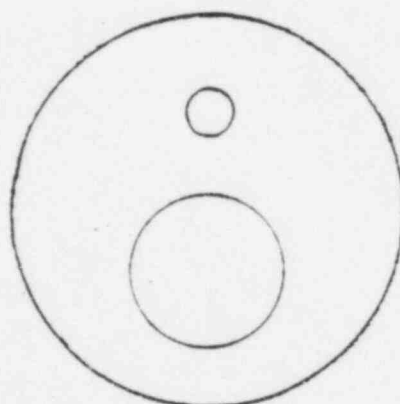
Figure 104. Schematic of the Apparatus for the Liquid Hold Up Test



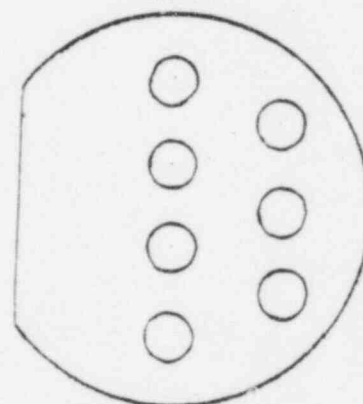
Type A



Type B



Type C



Type D

Figure 105. Different Types of Plates Used in the Liquid Hold Up Experiment

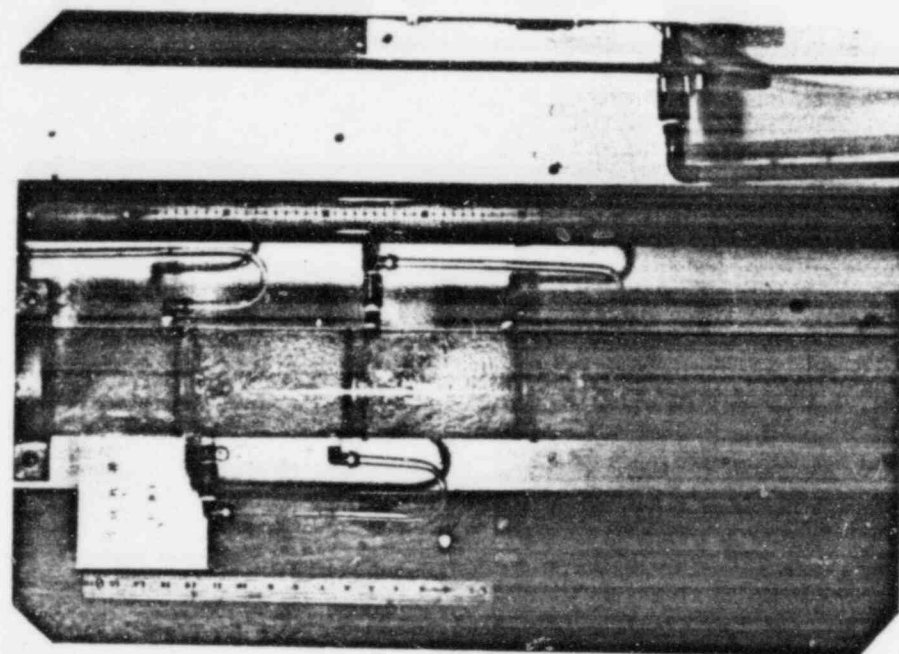


Figure 107. Results for Liquid Hold Up
Test Run F-BI

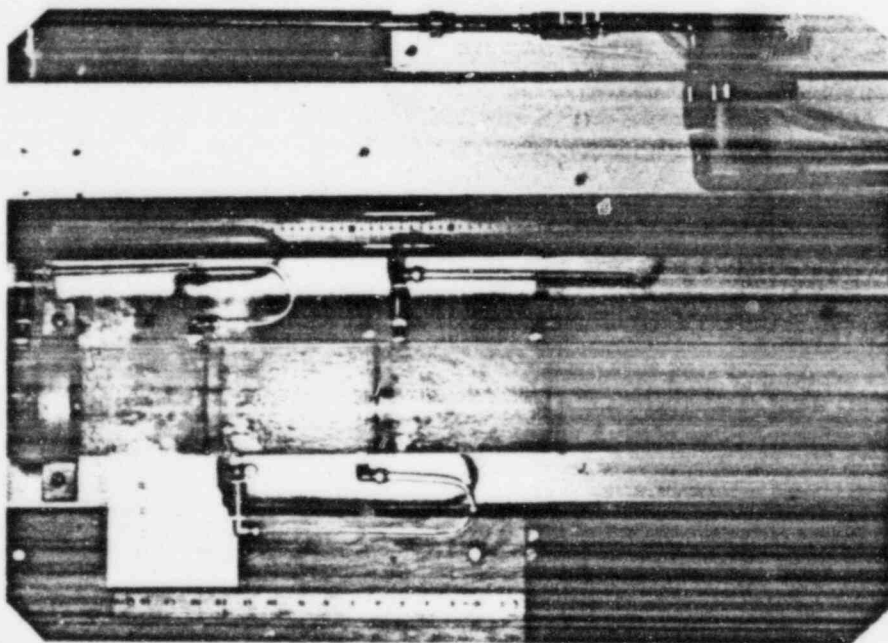


Figure 106. Results for Liquid Hold Up
Test Run F-AI

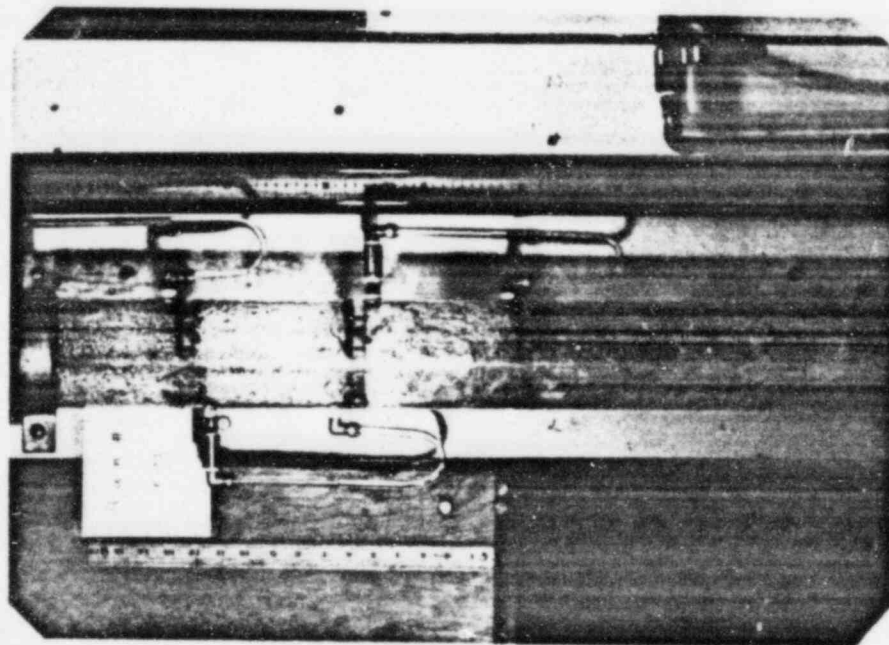


Figure 109. Results for Liquid Hold Up
Test Run F-DI

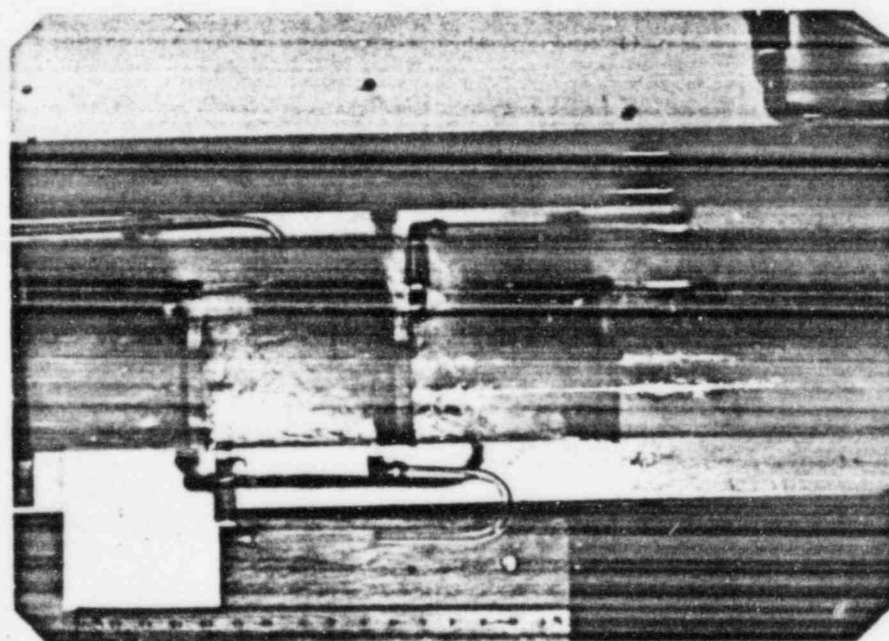


Figure 103. Results for Liquid Hold Up
Test Run F-CI

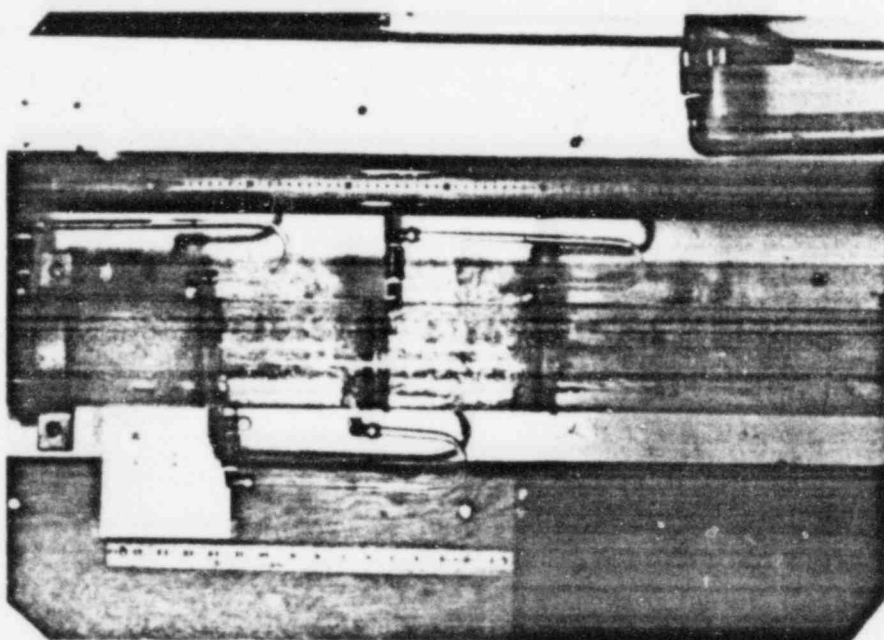


Figure 111. Results for Liquid Hold Up
Test Run W-B3

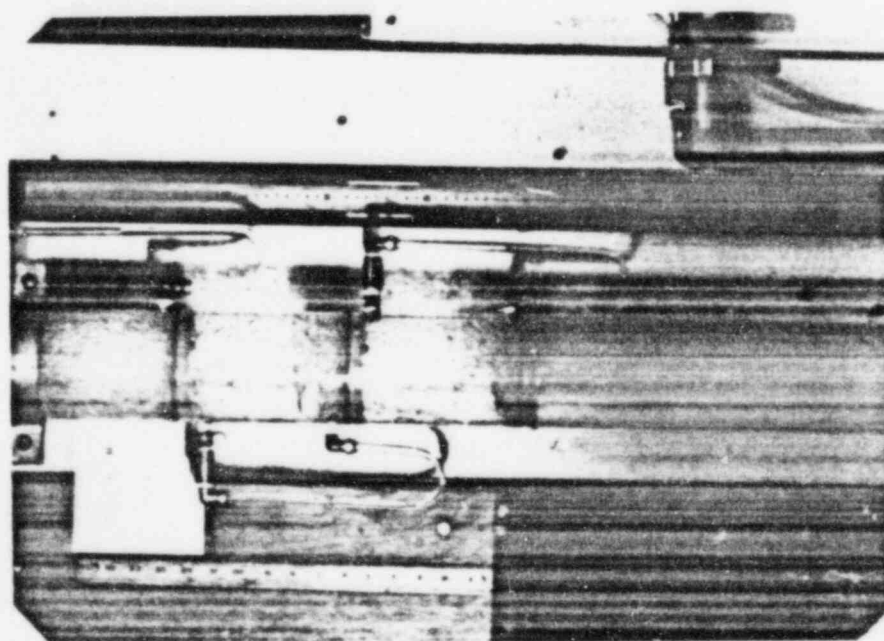


Figure 112. Results for Liquid Hold Up
Test Run W-A1

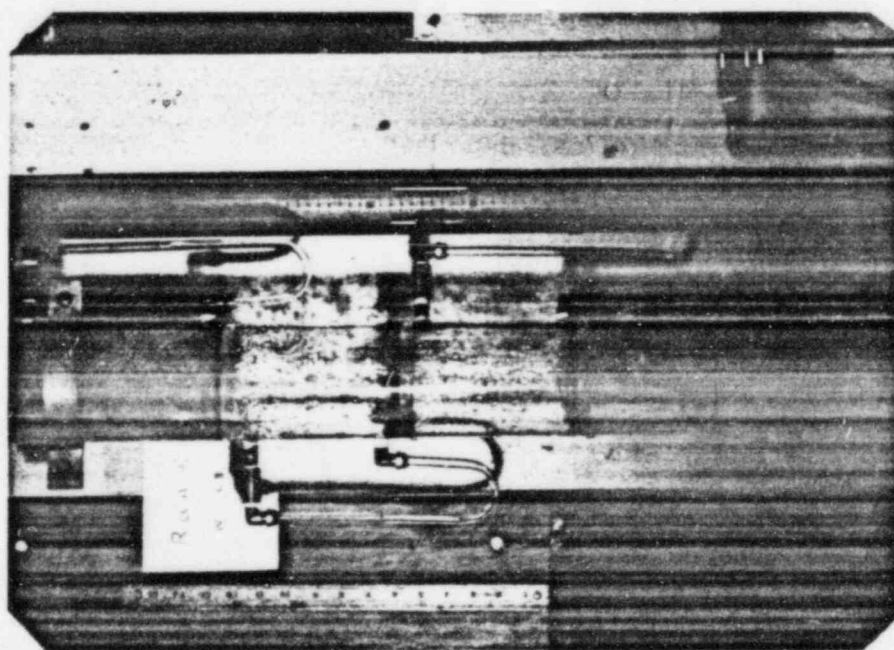


Figure 112. Results for Liquid Hold Up
Test Run W-C3

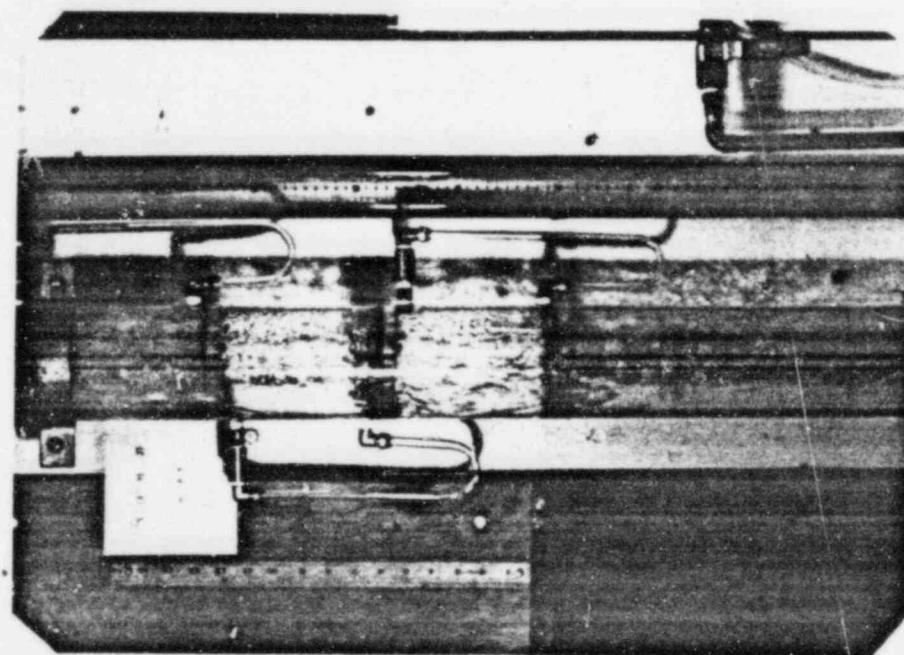


Figure 113. Results for Liquid Hold Up
Test Run W-D3

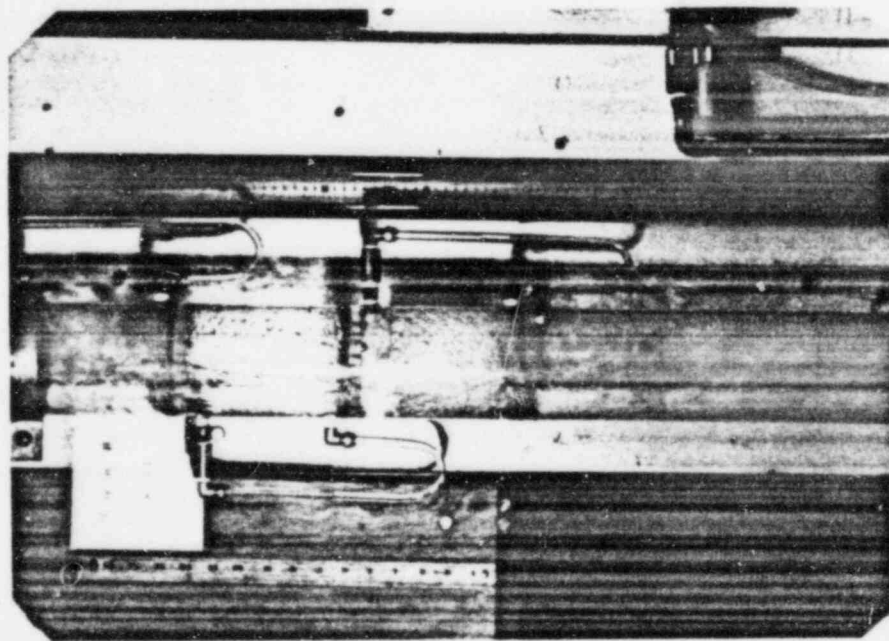


Figure 114. Results for Liquid Hold Up
Test Run W-D1, Bottom Plate
Liquid Hold Up

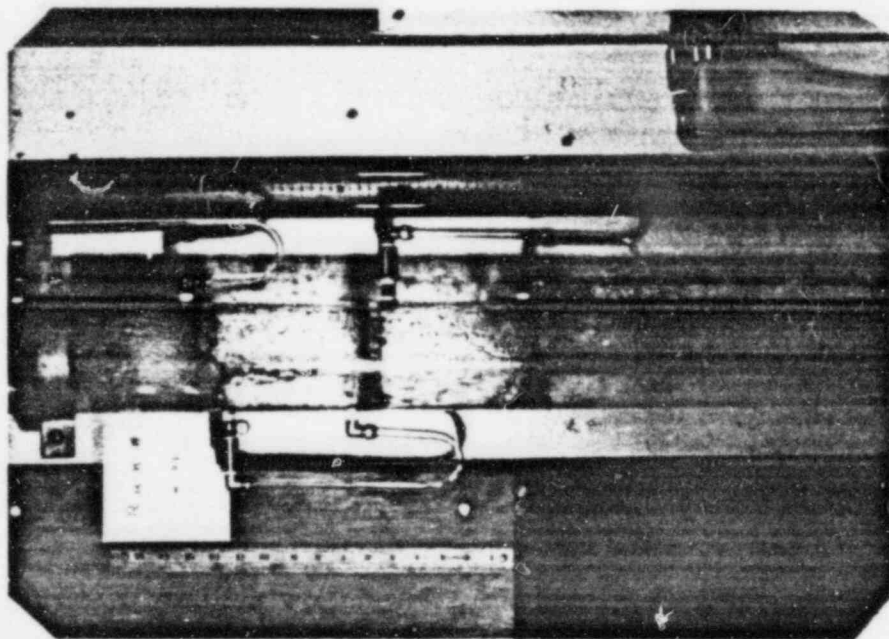


Figure 115. Results for Liquid Hold Up
Test Run W-D1, Top Plate
Liquid Hold Up

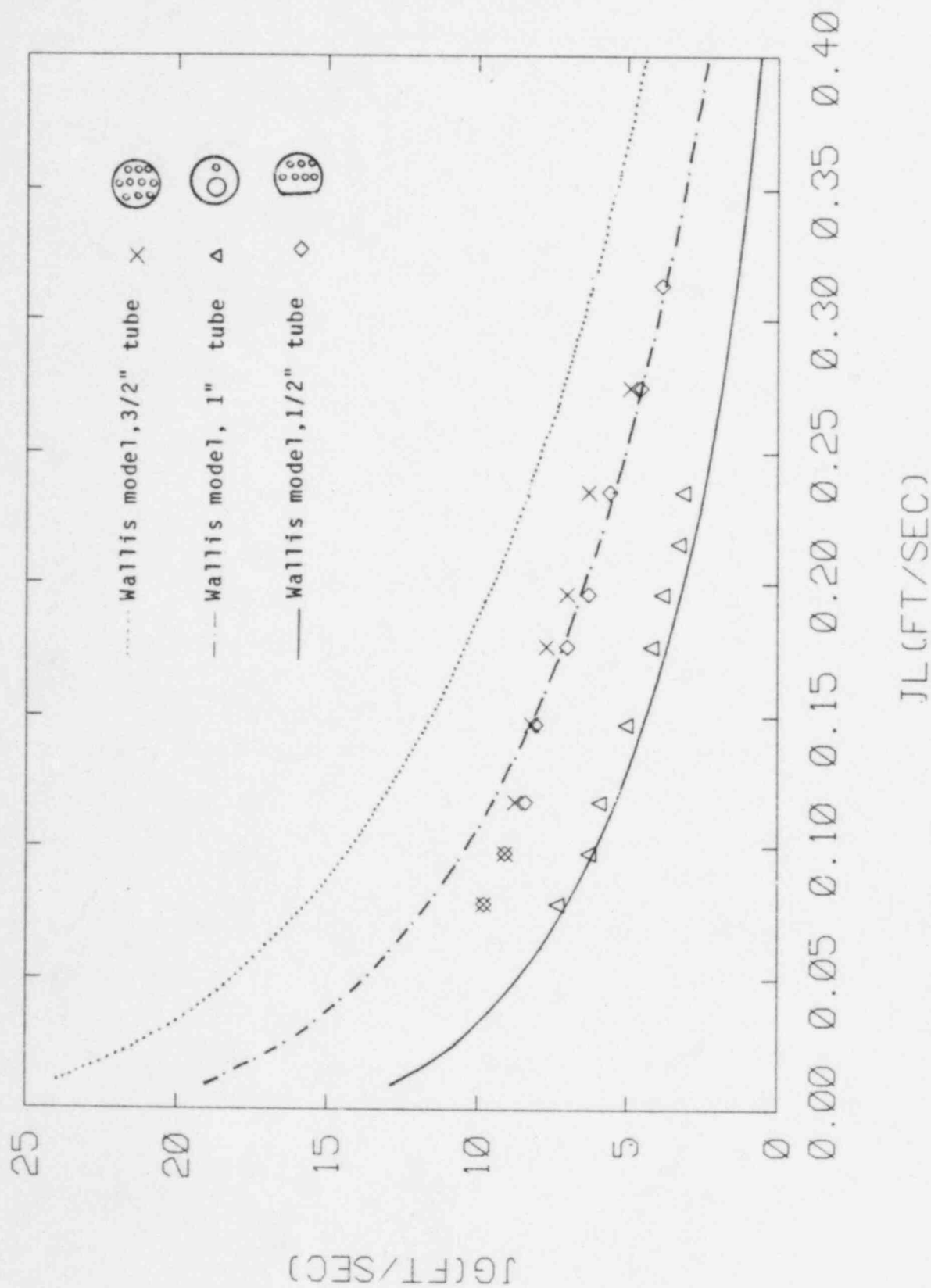


Figure 116. Comparison of Liquid Hold Up Experiment and Wallis Flooding Correlation

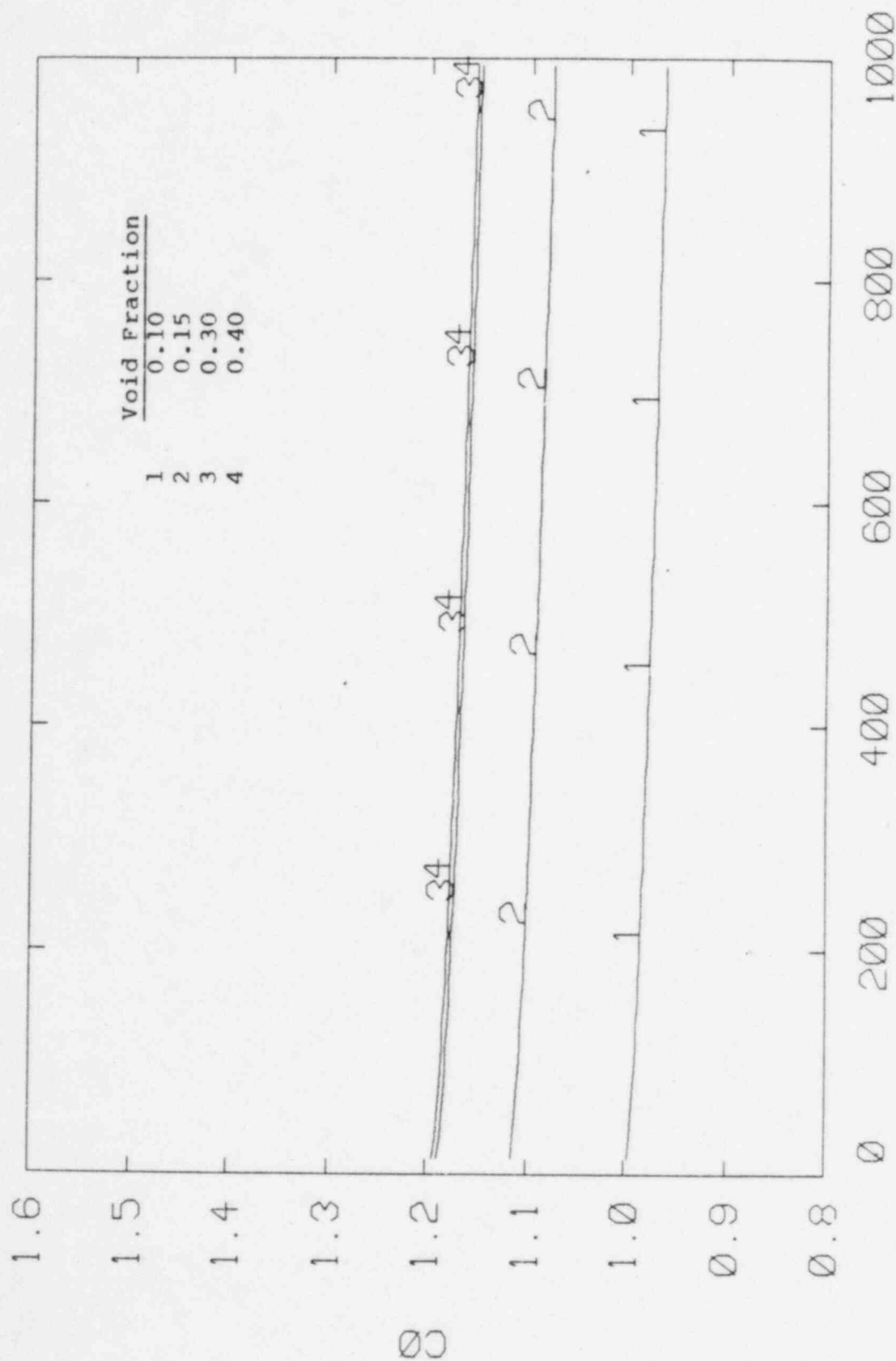


Figure 117. Recommended Drift Flux Model Constant C_0 ,
Churn-Turbulent Flow Regime

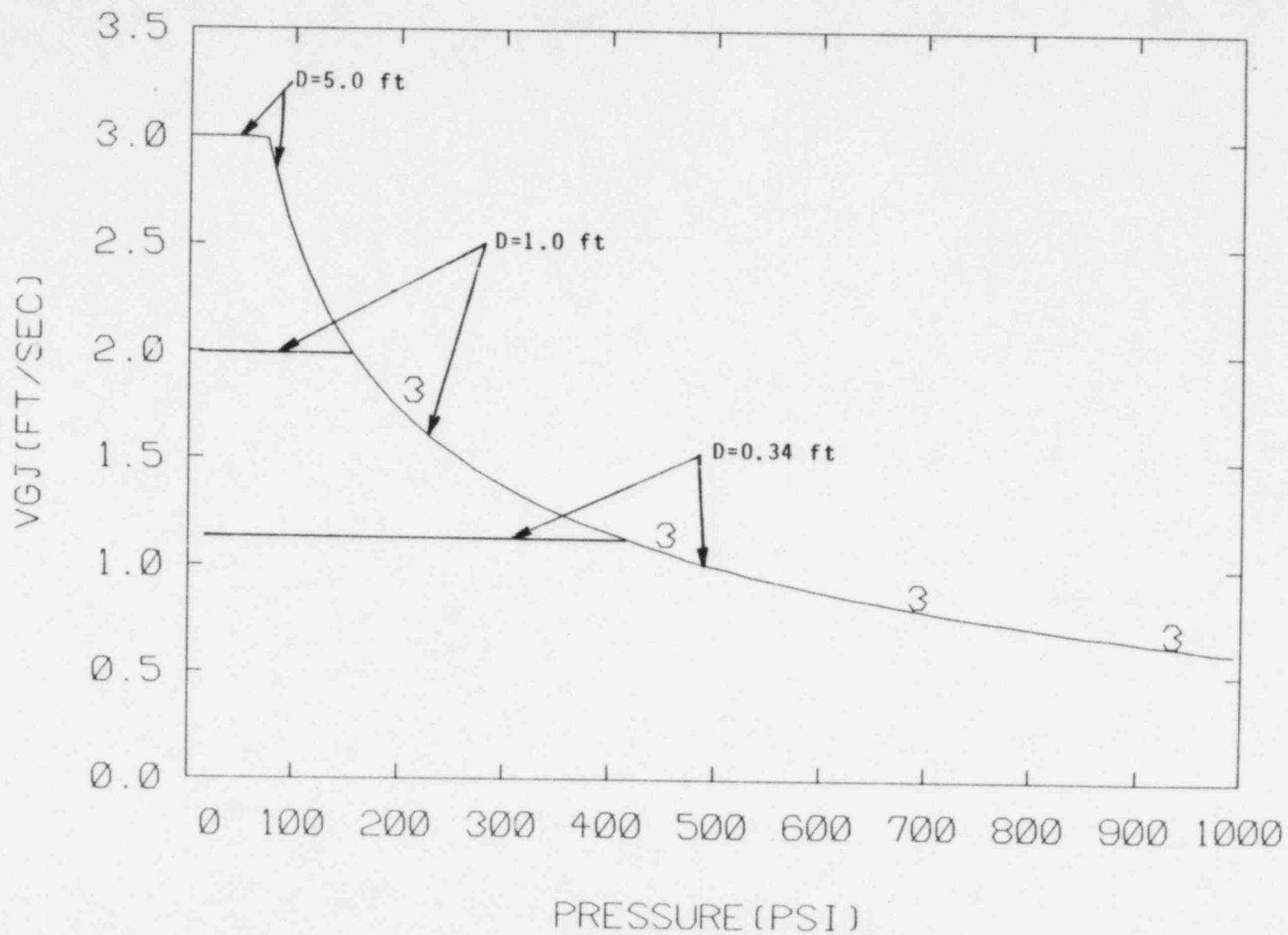


Figure 118. Recommended Drift Flux Model Constant V_{gj}
Churn-Turbulent Flow Regime

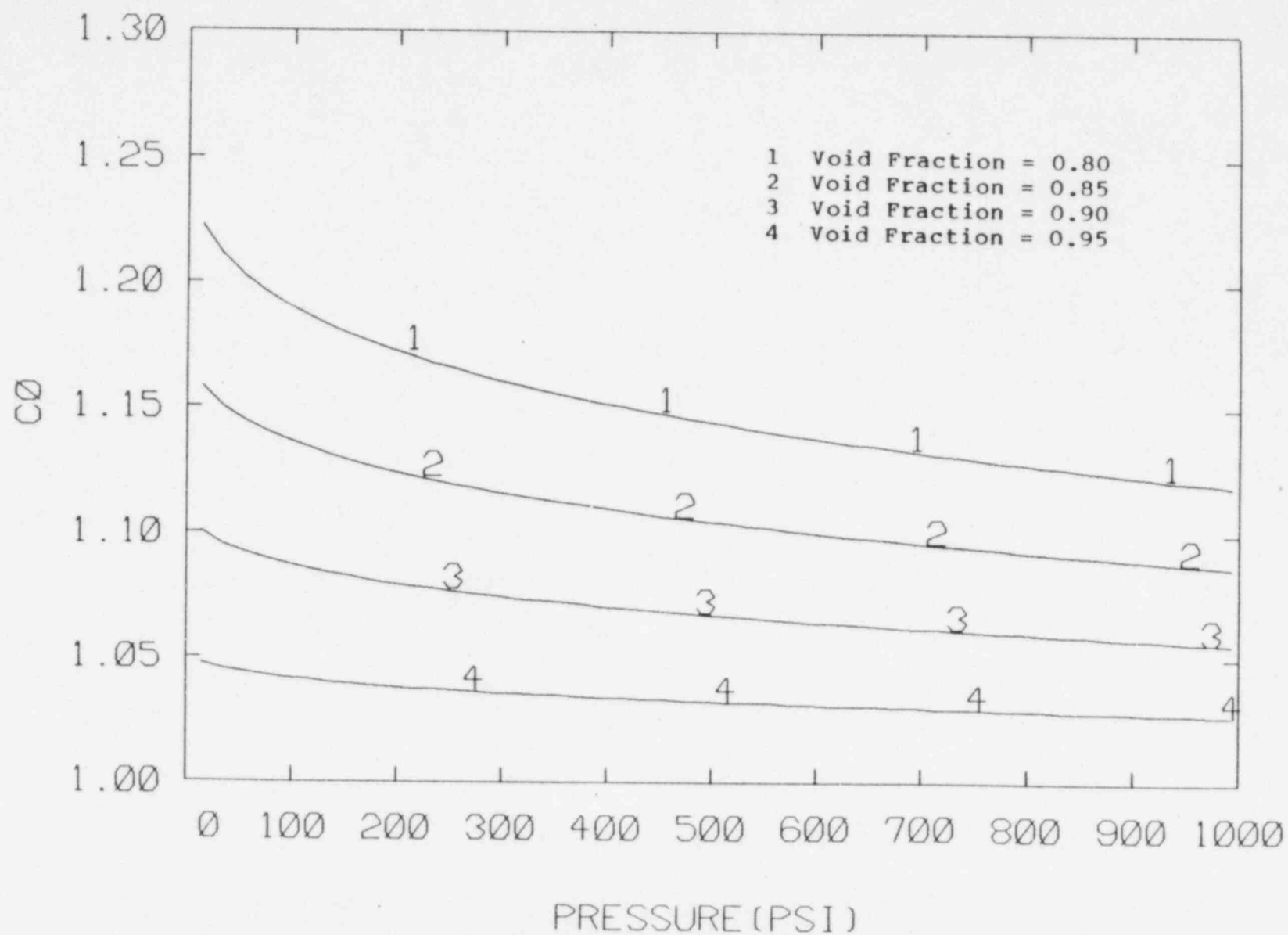


Figure 119. Recommended Drift Flux Model Constant C_0 ,
Annular Flow Regime

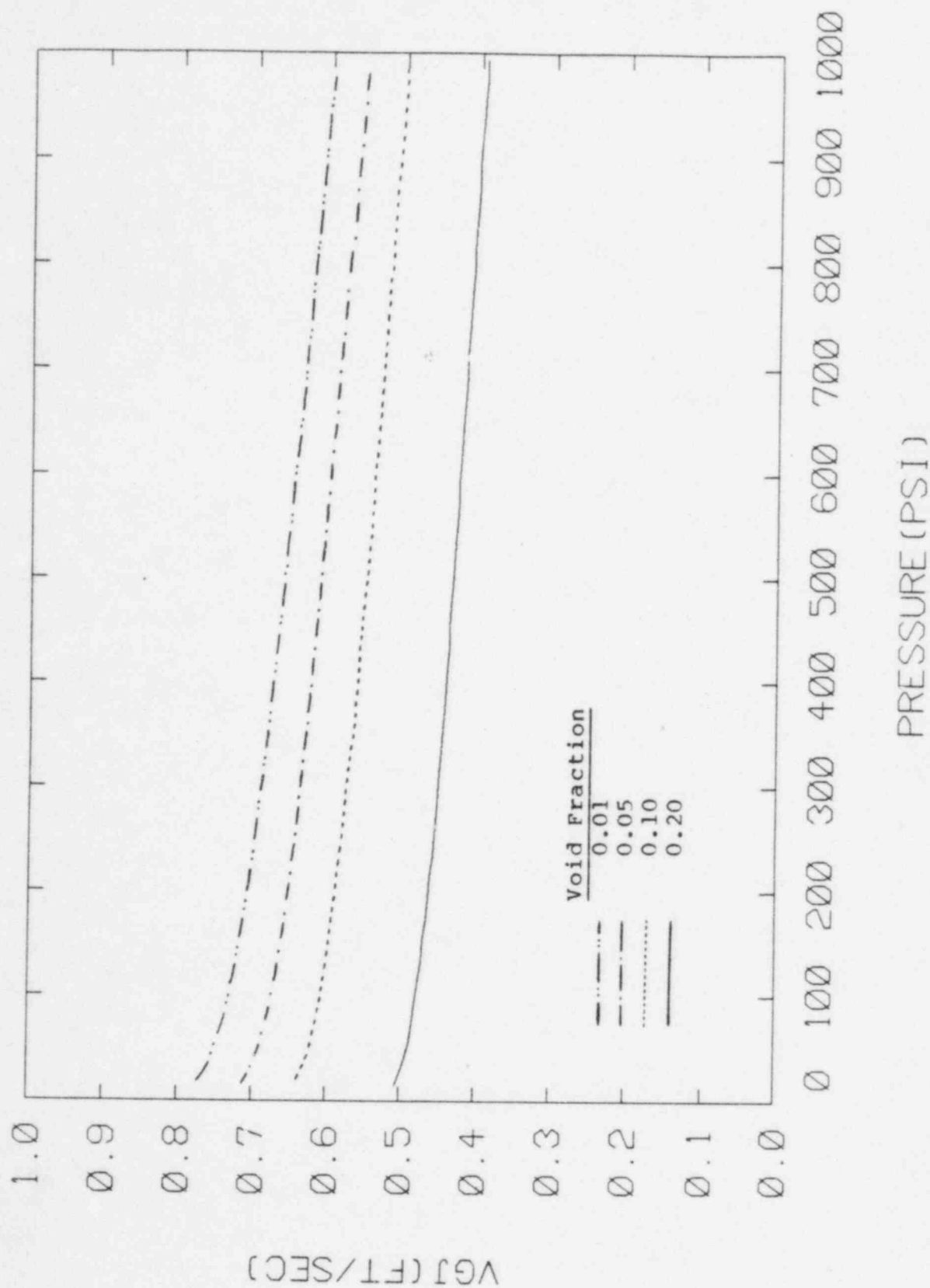


Figure 120. Recommended Drift Flux Model Constant V_{gj} ,
Bubbly Flow Regime

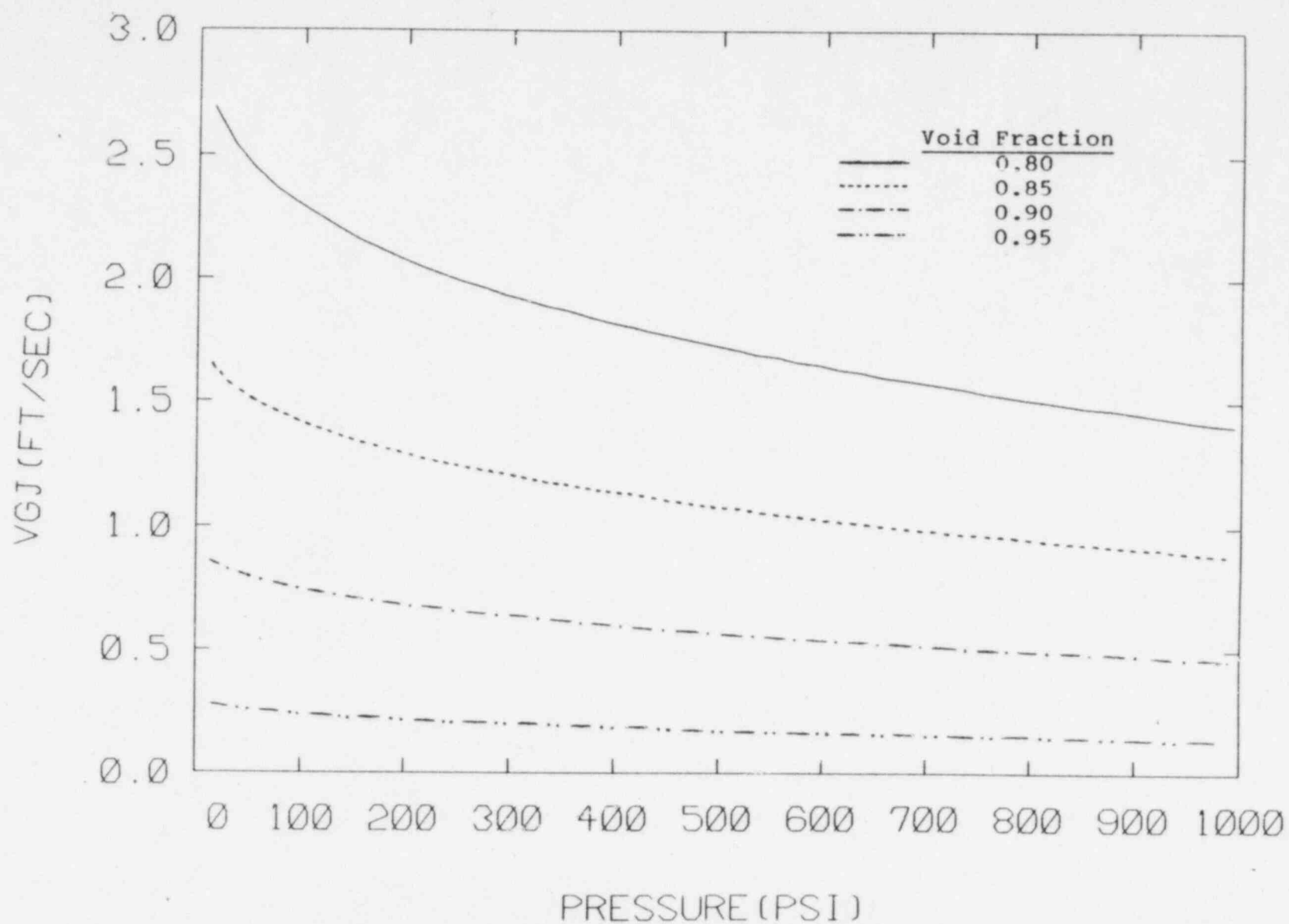


Figure 121. Recommended Drift Flux Model Constant V_{gj}
Annular Flow Regime

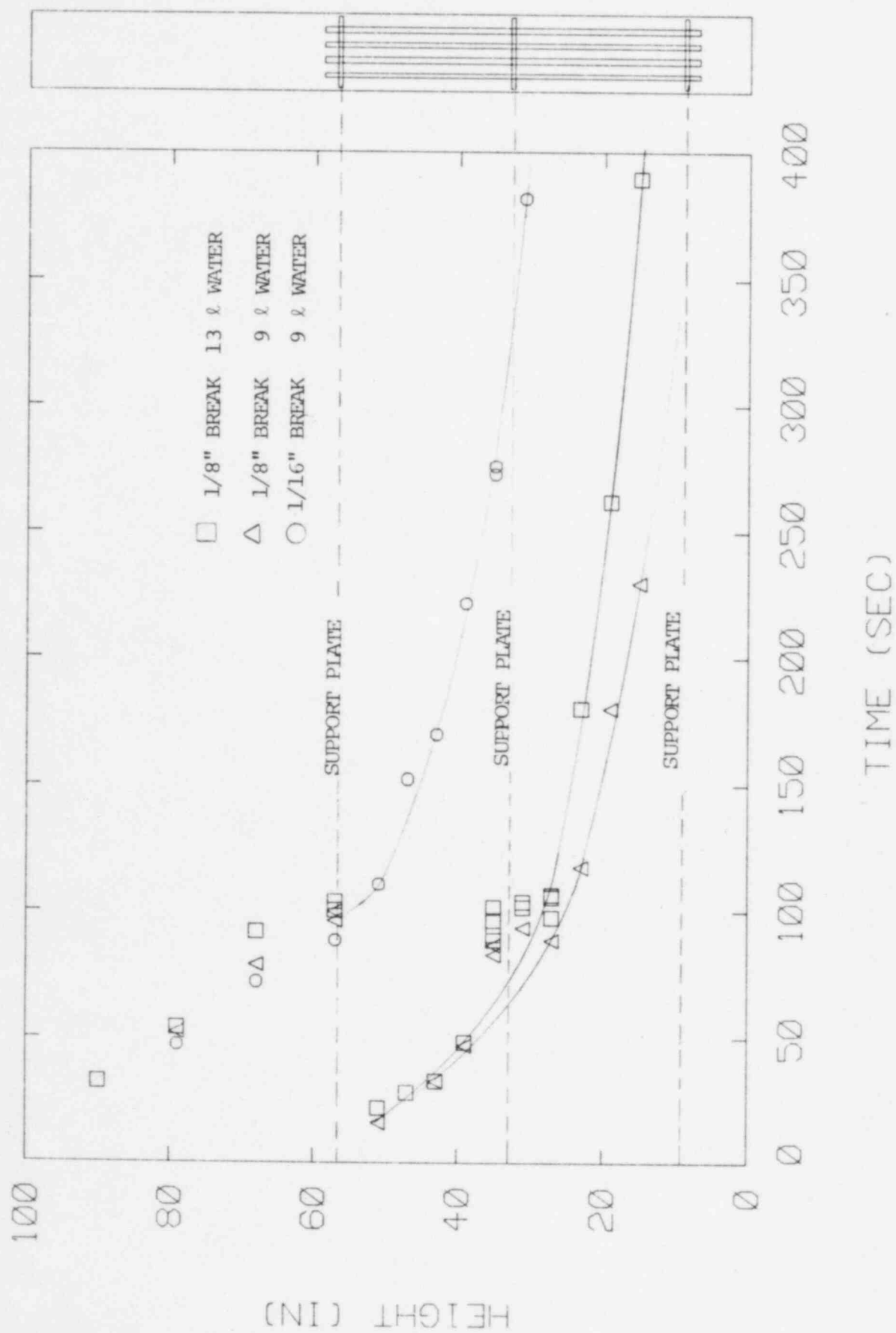


FIGURE 122. Dryout front data from blowdown experiment.

REFERENCE

1. Charlton, T.R., "RELAP5 Analyses and Support of Oconee-1 PTS Studies", NUREG/CP-0048, Vol.2, January 1984.
2. Ireland, J.R., "TRAC Analysis and Support of Oconee-1 PTS Studies", NUREG/CP-0048, Vol.2, January 1984.
3. Koenig, J.E., "TRAC Analysis of Potential Overcooling Transients at the Calvert Cliffs-1 PWR for PTS Risk Assessment", NUREG/CP-0048, Vol.2, January 1984.
4. Kryter, R.C., et al., "Evaluation of Pressurized Thermal Shock", ORNL TM-8072, NUREG/CR-2083, October 1981.
5. Young, M.Y., et al., "Prototypical Steam Generator Transient Test Program : Test Plan/Scaling Analysis", EPRI Np-3494, NUREG/CR-3661, WCAP-10475, September 1984.
6. White, J.D., "Integration of PTS Studies to Calculate Through Wall Crack Probabilities", NUREG/CP-0048, Vol.2, January 1984.
7. Rohatgi, U.S., et al., "Quality Assurance of PTS Thermal Hydraulic Calculations at BNL", NUREG/CP-0048, Vol.2, January 1984.
8. Chexal, B., et al., "Calvert Cliffs 1 Reactor Vessel : Pressurized Thermal Shock Analysis for a small Steam Line Break", EPRI NP-3752-SR, November 1984.
9. Boucher, T.J. and Wolf, J.R., "Experimental Operating Specification for Semiscale MOD-2C Feedwater and Steam Line Break Experiment Series", EGG-SEMI-6625, May 1984.
10. Collier, J.G., Convective Boiling and Condensation, McGraw-Hill Book Co., England, 1980.
11. Radovcich, N.A. and Moissis, R., "The Transition from Two-Phase Bubble Flow to Slug Flow", Report No. 7-7673-22 Dept. of Mech. Eng., MIT, 1962.
12. Taitel, Y. and Dukler, A.E., "Flow Regime Transitions for Vertical Upward Gas-Liquid Flow: a Preliminary Approach Through Physical Modeling", Paper Presented at AIChE 70th Annual Meeting, New York, Session on Fundamental Research in Fluid Mechanics (1977).
13. Ishii, M., "One-Dimensional Drift-Flux Model and Constitutive Equations for Relative Motion Between Phases in Various Two-Phase Flow Regimes", ANL-77-47, October 1977.

14. Zuber, N. and Findlay, J.A., "Average Volumetric Concentration in Two-Phase Flow Systems", Trans. ASME, J. of Heat Transfer, pp. 453-468, November 1965.
15. Wallis, G.B., One Dimensional Two-Phase Flow, McGraw-Hill Book Company, 1969.
16. Bertodano, M.A.L.D., "Fast Computational Methods for Two Phase Flow Situations in Pressurized Water Reactors", Nuclear Engineer Thesis at MIT, January 1983.
17. Wilson, J.F., Grenda, R.J., and Patterson, J.F., "The Velocity of Rising Stream in a Bubbling Two-Phase Mixture", Trans. ANS 5 Ser. 25, 151 (1962).
18. Styrikovich, M.A., and Vinokour, J.G., "Experimental Data on Hydrodynamics of Two-Phase Mixture", Teploenergetika, Vol. 8, no. 9, p. 56, 1961.
19. Fauske, H.K., "The Discharge of Saturated Water Through Tubes", Chem. Eng. Prog. Ser. 61, 59, 210-216, 1965.
20. Fauske, H.K., "Contribution to the Theory of Two-Phase, One-Component Critical Flow", ANL-6633, Argonne National Lab, October 1962.
21. Moody, F.J., "Maximum Flow Rate of a Single Component, Two-Phase Mixture", J. Heat Trans., 87(1), 134-142 (1965).
22. Levy, S., "Prediction of Two-Phase Critical Flow Rate", ASME 64-HT-8, 1964.
23. Henry, R.E., "The Two-Phase Critical Discharge of Initially Saturated or Sub-Cooled Liquid", Nuclear Sci. Eng., 41(3), 336-343 (1970).
24. Edmonds, D.K. and Smith, R.V., "Comparison of Mass Limiting Two-Phase Flow in a Straight Tube and in a Nozzle", Symposium on Two-Phase Flow, Vol. 1, G401-G414, Univ. Exeter, England, 1966.
25. Pasqua, P.F., "Metal Stable Liquid Flow Through Short Tubes", Ph.D. Thesis, Northwestern University, 1951.
26. Sozzi, G.L. and Sutherland, W.A., "Critical Flow of Saturated and Subcooled Water at High Pressure", NEDO-13418, July 1975, ASME Symposium of Non-Equilibrium Two-Phase Flow, Winter Annular Meeting, Houston, Nov.-Dec. 1975.
27. Lahey, Jr., R.T. and Moody, F.J., The Thermal Hydraulics of a Boiling Water Nuclear Reactor, ANS Publications.
28. El-Wakil, M.M., Nuclear Heat Transport, International Textbook, Scranton, Pa., 1971.

29. Tong, I.S. and Weisman, J., Thermal Analysis of Pressurized Water Reactors, ANS Publication, Illinois, 1979.
30. Taylor, D.D., et al., "TRAC-BD1/MOD1: An Advanced Best Estimate Computer Program for Boiling Water Reactor Transient Analysis", NUREG/CR-3633, EGG-2294, April 1984.
31. Wulff, W., "The Kinematics of Moving Flow Regime Interface in Two-Phase Flow", Proceeding of the Third CSNI Specialist Meeting, Hemisphere Publishing Corporation, 1983.
32. Raghuram, S., et al., "Iodine Behavior in Steam Generator Tube Rupture Accidents", NUREG-CR-2683, April 1982.
33. Kataoka, I. and Ishii, M., "Mechanistic Modeling and Correlations for Pool Entrainment Phenomena", NUREG/CR-3304, ANL-83-37, April 1983.
34. Holzer, B., et al., "Specification of OECD Standard Problem No.6 : Determination of Water Level and Phase Separation Effects During the Initial Blowdown Phase", Battelle-Institute of Frankfurt(Main) Report, February 1977.
35. Saha, P., et al., "Independent Assessment of TRAC-PD2 and RELAP5/MOD1 Codes at BNL in FY 1981", NUREG/CR-3148, BNL-NUREG-51645, December 1982.
36. Findlay, J.A., "BWR Refill-Reflood Program Task 4.8-Model Qualification Task Plan", NUREG/CR-1899, EPRI NP-1527, GEAP-24898, August 1981.
37. Sliter, B.C., "Loss of Coolant and Emergency Core Cooling Models for General Electric Boiling Water Reactors", NEDO-10329, Class 1, General Electric Company, April 1971.
38. Parlos, A.G., "Steam Generator Carryover and Heat Transfer During a Steam Line Break Accident", M.S. Thesis, MIT, February 1985.
39. Brown, D., and Griffith, P., MIT to Hopenfeld, J., NRC, "Carryover, Fallback and Heat Transfer in Steam Generator", Progress Report, May 1985.

NRC FORM 335 (2-84) NRCM 1102, 3200, 3202 SEE INSTRUCTIONS ON THE REVERSE		U.S. NUCLEAR REGULATORY COMMISSION		1. REPORT NUMBER (Assigned by T/DC, add Vol. No., if any) NUREG/CR-4376 EPRI NP-4298	
2. TITLE AND SUBTITLE Heat Transfer, Carryover and Fall Back in PWR Steam Generators During Transients				3. LEAVE BLANK	
5. AUTHOR(S) L-H. Liao, A. Parlos, P. Griffith				4. DATE REPORT COMPLETED MONTH: July YEAR: 1985	
7. PERFORMING ORGANIZATION NAME AND MAILING ADDRESS (Include Zip Code) Massachusetts Institute of Technology Cambridge, MA 02139				6. DATE REPORT ISSUED MONTH: September YEAR: 1985	
10. SPONSORING ORGANIZATION NAME AND MAILING ADDRESS (Include Zip Code) Division of Accident Evaluation Office of Nuclear Regulatory Research U.S. Nuclear Regulatory Commission Washington, D.C. 20555				8. PROJECT/TASK/WORK UNIT NUMBER B7229	
12. SUPPLEMENTARY NOTES				11a. TYPE OF REPORT Technical	
13. ABSTRACT (200 words or less) The concern over Pressurized Thermal Shock (PTS), along with many other concerns, indicates the need for accurate knowledge of the steam generator behavior during the blowdown of the steam generator secondary side. To fulfill this need a computer program, SIT-SG (Simulator of Transient in Steam Generator) is developed. This is a one-dimensional best-estimate code with the assumption that the vapor and liquid phases are in thermal equilibrium but not homogeneous. The drift flux model is used to describe the relationship between the vapor and the liquid phase velocity. No momentum equation is required for SIT-SG because the detailed pressure distribution in the vessel is not important for the blowdown process. Based on the comparisons between the code predictions and the data obtained from the experiments conducted in Battelle-Frankfurt and GE, the best drift flux model constants for various flow regimes are selected. SIT-SG has been used to predict the carryover, fall back, and heat transfer for the MIT steam generator blowdown experiments. The results are encouraging. It is found that the measured dryout front is much higher than the calculated mixture level. If the effective heat transfer area is determined from the mixture level, the primary-to-secondary heat transfer will be substantially underpredicted. From the result of the liquid hold up study we would expect to find two mixture levels, one in the bottom of the steam generator and one above the top tube support plate, provided that flooding occurs at all.				b. PERIOD COVERED (Inclusive dates)	
14. DOCUMENT ANALYSIS - a. KEYWORDS/DESCRIPTORS heat transfer steam generators				15. AVAILABILITY STATEMENT Unlimited	
b. IDENTIFIERS/OPEN ENDED TERMS				16. SECURITY CLASSIFICATION (This page) Unclassified (This report) Unclassified	
				17. NUMBER OF PAGES	
				18. PRICE	

UNITED STATES
NUCLEAR REGULATORY COMMISSION
WASHINGTON, D.C. 20555

OFFICIAL BUSINESS
PENALTY FOR PRIVATE USE, \$300

FOURTH CLASS MAIL
POSTAGE & FEES PAID
USNRC
WASH D C
PERMIT No G 87

(cover 4)